Harnessing Dithiolene Complexes For Carbon Dioxide Activation

Isaac Furney

A Thesis Submitted to

The University of East Anglia

For the Degree of Doctor of Philosophy

Submitted March 2025

This copy of the thesis has been supplied on condition that anyone who consults it is understood to recognise that its copyright rests with the author and that use of any information derived therefrom must be in accordance with current UK Copyright Law. In addition, any quotation or extract must include full attribution.

Abstract

Molybdenum and tungsten are found in the active site of a number of metalloenzymes. Bound to these atoms are sulphide-containing ligands, more commonly referred to in the literature as dithiolene ligands. The combination of metal and ligand allows for catalysis close to the thermodynamic limit of carbon dioxide reduction to formate to take place. Thus, these active sites are attractive targets for chemists, as their potential for industrial application is limitless.

This thesis focuses on the synthesis of mimics of the active site of the formate dehydrogenase enzyme (FDH). By providing functional models of the active site, we wish to identify the necessity of proton relays in close proximity to the central metal ion for catalysis; their presence is seen in the native enzyme, but is missing from the catalytically-competent models in the literature.

A route to a novel molybdenum-oxo bis-dithiolene complex was successfully created, streamlined and improved by previous researchers within the group. This novel route was then used to generate more ligands and subsequent complexes in an effort to showcase the versatility of the synthesis. The terminal functionality of the FDH active site is not limited to just oxo ligands, but to other elements in Group 18 such as sulphur and selenium. Attempts at synthesising the sulphido analogue of the target complex were made, but unfortunately this was unsuccessful. A 'third generation' pro-ligand was also synthesised with the goal of creating novel, bridged molybdenum-oxo dithiolene complexes. Unfortunately, attempts to synthesise this

new kind of dithiolene complex were unsuccessful. The synthesis of the tungsten analogues of these compounds was explored but merely added to the reputation of the difficulty in working with tungsten compounds; fortunately, the tungsten analogue of the target complex was synthesised for a time, and key data points were recorded.

Computational methods were employed to better understand the physical properties of the synthesised complexes, with a focus on the accurate prediction of the infrared stretching band of the Mo=O bond. This process of identifying this stretch was aided by the use of five functionals, each with varying constraints. The functionals that achieved the most accurate predictions can now be reused as a standard for other researchers to conduct computational studies on molybdenum-oxo dithiolene complexes with a high degree of certainty in the accuracy of their results.

The importance of electrochemical methods for understanding the behaviour of redox-active metals cannot be understated. Several of the synthesised complexes were subjected to cyclic voltammetry, allowing structure-activity relationships to be derived for the Mo^{IV}/Mo^V and Mo^V/Mo^{VI} redox couples.

The target complex and its non-functionalised analogue were tested for their catalytic activity with the goal of seeing the catalytic reduction of carbon dioxide into formate. Although the results for the reduction of carbon dioxide to formate and oxygen atom transfer catalysis were poor, oxidation catalysis of formate showed that the complexes were four times more effective with the proton relays than without.

Access Condition and Agreement

Each deposit in UEA Digital Repository is protected by copyright and other intellectual property rights, and duplication or sale of all or part of any of the Data Collections is not permitted, except that material may be duplicated by you for your research use or for educational purposes in electronic or print form. You must obtain permission from the copyright holder, usually the author, for any other use. Exceptions only apply where a deposit may be explicitly provided under a stated licence, such as a Creative Commons licence or Open Government licence.

Electronic or print copies may not be offered, whether for sale or otherwise to anyone, unless explicitly stated under a Creative Commons or Open Government license. Unauthorised reproduction, editing or reformatting for resale purposes is explicitly prohibited (except where approved by the copyright holder themselves) and UEA reserves the right to take immediate 'take down' action on behalf of the copyright and/or rights holder if this Access condition of the UEA Digital Repository is breached. Any material in this database has been supplied on the understanding that it is copyright material and that no quotation from the material may be published without proper acknowledgement.

Acknowledgements

I would like to thank the University of East Anglia for the opportunity to do a Ph.D. I give special thanks to my supervisor, Joseph Wright, for both his extensive chemistry and LaTeX experience, which was of tremendous help. This thanks also extends to Claire Jones and Trey Koev for their help with physical and spectroscopic techniques.

I would like to thank my mother, Norma, my father, Brian, and my three siblings, Seth, Ruby, and Lola, as well as my extended family.

Finally, I would like to acknowledge Dr. Richard Newbold for igniting my interest in chemistry all those years ago and starting me on my academic journey.

Contents

1	Intr	oducti	ion	1
	1.1	The H	lydrogen Economy	1
	1.2	Evolut	tionary Development of Molybdenum- and Tungsten-Containing	
		Enzyn	nes	5
1.3 The Families of Molybdenum and Tungsten Containing Enzyme			amilies of Molybdenum and Tungsten Containing Enzymes .	7
		1.3.1	Xanthine Oxidase	7
		1.3.2	Sulphite Oxidase	9
		1.3.3	Dimethyl Sulphoxide (DMSO) Reductase	11
		1.3.4	A Closer Look at Formate Dehydrogenase	13
	1.4	The A	active Site of Formate Dehydrogenase	20
		1.4.1	The Cellular Synthesis of Moco	21
		1.4.2	The Dithiolene	22
		1.4.3	The Pyran Ring	25
		1.4.4	The Pterin	26
		1.4.5	The Terminal Functionality and Protein Residues	27
	1.5	Biomi	metic/Non-Biomimetic Complexes of Molybdoenzymes and	
		their A	Associated Activity	27
		1.5.1	Xanthine Oxidase Mimics	27
		1.5.2	Sulphite Oxidase Mimics	28

		1.5.3	DMSO Reductase Mimics	29
		1.5.4	Alternative mimics	35
	1.6	Resear	ch Aims	39
2	Syn	$ ext{thesis}$	of a Molybdenum Functionalised Dithiolene Complex	41
	2.1	Introd	uction	41
		2.1.1	Why Formate Dehydrogenase?	41
		2.1.2	Molybdenum Dithiolene Complexes	43
		2.1.3	A Brief History of the Synthesis within the Wright Group .	44
		2.1.4	The Synthetic Strategy and Goals	47
	2.2	An Ini	tial Attempt at Synthesising the Target Molybdenum Complex	48
		2.2.1	2-(Propyn-1-yl)benzyl Alcohol	48
		2.2.2	Di <i>iso</i> propyl Xanthogen Disulphide	50
		2.2.3	The Functionalised Dithione	51
		2.2.4	Protected Dithiones	52
		2.2.5	Nickel Dithiolenes	54
		2.2.6	The Molybdenum-Oxo Precursor	55
		2.2.7	Direct Transmetallation	55
	2.3	Troubl	eshooting	57
		2.3.1	The Synthesis of $Ni(S_2C_2Ph_2)_2$	57
		2.3.2	The Synthesis of $Mo(CO)_2(S_2C_2Ph_2)_2$	58
		2.3.3	The Synthesis of $(Et_4N)_2[MoO(S_2C_2Ph_2)_2]$	58
		2.3.4	The Synthesis of $Mo(CO)_2(S_2C_2MeBnOH)_2$	59
		2.3.5	Inserting the Mo=O Functionality from the Molybdenum	
			Carbonyl Intermediate	60
		2.3.6	Alternatives to Transmetallation from Nickel to Molybdenum	61
		2.3.7	Alternative Routes to the Novel Ligand	62
	2.4	Stream	alining the Synthesis of the Functionalised Dithiolene Ligand	63

		2.4.1	Technique/Solvent	63
		2.4.2	Reagents	64
		2.4.3	Work-up	64
	2.5	The Sy	with the sis of $(Et_4N)_2[MoO(S_2C_2MeBnOH)_2]$	65
	2.6	Summ	ary	66
3	Fur	ther Sy	onthesis of Molybdenum and Tungsten Dithiolenes	67
	3.1	Introd	uction	67
	3.2	Adding	g to the Catalogue of Mo=O Dithiolene Complexes	69
		3.2.1	The Synthesis of 1,3-Dithiol-2-one-4-phenyl-5-methyl $ \dots $	69
		3.2.2	The Synthesis of 1,3-Dithiol-2-one-4-phenyl-5-ethyl $ \dots \dots $	69
		3.2.3	The Synthesis of 1,3-Dithiol-2-one-4-phenyl	70
		3.2.4	The Synthesis of 1,3-Dithiol-2-one-5-benzyl Alcohol	72
		3.2.5	The Synthesis of 1,3-Dithiol-2-one-4-para-aniline	72
		3.2.6	The Synthesis of $(Et_4N)_2[MoO(S_2C_2MePh)_2]$	73
		3.2.7	The Synthesis of $(Et_4N)_2[MoO(S_2C_2EtPh)_2]$	75
		3.2.8	The Synthesis of $({\rm Et_4N})_2[{\rm MoO}(S_2C_2HPh)_2]$	76
		3.2.9	The Synthesis of $({\rm Et_4N})_2[{\rm MoO}(S_2C_2HBnOH)_2]$	77
		3.2.10	The Synthesis of $({\rm Et_4N})_2[{\rm MoO}(S_2C_2HNH_2)_2]$	78
	3.3	Advan	ced Ligand Synthesis	79
		3.3.1	A Bridged Ligand	79
		3.3.2	Coordination of the Bridged Ligand	82
		3.3.3	Post-coordination Functionalisation	83
	3.4	Attem	pts at Accessing the Mo=S Functionality	84
		3.4.1	The Synthesis of Ammonium Tetrathiomolybdate	85
		3.4.2	The Synthesis of Tetraethylammonium Tetrathiomolybdate	85
		3.4.3	The Synthesis of $(Et_4N)_2[MoS(S_4)_2]$	86
		3 4 4	The Synthesis of (Et ₄ N) ₂ [MoS(S ₂ C ₂ MeBnOH) ₂]	87

	3.5	Tungs	ten Dithiolene Complexes	
		3.5.1	The Synthesis of $K_3Na[WO_2(CN)_4] \cdot 6H_2O \dots 89$	
		3.5.2	The Synthesis of $(Et_4N)_2[WO(S_2C_2HPh)_2]$ 89	
		3.5.3	The Synthesis of $(Et_4N)_2[WO(S_2C_2MePh)_2]$ 90	
		3.5.4	The Synthesis of $(Et_4N)_2[WO(S_2C_2MeBnOH)_2]$ 90	
		3.5.5	The Synthesis of $(Et_4N)_2[WO(S_2C_2HBnOH)_2]$ 91	
	3.6	Summ	nary	
4	Den	sity F	unctional Theory 94	
	4.1	Introd	luction	
		4.1.1	Selection of Approach	
		4.1.2	Symmetry Adapted Molecular Orbital Theory (SAMO) of	
			Square-based Pyramidal Complexes	
		4.1.3	Selection of Approach Continued	
	4.2	The Simulation of Dithiolene Complexes		
		4.2.1	$[MoO(S_2C_2MeBnOH)_2]^{2-} \dots \dots$	
		4.2.2	$[MoO(S_2C_2MePh)_2]^{2-} \dots \dots$	
		4.2.3	$[MoO(S_2C_2HBnOH)_2]^{2-}$	
		4.2.4	$[MoO(S_2C_2HPh)_2]^{2-}$	
		4.2.5	Summary	
5	Elec	ctroche	emistry 121	
	5.1	Introd	luction	
		5.1.1	Redox Processes and the Nernst Equation	
		5.1.2	Diffusion	
		5.1.3	Cyclic Voltammetry	
		5.1.4	Molybdenum Dithiolenes	
	5.2	Cyclic	Voltammetry of $(Et_4N)_2[MoO(S_2C_2MeBnOH)_2]$	

	5.3	Cyclic	$\label{eq:continuous_section} \mbox{Voltammetry of } (\mbox{Et}_4\mbox{N})_2[\mbox{MoO}(\mbox{S}_2\mbox{C}_2\mbox{MePh})_2] \ . \ . \ . \ . \ . \ . \ . \ . \ . \ $. 134	
	5.4	Cyclic	Voltammetry of $(Et_4N)_2[MoO(S_2C_2HBnOH)_2]$. 137	
	5.5	Cyclic	Voltammetry of $(Et_4N)_2[MoO(S_2C_2HPh)_2]$. 139	
	5.6	Cyclic	Voltammetry of $Mo(CO)_2(S_2C_2MeBnOH)_2$. 143	
	5.7	Cyclic	Voltammetry of $(Et_4N)_2[WO(S_2C_2MeBnOH)_2]$. 144	
	5.8	Summary			
6	Cat	alysis		147	
	6.1	Introdu	uction	. 147	
	6.2	Reduct	tion Catalysis	. 149	
		6.2.1	Electrocatalytic Reduction of Protons to Hydrogen $\ . \ . \ .$. 149	
		6.2.2	Photocatalytic Reduction of Carbon Dioxide to Formate $% \left(1\right) =\left(1\right) \left(1\right) +\left(1\right) \left(1\right) \left(1\right) +\left(1\right) \left(1$. 150	
	6.3	Oxidat	ion Catalysis	. 151	
		6.3.1	The Synthesis of Tetrabutylammonium Formate	. 153	
		6.3.2	Electrocatalytic Oxidation of Formate using $(\mathrm{Et_4N})_2$		
			$[\mathrm{MoO}(\mathrm{S_2C_2MeBnOH})_2]\ .\ .\ .\ .\ .\ .\ .\ .$. 154	
		6.3.3	Electrocatalytic Oxidation of Formate using $(\mathrm{Et_4N})_2$		
			$[\mathrm{MoO}(\mathrm{S_2C_2MePh})_2]\ .\ .\ .\ .\ .\ .$. 158	
		6.3.4	The Effect of Proton Relays on Oxidation Catalysts	. 161	
	6.4	OAT Catalysis		. 163	
	6.5	Summa	ary	. 168	
7	Sun	nmary a	and Conclusions	171	
8	Exp	erimen	ital	176	
	8.1	Genera	તી	. 176	
	8.2	2-(Prop	pyn-1-yl) benzyl Alcohol (24)	. 178	
	83	2-Ethy	nylbongyl Alcohol (76)	170	

8.4	Phenylprop-1-yne (72)
8.5	Potassium Iso propyl Xanthate (25)
8.6	Di iso propyl Xanthogen Disulphide (26)
8.7	1,3-Dithiol-2-one-4-benzyl alcohol-5-methyl (27)
8.8	1,3-Dithiol-2-one-4-phenyl-5-methyl (73)
8.9	1,3-Dithiol-2-one-4-phenyl-5-ethyl (74)
8.10	1,3-Dithiol-2-one-4-phenyl (75)
8.11	1,3-Dithiol-2-one-4-benzyl Alcohol (21)
8.12	1,3-Dithiol-2-one-4- $para$ -aniline (77)
8.13	Di-(1,3-dithiol-2-one-5-methyl-4-benzyl) ethyl Malonate (82) 188
8.14	1,3-Dithiol-2-one-5-methyl-4-benzyloxy-($tert$ -butyl)dimethylsilane (${f 28}$) 189
8.15	$Ni(S_2C_2MeBnOH)_2)$ (29)
8.16	$Ni(S_2C_2Ph_2)_2$ (31)
8.17	$Mo(CO)_2(MeBnOH)_2$ (22)
8.18	$Mo(CO)_2(S_2C_2Ph_2)_2$ (33)
8.19	$K_3Na[MoO_2(CN)_4] \cdot 6 H_2O (13) \dots 193$
8.20	$K_3Na[WO_2(CN)_4] \cdot 6 H_2O (87) \dots 194$
8.21	Ammonium Tetrathiomolybdate (84)
8.22	Tetraethylammonium Tetrathiomolybdate (85) 196
8.23	$(Et_4N)_2[MoS(S_4)_2]$ (86)
8.24	$(Et_4N)_2[MoO(S_2C_2MeBnOH)_2]$ (30)
8.25	$(Et_4N)_2[MoO(S_2C_2MePh)_2]$ (78)
8.26	$(Et_4N)_2[MoO(S_2C_2HPh)_2]$ (41)
8.27	$(Et_4N)_2[MoO(S_2C_2EtPh)_2]$ (79)
8.28	$({\rm Et_4N})_2[{\rm MoO}({\rm S_2C_2HBnOH})_2]$ (80)
8.29	$({\rm Et_4N})_2[{\rm MoO}({\rm S_2C_2HPhNH_2})_2]$ (81)
8.30	$(Et_4N)_2[MoO(S_2C_2Ph_2)_2]$ (34)

. 205
. 206
. 207
. 207
. 207
. 207
. 208
. 208
. 209
. 209
. 209
. 212

Chapter 1

Introduction

1.1 The Hydrogen Economy

As the years pass and the supply of fossil fuels continues to dwindle, with coal being the only fossil fuel that is feasible to extract after 2042, their negative impacts on the environment and society are becoming more noticeable. With the ever increasing demand for energy, the issue of finding a suitable alternative for fossil fuels will grow in importance. According to BP (British Petroleum), the fossil fuel supply will last 53 more years. Fortunately, many efforts to find an alternative are being made, for example, nuclear fusion at the International Thermonuclear Experimental Reactor (ITER), offshore wind farms, and the hydrogen economy.¹

Renewable energy currently accounts for 30% of global electricity production where wind and solar contributed 12% in 2022.² With regards to wind and solar, they suffer from one or both of two problems: they are not available all of the time, making them unreliable, and they can only supply energy to their local area. For example, solar panels built in the desert can only be used by people in the immediate area. These energy sources are dependent on the weather, which is temperamental; on certain days there will be no wind or it will be cloudy.

An obvious solution is to store the excess energy produced on days when the weather is favourable for days when the weather is inclement. Batteries, pumped-storage hydroelectricity (the water is pumped uphill so that it can run downhill through generators later), and solar farms that melt salt are all viable means for long-term energy storage.^{3,4}

Unfortunately, each solution has its own problems. A great amount of materials would need to be mined for the huge amounts of energy that would need to be stored. For example, lithium extracted from brine (by evaporitic mining techniques) is extracted from underground aquifers, further impoverishing the surrounding communities in some of the driest places on the planet by reducing the available water sources and contaminating the groundwater with heavy metals.⁵ In terms of pumped-storage hydroelectricity and molten salt, they are local solutions and will only work in areas within the immediate vicinity. These solutions are not global in scale.

Enter the hydrogen economy. At its core, the hydrogen economy is the direct replacement of fossil fuels with hydrogen. Hydrogen has a large gravimetric energy density, greater than conventional fossil fuels, but unfortunately a poor volumetric energy density.⁶ The mobility of hydrogen solves the main issue plaguing most renewable energies; for example, it can be shipped around the world and be bought and sold as a commodity; it is not limited to consumers in the immediate area. The real advantage of hydrogen is its potential scale and ability to seamlessly swap with fossil fuel infrastructure. For example, cities and towns across the UK feature natural gas storage tanks located on the outskirts. This natural gas infrastructure can be repurposed for hydrogen.⁷

Hydrogen also benefits from being renewable and carbon neutral: hydrogen can be obtained via the electrolysis of water, and water is the product of its combustion/oxidation. However, some external energy input is required to obtain

dihydrogen initially. As a result, it fulfils most of the requirements of the perfect alternative: a high-energy dense fuel with a low externality. The implementation of hydrogen has already begun, but on a small scale. There exist hydrogen-powered cars, buses, trains; even the international space station runs on hydrogen. But doing it on a global scale is challenging. This is because producing, storing and using hydrogen has several problems.

Classically, large quantities of hydrogen are produced through a method known as steam reforming, a process developed in the 1930s. A hydrocarbon, commonly natural gas, has superheated steam passed over it. Unfortunately, this process produces carbon monoxide, another greenhouse gas. The carbon monoxide can be captured and stored, but it is estimated that the carbon footprint is 20% greater than that of burning coal for heat when compared with this method of producing hydrogen.^{8,9} The product of hydrogen oxidation, water, is also a greenhouse gas, responsible for half of the greenhouse effect on Earth. However, water is regulated through geological and atmospheric processes; therefore, the anthropogenic influence on water vapour is minimal. But higher temperatures, as a consequence of global warming, do encourage more evaporation from bodies of water and a greater greenhouse effect contribution from water vapour.¹⁰

An alternative is to use the energy generated by renewable sources to produce hydrogen using electrolysis. Although carbon dioxide is not produced as a byproduct, it is very inefficient since the thermodynamic reduction potential of water to hydrogen at room temperature and pressure is 1.23 V, and all current electrocatalysts have some degree of overpotential (the difference between the thermodynamically determined potential and the experimental potential). The overpotential can be reduced by heating the water, but, consequently, the overall efficiency of hydrogen production is reduced because heating also requires energy. Classical electrocatalysts for this process are also heavily reliant on precious metals

such as platinum or iridium. The formation of hydrogen and oxygen gases at the electrodes contributes to the mass transport problem, where water must be transported to the electrode, and hydrogen/oxygen must be removed simultaneously to maintain the area of which the electrodes are working efficiently. Then, to use hydrogen to generate electricity, for example in a fuel cell, similar problems are also prevalent, such as the need for expensive precious metals like platinum and iridium to act as catalysts.^{11,12}

The storage and transportation of hydrogen are also issues. In most hydrogenoxygen ratios, there is an explosion risk, and therefore, the hydrogen must be stored in strong containers that are expensive to produce on an industrial scale. Unfortunately, because of the size and reactivity of hydrogen, it can penetrate metal crystals and start to corrode the tanks from the inside. ¹³ For long-term storage/transport, a hydrogen chemical transporter seems ideal, where hydrogen is present within another molecule. A common example is water, which contains $111\,\mathrm{g/L}$ of hydrogen, while a cubic metre of liquid hydrogen contains $71\,\mathrm{g/L}.^{14}$ An ideal carrier chemical should be much less dangerous, much less corrosive, and can be capable of being shipped and piped around easily. When needed, the carrier chemical can be used directly by a solid oxide fuel cell to produce energy, or the reaction can be reversed and the hydrogen retrieved. One might think that because water is so hydrogen dense that it would make the perfect hydrogen store; it is nontoxic, a liquid at room temperature, and stable in the atmosphere. Unfortunately, water is too stable. The energy required through electrolysis to convert water back into hydrogen and oxygen is greater than what would be obtained from using that hydrogen for electricity; in essence, it is a simple problem of thermodynamics.

In the project described in this thesis, the target carrier or liquid organic hydrogen carrier (LOHC) is formate. Formate can store $53 \,\mathrm{g}$ H₂/L vs. $0.089 \,870 \,\mathrm{g}$ H₂/L as gaseous hydrogen. Formate can be used as a food preservative, due to

its fungicidal properties, and a precursor to other chemicals, for example, acetic acid and methanol. Therefore the use of this molecule is not limited to just being a LOHC. With current demand at 732 000 metric tons per annum, synthesising formate/formic acid in large quantities is a highly economical pursuit. However, producing formate is a thermodynamically unfavourable process, so current methods must be improved towards catalytic means.¹⁵

1.2 Evolutionary Development of Molybdenumand Tungsten-Containing Enzymes

Molybdenum and tungsten occupy a unique position in the periodic table as being the only second and third row transition metals that contribute to biological functions in almost all organisms; from ancient archaea to modern day mammals, one or both elements are necessary. The two elements are in Group 6 of the periodic table and exhibit similar chemical properties that allow interchangeability within the active sites of the corresponding enzymes, bar nitrogenase, where no tungsten analogue is known. In fact, these metalloenzymes can be traced back to the last universal common ancestor. Therefore, it is important to understand their origin and why they are so ubiquitous in modern life.

In the present, only a few organisms prefer tungsten over molybdenum, which is unexpected given their chemical similarities and both having similar coordination spheres. For every molybdoenzyme there is an analogous tungstoenzyme, however, many billions of years ago, at the advent of multicellular evolution, tungsten was the more bioavailable of the two elements. There are many speculations on the origins of life, but one train of thought is that life began under hot, anaerobic conditions rich in sulphur.^{19–21} In such conditions, molybdenum sulphides form which are largely insoluble in water; this is in contrast to the readily soluble, low-valent

tungsten sulphides. This crucial difference in solubility would have allowed these organisms easier access to tungsten in comparison to molybdenum. Evidence for such a hypothesis can be found in the underwater hydrothermal vents of today, where microorganisms there use tungsten in the active sites of related enzymes, rather than molybdenum, mimicking the early primordial conditions thought to favour tungstoenzymes.²²

The cooling of the Earth's crust and the evolution of photosynthetic organisms allowed for cooler habitats with lower sulphur content and higher oxygen concentration in the atmosphere. Such conditions encourage the formation of water-soluble molybdate salts (MoO_4^{2-}) . This unmatched solubility in seawater means that molybdenum is the most abundant transition metal found in the oceans, even in the modern day. However, tungsten compounds are highly oxygen sensitive and have become a liability to these early organisms. Due to their chemical similarity, and increasing molybdenum availability in the environment, a switch from tungsten to molybdenum could be performed simply over evolutionary timescales. ^{19,21} In fact, it has been proposed that the lack of soluble molybdenum compounds resulted in a 'choke point' for the continued evolution of life since atmospheric dinitrogen fixation to ammonium relies heavily on molybdenum for the formation of the nitrogenase enzyme. ²³

Molybdenum's influence in our world is far-reaching. Within the carbon cycle, the formate dehydrogenase enzyme is used by acetogens (microorganisms that generate acetate) to fix carbon dioxide by reducing it into formate. These molybdenum enzymes are also potent oxidising catalysts, for example, aldehyde oxidoreductase which converts aldehydes to carboxylic acids.²⁴ In mammals, aldehyde oxidase has been linked to the synthesis of retinoic acid, essential for growth and development. Certainly in humans, sulphite oxidase is a prevalent example of our reliance on these metals, where genetic deficiency can result in neurological problems.^{25,26}

1.3 The Families of Molybdenum and Tungsten Containing Enzymes

To date, over 50 distinct types of molybdoenzymes have been identified, and they can be classified into three families based on their protein sequences and the structure of the active site: xanthine oxidase, sulphite oxidase, and dimethyl sulphoxide (DMSO) reductase. The vast majority of these enzymes belong to prokaryotes, with mammals only having four.²⁷ As mentioned above, bar nitrogenase, molybdo-and tungstoenzymes have remarkably similar active sites, but for the sake of a comprehensive understanding, each active site will be examined in turn. Due to the complexity of this super-family of enzymes, some debate has been raised as to whether greater specification for the name of each class is needed.²⁸

1.3.1 Xanthine Oxidase

Xanthine is a purine base, found in most organic tissue, and is a product of purine degradation. After its synthesis in certain biological processes, it is converted to uric acid by the action of the xanthine oxidase enzyme.²⁹ Despite the name of the enzyme class, the xanthine oxidase family of enzymes is not solely limited to this single process. These enzymes also perform catalysis as aldehyde oxidases, aldehyde oxidoreductases, nicotinate reductases, quinoline 2-oxidoreductases, 4-hydroxybenzoyl-CoA reductases, and carbon monoxide dehydrogenases. This class of enzymes is found in many biological processes, from the mammalian formation of retinoic acid to the synthesis of abscisic acid in plants.

The active sites found in enzymes of the xanthine oxidase family, shown in Figure 1.1, are characterised (in the oxidised form) by a central molybdenum atom coordinated by a terminal oxo group, a pyranopterindithiolene cofactor coordinated via the sulphurs, a labile hydroxy group, and a terminal Group 16

atom (Mo=O, S, Se).³⁰ Carbon monoxide dehydrogenase is anomalous, however, featuring a Mo/S-Cu cofactor, replacing the terminal Group 16 moiety (Mo-S-Cu-S(Cys)).^{25,31,32} The R group depends on the cell type. In eukaryotes, the cofactor is found in the monophosphate form where R is a hydrogen atom. In prokaryotes, R is found esterified with several nucleotides, for example, cytidine monophosphate, guanosine monophosphate and adenosine monophosphate.²⁷

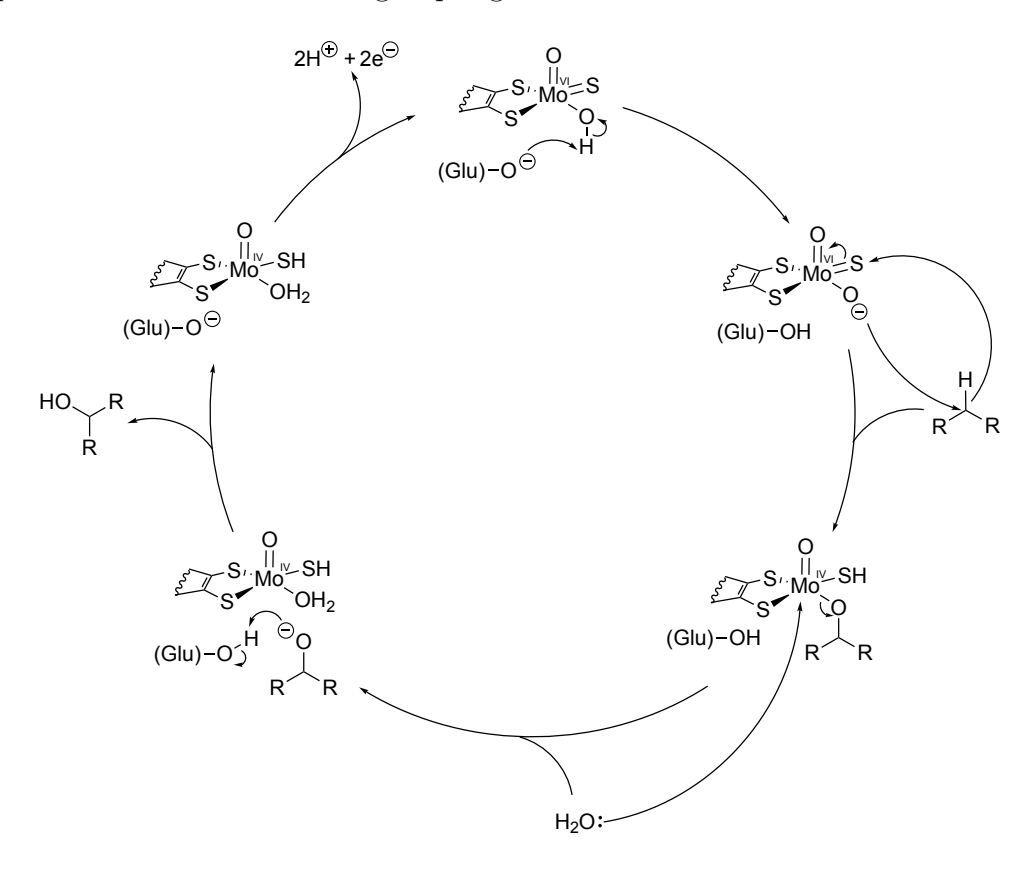
X = O, S, Se, S-Cu-S(Cys)

Figure 1.1: The Xanthine Oxidase Active Site. 18

Usually, the xanthine oxidase enzymes catalyse the hydroxylation of a C-H bond in aromatic heterocyclic compounds and aldehydes.¹⁸ This holds true but for two exceptions: carbon monoxide dehydrogenase, the oxidation of CO to CO₂, and hydroxybenzoyl-CoA reductase, the dehydroxylation of the phenol ring.^{31,33}

For this group of enzymes, there is little ambiguity of the reaction mechanism for the xanthine oxidase catalysed hydroxylation. Summarised by Moura and co-workers,²⁷ and shown in Scheme 1.1, the terminal hydroxy group is first deprotonated by a glutamate residue to form Mo^{VI}–O⁻. This is followed by a subsequent nucleophilic attack by the O⁻ on the requisite C atom whilst simultaneously the terminal Mo=S group abstracts a hydride; the molybdenum changes oxidation state from Mo^{VI} to Mo^{IV}. The hydroxylated product is displaced by a water/hydroxy group and the two electrons obtained by the molybdenum centre are transferred to

the flavin adenine dinucleotide (FAD) via Fe/S centres where dioxygen is reduced; deprotonation of the Mo-SH group regenerates Mo-S.



Scheme 1.1: The Xanthine Oxidase Catalytic Cycle. 27

1.3.2 Sulphite Oxidase

Sulphites are any compounds that contain the sulphite anion, SO_3^{2-} . Found in both eukaryotic and prokaryotic cells, sulphite oxidase is responsible for the oxidation of toxic sulphite to sulphate produced from the catabolism of large sulphur-containing amino acids and xenobiotic compounds. Mutations in the genes MOCS1, MOCS2, MOCS3, and GEPH result in a deficiency in sulphite oxidase which causes early onset seizures and neurological deterioration highlighting the importance of this class of enzymes in human biology.³⁴ The sulphite oxidase class of enzymes is not

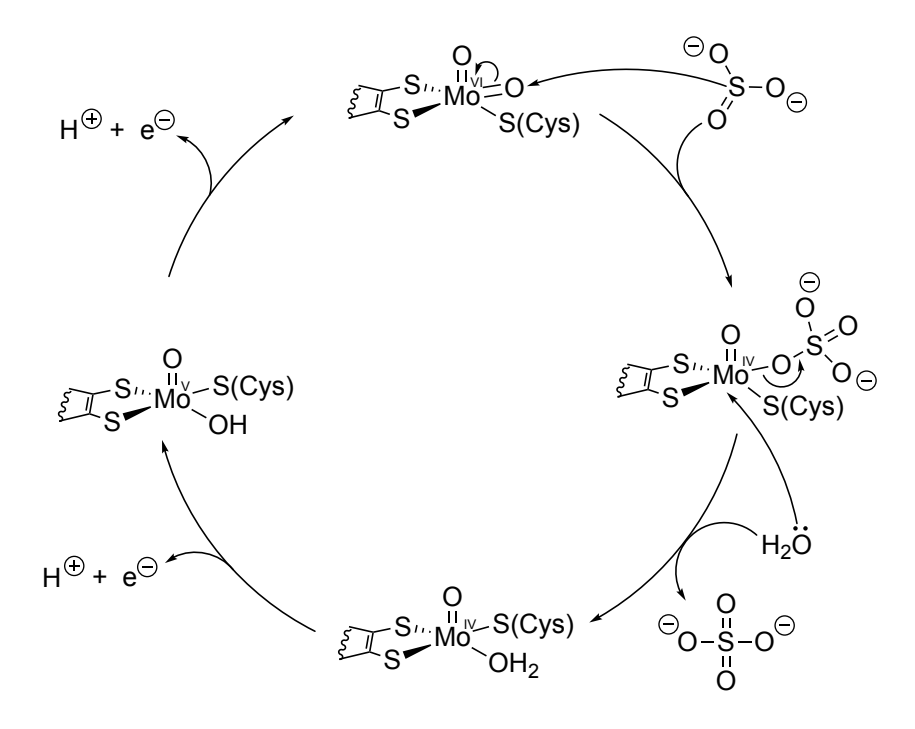
limited to just this one process: they are responsible for the eukaryotic assimilation of nitrate in plants, algae, and fungi (nitrate reductase); and the reduction of S-and N-hydroxylated compounds.²³

Figure 1.2: The Sulphite Oxidase Active Site.²⁷

Like all molybdenum-containing enzymes, there are similarities between the active sites of the various families. The molybdenum centre is coordinated, in a square-pyramidal geometry, to a pyranopterindithiolene cofactor, two oxo groups (Mo=O), and the distinct feature, the polypeptide chain coordinated directly to the molybdenum through a cysteine thiolate residue (Mo-S(Cys)) (Figure 1.2).³⁵ Like with xanthine oxidase, the R group in sulphite oxidase depends on the cell type: in eukaryotic enzymes R is a hydrogen and in prokaryotic enzymes R is an esterified nucleotide (cytidine monophosphate, guanosine monophosphate and adenosine monophosphate).²⁷

Sulphite oxidase catalyses the transfer of one oxygen atom to, or from, an electron lone pair on the substrate. A catalytic cycle is created by water transferring the oxygen back to the molybdenum, returning the active site to its initial state. This oxygen atom transfer earns this class of enzymes the moniker 'oxotransferases'.

Like xanthine oxidase, the catalytic cycle of sulphite oxidase is well documented. As can be seen in Scheme 1.2, the sulphur of the sulphite molecule attacks the equatorial oxo group bound to the molybdenum, simultaneously forming a Mo-O-SO_3^{2-} group whilst also reducing the molybdenum centre from Mo^{VI} to



Scheme 1.2: The Sulphite Oxidase Catalytic Cycle.²⁷

Mo^{IV}. The Mo^O bond is broken, releasing the synthesised sulphate (SO₄²⁻) and the vacant site is replaced by a water molecule. For oxidation of the molybdenum core from Mo^{IV} back to Mo^{VI}, the pathway differs depending on the enzyme type. For vertebrate sulphite oxidase (chicken SO), the two electrons are intramolecularly transferred individually to the heme where cytochrome c will be reduced. Unlike vertebrate SO, where this heme/SO pairing is crucial for catalysis to occur, the oxidation of the molybdenum centre in plant SO occurs without any additional redox cofactors by the one-electron reduction of oxygen to superoxide.³⁶

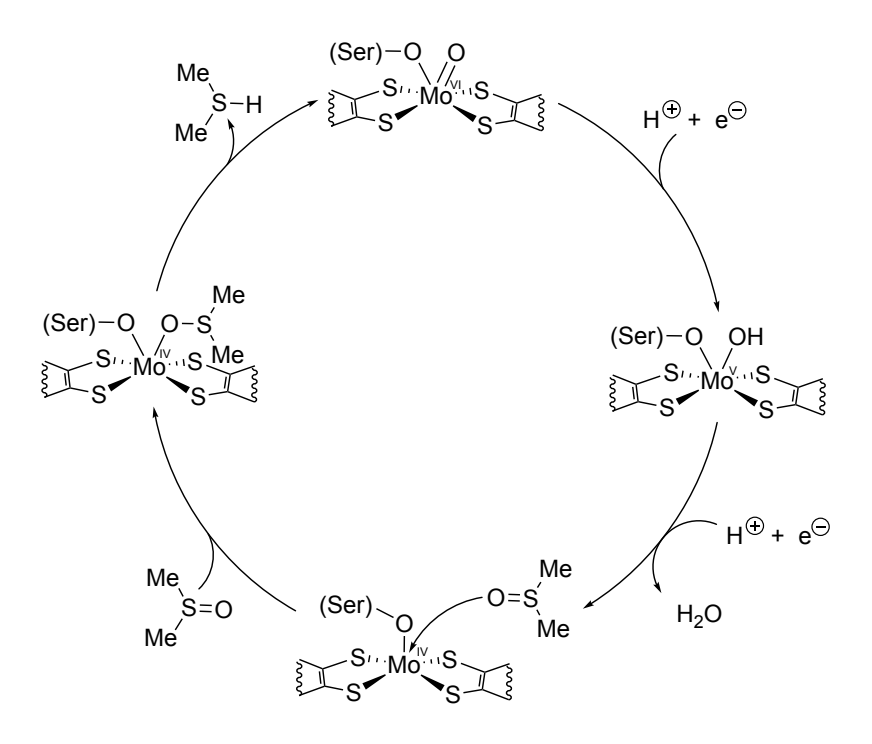
1.3.3 Dimethyl Sulphoxide (DMSO) Reductase

The DMSO reductase family of enzymes boasts the most diverse range of subunit structure and composition. Such diversity allows for this class of enzymes to be found in many biological processes not limited to the reduction of dimethyl sulphoxide, the reduction/oxidation of arsenate/arsenite, the reduction/oxidation of nitrate/nitrite, the reduction of carbon dioxide and the oxidation of formate, and the reduction of polysulphides.²⁷

Figure 1.3: The DMSO Reductase Active Site.³⁷

Unlike the previous two classes, in the reduced state two pyranopterindithiolenes coordinate to the molybdenum metal centre via four sulphur atoms, with a terminal Group 16 atom coordinated axially (Mo=O, S, Se). In the oxidised state (Figure 1.3), the terminally coordinated group is now a singly bound (Mo-X) and this free site allows for direct coordination of the molybdenum ion to the polypeptide chain through aspartate, serine, cysteine, or selenoscysteine residues. ^{27,37,38} Like the previous two classes of metalloenzymes, the identity of the R group changes depending on whether the enzyme is eukaryotic (R is a hydrogen atom) or prokaryotic (R is a cytidine monophosphate, guanosine monophosphate, or adenosine monophosphate). ²⁷

Through the use of resonance Raman spectroscopy, isotopic oxygen atom studies, X-ray absorption spectroscopy (XAS), and electron paramagnetic resonance spectroscopy (EPR) conclude, with relative certainty, the mechanism for the catalysis of DMSO shown in Scheme 1.3.^{38–41} Reduction of the molybdenum centre and protonation of the terminal oxo (Mo=O), facilitated by the penta-heme DorC protein, releases a water molecule, resulting in a Mo^{IV}-O(Ser) moiety via a Mo^V-O



Scheme 1.3: The DMSO Reductase Catalytic Cycle.

state. Subsequently, DMSO binds to the molybdenum core and cleavage of the O–S bond regenerates the ${\rm Mo^{VI}}{=}{\rm O}$ terminal group.²⁷

1.3.4 A Closer Look at Formate Dehydrogenase

Since this thesis focuses on this small subsection of the DMSO reductase family of enzymes, it is worth examining them in more detail to develop an understanding of why they are a particularly valuable target for CO₂ reduction.

Formate dehydrogenase enzymes can be divided into two categories: metal-dependent and metal-independent (NAD-dependent) enzymes. The metal-dependent enzymes contain redox active centres and are similar to what has been described above. The NAD-dependent class of enzymes has no metal ions or other redox-active centres. Similar to the rest of the DMSO reductase family of enzymes, the FDH subgroup is identifiable by having two pterindithiolene moieties coordin-

ated to the molybdenum atom in a square pyramidal geometry, and an oxygen, sulphur or selenium atom in various arrangements. The tungsten-containing formate dehydrogenases are similarly analogous, exemplified by *Desulfovibrio gigas*, bound by two pterindithiolates, one selenocysteinate and one hydroxyl/sulphide ligand (in the oxidised form).⁴² In total, three formate dehydrogenase enzymes have been characterised by X-ray crystallography: two molybdenum-based^{43,44} and one tungsten-based.⁴⁵ Each characterised enzyme varies in size, but some commonalities remain; for example, the [4Fe-4S] clusters to facilitate electron transfer and the geometry of the cofactors.

The formate dehydrogenase enzyme classification can be further subdivided into three more families: monomeric cytoplasmic enzymes (FDH H), which contain only the molybdenum centre and one iron-sulphur cluster;²² and two classes of heteromeric membrane-bound respiratory enzymes (FDH N and Z) which contain additional redox-active centres along with the molybdenum centre.²² These differ in the number of additional redox-active centres, seven and six, respectively, resulting in a system of subunits that ferry electrons and protons away from the active site.⁴⁴ They can be found in *Escherichia coli* as part of the respiration of nitrate.⁴⁶

Formate dehydrogenase catalyses the reversible inter-conversion between carbon dioxide (CO₂) and formate (HCOO⁻). Converting from CO₂ to formate requires the transfer of a hydride (two electrons and one proton), and can be seen in equation 1.1:

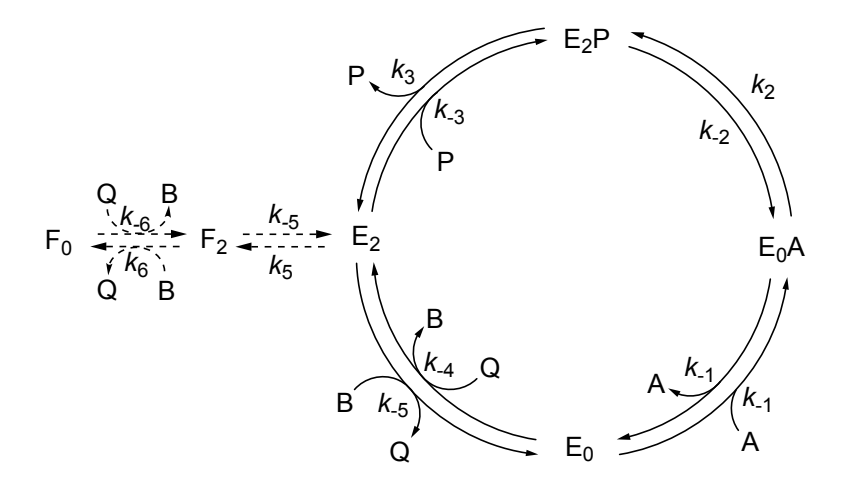
$$\mathrm{HCOO^{-}} \Longrightarrow \mathrm{CO_2} + 2\,\mathrm{e^{-}} + \mathrm{H^{+}}$$
 (1.1)

Generally, most FDH enzymes preferentially catalyse the oxidation of formate to CO_2 .⁴⁷ The resulting electrons are transferred via electron transfer reactions until they reduce a terminal electron acceptor. However, there are some FDHs that do reduce CO_2 to formate. Maia and co-workers demonstrated during their kinetic studies of *Desulfovibrio desulfuricans* in conjunction with a viologen (a redox active

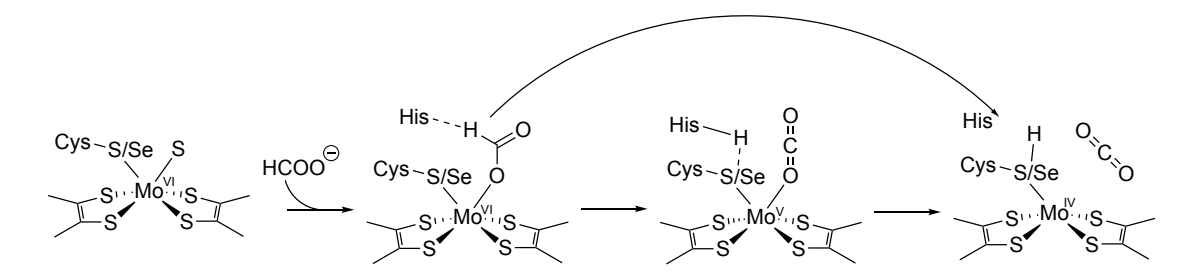
molecule)⁴⁸ as the reductant, the enzyme has a $[k_{cat}]$ of $47 \,\mathrm{s}^{-1}$ when it comes to the reduction of carbon dioxide to formate.^{47,49}

Scheme 1.4 details the kinetic model for the FDH-catalysed carbon dioxide reduction presented by Maia and co-workers.⁴⁷ The inactive F_0 enzyme is reduced by the viologen in the reduced form (benzyl viologen), Q, giving the oxidised viologen, B, and the inactive reduced enzyme, F_2 . Although the viologen is a one electron oxidiser/reductant, including two extra steps would add no additional value to the model. This is then followed by the slow isomerisation (k_{-5}) of F_2 into the active reduced E_2 enzyme. The reverse conversion is suggested to be unimportant as k_5 is much smaller than k_{-3} . E_2 reacts with carbon dioxide P to give formate A, and the oxidised active enzyme E_0 . The enzyme is then reduced by the viologen once again, returning to the active E_2 state. Initially the concentration of F_2 is high and the formation of formate and oxidised viologen is limited by the slow conversion of k_{-5} resulting in a lag in catalytic rate. However, after a number of catalytic cycles the active E_2 form builds up and catalysis continues through the faster $k_{-4} \rightarrow k_{-3} \rightarrow k_{-2} \rightarrow k_{-1}$ cycle, removing the early slow rate.

Although the process occurring at the enzyme's active site has been studied extensively through experimental and computational methods, the reaction mechanism is not well understood. Differing from the typical oxygen atom transfer catalysed reactions of the DMSO family of enzymes, it is suggested that the C–H bond is broken and the hydride is transferred to the terminal sulphido instead. To date, five mechanisms have been put forth: the first from Sun and co-worker based on the crystal structure of FDH H,⁴³ a reinterpretation of the crystal structure by Romão and Raaijmakers offered a new perspective on the mechanism,⁴⁵ a sulphurshift mechanism based on computational studies,^{50,51} a mechanism from Zampella and co-workers based again on computational studies,⁵² and finally a mechanism from Moura and co-workers based on experimental data.⁴⁷



In the first reaction mechanism (Scheme 1.5), formate is coordinated by the metal centre and displaces the sulphido group. Formate is then oxidised to carbon dioxide through either the proton moving to His141 along with an electron transfer to the molybdenum centre (Mo^{VI} to Mo^V) followed by the His141 proton transferring to Sec140 together with another electron transfer to the metal centre (Mo^V to Mo^{IV}), or through a more direct pathway of the proton transferring directly to Sec140 and two electrons transferring to the molybdenum centre, Mo^{VI} to Mo^{IV}.⁴³



Scheme 1.5: The FDH Catalytic Mechanism Proposed by Boyington and Coworkers. $^{43}\,$

The second proposed mechanism (Scheme 1.6) offers a reinterpretation of the crystal structure analysed by Romão and Raaijmakers. 45 It was discovered that the formate-reduced form had a poor fit of the electron density map for the loop (138)RV-SeC-HGPSVA(146) where Val139, part of the molybdenum ligand Se-Cys140 and His141 were out of density and other parts showed poor connectivity. The selenium atom was found 12 Å from the molybdenum atom, implying that molybdenum is not coordinated by Se-Cys140. Such a result contradicts the results obtained from the oxidised form of the enzyme, where the selenium atom does coordinate the metal. Differing from the interpretation from Sun and co-workers, the Sec/Cys residue dissociates, allowing formate to bind to the molybdenum centre. Similarly to the above, the formate proton is abstracted by His141, and two electrons are transferred to molybdenum in one step. The new interpretation has the selenium atom interacting with the conserved Arg333, which simultaneously pulls along the His141 residue. The Sec/Cys residue dissociates, allowing formate to bind to the molybdenum centre. Similarly to the above, the formate proton is abstracted by His141, and two electrons are transferred to molybdenum in one step.

Scheme 1.6: The FDH Catalytic Mechanism Derived from the Reinterpretation of a Crystal Structure. 45

A third reaction scheme was proposed using computational studies (Scheme 1.7).^{50,51} Here, the Sec/Cys moiety dissociates, followed by a rebinding to the complex through the remaining S/Se. The molybdenum is reduced from Mo^{VI} to Mo^{IV}, freeing a coordination position for formate to bind to. Cleavage of the Se/S–S

bond results in the free ionic form of Sec/Cys, which can abstract the proton from formate to give the desired products.

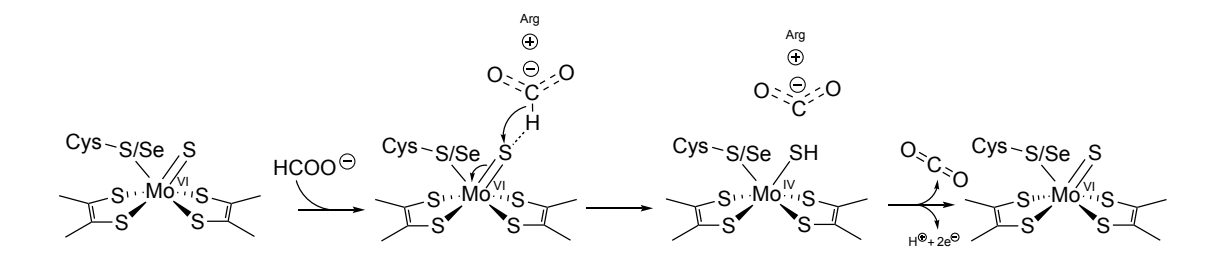
Scheme 1.7: One of the Proposed Mechanisms for FDH Catalysis Derived by Mota and Co-workers.⁵¹

In the fourth reaction mechanism (Scheme 1.8), the Sec/Cys group is displaced by the coordination of formate to the molybdenum.⁵² A hydride ion is then abstracted from formate, resulting in the release of carbon dioxide and creating a Mo–H bond. The hydride moves as a proton to the sulphido group to form Mo–SH together with a tandem reduction of the molybdenum centre to Mo^{IV}.

Scheme 1.8: A Mechanism for FDH Catalysis Proposed by Zampella and Coworkers.⁵²

Based on experimental data, unique in the fifth reaction mechanism (Scheme 1.9), formate does not bind to molybdenum in any capacity, but instead resides in a secondary coordination sphere.⁴⁷ The sulphido group abstracts a hydride from the formate substrate, resulting in a reduced molybdenum centre.

Ryde and co-workers have compared these five mechanisms using computational methods (a QM/MM approach).⁵³ They concluded that the formate substrate does not bind directly to the molybdenum centre but instead resides in a secondary coordination sphere. Two electrons are transferred to the molybdenum, and the



Scheme 1.9: An Experimentally Backed Mechanism for FDH Catalysis Proposed by Maia and Co-workers.⁴⁷

proton is transferred to the sulphido group. However, they proposed that the carbon dioxide product forms a thiocarbonate group with the Cys ligand and will not be released until the molybdenum centre is oxidised.

In the year before Ryde and Dong, Reisner and co-workers came to a different conclusion.⁵⁴ They showed that inhibition of FDH catalysis is strongly dependent on the oxidation state of the enzyme, suggesting that inhibitors and substrates interact intimately with the Mo centre of the active site (within the primary coordination sphere). From the data, they expanded on the approach that one of the ligands (Sec) dissociates from molybdenum, creating an open coordination site. Consequently, the mechanism transpires through a five-membered transition state. These findings are supportive of the correction made by Romão and Raaijmakers. A recent study performed by Schulzke and co-workers offers contrasting evidence to the heterolytic C-H school of thought, proposed originally by Thauer and co-workers, towards the direction of the traditional oxygen transfer mechanistic pathway of the DMSO reductase family.^{55,56} By using isotopic labelling and mass spectrometric analysis, bicarbonate was identified as the first intermediate in the reaction of formate oxidation through the production of H¹³C¹⁶O¹⁸O labelled formate. With conflicting catalysis discussions, much is to be done in the area to offer a concrete conclusion to the exact mechanism of action.

Interestingly, the literature lacks the same intensity of investigation when it

comes to the reverse, the reduction mechanism of CO_2 to formate. One supposes that reduction is merely the reverse of oxidation and the suggested mechanisms can be flipped to elucidate some understanding of the reverse process. However, without direct confirmation, any conclusions drawn about the reduction mechanisms using this logic must be held with great scepticism.

1.4 The Active Site of Formate Dehydrogenase

The active site of formate dehydrogenase is a location of key interest within the enzyme since this is where catalysis occurs. The active site has been covered in some detail in earlier sections of Chapter 1; however, it is worth analysing in more detail here.

Obviously the lone Mo/W metal atom lacks biological activity. A specific cofactor must be coordinated before catalysis can begin, namely the molybdopterin cofactor (also known as pyranopterin, pyranopterindithiolene or Moco). The catalytic subunit can contain up to five iron–sulphur clusters, and genomic analysis predicts the existence of more complex situations involving flavin as an additional cofactor. This diversity in the nature of cofactors increases as one moves away from the catalytic site, with the presence of further iron–sulphur clusters, b- or c-type hemes, and flavins in highly variable folds.

Raaijmakers and co-workers identified the crystal structure of formate dehydrogenase from *Desulfovibrio gigas*. ^{42,57} They determined that this enzyme contained four sulphur atoms from two pyranopterindithiolenes coordinated to a tungsten metal centre, a selenium atom, a Se-Cys residue, and one hydroxyl or sulphide ligand. The molybdoenzyme was identified from *Escherichia coli* through X-ray absorption data by Boyington and co-workers, and it was found to favour the hydroxyl ligand rather than the sulphide. ⁴³ However, a re-evaluation by Romão

and co-workers found the ligand was better refined as a sulphur atom (=S), thereby making the molybdenum a direct analogue of the tungsten variant.⁴⁵ The pyranopterindithiolene cofactor, Figure 1.4, can be broken into three distinct subunits: the dithiolene, the pyran ring and the pterin.

$$\begin{array}{c|c} O & H & S^{\scriptsize \bigcirc} \\ HN & N & N & N \\ H_2N & N & N & O \end{array}$$

Figure 1.4: The Pyranopterin cofactor.

1.4.1 The Cellular Synthesis of Moco

Other enzymes obtain their cofactors by being taken up as a nutrient, but for molybdenum and tungsten enzymes the cofactor requires de novo biosynthesis. This synthesis of the ligand occurs in three steps. To begin, the nucleotide, guanosine triphosphate (5'-GTP), undergoes radical cyclisation to form (8S)-3',8-cyclo-7,8-dihydroguanosine (3',8-cH₂GTP) through a series of complex reaction sequences where the C8 atom of the purine is inserted between the 2'- and 3'-ribose carbon atoms highlighted by the * in Scheme 1.10; this reaction is mediated by the radical SAM enzyme. ^{58,59} Through this process, the familiar scaffold can already be seen to be taking shape. 3',8-cH₂GTP is then converted to cyclic pyranopterin monophosphate (cPMP) by MPT Synthase where each sulphur is bound to the carbon as a thiocarboxylate in a sequential manner. ⁶⁰ After the sulphuration, the sulphurs of MPT synthases are regenerated by the enzyme MPT synthase sulfurase. ⁶¹

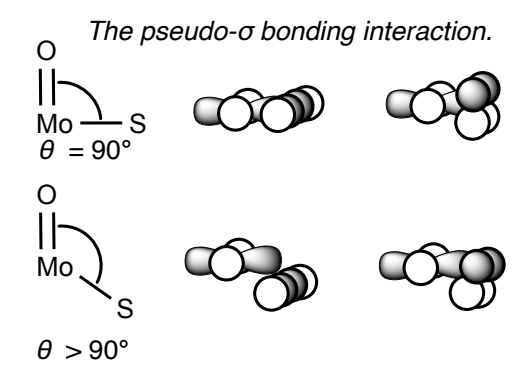
With the synthesis of MPT the chemical backbone is built to bind and coordinate a molybdenum atom. But firstly, it is worth considering how molybdenum is taken up into the body. Molybdenum is taken up into the body as tetraoxomolybdate, MoO₄²⁻. With keeping anions, specific protein channels are needed to direct the molybdate to the necessary locations, known as Mot1 and Mot2 in bacteria.⁶² However, the answer to the question of how the anion entered the animal cell was still unknown.^{63,64} Fortunately, results obtained from the alga *Chlamydomonas* reinhardtii identified another molybdate transporter which is also found in human cells.⁶⁵

Structural studies revealed that to coordinate molybdenum, MPT must be first activated by adenylation to form MPT-AMP since physiological molybdate concentrations are not sufficient to achieve any non-catalysed molybdenum ligation by MPT.^{66,67} Enzymatic cleavage of the adenylate from MPT catalyses the insertion of molybdate into the dithiolene group of MPT, affording Moco.^{68,69}

Scheme 1.10: The *de novo* biosynthesis of MPT.⁶⁹

1.4.2 The Dithiolene

The dithiolene coordinates with the rest of the pyranopterindithiolene to the metal centre, but more importantly, it tunes the metal centre through various mechanisms. Conjugation within the dithiolene is mediated by the two sulphur



The interaction of metal in-plane and sulphur- π orbitals.

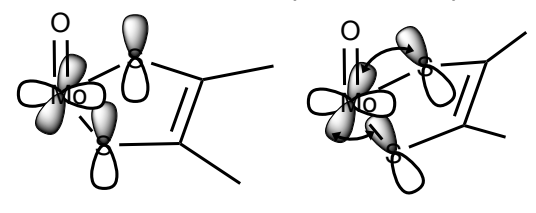


Figure 1.5: The Effect of the Fold Angle on the Pseudo- σ Bonding and Metal In-plane Sulphur- π Orbital Interactions.^{70–72}

atoms coordinated to molybdenum, creating an environment sensitive to electron density changes at the metal centre. The dithiolene can also respond to changes in the molybdenum oxidation state. First noted by Lauher and Hoffman for $Cp_2Mo(dithiolene)$ compounds, the fold angle varied depending on the d-electron count on the metal.⁷³ These changes are seen through a folding movement of the dithiolene that itself influences the electronic donation through pseudo- σ bonding and π -interactions. The movement in of the fold angle and the subsequent change in the orbitals is showcased in Figure 1.5. Larger fold angles occur for a higher oxidation state of molybdenum, thereby controlling the electronic environment of the dithiolene through the degree of overlap between the sulphur p orbitals and the metal d orbitals. These angles range from 6.9° to 29.5°. 70,71,74 The dithiolene also has redox capabilities and can exist in three forms shown in Figure 1.6: fully reduced, partially reduced, and fully oxidised.

In the case of most inorganic complexes, the oxidation state and electronic

$$\begin{cases} S^{\ominus} & \xrightarrow{e^{\ominus}} & \checkmark \\ S^{\ominus} & & \checkmark \\ S & & \\ S & & \\ \end{cases} \xrightarrow{e^{\ominus}} & \checkmark \\ S & & \\ \end{cases} \xrightarrow{S}$$

Figure 1.6: The Oxidation States of the Dithiolene Moiety.

configuration can be assigned using simple rules. When the coordination of certain ligands results in an ambiguous oxidation state of the metal centre, they are called redox non-innocent ligands.⁷⁵ Typically, upon coordination with metals, weak field dithiolene ligands exhibit redox non-innocent behaviour; therefore, it is worth touching on as it plays a crucial role in modulating metal complex reactivity.⁷⁶

A redox non-innocent ligand can have the following effects:

- influences the substrate affinity as well as the energy profile of subsequent follow-up reactions through modulation of the Lewis acidity of the metal by oxidation/reduction of the ligand;
- the ligand can act as an 'electron-reservoir' which allows the metal to store
 and accept electrons on the ligand in elementary steps either by generating
 excesses or deficiencies in electron density and as a result, uncommon oxidation
 states are avoided;
- some redox non-innocent ligands can form ligand-radicals that participate in the catalytic cycles.⁷⁰

These non-innocent effects can influence the reactivity such that base metals can behave more similarly to noble metals. Sulphur K-edge X-ray absorption spectroscopy used in parallel with density functional theory (DFT) calculations has been used to probe the bonding and covalency in the Mo(bdt)₃ and Ni(bdt)₂ complexes.^{77–79} An X-ray excites one of the core K-shell electrons (1s²) into an unoccupied S 4p orbital, shown by the appearance of an electric-dipole-allowed edge feature. Pre-edge features are also observed where transitions occur into

unoccupied or half-occupied d orbitals. The excitation of electrons into these higher energy S orbitals results in more covalent bonding. Matching these findings with DFT calculations allows for the identification of the metal oxidation and spin state. These experiments showed that the redox processes for $Mo(bdt)_3$ and $Ni(bdt)_2$ are all attributed to the dithiolene ligand.

1.4.3 The Pyran Ring

Compared to the dithiolene and pterin, the pyran ring appears largely unobtrusive. Work from Burgmayer and co-workers in recent years has drawn some attention to this often forgotten moiety.⁸⁰ A series of models synthesised by the group revealed that the pyran ring undergoes a low-energy reversible process of C—O bond scission and recyclisation, where the pyran ring can be in either an open or closed form, shown in Figure 1.7 .

$$\begin{array}{c|c} & & & & \\ & &$$

Figure 1.7: The Reversibility of the Pyran Ring.⁸¹

Pyran ring cleavage changes the electronic structure of the pterin by increasing the number of C=N bonds, a process similar to oxidation. The pyran ring helps to improve π -conjugation between the pterin and dithiolene by enforcing greater planarity and adding to the electron modifying ability of the chelating dithiolene.⁸⁰

1.4.4 The Pterin

The pterin also performs a similar role as the pyran ring and dithiolene, tuning the electronic environment of the active site. The pterin moiety is considered electron-poor and can be expected to give the MPT some electron-withdrawing character. Pterins also have redox capabilities and can exist in many states (Figure 1.8). Multiple tautomeric forms of these redox states exist. The fully reduced form lacks the conjugated π -system. Therefore, there will be less electronic communication between the pterin and the dithiolene; this increases the fine-tuning of the reduction potential of the molybdenum ion, modifying the electron donor capabilities of the dithiolene. The pterin has many H-donor and acceptor functional groups present, so it is important to note, for mimic synthesis, that these groups interact with the surrounding protein scaffold of the enzyme to give the pterin the correct geometry around the molybdenum.⁸²

$$\begin{array}{c|c} & O & \\ &$$

Figure 1.8: The Pterin Moiety and its Oxidation States.

Currently, the role of pterin in Moco for enzymatic catalysis is not well understood, but logically it is possible to deduce a number of potential functions: a pathway for electrons to regenerate the metal centre, modulating the redox potential, through hydrogen bonding, of the metal centre, and providing an anchor to the metal centre for the rest of the enzyme.⁸³

A collection of syntheses summarised by Joule and Garner highlighted methods to obtain highly similar compounds to molybdenum bound pyranopterindithiolenes.⁸⁴ These routes afforded asymmetric systems with only one pyranopterindithiolene instead of the two found in the active site of these molybdoenzymes. From a

(trispyrazolylborate)Mo(=X)(pterin-dithiolene), first synthesised by the Burgmayer group, it was concluded that the most significant effect of the pterin substitution was to shift the redox potential considerably in the positive direction. This could not be determined from the previous simpler models. This model determined that the pyranopterin group can participate in an easily reversible pyran ring scission and recyclisation.⁸⁵ Only the dithiolene coordinated to molybdenum shows this behaviour; the pyran dithiolene does not exhibit reversible pyran cyclisation.

1.4.5 The Terminal Functionality and Protein Residues

Finally, coordinated to the metal centres are a Group 16 element (oxygen, sulphur or selenium), a Se/Cys residue (depending on the oxidation state of the metal centre), and a highly conserved histidine and arginine residue near the active site. These Group 16 ligands exist in a L^{2-} form in a terminal fashion. Work done by Yan and co-workers suggests that these ancillary ligands, while innocent, play a part in deciding the electronic structure of the redox-active ligands. 86,87

1.5 Biomimetic/Non-Biomimetic Complexes of Molybdoenzymes and their Associated Activity

1.5.1 Xanthine Oxidase Mimics

When compared with sulphite oxidase and DMSO reductase mimics, the lack of structural mimics of xanthine oxidase is quite striking. Currently, the literature is awash with mechanistic insights and pathology but lacks any interest in mimetic synthesis. Again, Holm is generally recognised as the leading figure in this area, but

little has been done since his initial foray;⁸⁸ the ligand scaffold is simple in nature, for example, the edt (complex 1) or bdt (complex 2) ligands. So, whether those methods are applicable for more intricate systems remains to be seen. A handful of other organometallic molecules exist (non-dithiolene) that catalyse oxygen transfers but lack the structural makeup of the xanthine oxidase active site (Figure 1.9). For example, Sadhukhan and co-workers grafted their maltol-based ligand, MaI, to the molybdenum-oxo precursor, ammonium heptamolybdate, to give complex 3. This complex was catalytically active when it came to the oxidation of hypoxanthine to xanthine.⁸⁹

Figure 1.9: The Xanthine Oxidase Biomimetic Structures. 88,89

1.5.2 Sulphite Oxidase Mimics

Between sulphite oxidase and DMSO reductase, sulphite oxidase mimics are the more synthetically challenging of the two because of the tendency for molybdenum to preferentially form bis-dithiolene complexes. Holm developed two approaches to overcome this issue. 90

Scheme 1.11: The Bulky Ligand Approach to Synthesising a Biomimetic Sulphite Oxidase Complex (Ar = 2,4,6- ${}^{i}Pr_{3}C_{6}H_{2}$).⁹⁰

Scheme 1.12: The Molybdenum-oxo *bis*-Dithiolene Intermediate Approach for Synthesising a Biomimetic Sulphite Oxidase Complex $(Ar = 2,4,6^{-i}Pr_3C_6H_2)$. ⁹⁰

The first synthetic approach (Scheme 1.11) involved 'blocking' one side of the complex by coordinating a sufficiently sterically bulky ligand to prevent the second dithiolene from coordinating. In this case, the bulky triphenylsilyloxide anion is used to prevent the *bis*-product from forming upon the addition of $\text{Li}(\text{bdt})_2$. Removal of the second triphenylsilyloxide anion is achieved by proton transfer from the hindered thiol 2,4,6- ${}^{i}\text{Pr}_{3}\text{C}_{6}\text{H}_{4}$ to give 4.

The second approach (Scheme 1.12) was to start with both dithiolenes already coordinated to the molybdenum-oxo core and then to cleave one of them using a strongly electrophilic reagent, for example PhSeCl. Subsequent substitution of the chloride using 2,4,6- i Pr₃C₆H₃ gave novel complex **5**. In the 20 years since Holm, structural and non-dithiolene mimics have been made with limited success. $^{91-93}$

1.5.3 DMSO Reductase Mimics

The first reported biomimetic complex, $[MoO(mnt)_2]^{2-}$, was an accidental discovery by Wharton and co-workers in 1968, who were investigating tris-dicyano and tris-tetrachlorobenzenedithiolene complexes of vanadium and molybdenum. Ammonium heptamolybdate together with $Na_2(mnt)$ gave a mixture of red cubes, the five-coordinate molybdenum-oxo complex, and green needles, the six-coordinate molybdenum tris-dithiolene complex. Their observations upon dissolving the isolated complex in dimethylformamide suggest that they were unable to isolate the molybdenum-oxo bis-dithiolene complex from the molybdenum tris-dithiolene

complex as it was noted that the solution was 'pale green-brown'.

It would not be until 21 years later in 1987 where another molybdenum-oxo bis-dithiolene complex was synthesised, $[MoO(S_2C_2(COPh)_2)_2]^{2-.95}$ Sarkar and co-workers provided the first report of a targeted approach at accessing the molybdenum-oxo bis-dithiolene complexes. They took a different approach to Wharton and co-workers, relying on post-coordination functionalisation to access the target complex. To access the $[MoO(S_4)_2]^{2-}$ core, firstly $(Et_2NH_2)_2[MoOS_3]$ was synthesised from the addition of hydrogen sulphide to molybdic acid and diethylamine. Adding elemental sulphur to $(Et_2NH_2)_2[MoOS_3]$ gave the $[MoO(S_4)_2]^{2-}$ core. The reaction between $[MoO(S_4)_2]^{2-}$ and dibenzyl acetylene afforded dark brown crystals of $[MoO(S_2C_2(COPh)_2)_2]^{2-}$. Unfortunately, the versatility of this reaction is hampered by the need for activated alkynes, as noted later on by Kirk and co-workers.⁸⁵

During the following year (1988), Matsubayashi and co-workers developed a unique method of accessing the molybdenum-oxo functionality through the molybdenum precursor, $[MoOCl_5]^{2-}$ and the pro-ligand 1,3-dithiol-2-one-4,5-trithiocarbonate to afford red needles of $[MoO(dmit)_2]^{2-}$. Herein are the beginnings of how most of the biomimetic DMSOr/FDH mimics are accessed: a dithiolene pro-ligand activated by some base and subsequently coordinated to a molybdenum-oxo precursor.

During the 1990s, four other groups synthesised new complexes to add to the $\mathrm{Mo^{IV}}$ catalogue where the complexes were first studied for oxygen atom transfer reactivity. Oku and co-workers determined the importance of sterics for the reaction of $\mathrm{Mo^{IV}O}$ to $\mathrm{Mo^{VI}O_2}$ using trimethylamine N-oxide. ^{97–99} The most critical additions came in the later parts of the decade from the Holm group and the Garner group. ^{100,101} Arguably the most renowned paper in the field, the Holm group focused on collating a number of syntheses for $\mathrm{Mo^{IV}} = \mathrm{O}\ bis$ -dithiolenes, as well as their own novel methods. For instance, a new approach was devised for accessing

[MoO(mnt)₂]²⁻, the first Mo=O complex of its kind synthesised by Wharton and co-workers 30 years earlier. The procedure involved subjecting [MoOCl(MeCN)₄]⁻ to Na₂(mnt) obtaining [MoO(mnt)₂]²⁻ with a far greater yield than the previously reported method from Wharton and co-workers (67% and 23% respectively). Before the paper from Garner and co-workers, the ligands and their subsequent complexes could be viewed as being quite simple in terms of functionality. The Garner group synthesised a variety of amino functionalised compounds, more accurately modelling the FDH active site.

After several publications from Holm, more $Mo^{IV}=O$ bis-dithiolene complexes were added to the literature; however, most of the additions lacked extended functionality. This was largely the case until the complexes synthesized by Schulzke and Fontecave in the latter half of the $2010s.^{100-111}$

In 2019, Schulzke and co-workers synthesised an ester and hydroxy functionalised dithiolene complex (6), a unique approach that stands out because of the use of alkyl substituents instead of the traditional aromatic subunits.

Figure 1.10: The Novel Catalyst Developed by Schulzke and Co-workers. 104

Schulzke's group determined that the aromatic moiety was detrimental to catalysis and instead opted for an aliphatic approach because of their instability and therefore increased activity. This ester- and hydroxy-functionalised dithiolene catalyst (6), insofar, has only been tested as an oxygen atom transfer catalyst, more specifically in catalysing the reaction of DMSO to dimethyl sulphide (DMS), the oxidation half-reaction, and PPh₃ to PPh₃O, the reduction half-reaction. The

catalysts performed adequately with a 93% conversion over 56 hours. 104

Fontecave and co-workers used the pyranopterinditholate framework as inspiration for synthesising a novel dithiolene species, shown in Figure 1.11, to complex to a molybdenum ion with the goal of catalytically reducing carbon dioxide to formate. This newly synthesised ligand, named qpdt (7), lacked Moco's inherent instability, allowing the molybdenum-oxo-dithiolene catalyst to effectively reduce protons to evolve hydrogen.¹¹²

Figure 1.11: The Evolution of Fontecave's Ligand. 112

The qpdt ligand (7) was reduced on the pyrazine ring to form the H-qpdt (8) and 2H-qpdt (9) ligands in an effort to mimic how some DMSO reductase enzymes exhibit different oxidation states on the pyranopterin cofactor, for example, a reduced dihydropyranopterin form.¹¹³

In 2018, the group synthesised a mononuclear Ni(qpdt)₂ species used as an electrocatalyst to reduce carbon dioxide, further proving the versatility of the qpdt ligand.¹¹⁴ In the latter half of the year, the group produced their second and third true formate dehydrogenase mimics, following on from the synthesis of the [Mo^{IV}O(qpdt)₂]²⁻ (10) species in 2015,¹¹² a molybdenum metal centre chelated by the 1H-qpdt (8) and 2H-qpdt ligand (9); each consists of a *cis*- and *trans*-isomer (Scheme 1.13 and Scheme 1.14).

All species presented an exceptional ability to act as photocatalysts to reduce carbon dioxide to formate and the results are displayed in Table 1.1. The largest turn over numbers (TONs) were obtained by $[MoO(qpdt)_2]^{2-}$ (10), then $[MoO(2H-1)]^{2-}$

Scheme 1.13: The Synthesis of $(Bu_4N)_2[MoO(H\mbox{-}qpdt)_2]$ (11) (R = $CH_2CH_2CO_2Et).^{103}$

Scheme 1.14: The Synthesis of $(Bu_4N)_2[MoO(2H\text{-}qpdt)_2]$ $({\bf 12})$ $(R=CH_2CH_2CO_2Et).^{103}$

 $qpdt)_2]^-$ (12) and finally $[MoO(H-qpdt)_2]^{2-}$ (11). However, the selectivity of carbon dioxide reduction vs. proton reduction decreases from $[MoO(2H-qpdt)_2]^-$ (12), to $[MoO(H-qpdt)_2]^-$ (11) and then $[MoO(qpdt)_2]^{2-}$ (10).¹⁰³

Table 1.1: The TONs of Formate, CO, and H_2 for Catalysts **10**, **11**, and **12** after 15 h Irradiation with a 300 W Xenon Arc Lamp Equipped with a 400 nm Filter at $20 \,^{\circ}\text{C}$.

Complex	НСООН	СО	H_2	Selectivity CO_2/H^+
10-qpdt	80		670	0.23
$11 ext{-} ext{Hqpdt} \ 12 ext{-}2 ext{Hqpdt}$	31 83	13 40	51 89	$0.86 \\ 1.38$

Fontecave's findings seem to be in contrast to Schulzke's data, where the highly conjugated qpdt system containing aryl groups still provides catalysis, while Schulzke claimed it was detrimental. This further adds to the mysteries surrounding FDH catalysis.

Comparing the catalysts developed by Schulzke (6) and Fontecave (10) offers interesting insight with regard to how the substituents on the dithiolene influence the target catalysis. Fontecave and co-workers chose to closely follow the MPT scaffold in the design of their qpdt ligands to more closely study biomimetic ligands. Such a design choice gave rise to the first reported FDH-based carbon dioxide reduction catalyst. As mentioned previously, Schulzke and co-workers did not choose aromatic substituents as they were deemed detrimental for oxygen atom transfer catalysis, whereas alkyl, asymmetric, substituents improved activity. However, the poor OAT results indicate that there is some other factor influencing OAT catalysis. Further functionalised mimics are needed to identify those key components.

1.5.4 Alternative mimics

Carbon dioxide to formate catalysts are not limited solely to biomimetic systems that try to closely match the coordination sphere of the natural FDH active site. Work from the DuBois group used proton relays to speed up the reversible reaction of formate to CO_2 in an effort to better understand the components necessary for better catalyst design. The proton relays operate by either losing or gaining a proton at the end of each catalytic cycle and need to be re-protonated/deprotonated; an acidic or basic solution can accomplish this. In 2012, DuBois and co-workers highlighted the importance of the proton relays in the mechanism for their novel nickel system in the use of formate oxidation (Scheme 1.15). In their catalysts, the P_2N_2 ligands coordinate to the metal via the phosphorus atoms, and the amine groups are able to act as proton relays. These outer sphere relays were found to be instrumental in facilitating catalytic reactions, since the analogous complexes without the pendant bases did not show catalytic activity. 115

The effects of these proton relays in catalysis can be further examined using them in conjunction with 'hangman' porphyrins. A hangman porphyrin manages the proton and electron directionality by establishing the proton transfer distance with an acid-base group poised above the electron transfer conduit of the porphyrin macrocycle. Hangman porphyrins can influence the reaction rates of small molecule activation by positioning a molecule in the secondary coordination sphere of the metal centre. ¹¹⁶ For nickel hangman porphyrins, used to evolve hydrogen, the effect of a proton relay close to the metal centre has led to an improvement in catalysis. ¹¹⁷

Significant efforts have been made to generate a collection of formate dehydrogenase mimics that can perform the catalysis between carbon dioxide and formate in either a photocatalytic or electrocatalytic manner. These mimics vary massively in structure, whether that is, changes in the ligand scaffold, the ancillary ligand, or the metal centre. Below will be a summation of the key, non-dithiolene mimics,

Scheme 1.15: A Proposed β -Deprotonation Catalytic Cycle by DuBois for Operation of the Ni(P₂N₂) Systems (ACN = acetonitrile, R = Cy C₆H₁₁, R' = PhOMe). ¹¹⁵

synthesised.

Homogenous ruthenium and cobalt catalysts have been synthesised with the goal of generating formate. In 1985, Lehn and co-workers reported the first-ever catalyst capable of photocatalytic conversion of carbon dioxide to formate using [Ru(bpy)₃]Cl₂ as the photocatalyst in the presence of triethanolamine (TEOA) as the sacrificial reductant; the TON of formate in acetonitrile was reported as 27 after irradiation for 24 hours. 118 Further analysis revealed that the generation of formate remained linear over time when carbon dioxide was added regularly, indicating that carbon dioxide played a vital role in the rate-determining step. An increase in carbon dioxide pressure to seven atmospheres caused the selectivity toward formate production to decrease. This was determined to be caused by an increased acidity of the reaction mixture from the carbon dioxide, causing the TEOA to be protonated and, therefore, less efficient. When water was not present, no formate was produced, but too much water caused selectivity to skew away from formate towards carbon monoxide and hydrogen. Isheda and co-workers rationalised this behaviour as being due to the decrease of basicity of TEOA, which was not suitable as an electron donor due to the conversion to the corresponding protonated form; consequently, TEOA was replaced with 1-benzyl-1,4-dihydronicotinamide (BNAH), since it followed the biological NAD(P)H model in an aqueous medium for carbon dioxide fixation. Unfortunately, formate selectivity dropped off completely. 119 The most recent advances in the use of ruthenium come from Arikawa and co-workers, where CNC pincer complexes (14) in conjunction with a sacrificial electron donor (1,3dimethyl-2-(o-hydroxyphenyl)-2,3-dihydro-1H-benzo[d]imidazole otherwise known as BI(OH)H, 15) and a photosensitiser ([Ru(dmbpy)₃]²⁻, 16) gave a TONs and selectivity for formate of 4593 and 72%, respectively (Figure 1.12). 120,121

Fontecave and co-workers did not limit the application of their novel ligand systems to molybdenum but also sought out other earth abundant transition metals

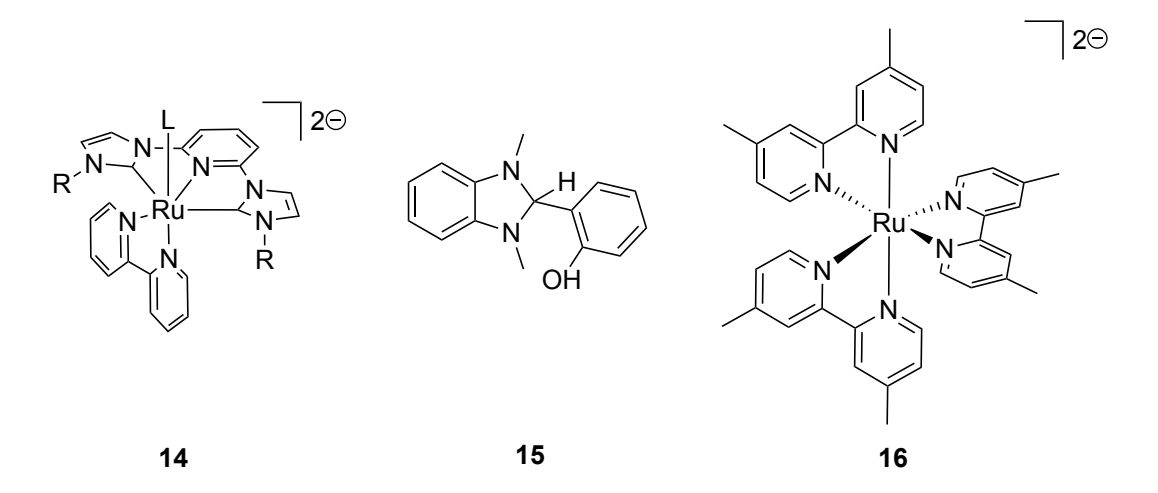


Figure 1.12: The Ruthenium Catalyst (14) (L = MeCN/CO, R = tBu/Me), the Sacrificial Electron Donor BI(OH)H (15), and the Photosensitiser [Ru(dmbpy)₃]^{2–} (16) Necessary for the Carbon Dioxide Reduction Experiments Carried Out by Arikawa and Co-workers.¹²⁰

to be the central metal ion, starting with the synthesis of a dimeric cobalt species. Electrocatalytic proton reduction of this species was studied under weakly acidic conditions and performed exceptionally well compared to other cobalt species, even being somewhat comparable to high-performing nickel catalysts. The team also studied photocatalytic proton reduction, but it was not as successful; after 2 hours the mimic became inactive under the conditions used. For photocatalytic proton reduction, the cobalt mimic could not match other similar cobalt species. The results from this research showed that the novel ligand species was capable of having catalytic effects, and therefore, could be applied to different metal centres. Although few cobalt complexes have been reported, it can be said that they possess good selectivity toward reducing carbon dioxide to formate.

1.6 Research Aims

Currently, most synthetic catalysts excel in the oxidation of formate to carbon dioxide with the majority using precious metals, making them undesirable for industrial application. The aims of the research are to develop a novel total synthetic route to molybdenum-oxo bis-dithiolene complexes that, in a few steps, can synthesise metal-dithiolene compounds with relative ease and in great numbers. Within the literature, most complexes are synthesised with the Mo=O terminal functionality, but this is not truly representative of the active sites found within the FDH enzymes. Therefore, it is important to expand on the functionality at the terminal position by synthesising complexes with the Mo=S terminal functionality as well. These investigations are outlined in Chapters 2 and 3.

Computational studies of Mo^{IV} dithiolene complexes are limited to the most basic systems, featuring simple alkyl or aryl substituents with Schulzke and McNamara being the only groups who investigated more functionalised ligands. Computational methods and their use in investigating molybdenum dithiolene complexes is more thoroughly discussed in Chapter 4.^{88,100,126–135} Consequently, standardising the use of computational methods for these Mo^{IV}=O dithiolene complexes is paramount to a more rounded understanding of the intricacies of these Mo^{IV} dithiolene complexes. Currently, the ability to identify the position of the Mo=O bond in the infrared spectrum of molybdenum-oxo dithiolene complexes is very challenging. Using computational studies, predicting the Mo=O stretch will allow IR spectroscopy to become a diagnostic technique for the synthesis of these Mo^{IV}=O dithiolene complexes. Computational studies will also be used to explain and give a reason for the difficulty in obtaining crystals suitable for X-ray diffraction.

Whenever a new molybdenum-oxo *bis*-dithiolene complex is synthesised it is common for electrochemical studies to be performed on it. Unfortunately, like the computational studies regarding these systems, there is no standard methodology

when it comes to the choice of electrolyte, reference electrode, and solvent. For many of these molybdenum complexes the Mo^V/Mo^{VI} is not recorded. The literature will be outlined in Chapter 5 where the electrochemistry of a selection of the complexes synthesised in Chapters 2 and 3 will be tested through cyclic voltammetry to examine how variations in the substituents of the dithiolene affect the redox potential of the Mo^{IV}/Mo^V and Mo^V/Mo^{VI} couples. From this, more accurate predictions can be made for the behaviour of future ligands on the molybdenum redox couples to better target the research aims of future researchers.

Chapter 6 will detail the catalytic studies performed on a selection of the complexes synthesised in Chapters 2 and 3. The complexes will be investigated for their ability to electrocatalytically reduce protons, photocatalytically reduce carbon dioxide, electrocatalytically oxidise formate, and for their catalytic oxygen atom transfer capabilities.

Chapter 2

Synthesis of a Molybdenum Functionalised Dithiolene Complex

2.1 Introduction

2.1.1 Why Formate Dehydrogenase?

One of the subgroups of the DMSO reductase family of enzymes is formate dehydrogenase. This enzyme class catalyses both the oxidation and reduction of formate and carbon dioxide. Mimics of FDH are an attractive target because of their ability to synthesise formate, from CO_2 close to thermodynamic limit of the reaction. Formate itself is an attractive target since it is much more volumetrically energy-dense than gaseous hydrogen storing 53 g H_2/L .

General synthesis of the formate/formic acid molecule can be achieved relatively simply; there are a multitude of ways of synthesising it. However, most methods come with some key disadvantages that make them unusable for an industrial purpose to replace fossil fuels: they are stoichiometric, lack scalability, and are energy-intensive. Therefore, catalytic processes are the more desirable option for the industrial production of formate.

Most catalysts for formate generation involve a precious metal such as rhodium, iridium, ruthenium, and platinum. Scaling these systems for industrial application is a difficult endeavour because these metals are not Earth abundant and consequently they are more expensive; cheaper alternatives are necessary. Fortunately, the active site of formate dehydrogenase contains molybdenum and tungsten as metal centres; these metals are more Earth abundant and much more attractive than the rarer transition metals listed above.

As an electrocatalyst, formate dehydrogenase works close to the thermodynamic potential of the formate to carbon dioxide interconversion. Therefore, it does not have the energy loss associated with an overpotential. Consequently, the FDH enzyme is already highly efficient as an electrocatalyst, making it an appropriate target.³⁷ This advantage is made clear when comparing formate dehydrogenase with its contemporaries, namely Ir, Co and Ni-based ('DuBois') catalysts. These require hundreds of millivolts of overpotential even to perform unidirectional catalysis, whereas formate dehydrogenase can perform reversible catalysis with little overpotential.^{54,115,137–144} One might think to utilise the enzyme itself from a bacterial source as an electrocatalyst; however, the enzyme is highly oxygensensitive. Also, the enzyme's size limits current in solution and when immobilised on surfaces.⁴²

The above matters clearly explain why the formate dehydrogenase enzyme makes an attractive target to base a mimic on and the challenges to work around. However, the synthesis of these bioinspired mimics has been difficult, stemming from the arduous synthesis of the pyranopterindithiolene cofactor. Therefore, current efforts are on the synthesis of small molecule cofactor mimics for subsequent

complexation.

2.1.2 Molybdenum Dithiolene Complexes

The targeted synthesis of DMSOR/FDH biomimetic systems truly began with Donahue and Holm in the 1990s with their syntheses of the molybdenum-oxo dithiolene complexes using the edt (17), bdt (18) and mnt (19) ligands. Following coordination of these ligands to a molybdenum-oxo core to synthesise a molybdenum-oxo bis-dithiolene, various post-coordination syntheses could be performed, which generated several analogous complexes based on changing the functionality at the terminal position (Figure 2.1).¹⁰⁰

Figure 2.1: The Early Ligands of Donahue and Holm. 100

Complexing these ligands to molybdenum took varying approaches from direct coordination through a molybdenum precursor (13), Scheme 2.1, to transmetallation via a nickel intermediary. Obtaining these complexes is relatively straightforward since the ligand itself lacks any real functionalisation. Therefore, determining which route is the most robust for a wide range of ligands/applications is impossible. These simple ligands and their associated complexes do not show any signs of catalytic activity and are only regarded as the first generation of FDH mimics. This is not to understate their value since almost all work that came after is based on this chemistry initially summarised by Holm and co-workers. ¹⁰⁰

Notable additions to this catalogue of DMSO reductase mimics started by Holm come from Schulzke and Fontecave, whose systems both display catalytic activity

Scheme 2.1: The synthesis of $MoO(bdt)_2^{2-}$ (20) by Holm and Donahue.

but for different reactions (Figure 2.2). A key point to note for both complexes is that they have Mo=O terminal functionality. This highlights the lack of Mo=S and Mo=Se functionalised mimics with complex ligand scaffolds present in the literature. That is not to say there have been no sulphur-based terminally coordinated systems; instead, accessing the dithiolene-terminal sulphur core is extremely synthetically challenging. 103,104

Figure 2.2: The Catalysts Synthesised by Fontecave (10) and Schulzke (6). 104,112

2.1.3 A Brief History of the Synthesis within the Wright Group

Whilst successful formate dehydrogenase mimics have been synthesised, efforts have been focused on replicating the metal coordination sphere, but the majority lack any secondary donor features like proton relays; these secondary donor features are believed to be of central importance in the activity of many metalloenzymes, so the logic can be transferred to the design of formate dehydrogenase mimics.

Relayed by personal communication, the first-generation pro-ligand afforded by the Wright group was a 1,3-dithiol-2-one system (Figure 2.3), synthesised via a known radical procedure, grafted with a hydroxyl group to carry out the desired proton relay function. This dithione (21) was protected using tert-butyldimethylsilyl chloride, and followed by a reaction with nickel acetylacetonate (Ni(acac)₂) to give the desired complex. Protection was a necessary step as complexation to the nickel required base hydrolysis of the dithione, and the hydroxyl group may therefore require protection. The deprotection of the nickel complex using a weak acid followed by a transmetallation step using $Mo(CO)_3(PhMe)$ gave the desired $Mo(CO)_2(S_2C_2HBnOH)_2$ complex. A one pot-complexation of $Mo(CO)_3(PhMe)$ and the first generation ligand was attempted to avoid the nickel transmetallation step to improve atom economy but was ultimately unsuccessful with only the isolation of green oils, which are indicative of the formation of $Mo^{VI}(S_2C_2HBnOH)_3$, the oxidised molybdenum tris-dithiolene complex.

Figure 2.3: The First Generation Target Dithione (21).

As a remedy to this issue, the second-generation ligand was conceived – a methyl group replaced the proton on the dithione heterocycle as it was believed the acidity of the alkenyl proton was responsible for the rapid oxidation to the molybdenum tris-dithiolene complex. This would be more in line with the simple model pro-ligand ($S_2C_2Me_2$) complex trialled successfully for the idea of the one-pot

complexation, where both alkyl groups donated electron density to the metal centre. The dithione was synthesised using the known radical procedure (Scheme 2.2), using more forcing conditions to account for loss of yield. These losses were because of how the substituents bound to the radical vinyl moiety influence the geometry of said radical. To understand this two points must be considered: the addition of thio-radicals to alkynes is a reversible process; aliphatic substituents favour the formation of the *cis* adduct, which must then isomerise to the *trans* adduct for cyclisation to occur. While isomerisation is likely 'absolutely' quick, it is 'relatively' slow compared to the elimination of alkyne and radical thiol. Therefore, more starting material is retrieved.¹⁴⁵

Scheme 2.2: The Mechanism for the Radical Synthesis of Dithiones. 145

The second generation ligand was then protected using tert-butyldimethylsilyl chloride and the one-pot molybdenum complexation was tried again in non-polar conditions, affording decent yields. However, upon deprotection, only the triscomplex was isolated. Returning to the transmetallation route using nickel and subsequent deprotection, $Mo(CO)_2(S_2C_2MeBnOH)_2$ (22) was synthesised.

 $Mo(CO)_2(S_2C_2MeBnOH)_2$ (22) was subsequently used as a precursor to isolate

the final target; a bio-mimetic Mo(IV) dithiolene complex ligated with a terminally-bound sulphur, mirroring the active site of the formate dehydrogenase enzyme.¹⁴⁶ Using disodium sulphide, a dark green emulsion was obtained but unfortunately, attempts to separate and purify a compound have been unsuccessful to date (Scheme 2.3).

Scheme 2.3: The Failed Synthesis of $(Bu_4N)_2[MoS(S_2C_2MeBnOH)_2]$ (23).

2.1.4 The Synthetic Strategy and Goals

The success Fontecave and Schulzke had with synthesising the Mo=O dithiolene complexes and their catalysts' subsequent activity is a positive indicator that synthesising similar catalysts are worth pursuing since trying to achieve Mo=S terminal functionality is extremely difficult. 103,104 Examining the FDH active site one can see a variety of protonatable sites, for example, amines and alcohols on the pterin moiety of pyranopterin (Figure 1.4) and the protein residues found around the active site. One can make the assumption that these protonatable sites act as proton relays and shuttle protons towards the metal core of the active site, aiding in catalysis. The proton relays can lower the kinetic barrier to a reaction, and the access to an environment with a high concentration of protons can reduce the chance of unwanted reaction pathways.

Continuing this logic, combining the Mo=O bis-dithiolene core with a proton relay in the ligand framework such that it would be positioned relatively close to

the central metal ion could result in highly selective catalysts for CO₂ reduction to formate. As mentioned above, previous work in the group managed to achieve synthesising this ligand along with its corresponding molybdenum-carbonyl complex; however, adding that Group 16 terminal functionality has been evasive so far.

A successful working mimic can be used to improve the mechanistic understanding behind the reversible catalysis of formate and carbon dioxide. As mentioned in Chapter 1, there is plenty of debate about the exact series of events that take place at the active site. There are exceptionally few working mimics, and an addition to their number would allow a better understanding of the mechanisms occurring at the active site of FDH through an increase in structural variation in the modelling.

Perhaps a far-off goal, but if a mimic is discovered with a high selectivity towards carbon dioxide reduction, there is an avenue for it to be used for geoengineering as a carbon-capture and utilisation tool. Fortunately, it will ignore common issues affecting other agents in the area, such as leakage and disturbing the natural ecosystem.

In essence, our systems will hope to replicate the increase in activity seen for catalysis when proton relays are grafted to the ligands' scaffold along with additional directionality of these proton relays towards the metal centre; a combination of ideas from DuBois and 'hangman' porphyrins.

2.2 An Initial Attempt at Synthesising the Target Molybdenum Complex

2.2.1 2-(Propyn-1-yl)benzyl Alcohol

As mentioned, previous work within the group established the necessity of a methyl group on the alkyne as the terminal analogue resulted in decomposition when one-pot synthesis was attempted to access the molybdenum-carbonyl complex. At the time, this synthetic strategy of minimising complications of an acidic proton was carried forward in order to access the target complex (30).

As shown in Scheme 2.4, a seemingly straightforward Sonogashira coupling between *ortho*-iodobenzyl alcohol with the *in situ* generation of propyne gave the known alkyne (24).^{147,148} The addition of a resonance due to a methyl group at 2.1 ppm and 4.62 ppm made ¹H and ¹³C NMR spectra powerful tools for identifying that the correct product was made (Figure 2.4).

Scheme 2.4: The Synthesis of 2-(Propyn-1-yl)benzyl Alcohol (24). 147,148

Obtaining reliable yields and purity proved challenging, so certain modifications were made to the literature preparation. Firstly, propyne was generated in an almost 3 eq. excess to ensure all of the iodobenzyl alcohol had a chance to couple to the gaseous alkyne; perhaps an innocuous step, but the product and the starting material are inseparable by chromatography, the initial purification method, so it was important to ensure that all the starting material had been consumed. To aid this approach, a cold-finger was attached to condense any remaining propyne back into the Sonogashira solution. Variation in colour, and therefore purity, of the final product (whilst simultaneously being indistinguishable via ¹H NMR spectroscopy) was also a cause of concern. A thorough degassing of both the Sonogashira solution and the propyne generation solution was undertaken with the aim of removing

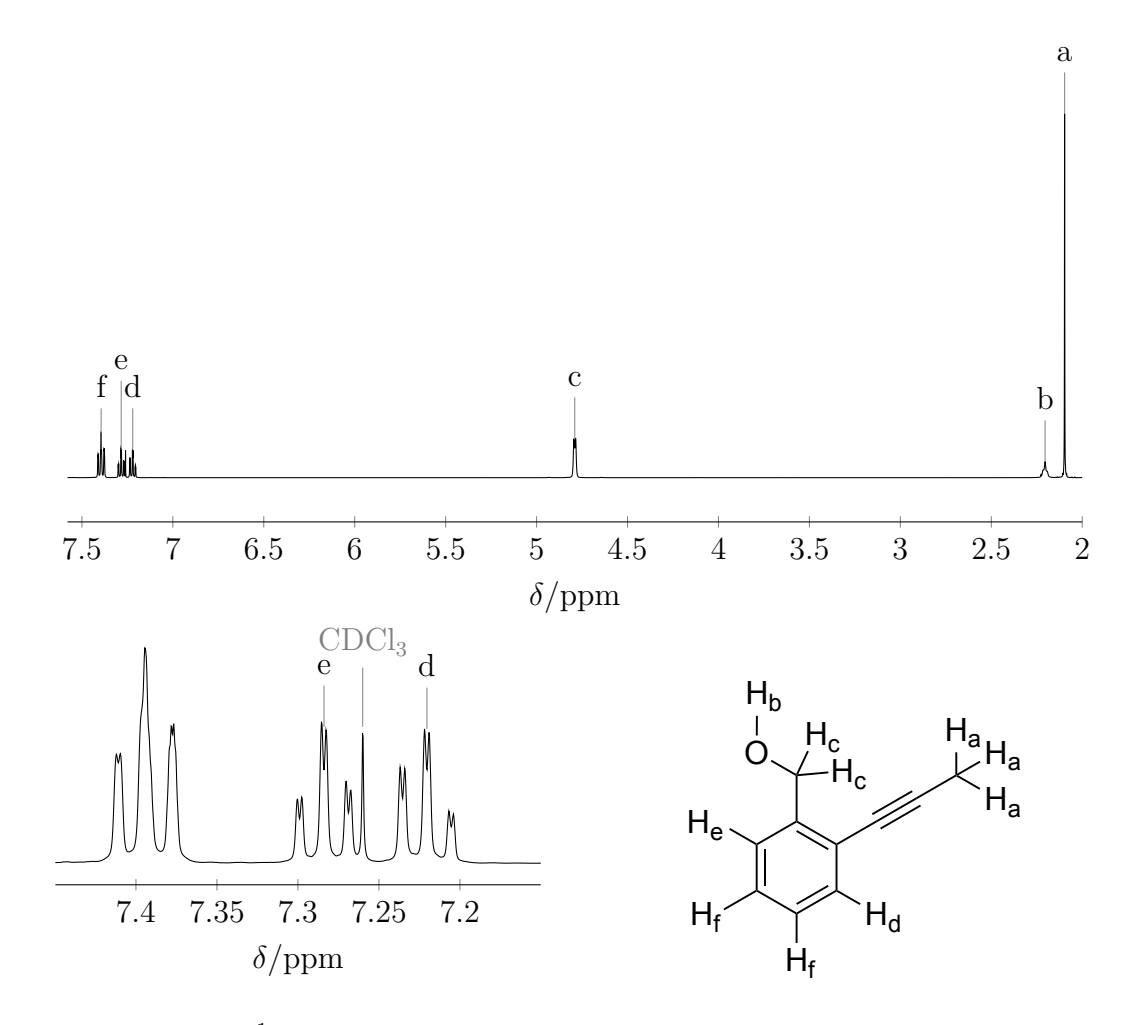


Figure 2.4: ¹H NMR Spectrum of 2-(Propyn-1-yl)benzyl Alcohol (24).

any remaining oxygen present in the hopes of eliminating any homo-coupling; this seemed to fix the issue and afforded pale-yellow prisms, matching the literature.

2.2.2 Diisopropyl Xanthogen Disulphide

A key reagent for the one-pot reaction of creating the target dithione, developed by Gareau and co-workers, 145 diiso propyl xanthogen disulphide transfers the 1,3-dithiol-2-one functionality to the alkyne. Firstly, potassium isopropyl xanthate (25) was synthesised and from this diiso propyl xanthogen disulphide (26). A straightforward

synthesis that yielded a yellow crystalline product that was shown to be pure through ¹H and ¹³C NMR spectroscopy (Scheme 2.5). ^{149,150}

OH + S=C=S
$$\xrightarrow{\text{KOH}}$$
 $\xrightarrow{\text{S}}$ $\xrightarrow{\text{KOH, I}_2}$ $\xrightarrow{\text{S}}$ $\xrightarrow{\text{$

Scheme 2.5: The Synthesis of Diisopropyl Xanthogen Disulphide (26). 149,150

2.2.3 The Functionalised Dithione

Scheme 2.6 shows a seemingly well-documented synthesis within the group. The previously synthesised alkyne (24) was refluxed together with di *iso* propyl xanthogen disulphide (26) and 1,1'-azobis(cyclohexanecarbonitrile) (the radical initiator more commonly referred to as ACHN) in ortho-xylenes to give the functionalised proligand 27. As mentioned previously, more forcing conditions were used to maximise yields of the product; traditionally, radical reactions utilise azobis isobutyronitrile (AIBN) and benzene as the initiator and solvent. After the reaction was completed, the pungent brown crude material, when worked up via chromatography, even with these harsher conditions, did not result in all the starting alkyne being converted to the desired product (starting material was recovered as a fraction). Upon performing thin layer chromatography (TLC), thirty-one spots could be counted with each sequential spot coincident to the next. Obtaining a completely clean product was exceedingly challenging; multiple attempts to purify the dithione by chromatography resulted in diminishing returns when reducing the number of spots in the TLC, but interestingly, two sequential columns, where the second column focused purely on the fraction containing the dithione product, gave clean ¹H and ¹³C NMR spectra and only 4 TLC spots. A detailed analysis of the ¹H NMR spectrum base line revealed numerous peaks. It could then be determined

that dithione 27 was only 91% pure. Elemental analysis was then performed on dithione 27. The calculated values were C 55.44; H 4.23; N 0; S 26.91; the found values were C 54.75; H 4.35; N 1.12; S 23.68%. The discrepancies between the calculated and the found values indicates the presence of inseparable impurities belonging to the remaining three spots found on the silica gel plate. The identity of these by-products is difficult to determine; however, it can be deduced that these molecules are very large. With three different compounds and 60 different H signals, the compounds must be big to accommodate the variety of environments seen on ¹H NMR spectrum, perhaps some kind of polymeric structure.

Scheme 2.6: The Second Generation Ligand Synthesis (27).

The viscous yellow oil obtained was easily characterised by identifying the presence of the carbonyl moiety via ¹³C NMR and IR spectroscopies (Figure 2.5). A point of interest is that despite the quaternary nature of the C=O it was easily identifiable, via ¹³C NMR spectroscopy, at 191.95 ppm. Previous researchers noted that the IR band of the C=O, seen at 1623 cm⁻¹, was too weak to be used to definitively characterise dithione compounds; notably, no such issue was found, making it a strong diagnostic feature for these kinds of compounds.¹⁴⁶

2.2.4 Protected Dithiones

To coordinate the dithione to a metal it must be first ring opened; this step involves using a base. Previous reports deemed it necessary to protect the alcohol group,

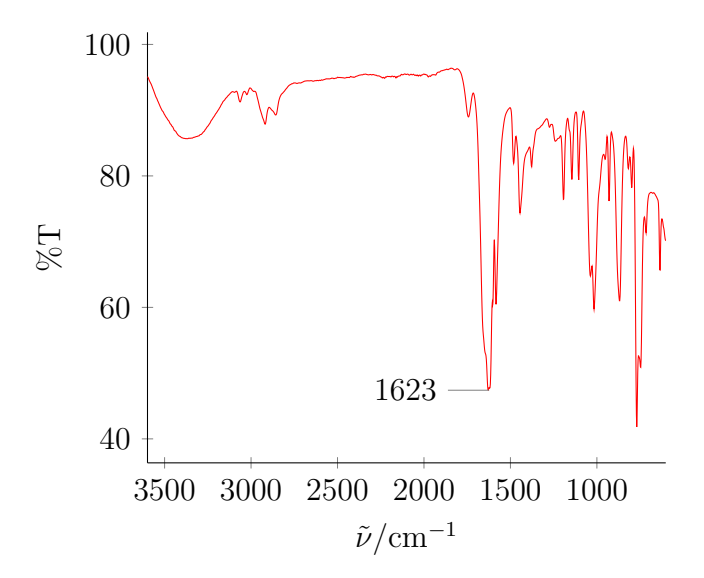


Figure 2.5: The IR Spectrum of the Functionalised Dithione (27).

present on the dithione, as it was believed that the addition of a strong base (n-butyllithium) would cause the ligand to decompose. Several protecting groups were trialled and *tert*-butyldimethylsilyl chloride was green-lit since the others could not be subsequently complexed successfully, affording **28** (Scheme 2.7). Such reactions are easily followed by ¹H NMR spectroscopy, through the disappearance of the alcohol peak at 2.09 ppm and the introduction of the dimethyl and *tert*-butyl proton resonances at 0.09 ppm and 0.94 ppm, respectively.

Scheme 2.7: The Synthesis of the Protected Dithione (28).

2.2.5 Nickel Dithiolenes

To achieve the Mo=O dithiolene functionality, the synthetic conclusion of a prior thesis remarked that transmetallation from nickel to molybdenum was the most promising route for this type of dithione ligand since the protecting group can be removed from the ligand in a straightforward manner whilst maintaining a modest yield. The protected dithione ligand (28) was ring-opened using nbutyllithium and then added to Ni(acac)₂, both having been dissolved in toluene; iodine was used to oxidise the ligand to achieve a neutral complex. The addition of a 1 M HCl solution removed the protecting group and purification by column chromatography gave 29, a deep blue, almost-black solid (Scheme 2.8). ¹⁵¹ Whilst the reaction needed to be treated under air and moisture sensitive conditions, the complex itself is bench-stable for months on end. Therefore, no additional thought was needed to be given for purification or on how to characterise this type of compound. Matrix-assisted laser desorption/ionisation time-of-flight mass spectrometry (MALDI-TOF) and ¹H NMR spectroscopy excelled as tools for characterising this complex. Figure 2.6 shows the experimental (m/z = 477.91)and theoretical mass spectrum of $Ni(S_2C_2MeBnOH)_2$ (exact m/z calculated for 58 NiC₂₀H₂₀O₂S₄: 477.97).

Scheme 2.8: Synthesis of $Ni(S_2C_2MeBnOH)_2$ (29).

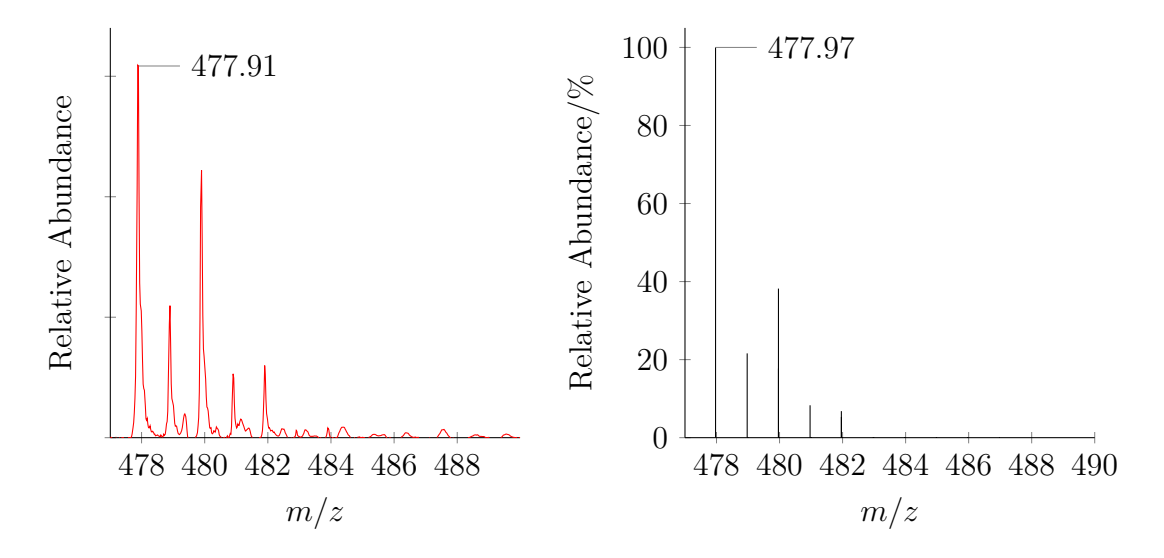


Figure 2.6: The Experimental (Left) and Theoretical (Right) Mass Spectra of $Ni(S_2C_2MeBnOH)_2$ (29).

2.2.6 The Molybdenum-Oxo Precursor

Roodt and co-workers developed the synthesis to $K_3Na[MoO_2(CN)_4] \cdot 6 H_2O$ (13), starting from sodium molybdate (Scheme 2.9) in the early 1990s. This salt was used by Holm as a molybdenum precursor to complex dithiolene ligands and for achieving the desired Mo=O terminal functionality. Special attention should be paid to this reaction as it involves the *in situ* generation of hydrogen cyanide, stimulating cyanide to coordinate to the molybdenum. After recrystallisation, bright pink crystals were obtained, and X-ray diffraction (XRD) gives a structure suitable for connectivity, which, used in conjunction with elemental analysis, allows for confirmation of the product 13.

2.2.7 Direct Transmetallation

Transmetallation was attempted using the nickel complex (29) and the molybdenum precursor (13). This afforded a red/brown precipitate upon addition of the salt n-Bu₄NBr. TLC revealed multiple spots, and air-sensitive flash chromatography

NaO-Mo-ONa
$$\xrightarrow{\text{KBH}_4, KCN,}$$
 $\xrightarrow{\text{EtOOH}}$ $\xrightarrow{\text{H}_2O}$ $\xrightarrow{\text{K}_3}$ Na $\begin{bmatrix} \text{NC,} & \text{II} & \text{CN} \\ \text{NC} & \text{II} & \text{CN} \\ \text{O} & \text{CN} \end{bmatrix}$ $6\text{H}_2\text{O}$

Scheme 2.9: Synthesis of the Molybdenum Precursor $K_3Na[MoO_2(CN)_4] \cdot 6H_2O(13)$. ¹⁵²

was attempted. Unfortunately, none of the fractions gave a convincing ¹H NMR spectrum or MALDI-TOF mass spectrum, so it was assumed that the reaction had failed. Further consideration of the reaction identified that the ligand would be in the radical state upon complexation to the metal. To remedy this, the ligand was reduced using Na/NaCl to the fully reduced oxidation state, elucidating a purple oil which also gave several spots upon TLC analysis (Scheme 2.10). Air-sensitive chromatography was also performed, but the reaction still seemed to have failed to give the desired product when the fractions were subjected to ¹H NMR spectroscopy and MALDI-TOF mass spectrometry.

Scheme 2.10: The Failed Transmetallation from Nickel to the Target Molybdenum Complex (30).

2.3 Troubleshooting

With the transmetallation from the nickel to molybdenum failing, a new approach needed to be used. Returning to the literature, more specifically Holm,¹⁰⁰ the group managed to achieve the Mo=O functionality by going through the Mo(CO)₂ analogues. Fortunately, previous work in the group had developed a robust approach for synthesising the molybdenum-carbonyl dithiolene for this hydroxy-functionalised ligand. Although previous researchers were unsuccessful with the post-complexation insertion of the Mo=S terminal functionality, insertion of the Mo=O was not tested.¹⁴⁶ But before continuing in this direction, Holm's work was repeated to ensure that an equipment issue, for example, dirty stirrer bars, or an impure reagent, was not hampering efforts.

2.3.1 The Synthesis of $Ni(S_2C_2Ph_2)_2$

To synthesise Ni complex 31, Schrauzer and Mayweg developed a quasi-one-pot synthesis starting from refluxing benzoin in dioxane with phosphorus pentasulphide (Scheme 2.11). Upon cooling and filtration, the Ni precursor was added. Whilst a relatively straightforward reaction, the purification step was modified slightly from a crystallisation to an unconventional usage of the silica plug. The product was trapped onto the silica first, using a minimum of methanol, and then washed thoroughly with toluene until the eluent ran clear. The product was then washed off the silica plug with methanol. MALDI-TOF mass spectrometry identified the molecular ion peak of 23 at m/z = 541.43 (exact m/z calculated for 58 NiC₂₈H₂₀S₄: 541.98).

Scheme 2.11: The Synthesis of $Ni(S_2C_2MeBnOH)_2$ (31). ¹⁵³

2.3.2 The Synthesis of $Mo(CO)_2(S_2C_2Ph_2)_2$

In Holm's synthesis,¹⁵⁴ the prepared Ni complex (31) was stirred together with the molybdenum-carbonyl precursor $Mo(CO)_3(MeCN)_3$ (32).¹⁵⁵ Previous efforts in the group found that establishing the correct ratio of acetonitrile to carbonyl was tricky as, depending on the solvent, the number of carbonyl peaks present in the infrared spectrum alternated between two and three; this would impact the stoichiometry and related mass calculations. This issue was mitigated by refluxing molybdenum hexacarbonyl in toluene to achieve the toluene adduct instead (32). Upon work-up, the IR spectrum gave the expected signals that matched with the literature values.

The $Mo(CO)_2(S_2C_2Ph_2)_2$ complex (33) was synthesised in the same manner as the literature, with the pre-prepared Ni complex 31 and the group's $Mo(CO)_3(PhMe)$ precursor (32), where, after an air-sensitive column, a purple solid was obtained (33). The identity of the product was confirmed by IR, NMR, and ultraviolet-visible (UV-VIS) absorption spectroscopy.

2.3.3 The Synthesis of $(Et_4N)_2[MoO(S_2C_2Ph_2)_2]$

 $Mo(CO)_2(S_2C_2Ph_2)_2$ (33) was dissolved in tetrahydrofuran and tetraethylammonium hydroxide was added to simultaneously insert the oxo functionality and the NEt_4^+ cations, giving $(Et_4N)_2[MoO(S_2C_2Ph_2)_2]$ (34) as a red precipitate with a yield

Scheme 2.12: The Synthesis of $Mo(CO)_2(S_2C_2Ph_2)_2$ (33). ¹⁵⁴

of 31%. The nature of this solid was confirmed by MALDI-TOF mass spectrometry $(m/z = 597.68, \text{ exact mass } m/z \text{ calculated for }^{97}\text{MoC}_{28}\text{H}_{20}\text{OS}_4\text{: }597.95)$. The only consideration made was that the solvent and reactants were heavily degassed before use. Therefore, one can assume that the success of the subsequent attempts to target 30 was decided not by external factors but by the chemicals themselves.

2.3.4 The Synthesis of $Mo(CO)_2(S_2C_2MeBnOH)_2$

Shown in Scheme 2.13, the novel nickel dithiolene complex (29) was stirred with $Mo(CO)_3(PhMe)$ (32) in ethyl acetate to give a purple solid after an air-sensitive column. Like the diphenyl analogue, the purple solid (22) was confirmed as the product by infrared spectroscopy and UV-VIS absorption spectroscopy. Interest-

Scheme 2.13: The Synthesis of $Mo(CO)_2(S_2C_2MeBnOH)_2$ (22).

ingly, obtaining the mass spectra and elemental analysis data of molybdenumcarbonyl dithiolene complexes is exceedingly challenging; this can be seen in the original paper from Schrauzer and co-workers where these complexes were first synthesised.¹⁵⁶ They reported a calculated value for ⁹⁷MoC₃₀H₂₀O₂S₄ (**33**) of 636.7 and in the mass spectrum they found a value of 615. Similarly for the elemental analysis, the calculated values were Mo 15.1; C 56.6; H 3.2; S 20.1%; the found values were Mo 14.9; C 57.0; H 3.4; S 20.5%. Probably due to similar difficulties Holm did not report the elemental analysis or the mass spectrometry values, simply remarking 'Comparison of the absorption spectrum with that previously reported¹⁵⁶ confirmed the identity of the compound.' Similar difficulties occurred when trying to obtain the mass spectrum and elemental analysis values for **22** so the identity of the complex was confirmed by the UV/Vis and IR spectrums.

2.3.5 Inserting the Mo=O Functionality from the Molybdenum Carbonyl Intermediate

Shown in Scheme 2.14, Mo(CO)₂(S₂C₂MeBnOH)₂ (**22**) was dissolved in tetrahydrofuran, and dropwise addition of Et₄NOH gave an immediate colour change to green, indicative of the Mo^{VI} oxidation state and the formation of the tris-complex, Mo(S₂C₂MeBnOH)₃ (identified by previous workers in the group).¹⁴⁶ Unfortunately, the reaction had failed.

OH OH OH

OC CO

$$S \cap M \cap S$$
 $S \cap M \cap S$
 $S \cap M \cap S$

Scheme 2.14: The Failed Synthesis of the Target Complex 30 via $Mo(CO)_2(S_2C_2MeBnOH)_2$ (22).

2.3.6 Alternatives to Transmetallation from Nickel to Molybdenum

Since transmetallation is impossible, the literature was re-examined to find other alternative routes. Holm, Fontecave, and Schulzke enjoyed success by going through the $K_3Na[MoO_2(CN)_4] \cdot 6\,H_2O$ (13) molybdenum precursor. $^{100,103-105,111}$ Holm, Fontecave, and previous iterations of similar syntheses employed by the Wright group used strong bases to open the ligands to coordinate to molybdenum. The fear was such a route would decompose the novel ligand at the hydroxy moiety if left unprotected and was initially considered a non-viable method. A thorough search of the literature revealed Schulzke and co-workers succeeded in generating their ligand from their dithione pro-ligand using potassium hydroxide; this base should have no issues with dithione 27.

Initially, attempts were made to complex the protected ligand (28) and then to deprotect once complexation had occurred. A red solution was generated, but upon deprotection with a weak acid to remove the protecting group, a green emulsion formed, indicative of the formation of Mo(dithiolene)₃. It was initially hypothesised that the Mo=O bond was strong enough to avoid being replaced by a neighbouring dithiolene moiety; however, this clearly is not the case.

The unprotected dithiolene ligand (27) was trialled next. This route also affords a red solution. However, after the addition of a salt containing a large cation (Et_4N^+) , a dark brown oil separated from the solution. Layered recrystallisation using THF/Et₂O was attempted to purify the product but to no avail; the reaction had failed, as shown in Scheme 2.15.

Scheme 2.15: The Failed Direct Complexation of the Ligand to Afford the Desired Target Complex (30).

2.3.7 Alternative Routes to the Novel Ligand

Schulzke and co-workers successfully coordinated a similarly hydroxy-functionalised ligand to molybdenum using 13.¹⁰⁴ Comparing the two syntheses showed a high similarity; consequently, it can be deduced that the inseparable impurities present after the radical reaction influenced the outcome of the coordination reaction. Therefore, it was deemed necessary to look towards other synthetic routes to the novel ligand to avoid the inseparable impurity issue associated with the radical cyclisation route.

A paper from Ried and co-workers offered a new possible route to the proligand (27).¹⁵⁷ This involved the addition of carbon disulphide and elemental sulphur to the previously prepared alkyne. The reaction was tried with both the alkyne protected and unprotected; protection was thought to be necessary to prevent any unwanted reactions between the carbon disulphide and the hydroxy group. The potential advantages of this route were that the ability to scale the reaction is significantly improved compared to the radical reaction, which is limited to 7 mmol of starting material per reaction; the workup should be more straightforward, seeing as the reaction is not radical and, therefore, the number of side products should be limited in comparison. The monetary cost of the reaction is also lowered as there is no need for the expensive radical initiator. However, only starting material was

recovered. The reaction was retried again, but instead, the reaction took place at 80 °C to force the reaction towards completion (to prevent the carbon disulphide from evaporating off, a microwave tube was used). Again, however, the reaction only gave back starting material.

The second route considered was also a radical reaction, but this time it was initiated via ultraviolet (UV) light, avoiding the need for the ACHN initiator. Although lacking the scalability of the aforementioned route, the lack of a radical initiator means that the workup should be greatly simplified due to the limited number of products. But unfortunately, only starting material was afforded.

2.4 Streamlining the Synthesis of the Functionalised Dithiolene Ligand

With each successive failure to achieve the Mo=O functionality, the original radical synthesis was re-examined; the reaction could be broken down into three distinct areas: technique/solvent, reagents, and work-up.

2.4.1 Technique/Solvent

Radical reactions are known to be extremely oxygen-sensitive due to the paramagnetic nature of oxygen and therefore having a strong ability to quench such reactions. Therefore, it was initially presumed that oxygen interfered with the reaction in some way. As a countermeasure, thorough purging of the glassware was performed by cycling the Schlenk line between argon gas and a vacuum; the solvent was also degassed by six rounds of freeze-pump-thaw. Successive complexations to Mo still failed. However, the influence of trace oxygen hampering the reaction could be ruled out.

2.4.2 Reagents

When looking at simple organics, it is very common for them to be colourless when nearing absolute purity. Thus, 2-(propyn-1-yl)benzyl alcohol (24) presenting as a pale-yellow solid was concerning. Sublimation of 2-(propyn-1-yl)benzyl alcohol (24) gave a white powder, with a brown oil was left behind. A ³¹P NMR spectrum of the oil showed a massive PPh₃=O peak at 29.34 ppm, not to mention other impurities found when liquid chromatography mass spectrometry (LC-MS) was performed. ¹⁶⁰

To be certain of the purity of di*iso* propyl xanthogen disulphide (26), the compound was worked up again. To ensure no iodine was left, it was washed thoroughly with sodium thiosulphate. Crystallisation now gave green prisms. Performing the radical reaction gave a deep red, clear oil that had a far less offensive odour. TLC revealed far fewer spots, and the orange oil characteristic of the target dithione (27) was obtained again. Unfortunately, once again, the coordination of dithione 27 with the molybdenum precursor (13) failed.

2.4.3 Work-up

As mentioned previously, TLC after flash chromatography revealed 4 spots. Upon implementing the changes listed above, striving to reduce this number seemed to be the final avenue to explore before the idea to synthesise a Mo=O functionalised system with our novel ligand would need to be abandoned. However, it seemed that catching one of these spots before it entered the collective fraction was not achievable through traditional flash chromatography. Fortunately, automatic flash chromatography systems track changes in the UV-VIS spectra of molecules in solution passing by their detector, allowing for more accurate separation of compounds when performing chromatography. Using the automatic column reduced the number of spots on the TLC for the dithione from four to three (one spot

corresponding to the target dithione 27 and two inseparable impurities).

2.5 The Synthesis of

$(\mathrm{Et_4N})_2[\mathrm{MoO}(\mathrm{S_2C_2MeBnOH})_2]$

After adjusting the reaction conditions and a series of synthetic attempts, the reaction was a success, giving a brown precipitate (Scheme 2.16); MALDI-TOF gave a large molecular ion peak at m/z = 533.82 (exact mass m/z calculated for $^{97}\text{MoC}_{20}\text{H}_{20}\text{O}_3\text{S}_4$: 533.94) shown in Figure 2.7. However, the complex decomposed rapidly (within 24 hours after synthesis). Multiple recrystallisations from acetonitrile and diethyl ether afforded a red precipitate that must be stored under Ar, in the absence of light and at $-25\,^{\circ}\text{C}$; the lifetime of the complex can now be extended. Identifying the Mo=O bond in the IR spectrum and obtaining X-ray suitable crystals was challenging; Chapter 4 aims to address the former and explain the latter by using computational methods.

Scheme 2.16: The Successful Synthesis of the Target Complex $(Et_4N)_2[MoO(S_2C_2MeBnOH)_2]$ (30).

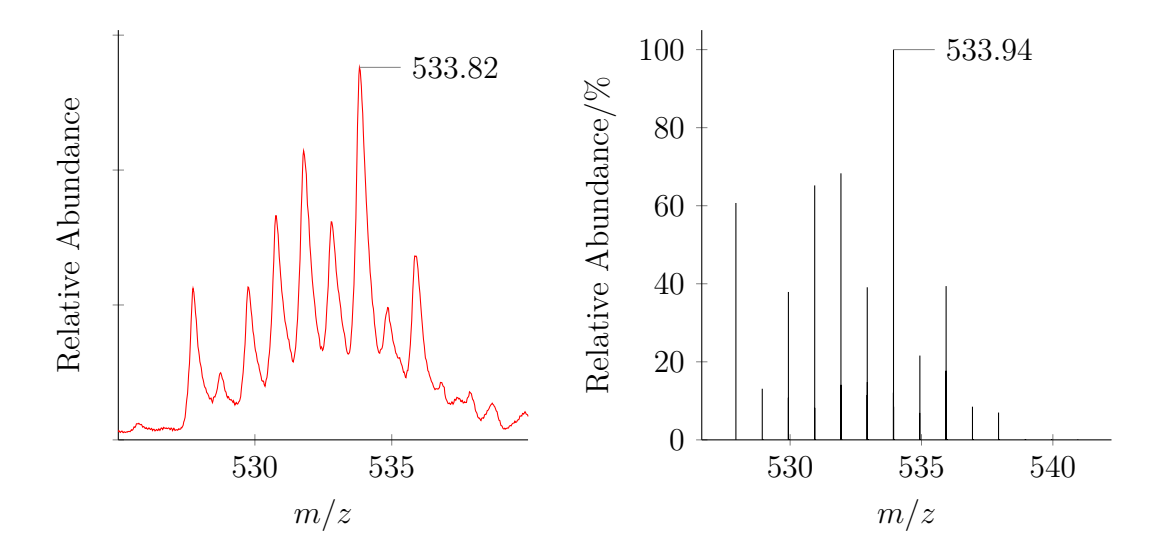


Figure 2.7: The Experimental MALDI-TOF Mass Spectrum (Left) of $(Et_4N)_2[MoO(S_2C_2MeBnOH)_2]$ (30) and its Associated Theoretical Mass Spectrum (Right).

2.6 Summary

An alcohol functionalised dithione ligand (27) has been successfully developed and the number of synthetic steps to the target complex (30) has been reduced from initial predictions. Synthesising the target complex (30) was hindered by the purity of the dithiolene ligand due to the purity of previous compounds; an extremely stringent work up was necessary to achieve a successful coordination of the dithiolene to molybdenum. From these syntheses, it would be recommended to ensure that all compounds synthesised by a metal catalysed cross-coupling reaction are carefully tested to ensure trace metals or reagents are not carried through to subsequent reactions. In essence, a novel ligand and its corresponding synthesis have been developed, allowing for a new method to target FDH mimics. This complex is extremely air, temperature, and light sensitive. Manipulations to this compound post-synthesis must be kept to a minimum to avoid decomposition.

Chapter 3

Further Synthesis of Molybdenum and Tungsten Dithiolenes

3.1 Introduction

Nearly 25 years ago, Holm and Donahue summarised several methods to synthesise molybdenum-oxo dithiolene complexes;¹⁰⁰ however, the current catalogue of these molecules is fairly small. Highlighted in Figure 3.1, only 43 complexes have been reported with only a couple going beyond what can be called simple ligand scaffolds.^{94–99,101–111} This is likely due to the technical difficulty in inserting the dithiolene functionality and subsequent complexation.

In Chapter 2, a novel, streamlined synthesis for a molybdenum-oxo complex was reported. To test the robustness of this pathway, a series of complexes were synthesised. Essentially, the complex can be accessed in three simple steps: alkyne \rightarrow dithione derivative \rightarrow molybdenum-oxo dithiolene complex. The insertion of the dithiolene functionality reported by contemporary groups is often multi-step (approximately five steps), which obviously impacts the cost of production, final ligand yields, and becomes specialist syntheses within the group (reproducibility

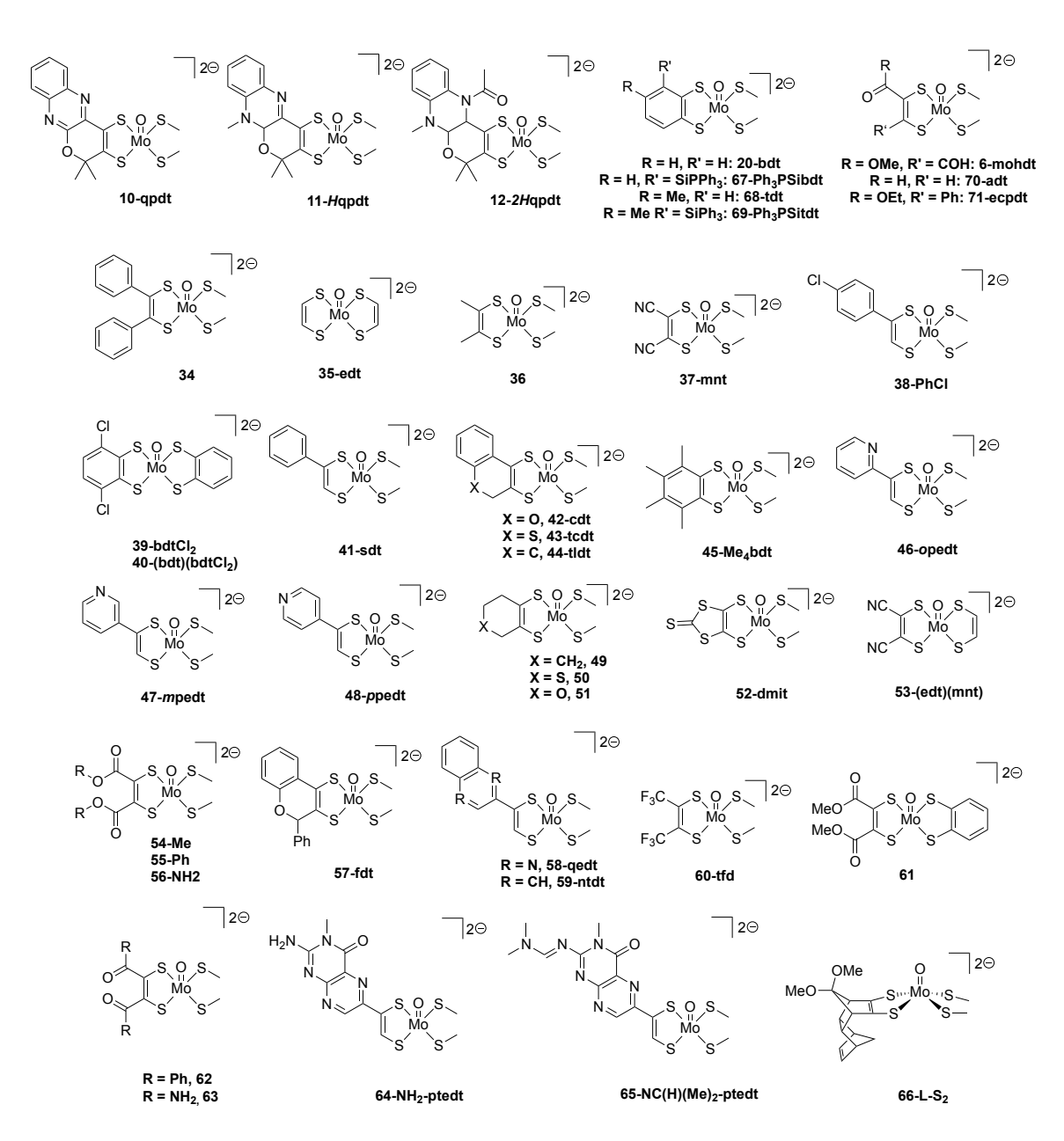


Figure 3.1: A Compete Catalogue of $\mathrm{Mo^{IV}O}(\mathrm{dithiolene})_2$ Complexes Found in the Literature. 94–101,103,105–109,111,161

is difficult). The single-step insertion of the dithiolene/dithione moiety with the radical cyclisation synthesis does not suffer from these issues, making metal-complex synthesis more accessible. Using this method developed by Gareau and co-workers, a host of pro-ligands can be generated and tested for complexation to the molybdenum-oxo precursor. ¹⁴⁵

3.2 Adding to the Catalogue of Mo=O Dithiolene Complexes

3.2.1 The Synthesis of 1,3-Dithiol-2-one-4-phenyl-5-methyl

The first ligand synthesis attempted was the phenyl analogue of the target pro-ligand (27). To access 72, iodo-benzene was coupled to propyne through a Sonogashira reaction. After ensuring the absolute purity of alkyne 72, accomplished by using an automatic column with an adjusted solvent ratio, by NMR spectroscopy and LC-MS, the alkyne was refluxed with disopropyl xanthogen disulphide (26) and ACHN in ortho-xylenes, shown in Scheme 3.1; an orange oil was afforded (73). Despite only missing the methanol group, found on 27, there was a large change in the viscosity of the oil, highlighting the strength of hydrogen bonds. IR and ¹³C NMR spectroscopy played a key role in identifying the correct fraction, after purification via flash chromatography, by the presence of the C=O bond at 1668 cm⁻¹ and 191.55 ppm, respectively.

3.2.2 The Synthesis of 1,3-Dithiol-2-one-4-phenyl-5-ethyl

1,3-Dithiol-2-one-4-phenyl-5-ethyl (**74**) was prepared from commercially purchased 1-phenyl-1-butyne, di*iso* propyl xanthogen disulphide (**26**) and ACHN refluxed in *ortho*-xylenes (scheme 3.2). After an automatic column a yellow oil was obtained,

Scheme 3.1: The Synthesis of the Phenyl Analogue of the Target Ligand (73). 145

slightly more viscous than **73**. This compound was easily characterised by IR and ¹³C NMR spectroscopy by identifying the C=O present at 1643 cm⁻¹ and 191.64 ppm, respectively.

Scheme 3.2: The Synthesis of 1,3-Dithiol-2-one-4-ethyl-5-phenyl (74). 145

3.2.3 The Synthesis of 1,3-Dithiol-2-one-4-phenyl

The dithione was synthesised by refluxing phenylacetylene, di*iso* propyl xanthogen disulphide (26) and ACHN in *ortho*-xylenes (Scheme 3.3). This afforded yellow crystals of 75 but NMR spectroscopy proved insufficient to convincingly characterise the compound due to inseparable impurities; the ¹H NMR spectrum had many peaks in the region 0 ppm to 2 ppm. Fortunately, from the crystals, a structure could be obtained by X-ray diffraction, suitable for connectivity (Figure 3.2).

Scheme 3.3: The Synthesis of 1,3-Dithiol-2-one-4-phenyl $(\mathbf{75})$. 145

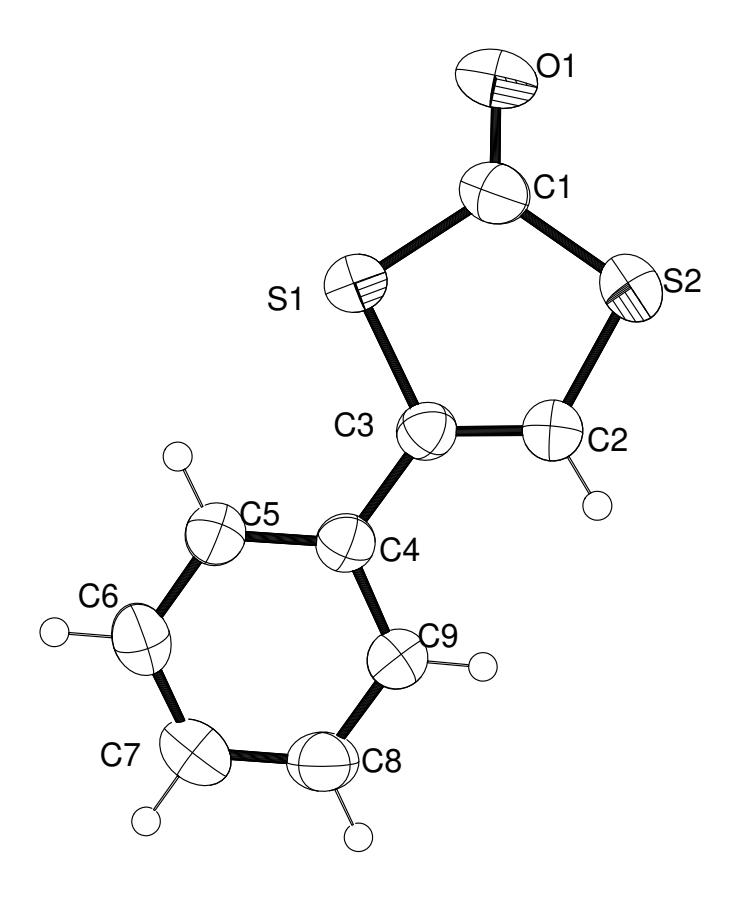


Figure 3.2: The X-ray Crystal Structure of 1,3-Dithiol-2-one-4-phenyl (75).

3.2.4 The Synthesis of 1,3-Dithiol-2-one-5-benzyl Alcohol

With the successful synthesis of the target complex, it was worth revisiting the first generation ligand (21) in order to access the analogue of the target complex (30) with the alkenyl proton instead of the methyl group. Firstly, the alkyne (76) must be synthesised by a Sonogashira cross-coupling reaction between trimethylsilylacetylene and iodobenzyl alcohol, affording a white solid. Prior to sublimation, a yellow solid was obtained, highlighting the need for more thorough cleaning steps not mentioned in the literature; for instance, this compound is reported as being an orange-yellow oil which is clearly incorrect. The alkyne was refluxed in *ortho*-xylenes with diisopropyl xanthogen disulphide (26) and ACHN, giving orange crystals of 1,3-dithiol-2-one-5-benzyl alcohol (12) after automatic flash chromatography (Scheme 3.4). This dithiolene was characterised by the appearance of the C=O moiety at 193.13 ppm in the ¹³C NMR spectrum (Figure 3.3) and 1627 cm⁻¹ in the IR spectrum.

Scheme 3.4: The Synthesis of 1,3-Dithiol-2-one-5-benzyl alcohol (21).

3.2.5 The Synthesis of 1,3-Dithiol-2-one-4-para-aniline

Whilst Gareau and co-workers developed an extensive catalogue of dithione analogues, they did not foray past hydroxy and halide functional groups to test the robustness of their radical cyclisation; the addition of an amine-dithione variant would be an interesting assessment of this reaction's selective capabilities.

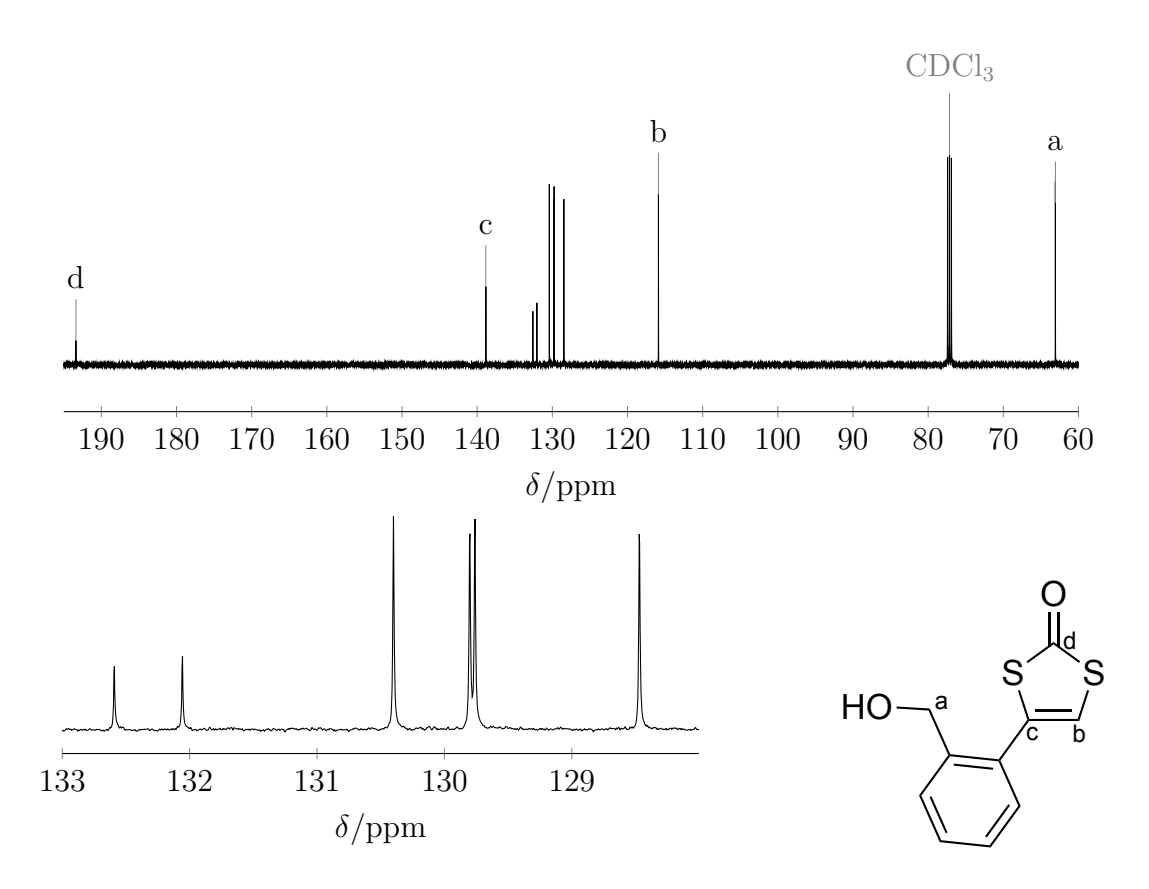


Figure 3.3: The $^{13}\mathrm{C}$ NMR Spectrum of 1,3-Dithiol-2-one-5-benzyl Alcohol (21).

4-ethynylaniline was refluxed with di*iso* propyl xanthogen disulphide (26) and ACHN in *ortho*-xylene to give an orange solid after automatic flash chromatography (Scheme 3.5). The identity of the solid dithione (77) was confirmed by identifying the N-H and C=O stretches in the IR spectrum (Figure 3.4), 3369 and $1626 \,\mathrm{cm}^{-1}$, respectively, the amine protons (3.85 ppm) in the ¹H NMR spectrum, and the molecular ion peak in LC-MS (experimental m/z = 210, calculated m/z for $C_9H_7NOS_2 + H^+ = 210.00$).

3.2.6 The Synthesis of $(Et_4N)_2[MoO(S_2C_2MePh)_2]$

The dithione pro-ligand **73** was deliberately chosen because it has the same scaffold as dithione **18** but lacks the hydroxy group. This would allow for insight into

Scheme 3.5: The Synthesis of 1,3-Dithiol-2-one-4-para-aniline (77).

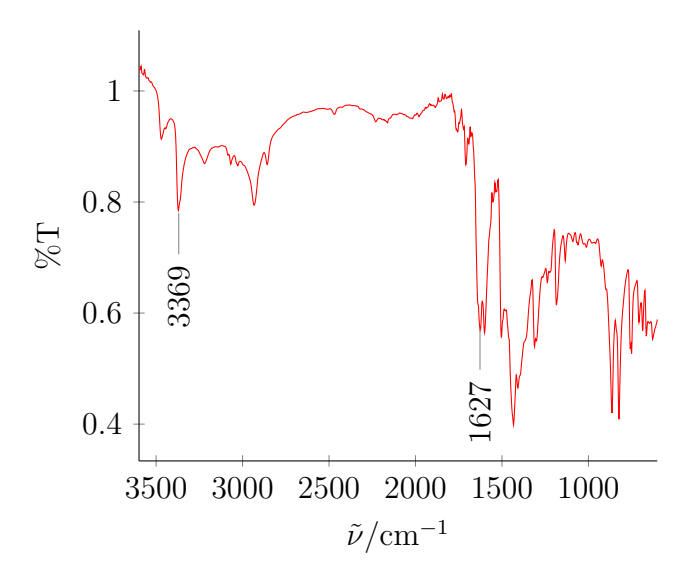


Figure 3.4: The IR Spectrum of 1,3-Dithiol-2-one-4-para-aniline (77).

the electrochemical and catalytic behaviour of the molybdenum-oxo bis-dithiolene complexes with/without said hydroxy group. The dithione **73** was ring opened via the addition of potassium hydroxide; the molybdenum precursor **13** was added, rapidly followed by the addition of the ammonium cation (Scheme 3.6). Subsequent work-up afforded a red, extremely sticky film (**78**). This complex lacks any defining groups, making characterisation via IR spectroscopy difficult. However, MALDITOF mass spectrometry gave a clear molecular ion peak (m/z = 473.76, exact m/z calculated for ${}^{97}\text{MoC}_{18}\text{H}_{16}\text{OS}_4$: 473.91).

Scheme 3.6: The Synthesis of $(Et_4N)_2[MoO(S_2C_2MePh)_2]$ (78).

3.2.7 The Synthesis of $(Et_4N)_2[MoO(S_2C_2EtPh)_2]$

The dithiolene pro-ligand **74** was chosen to investigate how the bulkier ethyl group, substituted at the methyl position, influences the behaviour and success of the complexation reaction. To a solution of the dithione in methanol, potassium hydroxide was added to ring-open the pro-ligand. The addition of the molybdenum precursor **13** did not give the rapid colour change to red expected when successful complexation had occurred; the coordination process took three times as long (2 hours and 30 minutes versus 45 minutes for the reaction with ligand **27**) indicating that the sterics of the dithiolene influence the kinetics of coordination to molybdenum (Scheme 3.7). NMR and IR spectroscopies were not definitive for the identity of the resultant yellow/orange film, but yet again, MALDI-TOF

mass spectrometry (Figure 3.5) offered irrefutable evidence for the presence of complex **79** through the presence of the molecular ion peak (m/z = 501.92, exact m/z calculated for $^{97}\text{MoC}_{20}\text{H}_{20}\text{OS}_4$: 501.95).

Scheme 3.7: The Synthesis of $(Et_4N)_2[MoO(S_2C_2EtPh)_2]$ (79).

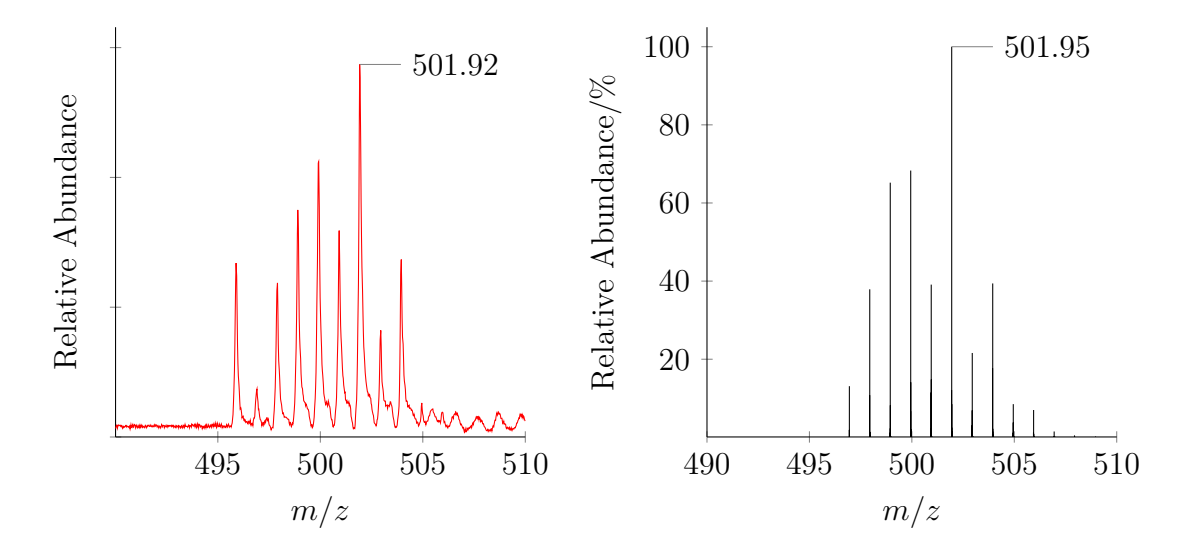


Figure 3.5: The Experimental (Left) and Theoretical (Right) Mass Spectra of of $(Et_4N)_2[MoO(S_2C_2EtPh)_2]$ (79).

3.2.8 The Synthesis of $(Et_4N)_2[MoO(S_2C_2HPh)_2]$

Although complex **41** already exists in the literature, following the same coordination procedure using the molybdenum precursor (**13**), the ligand synthesis is a much more involved process starting from a bromoacetyl moiety which is then protected

to a dimethylamino-derivative.¹⁰¹ In terms of atom economy, the radical insertion of the dithione is a far better approach. This particular complex was targeted as the unfunctionalised analogue of **80** in order to investigate the effects of the hydroxy group on the electrochemical behaviour of the complex. The molybdenum precursor **13** was added rapidly after the pro-ligand **75** was ring opened using potassium hydroxide, affording a deep red film after subsequent recrystallisations (Scheme 3.8). Complex **41** was confirmed through MALDI-TOF mass spectrometry $(m/z = 445.77, \text{ exact } m/z \text{ calculated for } ^{97}\text{MoC}_{16}\text{H}_{12}\text{OS}_4$: 445.88).

Scheme 3.8: The Synthesis of $(Et_4N)_2[MoO(S_2C_2HPh)_2]$ (41).

3.2.9 The Synthesis of $(Et_4N)_2[MoO(S_2C_2HBnOH)_2]$

Since the hydroxy functionalised target complex 30 was successfully synthesised from the second generation pro-ligand 27, it was appropriate to re-examine the first generation pro-ligand 21 for complexation with molybdenum. This pro-ligand differs from 27 at the alkenyl position, where the methyl group is substituted for a proton. From this, it is possible to examine the effect this substituent has on the redox properties of the complex. The orange crystals of 21 were dissolved in methanol, where the addition of potassium hydroxide opened the pro-ligand for coordination to the molybdenum precursor 13 (Scheme 3.9); like the other alkenyl proton system synthesised previously, the coordination process took place extremely quickly (5 minutes). A red film of 80 was afforded, which was confirmed

by MALDI-TOF mass spectrometry (Figure 3.6), where a molecular ion peak at m/z = 505.86 could be observed (exact m/z calculated for $^{97}\text{MoC}_{18}\text{H}_{16}\text{O}_3\text{S}_4$: 505.90).

Scheme 3.9: The Synthesis of $(Et_4N)_2[MoO(S_2C_2HBnOH)_2]$ (80).

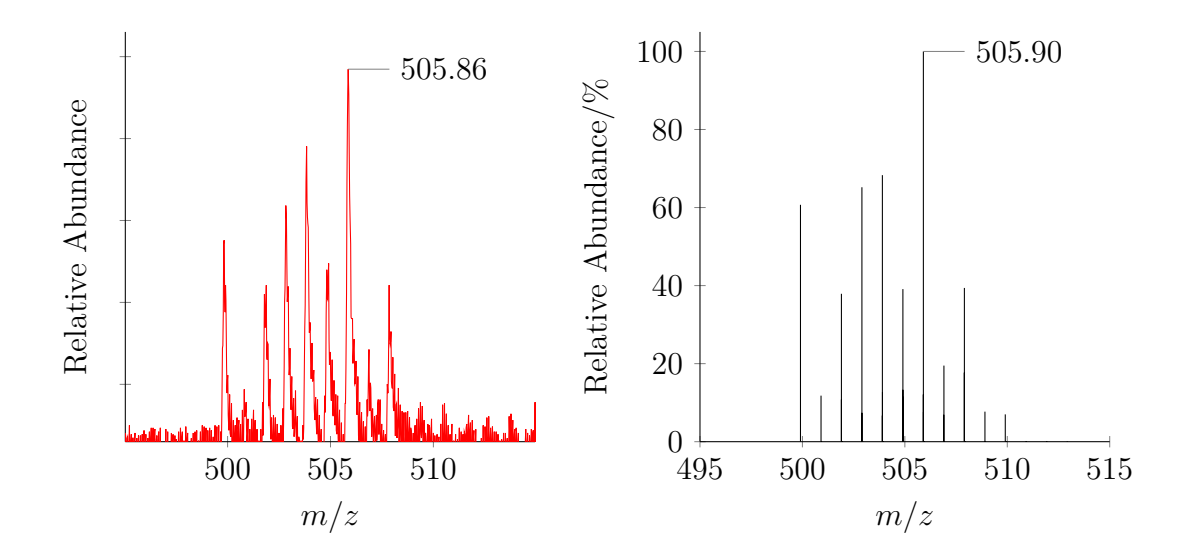


Figure 3.6: The Experimental (Left) and Theoretical (Right) Mass Spectra of of $(Et_4N)_2[MoO(S_2C_2HBnOH)_2]$ (80).

3.2.10 The Synthesis of $(Et_4N)_2[MoO(S_2C_2HNH_2)_2]$

When examining the catalogue of previously synthesised MoO(dithiolene)₂, only one shows an amine group with free protons, but this could not be considered within the secondary coordination sphere (perhaps the tertiary).¹⁰¹ Therefore, one must

examine if these amine protons would inhibit the complexation of dithione 77. The dithione was treated with potassium hydroxide in methanol and the molybdenum precursor (13) was added (Scheme 3.10); the coordination process took slightly longer than the other alkenyl-proton systems, but was still much faster than the bulkier alkenyl groups. A dark red film of 81 was afforded and was confirmed via MALDI-TOF mass spectrometry (m/z = 476.37, exact m/z calculated for $^{97}\text{MoC}_{16}\text{H}_{14}\text{N}_2\text{OS}_4$: 475.90). Although MALDI-TOF suggests that coordination had indeed occurred through the dithiolene and not via the amine it is not conclusive. IR spectroscopy was used to show that an amine group is present at 3310 cm⁻¹ (Figure 3.7) confirming that the dithiolene is what coordinated to the molybdenum.

Scheme 3.10: The Synthesis of $(Et_4N)_2[MoO(S_2C_2HNH_2)_2]$ (81).

3.3 Advanced Ligand Synthesis

3.3.1 A Bridged Ligand

Quite well documented in the literature is the difficulty of obtaining a crystal structure of these molybdenum dithiolene complexes when the ligand scaffold moves away from simple structures and becomes more advanced. It can be argued that the 2H-qpdt complex (12) developed by Fontecave and co-workers is the most func-

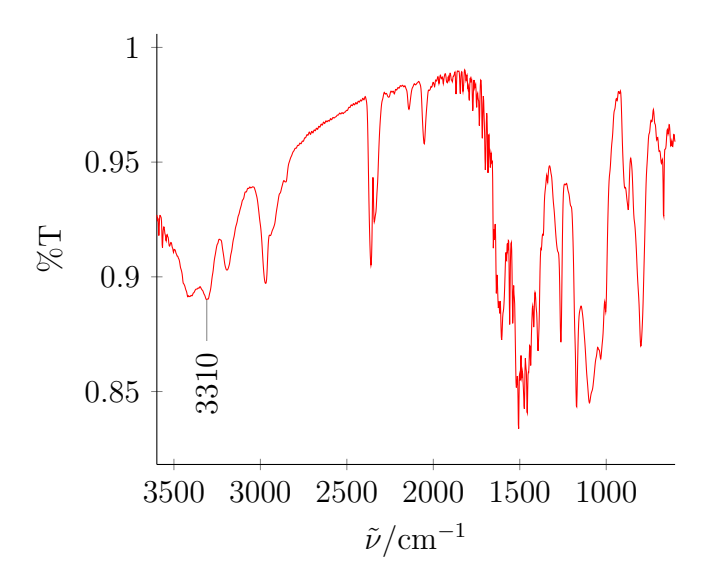


Figure 3.7: The IR Spectrum of $(Et_4N)_2[MoO(S_2C_2HPhNH_2)_2]$ (81).

tionalised in the catalogue of molybdenum-oxo dithiolene complexes and no crystal structure was able to be obtained. But, a crystal structure exists for complexes 10 and 11.¹⁰³ This would contradict the prior statement that functionalised ligands do not produce crystal structures; however, when one considers the nature of the qpdt (7) and H-qpdt (8) ligands, we can formulate a hypothesis that preventing isomers results in single-crystals suitable for X-ray diffraction. Both substituents of the dithiolene moiety of the qpdt ligand are joined in a pyran ring. This would greatly reduce the number of possible spatial isomers by providing rigidity to the structure. Further evidence for this hypothesis hypothesis is given by the 2H-qpdt ligand (9) where the addition of the acetyl group does not provide a crystal structure when coordinated to molybdenum, ¹⁰³ implying that additional spatially free moieties quickly add to the number of isomers and prevent the formation of a single crystal.

Through the use of computational methods, further expounded upon in Chapter 4, it was identified that numerous spatial isomers exist for the novel system **30**: the ligands can be both *cis* and *trans*, and the relative positions of the benzyl alcohol substituent can be up and down. Perhaps adding rigidity to this structure would

afford a crystal suitable for XRD.

The hydroxy functionality is well known for its chemical versatility, even being highlighted within this thesis as a proton relay for the purpose of aiding catalysis. A paper from Bunz and co-workers offered inspiration for the development of a 'third' generation ligand. They developed a bridged organic from a diol in an effort to remove internal twisting within the molecule. This synthesis could be repurposed to provide the extra rigidity necessary to form a crystal structure. The length of the 'bridge' moiety must be considered; too long and no spatial locking would occur resulting in a system that had access to both the *cis* and *trans* isomers; too short and the sterics of the ligand would prevent tetradentate coordination to the molybdenum from occurring. Acetylacetone was deemed the correct length in order to force the resulting complex into the *cis* conformation, halving the number of potential isomers.

Scheme 3.11: Synthesis of the Bridged Ligand (82).

Dithione 27 and malonyl chloride were dissolved in dichloromethane in the presence of sodium bicarbonate. After flash chromatography, a yellow oil was obtained (Scheme 3.11). 1 H and 13 C NMR spectroscopy gave the expected peaks found in 18, but with the addition of new peaks at 3.44 and 41.42 ppm, respectively, corresponding to the -CH₂ of the newly introduced moiety. LC-MS was performed to ensure the correct characterisation of the molecule; a molecular ion peak at m/z = 545.022 (exact m/z calculated for $C_{25}H_{20}O_6S_4$: 544.01) confirmed the presence of 82.

3.3.2 Coordination of the Bridged Ligand

With the successful synthesis of 82, coordination to molybdenum was attempted. Looking at the bridged ligand, one can see that there are two dithiolenes. There was concern that because of the presence of multiple coordination sites per ligand, multiple products were possible: the ideal tetra-coordinated complex (the target), a dimer system, or even an oligomeric/polymeric structure. Therefore, considerable efforts were made to limit the formation of these unwanted by-products.

In the synthesis of porphyrins, it is well known that without careful control of the reaction conditions, cyclisation will not occur and instead polymers will form. To combat this, high dilution and slow addition are methods that are used to reduce the chances of this occurring. These methods were applied to the general synthesis of these molybdenum-oxo dithiolene systems. The molybdenum precursor 13 was dissolved in a great excess of solvent and the ligand was added slowly over a three hour period. The ligand itself required a bit more consideration than usual due to the acidic protons found between the two carbonyl moieties. It was presumed that enolisation would not be detrimental to the reaction, but an excess of the base was added to ensure that both of the dithione moieties were ring opened (Scheme 3.12).

Scheme 3.12: The Failed Synthesis for Accessing the Bridged Complex 83.

Unfortunately, upon performing MALDI-TOF mass spectrometry, the expected molecular ion peak at m/z = 600.60 was not seen, and instead, a peak at m/z

= 532.57 appeared, characteristic of **30**. ¹H NMR spectroscopy showed that the acidic protons belonging to the malonyl derivative were no longer present, usually found at 3.44 ppm. One may presume that the base was not selective enough to ring-open the dithione and instead hydrolysed the ester, where the resulting malonic acid was removed upon recrystallisation. Therefore, in order to access these bridge-type complexes, other avenues must be explored.

3.3.3 Post-coordination Functionalisation

Within the literature, most post-coordination syntheses involving metal-dithiolene complexes have been focused on the terminal functionality of the Group 16 moiety or adding an oxo group by the addition of trimethylamine N-oxide to access the $\mathrm{Mo^{VI}}$ oxidation state. However, almost nothing has been reported with regard to any manipulations to the ligand after it has been coordinated to the metal.

With failing to directly coordinate the bridged ligand to the metal, an alternative route to the desired complex 83 must be explored. Post-coordination functionalised was a viable alternative. Complex 30 was dissolved in acetonitrile, and sodium hydrogen carbonate was suspended in the solution to neutralise any HCl that was produced as a by-product. Malonyl chloride was added drop-wise, but unfortunately, the solution immediately took on a green tinge. Such colour changes for molybdenum dithiolene complexes suggest that the molybdenum centre has oxidised, and the colour of the complex is now a result of a ligand to metal charge transfer (LMCT) as there are no longer any d-electrons present to give rise to the d-d transitions responsible for the characteristic red colour of molybdenum dithiolene. The introduction of similar acidic species has also caused rapid changes in colour from red to green: deprotection of ligand 28 when it was coordinated to molybdenum (Chapter 1); the addition of trifluoroacetic acid (TFA) to 30, to investigate the ability of the complex to reduce protons (Chapter 6). Then one

could postulate that the HCl released as part of the reaction inadvertently oxidised the complex before it could react with sodium bicarbonate. In fact, HCl has been used by Boyde and co-workers to obtain *tris*-dithiolene complexes before.¹⁶⁶

Scheme 3.13: The Failed Synthesis of the Bridged Complex 83 Using a Post Functionalisation Approach.

3.4 Attempts at Accessing the Mo=S Functionality

So far several biomimetic FDH catalysts have been synthesised where these synthesised complexes all share the same terminal functionality, a molybdenum-oxo group. The active site of FDH is not limited only to oxygen in the terminal position, but is also coordinated by sulphur and selenium (Figure 1.3). Therefore, it is worth trying to access this functionality by synthetic means.

This has been a previous target within the group using the molybdenum-carbonyl dithiolene (22) and sodium sulphide (Scheme 2.3). However, this reaction only returned a green emulsion of the molybdenum tris-dithiolene complex. As a result, a new approach must be considered.

Most of the literature methods revolve around using a molybdenum-carbonyl bis-dithiolene analogue to access these challenging Mo=S functionalities. Kirk and Holm both found success but used simple ligand scaffolds to do so, for example, 20 or

 $36.^{167,168}$ Such methods are obviously not suitable for 27 derivatives. Burgmayer and Itoh hinted at accessing this functionality by first building the core by synthesising $[MoS(S_4)_2]^{2-}$ and then inserting the ligand, a post-coordination functionalisation approach. This seemed like an avenue worth pursuing.

3.4.1 The Synthesis of Ammonium Tetrathiomolybdate

Ammonium tetrathiomolybdate is a well-known transition metal complex that has been used in the treatment of Wilson's Disease and was first synthesised in 1884 by Krüss. 171,172 Preparation of this molybdenum salt is relatively straightforward: hydrogen sulphide is pumped through a solution of ammonium heptamolybdate (Scheme 3.14). The hydrogen sulphide was generated *in situ* using iron sulphide and an acid. A deep red solution developed, and after recrystallisation, red crystals were afforded. XRD gave the expected structure of ammonium tetrathiomolybdate (84).

$$(NH_4)_6Mo_7O_{24} + H_2S \xrightarrow{NH_4OH (28-30\%)} (H_4N)_2 \begin{bmatrix} S \\ || \\ || \\ S & S \ominus \end{bmatrix}$$

Scheme 3.14: The Synthesis of Ammonium Tetrathiomolybdate (84). 172

3.4.2 The Synthesis of Tetraethylammonium Tetrathiomolybdate

According to the literature, the preparation of **86** required the tetraethylammonium cation, so a salt metathesis was necessary.¹⁷³ Tetraethylammonium bromide and potassium hydroxide were dissolved in water and added to a solution of ammonium tetrathiomolybdate (**84**). The literature recommends a simple crystallisation

to obtain the final compound, but the crystals were found to be contaminated with the potassium bromide by-product (scheme 3.15).¹⁷⁴ Therefore, the solution was taken to dryness under reduced pressure and then redissolved in acetonitrile, leaving behind a white powder, potassium bromide. This afforded much purer deep-red crystals. Again, XRD gave the expected structure of tetraethylammonium tetrathiomolybdate (85).

$$(H_{4}N)_{2}\begin{bmatrix} S \\ || \\ || \\ S \ominus \end{bmatrix} + Et_{4}NBr \xrightarrow{1. KOH, H_{2}O} (Et_{4}N)_{2}\begin{bmatrix} S \\ || \\ || \\ S \ominus \end{bmatrix}$$
84
85

Scheme 3.15: The Synthesis of Tetraethylammonium Tetrathiomolybdate (85). 174

3.4.3 The Synthesis of $(Et_4N)_2[MoS(S_4)_2]$

There are two methods for synthesising the $[MoS(S_4)_2]^{2-}$ salt, reported by Coucouvanis and co-workers.¹⁷⁵ The first involves using dibenzyl trisulphide and the second just elemental sulphur. Both methods were tested, but only the method that used sulphur provided the expected brown crystals, which occurred within 5 minutes of the initial addition; the former method only gave starting material. After recrystallisation using dimethylformamide and diethyl ether, crystals suitable for XRD were afforded and the expected structure of tetraethylammonium nonathiomolybdate (86) was obtained (Figure 3.8).

Scheme 3.16: The Synthesis of $(Et_4N)_2[MoS(S_4)_2]$ (86). ¹⁷⁵

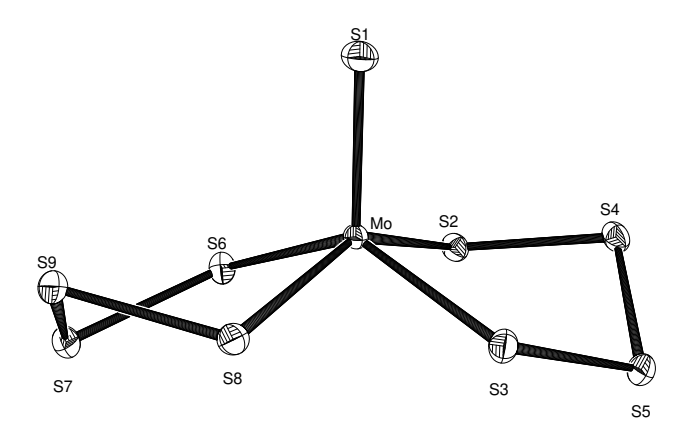


Figure 3.8: The Crystal Structure of $[MoS(S_4)_2]^{2-}$ (The Cation has been Removed for Clarity) (86).

3.4.4 The Synthesis of $(Et_4N)_2[MoS(S_2C_2MeBnOH)_2]$

For the final reaction, $(Et_4N)_2[MoS(S_4)_2]$ (84) was dissolved in dimethylformamide. The previously synthesised alkyne (24) was added, and the solution was left to stand for two days (Scheme 3.17). After a brown solid was precipitated using diethyl ether, MALDI-TOF confirmed that only the starting material had been recovered. Unfortunately, the reaction had failed.

$$(\mathsf{Et_4N})_2 \begin{bmatrix} \mathsf{S} & \mathsf{S} & \mathsf{S} \\ \mathsf{S} & \mathsf{S} & \mathsf{S} \\ \mathsf{S} - \mathsf{S} & \mathsf{S} - \mathsf{S} \end{bmatrix} + \begin{matrix} \mathsf{HO} \\ \mathsf{DMF} \\ \mathsf{Ar} \end{matrix} \qquad (\mathsf{Et_4N})_2 \begin{bmatrix} \mathsf{OH} & \mathsf{OH} \\ \mathsf{S} & \mathsf{S} \\ \mathsf{S} & \mathsf{S} \\ \mathsf{S} & \mathsf{S} \end{bmatrix}$$

Scheme 3.17: The Failed Synthesis of the Sulphido Functionalised Target Complex Analogue (23).

3.5 Tungsten Dithiolene Complexes

So far only molybdenum dithiolene complexes have been targeted. It is well known and has been covered in Chapter 1, that the FDH active site is not limited to just molybdenum. In fact, the first FDH structurally characterised, from *Desulfovibrio gigas*, used tungsten as the metal centre.⁵⁷ These tungsten enzymes have been measured to operate closer to the thermodynamic potential of CO₂ reduction catalysis than molybdenum-based FDH enzymes due to their more reducing redox potentials. This makes tungsten mimics a prime target for biomimetic catalysts.

Holm accessed these tungsten dithiolene complexes by going through a tungsten carbonyl intermediate which itself was prepared from a transmetallation reaction from nickel. This synthetic strategy was applied to simple ligands, ($S_2C_2Me_2$ and $S_2C_2Ph_2$), which lacked any secondary functionality. From previous failures that used the analogous molybdenum-carbonyl route to access $\bf 30$, it was likely that the same approach would also fail for $\bf 90$.

Therefore, the strategy for accessing these complexes will be largely the same as that for molybdenum, relying on a tungsten pre-cursor carrying the oxo functionality and a dithione pro-ligand. This method has been successfully implemented before, although each group came about the tungsten precursor, $K_3Na[WO_2(CN)_4] \cdot 6H_2O(87)$, through different methods. ^{105,177} However, tungsten synthetic chemistry has a reputation of being much more challenging than molybdenum chemistry, even though they both belong to Group 6 of the periodic table. Knowing this, the approach was to start with the more simple pro-ligands such as **75** and then synthesise the complexes with the more complex ligands.

3.5.1 The Synthesis of $K_3Na[WO_2(CN)_4] \cdot 6H_2O$

First prepared in the 1950s, pre-dating its molybdenum analogue by some time, this tungsten-cyano salt has found a variety of uses.¹⁷⁸ Both syntheses are largely similar, so, again, special attention should be paid as the reaction involves the *in situ* generation of hydrogen cyanide, where the cyanide moiety then coordinates to the tungsten ion. After recrystallisation, brown crystals were obtained (Scheme 3.18). The diffraction data could be obtained in an XRD experiment, but it was only of sufficient quality to confirm connectivity. Therefore, **87** was also confirmed by elemental analysis.

NaO-W-ONa
$$\xrightarrow{\text{KBH}_4, KCN,}$$
 $\xrightarrow{\text{EIOOH}}$ $\xrightarrow{\text{H}_2O}$ $\xrightarrow{\text{K}_3}$ Na $\begin{bmatrix} \text{NC}_{1}, & \text{II}_{1}, & \text{CN} \\ \text{NC} & \text{II}_{2}, & \text{CN} \\ \text{O} & \text{O} \end{bmatrix}$ 6H₂O

Scheme 3.18: The Synthesis of $K_3Na[WO_2(CN)_4] \cdot 6H_2O$ (87). ¹⁷⁸

3.5.2 The Synthesis of $(Et_4N)_2[WO(S_2C_2HPh)_2]$

Previously prepared by Garner and co-workers, preparation of this complex would test the synthetic strategy developed so far and it would also be necessary for future catalytic comparisons. The tungsten precursor 87 was dissolved in heavily degassed water and added to the ring-opened pro-ligand analogue of dithione 75. This gave a red solution, which after the addition of diethyl ether, afforded a red film (Scheme 3.19). The identity of this solid was confirmed by MALDI-TOF mass spectrometry (m/z = 531.94, exact m/z calculated for $^{184}WC_{16}H_{12}OS_4$: 531.93).

Scheme 3.19: The Synthesis of $(Et_4N)_2[WO(S_2C_2HPh)_2]$ (88).

3.5.3 The Synthesis of $(Et_4N)_2[WO(S_2C_2MePh)_2]$

With the successful preparation of 88, the novel complex 89 was prepared in the hope of demonstrating the validity of this synthetic strategy. Pro-ligand 73 was dissolved in methanol and the dithione ring opened with potassium hydroxide. The tungsten precursor 87 was added and afforded a deep red solution that after recrystallisation gave a red film (Scheme 3.20). However, structural data could not be obtained because the complex quickly oxidised. The synthesis was repeated multiple times, but even with the utmost care, oxidation occurred within minutes during or after the final recrystallisation.

Scheme 3.20: The Failed Synthesis of $(Et_4N)_2[WO(S_2C_2MePh)_2]$ (89).

3.5.4 The Synthesis of $(Et_4N)_2[WO(S_2C_2MeBnOH)_2]$

Accessing tungsten dithiolenes, especially those that are functionalised in any way, can be seen as the penultimate challenge with respect to the synthesis of

bio-mimetic FDH systems. This reputation is not unfounded, as initial attempts to synthesise **90** failed. Success was achieved once, where heavily degassed methanol was used to dissolve the pro-ligand **27** followed by the addition of potassium hydroxide, which gave the expected gold-coloured solution. Addition of the tungsten precursor (**87**) elucidated a red/yellow solution after 45 minutes of stirring, mirroring the molybdenum analogue (Scheme 3.21). The successive work up afforded a brown/red film which was identified by MALDI-TOF mass spectrometry (Figure 3.9) via the presence of the molecular ion peak at m/z = 619.84 (exact m/z calculated for $^{184}WC_{20}H_{20}O_3S_4$: 619.98).

Scheme 3.21: The Synthesis of $(Et_4N)_2[WO(S_2C_2MeBnOH)_2]$ (90).

3.5.5 The Synthesis of $(Et_4N)_2[WO(S_2C_2HBnOH)_2]$

Like the methyl substituted analogue (90), 91 was equally challenging to synthesise. The solvents were heavily degassed and all precautions were taken to prevent the entry of oxygen into the flask. This afforded a red/green film (Scheme 3.22). The combination of colours indicated that oxidation had begun to occur. MALDI-TOF mass spectrometry showed a small peak corresponding to the expected molecular ion peak, occurring at m/z = 592.31 (exact m/z calculated for $^{184}WC_{18}H_{16}O_3S_4$: 591.95). However, upon returning to the sample, it had completely decomposed.

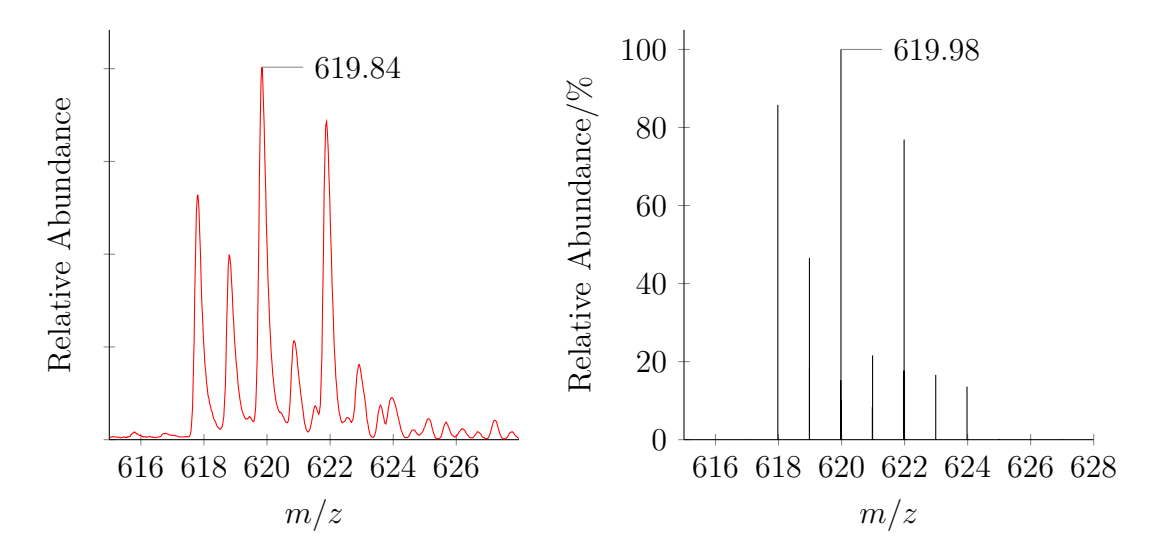


Figure 3.9: The Experimental (Left) and Theoretical (Right) Mass Spectra of of $(Et_4N)_2[WO(S_2C_2MeBnOH)_2]$ (90).

HO
$$(Et_4N)_2$$
 $(Et_4N)_2$ $($

Scheme 3.22: The Attempted Synthesis of $(Et_4N)_2[WO(S_2C_2HBnOH)_2]$ (91).

3.6 Summary

The novel route used to develop the initial target dithiolene ligand (27) has been used to synthesise several novel dithione analogues with varying functionalities from which the molybdenum-oxo bis-dithiolene complex can be made. Therefore, we can assume that this radical cyclisation reaction is highly selective toward the alkyne functional group, and it can be hypothesised to work for any alkyne in any environment. As a result, the ability to synthesise and add to the number of molybdenum-oxo bis-dithiolene complexes has been made more accessible.

A method to reliably synthesise molybdenum-sulphido bis-dithiolene complexes still remains to be obtained. Taking inspiration from the molybdenum-oxo synthesis, one could attempt to generate the $K_3Na[MoS_2(CN)_4] \cdot 6 H_2O$ precursor. This could be achieved by starting from $(NH_4)_2[MoS_4]$ and replacing the ammonium cation with the sodium cation to afford $Na_2[MoS_4]$. Then following the synthesis for $K_3Na[MoO_2(CN)_4] \cdot 6 H_2O$, the addition of KBH_4 , KCN and acetic acid to $Na_2[MoS_4]$ could synthesise $K_3Na[MoS_2(CN)_4] \cdot 6 H_2O$. The coordination of the dithiolene ligand with this hypothetical precursor might be a viable approach to obtain $(Et_4N)_2[MoS(dithiolene)_2]$.

The synthesis of an intermolecular-bridged complex is still worth pursing. The post-coordination route still has promise, but the by-product of the 'bridging' reaction must avoid anything remotely acidic to prevent oxidation of the complex. Perhaps starting from a completely unfunctionalised homoatomic molecule like pentadeca-1,14-diyne, performing the dithione insertion and then the subsequent coordination reaction to achieve the complex would be a good starting point to see if a tetradentate coordinate system is possible for these molybdenum-oxo systems.

Tungsten compounds live up to their reputation as exceedingly challenging syntheses, with tungsten-oxo bis-dithiolenes being no different. They are highly sensitive to oxygen and even when synthesised, the lifetime of these complexes can be measured in minutes if the utmost care is not taken with them. Any future chemist should make sure their equipment is of the highest grade to prevent oxygen from contacting these compounds, ensuring the greatest chance of success.

Chapter 4

Density Functional Theory

4.1 Introduction

First developed in the 1960s, ^{179,180} density functional theory, most commonly referred to by its acronym DFT, is a computational modelling method used to examine the electronic ground state of synthetically inaccessible systems, confirm experimental data, and probe reaction pathways. Solving the Schrödinger equation analytically is limited to hydrogenic atoms as the motion of each electron is coupled to the motion of every other electron through the Coulomb repulsion among the electrons; numerical methods need to be used, and these suffer from scalability issues due to the number of interactions to be modelled. Through the use of functionals and basis sets, DFT provides a framework to accurately model molecular systems.

A functional is a function which itself requires a function as the input, and yields a numerical output. In this context, it is an approximation that suggests that the energy of a system can be written as a functional of the one-particle electron density.^{181–183} To improve the accuracy of the results, a number of approaches are used to calculate the exchange and correlation energies. These build in complexity from local density approximations (LDA) to generalised gradient approximations

(GGA), meta-GGA and beyond.¹⁸⁴ Each additional refinement helps to improve the accuracy of the calculated values. Basis sets are a mathematical description of the atomic orbitals. Mathematically, these can take the form of Gaussian-type orbitals (GTOs), Slater-type orbitals (STOs), or numerical atomic orbitals.^{185,186} All-electron basis sets of varying complexity can be applied to light atoms, with the degree of coverage of polarisation often referred to as ζ . ζ corresponds to the orbital polarisation parameter to more accurately model the diffuse nature of orbitals. For heavier elements, all-electron basis sets are unavailable, and a so-called effective core potential (ECP) must be used: this splits the orbitals into a core, handled as a single potential, and outer orbitals which are modelled fully.

The earliest published research used computational methods to investigate bonding character in the FDH active site in 1999.⁷¹ Although this paper does not directly model the $[MoO(S_4)_2]^{2-}$ core, with the computational focus directed toward the organic pyranopterin cofactor, it is the first published article in the field that uses computational methods to investigate molybdenum-oxo dithiolene complexes. Kirk and co-workers used computational methods, along with spectroscopic techniques (magnetic circular dichroism, solution and solid-state electronic absorption, and resonance Raman spectroscopies), to probe how low energy sulphur to molybdenum charge transfer transitions on the dithiolene ligand fragment ($^-SC=CS^-$) are a result of one electron promotions originating from an isolated set of four filled dithiolene orbitals that are primarily sulphur in character. These calculations were performed using the B3LYP functional and the 6-31 G** basis set. $^{187-190}$

The first study applying DFT to the metal centre and coordination sphere in Mo(dithiolene)₂ was reported by Solomon and co-workers in 1999. DFT was used in conjunction with spectroscopic techniques (K-edge and L-edge X-ray absorption) to provide a description of the bonding of Mo^{VI}O₂ complexes (sulphite oxidase mimics) to give an insight into the relationship between the electronic structure

and the oxygen transfer chemistry.¹⁹¹ This early study used the Vosko, Wilk, and Nusair local density approximation (LDA) functional,¹⁸⁹ along with the Becke 1988 functional for the exchange energy¹⁹² and the Perdew 1986 functional for the correlation energy,¹⁹³ (together called BP86). For the molybdenum atom, the triple- ζ STOs were used for molybdenum, and single- ζ STOs were used for the carbon, nitrogen, oxygen, phosphorus, sulphur, and chlorine atoms. All the core electron levels were treated using an ECP.

In 2001 Holm and co-workers performed computational studies on simple $Mo(CO)_2(dithiolene)_2$ complexes previously prepared by the research group. ¹²⁶ DFT was used together with previous cyclic voltammetry studies to give further insight into the electronic properties of these complexes. The DFT calculations identified the non-innocent nature of the dithiolene ligands when the complexes underwent redox processes and provided a description of the delocalised ground states. This study used a similar computational approach to that of Solomon, but included relativistic effect.

In 2002, Kirk and co-workers investigated the oxygen atom transfer reactivity of sulphite oxidase. ¹⁹⁴ DFT was performed on the sulphite oxidase mimic $[\text{Mo}^{\text{VI}}\text{O}_2(\text{S}_2\text{C}_2\text{Me}_2)(\text{SCH}_3)]^-$ to evaluate the composition of the lowest unoccupied molecular orbital (LUMO). The LUMO is considered the electron-accepting orbital in the OAT reaction with the sulphite substrate. In the model, the LUMO is composed of a molybdenum $d_{xy} - p\pi^*$ interaction between the molybdenum and the equatorial oxygen (O_{eq}) atom. The axial oxygen (O_{ax}) atom possesses no contribution to this orbital and instead contributes substantially to the LUMO+1. Also, it had been suggested that varying the O_{ax} -Mo- $S_{\text{dithiolene}}$ torsion angle aids in the selection of O_{eq} for catalysis. Kirk and co-workers varied this torsion angle, demonstrating that the LUMO is indeed heavily influenced by the molybdenum $d_{xy} - p\pi^*$ interaction, and consequently O_{eq} character always dominated the LUMO.

Later in the same year, Nordlander and co-workers utilised DFT to investigate OAT reactions between trimethylamine N-oxide and DMSO with $[MoO(mnt)_2]^{2-}$ (37). The group reported that the reaction between $[MoO(mnt)_2]^{2-}$ and trimethylamine N-oxide proceeded through a transition state with distorted octahedral geometry where trimethylamine N-oxide bound to molybdenum through the oxygen and consequently weakened the N-O bond.

In 2003, Enemark and co-workers used photoelectron spectroscopy and DFT to investigate the sulphur π -orbitals of metal (molybdenum and titanium) dithiolenes, with electronic arrangements of d^0 , d^1 , and d^2 .⁷⁰ It was observed that the ionisation energies compared well with those of DFT and to rationalise this a dithiolene folding effect (Chapter 1) was proposed. This phenomenon, involving metal inplane and sulphur π -orbitals, was identified as a potential factor in the electron transfer reactions that regenerate the metal centres at the active sites of Group 6 metalloenzymes.

From 2004 onwards DFT studies focusing on purely molybdenum^{IV}-oxo *bis*-dithiolene complexes became more numerous. The edt (17),¹³¹ bdt 18,^{88,132–134} and mnt 19 ligands were all investigated in some capacity.^{132,195} Systems with more functional groups were ignored, likely to reduce computational time. McNamara and co-workers were the exception, where they investigated pterin dithiolene analogues bound to molybdenum centres.¹³⁵

In 2009, Schulzke and co-workers conducted a systematic study of the MPT at varying levels of functionality coordinated to a molybdenum-oxo core at varying oxidation states.¹²⁸ Starting with the most simple ligand, edt, and becoming increasingly more functionalised: pdt, prz and finally mpt (Figure 4.1). They compared the results obtained to see how these changes in functionality influenced bond lengths, angles, charge distribution, composition of the binding orbitals, and redox potentials differed in relation to each other. They concluded that the

dithiolene, pyran ring and the first ring of the pterin contributed significantly to the behaviour of the complex whereas the second ring of the pterin had minimum influence.

Figure 4.1: The Dithiolene Ligands Utilised by Schulzke and Co-workers for their Computational Studies. 128

In 2012, Zampella and co-workers used computational methods to systematically investigate reaction pathways associated with the H-transfer step, considered to be the rate-determining step of the formate to carbon dioxide catalytic reaction. They investigated every H (proton or hydride) acceptor within the FDH active site and proposed a mechanism by which the metal centre mediates H-transfer from formate to the final acceptor through the selenocysteine residue.

In 2014 Edward and co-workers used X-ray absorption spectroscopy and DFT calculations to provide insight into the oxygen transfer in sulphite oxidase and its relation to DMSO reductase.¹²⁹ This work involved the oxo transfer reaction between [Mo^{VI}O₂(bdt)₂]²⁻ and P(OMe)₃ affording [Mo^{IV}O(bdt)₂]²⁻ and O=P(OMe)₃. DFT calculations identified three possible transition states where the lowest energy state (stabilised by a P-S interaction) matched the experimental data well. These results were then compared with other similar experiments for DMSO reductase mimics, allowing Holm and co-workers to draw certain conclusions: in DMSO reductase, where the oxygen is transferred from the substrate to the metal ion, the oxygen transfer causes electron transfer; conversely, in sulphite oxidase, where the

oxygen transfer is from the metal to the substrate, the electron transfer initiates the oxygen transfer.

In 2018, Ryde and co-workers evaluated five mechanisms of catalysis at the FDH active site previously proposed in the literature, including the computationally derived mechanism from Zampella and co-workers.⁵³ They concluded that the formate substrate does not coordinate directly to molybdenum when it enters the oxidised active site of the FDH, but instead resides in the secondary coordination sphere.

The computational studies detailed above made use of a variety of functionals and basis sets: these are summarised in Table 4.1. As can be seen, there is a heavy reliance on the B3LYP hybrid functional. This functional is widely used for organic molecules, but is less commonly used in organometallic DFT as it can give less reliable results. What is lacking in the literature to date is clear benchmarking of varied or more recent functionals.

This short summation of the literature shows that although computational modelling has been performed on molybdenum dithiolenes, most of the research has focused on the FDH active site itself and adjacent topics, for example, dithiolene bonding interactions to a molybdenum centre or catalysis at the active site. Few papers have been published on biomimetic structures of the FDH active site with efforts focused on predicting the experimental properties of the synthesised complexes. The paper from Schulzke and McNamara dealt with the most complex Mo=O systems, 128,135 but they are fifteen and nineteen years old, respectively. Since these studies were published, advances in computation mean that a wider range of basis sets and levels of theory are now viable for studying these systems.

Table 4.1: A Table Showing the Functionals and Basis Sets Used by Different Research Groups (ECP is an Acronym for Effective Core Potential).

Research Group	Year	Functional	Basis Set
Kirk and Co-workers ⁷¹	1999	N/A	6-31**187
Solomon and Co-workers ¹⁹¹	1999	LDA, ¹⁸⁹ BP86 ^{188,192}	triple-/single- ζ STO
Holm and Co-workers 126	2001	LDA, BP86	triple-/single- ζ STO
Kirk and Co-workers ¹⁹⁴	2002	$B3LYP^{187-190}$	6-31G, 6-31G*** ^{187,196,197}
Nordlander and Co-workers ¹²⁷	2002	LDA, BP86	triple- ζ STO, ECP
Enemark and Co-workers ⁷⁰	2003	$GGA^{188,192}$	triple- ζ STO, ECP
McNamara and Co-workers ¹³⁵	2005	B3LYP	$LANL2DZ^{196-198}$
Wedd and Co-workers ¹³²	2007	B3LYP	$6-31+G*,^{199}$ ECP
Amano and Co-workers ¹³¹	2007	B3LYP	LANL2DZ, ECP
Holm and Co-workers ⁸⁸	2007	LDA	triple- ζ STO, ²⁰⁰ ECP
Hoffman ⁷³	2007	B3LYP	LANL2DZ
Sabyasachi and Co-workers ¹⁹⁵	2007	B3LYP	6-31G*+
Schulzke and Co-workers ¹²⁸	2009	B3LYP	LANL2DZ, 6-311G
Zampella and Co-workers	2012	BP86	TZVP^{201}
Edward and Co-workers ¹²⁹	2014	BP86, B3LYP	SDD, ²⁰² 6-311(d) ²⁰³
Ryde and Co-workers ⁵³	2018	TPSS, ²⁰⁴ B3LYP	TZVP

4.1.1 Selection of Approach

As mentioned above, due to the lack of DFT studies on the most appropriate functionals and basis sets for functionalised molybdenum dithiolene systems, we were free to choose the level of theory and basis sets to implement. Trials were begun with the simple $[\mathrm{Mo^VO(bdt)_2}]^-$ system, mirroring Hrobárik and co-workers, to compare the Orca outputs (a DFT tool)^{205,206} against their respective experimental values.¹³⁰

The work from Hrobárik and co-workers was matched by utilising the BP86 and B3LYP functionals along with the def2-TZVP basis set. 192,193,207 The def2-TZVP basis set is a valence triple- ζ basis set with polarization functions. Other basis sets such as 6-31+(G) tend to lack accuracy with more complex structures; these basis sets are sufficient for complexes using simpler ligands such as bdt, but the MeBnOH dithiolene ligand is much larger and, therefore, 6-31+(G) would not be appropriate. The Orca program has a large catalogue of basis sets to choose from whereas Gaussian is largely limited with LANL2DZ; 208 this basis set also lacks accuracy, with the polarisation function being only double- ζ . $^{196-198}$ By comparing the calculated Mo=O bond length against the crystal structure of $[\text{MoV}(\text{bdt})_2]^-$ it was confirmed that a successful benchmark had been obtained.

With any theoretical system, determining the correct charge and multiplicity is necessary before performing a calculation. With transition metal complexes one must consider whether the system that will be modelled is paramagnetic or diamagnetic, especially when there is more than one d electron. An undergraduate, base-level approach to ligand field theory of the $[\mathrm{Mo^{IV}O(S_4)}]^{2-}$ core would predict that the d orbitals would split into five orbitals, varying in energy in relation to each other due to the geometry of the ligands surrounding the metal ion and their corresponding symmetry. It was initially assumed that the lowest energy level orbitals would have some degree of degeneracy (Figure 4.2). Therefore, the two

d electrons were modelled as unpaired.

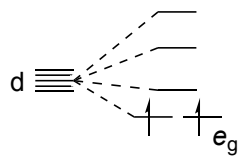


Figure 4.2: The Assumed Splitting Pattern of the $[\mathrm{Mo^{IV}O(S_4)}]^{2-}$ core.

Such an orbital arrangement would imply that our systems would have a spin multiplicity of 3. When these parameters were applied to the $[Mo^{IV}O(bdt)_2]^{2-}$ system, a distorted geometry was obtained, differing significantly compared to the crystal structure of the same Mo^{IV} complex.

To truly understand why this distortion has happened, it is important to first understand symmetry-adapted molecular orbital (SAMO) theory, from which we can determine the electronic structure of the complex and then the spin-multiplicity parameter.

4.1.2 Symmetry Adapted Molecular Orbital Theory (SAMO) of Square-based Pyramidal Complexes

Square-based pyramidal geometries can exist in one of two forms: the metal centre may exist in or above the plane of the four ligands. [MoO(dithiolene)₂]²⁻ complexes exist in the latter geometry, so that is where the focus will be. Just by inspection, we can determine that the relative geometries of octahedral/square planar complexes and square-based pyramidal complexes differ, so there will be a departure from the typical splitting pattern of octahedral and square planar structures. From Figure 4.3 we can see that the four basal orbitals point up and in towards the metal centre. The position of the apical orbital has no real difference in symmetry from the typical octahedral geometry.

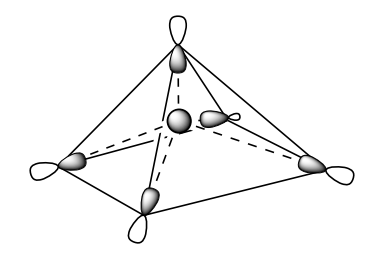


Figure 4.3: The Square-based Pyramidal Geometry.

The d_{xy} , d_{zy} , d_{xz} and $d_{x^2-y^2}$ orbitals do not interact with the one axial ligand, leaving only the d_{z^2} . However, with the removal of one of these ligands, one of the two antibonding interactions on the d_{z^2} is also eliminated. With the removal of a ligand, the change in the symmetry of the complex must also be established; it drops from O_h to C_{4v} . Since there is only one apical ligand, the xy plane is no longer a symmetry element for the complex, giving the p_z and d_{z^2} the same symmetry (a_1) . These orbitals can now mix, forming a hybrid orbital stabilised by the bonding interaction between the lobe of the p and ligand orbitals of the same sign. Analysis of the polarised d_{z^2} orbital can be separated into three parts:

- The overlap between the p_z and the d_{z^2} is zero as they are located on the same atom.
- The interaction of the four other ligands and p_z is zero since they are located along the nodal plan of the p_z orbital.
- The interaction of p_z and the axial ligand is non-zero.

The orientation of p_z relative to the apical ligand can be positive or negative. When the positive lobe faces the ligand orbital, each orbital would have a different sign and cancel each other out; when the negative lobe is facing the ligand orbital, the orbitals have the same sign, so they would add together. Clearly, the two d_{z^2} lobes are not equivalent, and a polarisation occurs toward the vacant site. There is now a smaller antibonding interaction because of the smaller hybridised lobe and the axial ligand. Since the four other ligand orbitals have moved out of the xy plane, and into the nodal cone in the most extreme cases, a complete elimination of the antibonding contribution on the ligands could occur; therefore, the energy of the orbital is lowered (Figure 4.4).

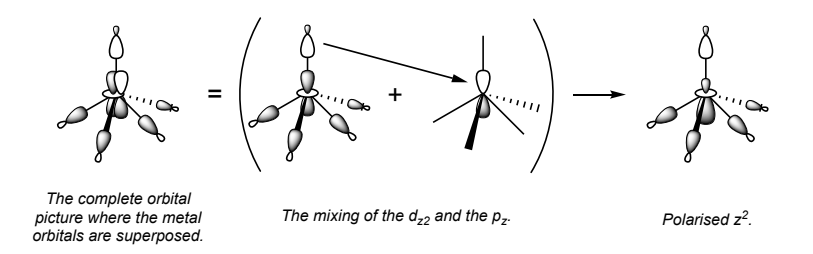


Figure 4.4: The Formation of the Polarised d_{z^2} Orbital.²⁰⁹

Our attention can now turn towards the remaining orbitals. The change in geometry is more easily understood by observing Figure 4.5. Starting with the d_{xy} metal orbital, the ligand orbitals lie in the two nodal planes (xz and yz) where no overlap can occur. This results in a non-bonding orbital.

When we examine Figure 4.5 we can see that ligands L_1 and L_3 stay within the yz plane and move into a geometry where they can overlap with the lobes of the d orbital in the yz plane. The previously non-bonding orbital is destabilised and a new antibonding orbital is formed. However, we must consider hybridisation and subsequent polarisation once again. The p_y orbital adds to and takes away depending on the parity of the yz orbital. Consequently, two lobes are enlarged and two are shrunk. The two shrunk lobes are those which point towards the ligand orbitals. With less orbital lobe to overlap with, there will be a decrease in the strength of the antibonding character of the yz orbital. The behaviour of the xz orbital is analogous to yz just with ligands L_2 and L_4 .

With regards to the $d_{x^2-y^2}$ orbital, since the basal ligands are pushed out of the xy plane, the ability of these orbitals to overlap is reduced, and the antibonding

contribution is shrunk, proportional to the angle of the ligands in relation to the metal centre. The orbital is stabilised and the energy lowered.

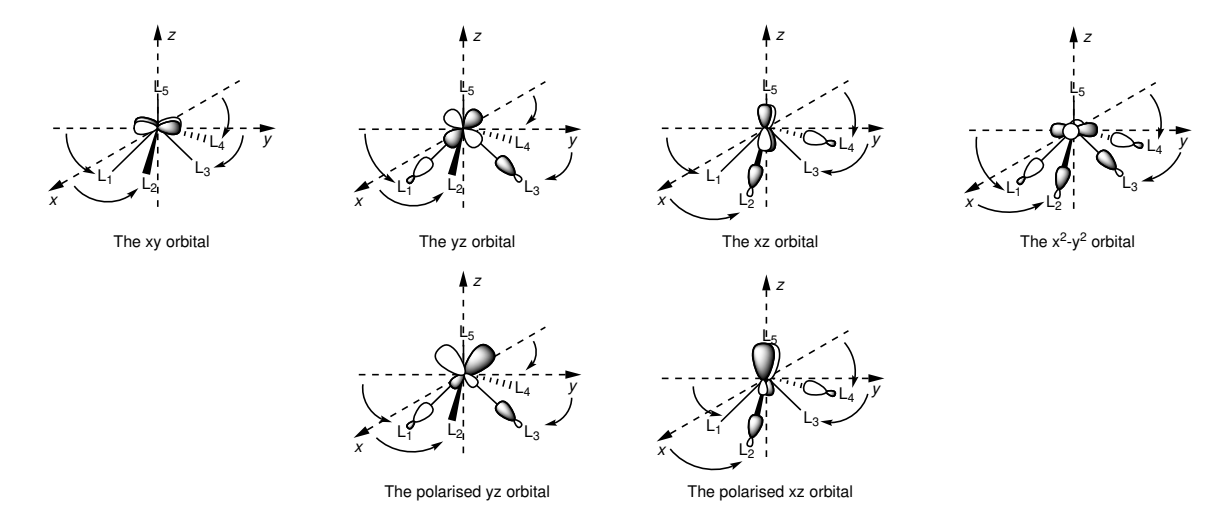


Figure 4.5: The Ligand-metal Orbital Geometries for the d_{xy} , d_{yz} , d_{xz} and the $d_{x^2-y^2}$.

We can now construct the square-based pyramidal splitting diagram. The d_{xy} orbital is a non-bonding orbital. The d_{yz} , d_{xz} both have some antibonding character and their energies are raised. The d_{z^2} and $d_{x^2-y^2}$ orbitals are more destabilised as there is greater antibonding character in the overlap between the metal and ligand orbitals when compared to the d_{yz} and d_{xz} .

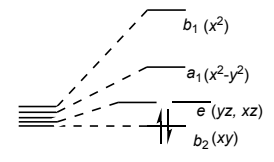


Figure 4.6: The Squared-based Pyramidal Splitting Diagram

With the construction of Figure 4.6 we can now fill it with electrons. As mentioned previously, the $[MoO(bdt)_2]^{2-}$ complex we are investigating has a +IV oxidation state. Being in Group 6, a +IV oxidation state leaves two electrons. With our new understanding of the orbital splitting pattern, it is clear that electrons

solely occupy the b_2 orbital. The complex is now closed-shell and diamagnetic with the spin multiplicity being equal to 1 (2(0) + 1). With the new spin multiplicity value, the calculations were retried and no distortion of the basal ligands occurred.

4.1.3 Selection of Approach Continued

Now that the spin multiplicity value had been established, geometry optimisation of [MoO(bdt)₂]²⁻ using BP86 and B3LYP was performed to reaffirm a standard benchmark although with a change in oxidation state.^{193,210} Interestingly, in the original synthetic paper where the [MoO(bdt)₂]²⁻ complex was first prepared by Holm and co-workers,¹⁰⁰ no crystal structure was reported; the Cambridge Structural Database (CSD) also lacks a crystal structure for [MoO(bdt)₂]²⁻, despite being such a common ligand.²¹¹ Instead, benchmarking against the infrared stretching frequency of the Mo=O bond was attempted. To do this accurately, a stretch must be identified on the experimental IR that can act as an internal standard, for example, an asymmetric stretch (-CH₃) which is quite easily identifiable at approximately 3000 cm⁻¹. However, the paper does not provide images of the IR spectra to identify this standard. We instead settled for a reasonable geometry optimisation with no change to the geometrical positions relative to each complex. We were now confident to begin trialling our own systems.

4.2 The Simulation of Dithiolene Complexes

The three main aims of these computational studies are to:

- 1. use geometry optimisation to make sense of the difficulty of obtaining a suitable crystal structure for single crystal X-ray diffraction.
- 2. identify the most appropriate functional/basis set for the $[MoO(dithiolene)_2]^{2-}$

family of complexes.

3. clearly identify the Mo=O stretch in the experimental IR spectra of the target complex **30**.

Identifying the Mo=O IR band in these kinds of molybdenum-oxo bis-dithiolene complexes is of particular interest as it can act as a strong indicator for the successful synthesis of the target complexes. Unfortunately, no particular attention has been paid to identify this bond when influenced by increasingly complex dithiolenes. Muralidharan and co-workers suggest looking at the region between 900 cm⁻¹ to 1000 cm⁻¹. However, their work concerns molybdenum oxides and suggests no way to identify the correct band if more than one is present in the expected region; therefore, such a suggestion is not directly applicable for molybdenum-oxo bis-dithiolene complexes.²¹² Most of the synthesised complexes have an IR value associated with the Mo=O bond, but these complexes involve a simple ligand scaffold that lacks any extended functionality, for example, the initial ligands from Holm and co-workers (Figure 2.1). As the ligands become more complex, the IR spectrum follows suit, thereby increasing the difficulty of correctly identifying the Mo=O bond. The method of data collection, the Mo=O stretching frequencies, and their peak sizes of various complexes are summarised in Table 4.2.

$4.2.1 \quad [MoO(S_2C_2MeBnOH)_2]^{2-}$

In the target [MoO(S₂C₂MeBnOH)₂]²⁻ (**30**) complex, there are three bands that appear in the 900–1100 cm⁻¹ region of the IR spectrum, the region where Mo=O is commonly found as described by Saleem and Key (Figure 4.7).^{214,215} Barring the use of ¹⁸O-labelled complexes for IR spectroscopy experiments, it is impossible to decide which of the three bands belongs to Mo=O stretch without DFT calculations for this complex. However, to come up with an accurate prediction requires investigating

Table 4.2: A Table Showing the Complete Catalogue of Mo^{IV} Dithiolene Complexes and Their Associated Mo=O Stretching Values, bRaman

Complex	Method	$\tilde{\nu}/\mathrm{cm}^{-1}$	Peak Size
$\overline{\mathbf{10\text{-}qpdt}^{112}}$	KBr Pellet	905	
$11 ext{-} ext{Hqpdt}^{103}$	KBr Pellet	901	
$oxed{20 ext{-}\mathrm{bdt}^{100}}$	KBr	903	vs
$6 ext{-}\mathbf{mohbdt}^{104}$	KBr	925	
$34^{154,168}$	solution	903^{b}	
$35 ext{-}\mathbf{edt}^{100}$	KBr	917	vs
36^{154}	Nujol	889	
$37\text{-mnt}^{100,213}$	CsI	928	vs
$\mathbf{39\text{-}bdtCl_2}^{108}$	KBr	910	
$40 ext{-}(ext{bdt})(ext{bdtCl}_{2})^{101}$	KBr	907	\mathbf{S}
$41 ext{-}\mathrm{sdt}^{101}$	KBr	879	
$f 42 ext{-}{f cdt}^{105}$		905	\mathbf{S}
$oldsymbol{46-o}{ m pedt}^{101}$	KBr	902	
$oldsymbol{47-m}{f pedt}^{101}$	KBr	882	
$oldsymbol{48-p}{ m pedt}^{101}$	KBr	900	
49^{109}	KBr	896	vs
${f 50}^{109}$	KBr	899	vs
${f 51}^{109}$	KBr	902	vs
${f 52\text{-}dmit}^{96}$		930	
$45 ext{-}(ext{edt})(ext{mnt})^{100}$	KBr	919	vs
54^{97}	CsI	914	\mathbf{s}
${f 57 ext{-}}{f fdt}^{107}$	KBr	1017	
$f 58 ext{-}f qedt^{101}$	KBr	905	
$59 ext{-}\mathbf{ntdt}^{111}$	KBr	873	
61^{106}	KBr	908	
62^{95}		950	
63 [99]		907	
$64 ext{-} ext{NH}_2 ext{-} ext{ptedt}^{101}$	KBr	886	
$\mathbf{65\text{-}NC(H)(Me)_{2} ext{-}}$ pted \mathbf{t}^{101}	KBr	890	
$ m 67 ext{-}PPh_{3}Sibdt^{98}$	KBr	915^{b}	
$\mathbf{68-tdt}^{98}$	KBr	900^{b}	
$69 ext{-}\mathbf{PPh_{3}Sitdt}^{98}$	KBr	904^{b}	
$70 ext{-}\mathrm{adt}^{110}$	KBr	936	
$71 ext{-}\mathrm{ecpdt}^{110}$	KBr	929	

another peculiarity of these molybdenum dithiolene complexes.

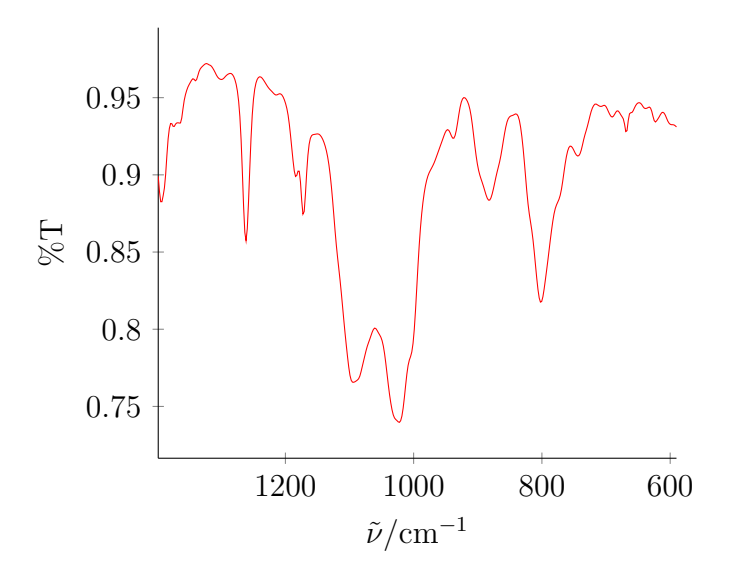


Figure 4.7: The Experimental KBr IR Spectrum of $(Et_4N)_2[MoO(S_2C_2MeBnOH)_2]$ (30).

As mentioned in Chapter 3, a common reason as to why a suitable crystal structure cannot be obtained is that upon crystallisation, many geometric isomers are formed. Just from simple inspection, the $[MoO(S_2C_2MeBnOH)_2]^{2-}$ target complex has many freely rotating moieties, not to mention the potential for *cis* and *trans* isomerisation. Computational DFT analysis using BP86, B3LYP, PBE0, TPSS, and ω B97X showed six stable ligand isomers after geometry optimisation shown in Figure 4.8. ^{188–190,192,193,204,216–220} The overall square-based pyramidal geometry was conserved upon geometry optimisation.

The relative energy difference between the six isomers is tiny, demonstrated in Table 4.3 (9.6 kJ mol⁻¹ was the greatest range of the 5 functionals). This value makes up only 0.000 14% of the calculated energy of the complex. This demonstrates how energetically indistinguishable these isomers are from each other, falling well within what is typically regarded as insignificant with regards to DFT calculations. With such a flat energy surface, one can assume a dynamic equilibrium

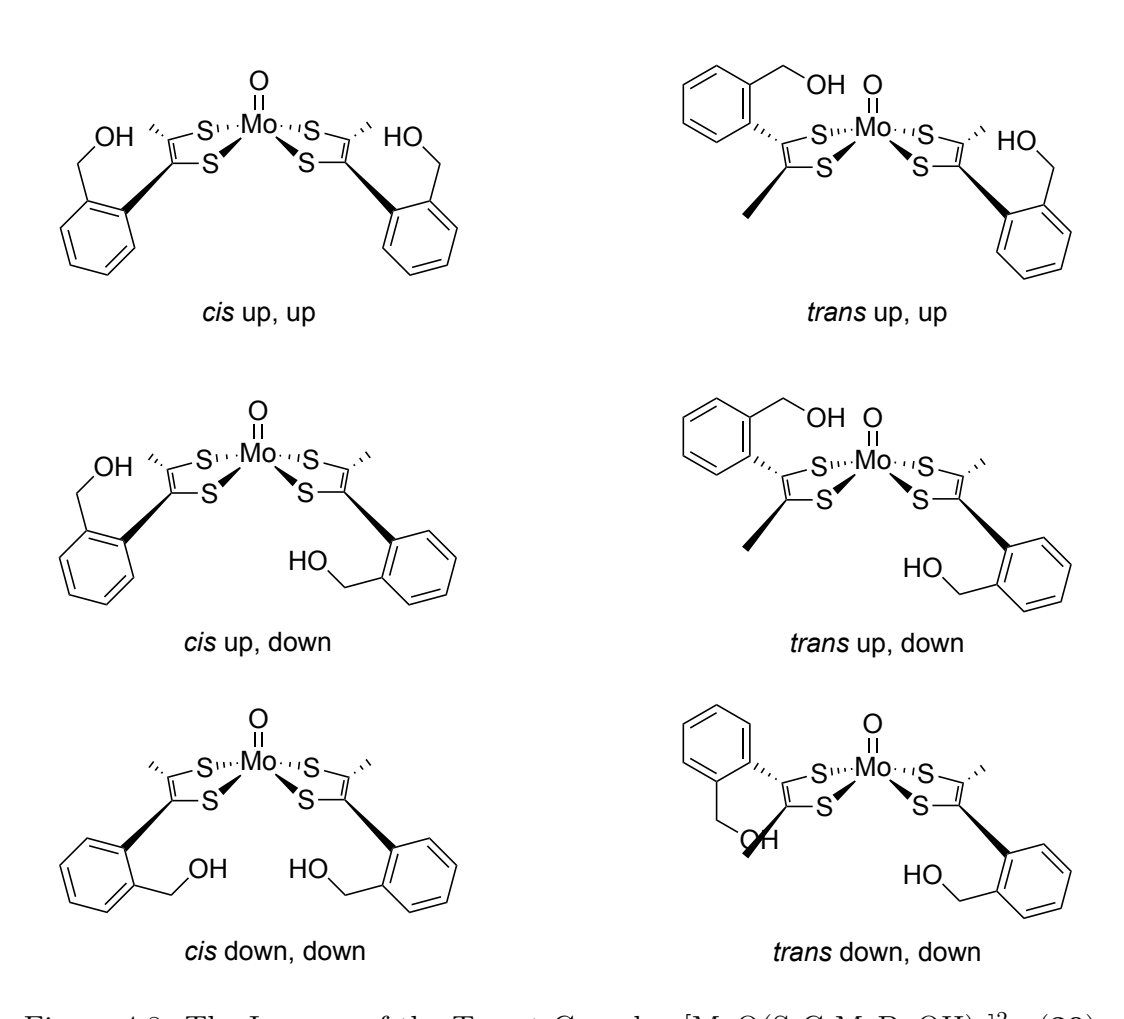


Figure 4.8: The Isomers of the Target Complex $[MoO(S_2C_2MeBnOH)_2]^{2-}$ (30).

in solution between the different isomers. Consequently, crystallisation of a single isomer would depend on the relative solubility values, as the flat energy surface likely means that no one isomer dominates in solution. Such findings are consistent with those of the four other functionals.

Table 4.3: Calculated relative energy values for $[MoO(S_2C_2MeBnOH)_2]^{2-}$ (30) using the BP86 functional and the def2-TZVP basis set.

Entry	Isomer	$E/\mathrm{kJ}\mathrm{mol}^{-1}$
1	cis up,up	0.13
2	cis up,down	-0.93
3	cis down,down	0.00
4	trans up,up	-1.25
5	trans up,down	6.88
6	trans down,down	6.30

This result helps to explain the difficulty when it comes to the ¹H NMR spectrum peak assignment. As the complex is diamagnetic, it would be anticipated to give sharp signals for the ligand environment in the ¹H NMR spectrum. At first glance, the spectrum appears to be complex, perhaps indicating a lack of purity. However, the MALDI-TOF mass spectrum, Figure 2.7 suggests that there is no such indication of an issue with purity and the correct product had been formed. However, if one considers that the ¹H NMR spectrum is taken in solution at room temperature, a dynamic equilibrium of possible isomers could be the reason for the 'messy' spectrum. A series of spectra were taken, at sequentially lower temperatures, an increased number of scans, and with longer relaxation times to encourage better peak resolution as the proton environments should be 'locked' in space over the time scale of the new ¹H NMR spectroscopy experiment. This was to test whether the proposed dynamic equilibrium and many possible isomers was indeed responsible. Figure 4.9 shows the improved resolution of peak shape at 293 K, 273 K, and 263 K focused on the region where the CH₂–OH peak is

expected. This improved resolution and appearance of multiple peaks definitively proves the presence of multiple isomers in solution. However, integration of the peaks does seem to indicate that some isomers are more common than others; determining which though would require computational studies beyond the scope of this thesis.

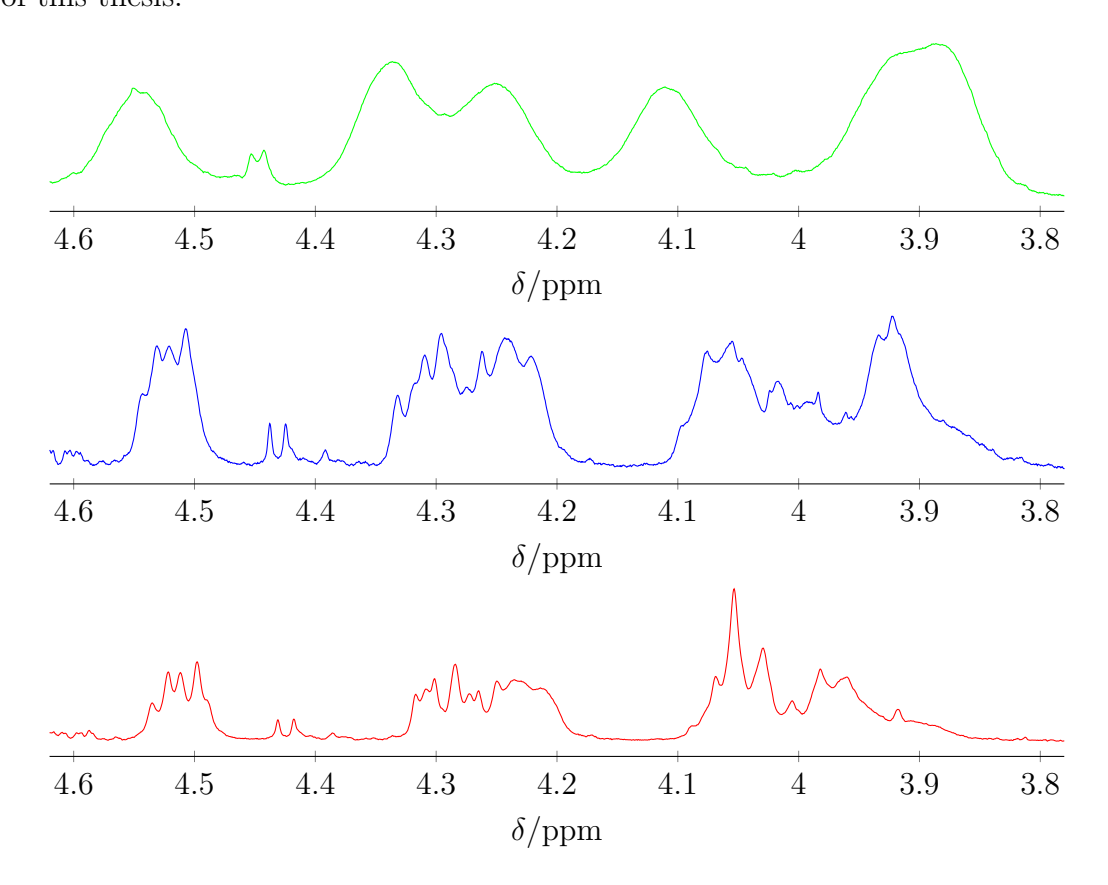


Figure 4.9: The ¹H-NMR Spectrum of complex **30** at 293 K (Green), 273 K (Blue), and 263 K (Red).

With the determination of several isomers, we could now make an informed calculation of the stretching frequency of the Mo=O bond. It is not as simple as to take the calculated values for a single isomer and present it as an accurate representation of the whole. Depending on the functional, more than one stretching frequency is calculated for the Mo=O bond with differing strengths, so a weighted

average of the several stretching frequencies and their respective strengths must first be calculated. The value must next be calibrated to a particular bond in the experimental spectra; for $[MoO(S_2C_2MeBnOH)_2]^{2-}$ (30), the C-H of asymmetric stretch of CH₃ was chosen. This process must then be replicated for the other five isomers as each gave a range of values, differing in magnitude depending on the functional used. Consequently, another average was taken.

Table 4.4: Calculated Energies of the Mo=O bond in $[MoO(S_2C_2MeBnOH)_2]^{2-}$ (30).

Entry	Functional	$\tilde{\nu}/\mathrm{cm}^{-1}$
1	BP86	924
2	B3LYP	944
3	PBE0	943
4	TPSS	926
5	$\omega \mathrm{B97X}$	975

These calculated values, shown in Table 4.4, can now be compared against the experimental spectra. All five functionals give a stretching frequency between 920 cm⁻¹ and 980 cm⁻¹ which eliminates the two peaks either side of the smaller, third peak. Annotating the experimental IR spectrum with these calculated values offers a more obvious picture (Figure 4.10). The B3LYP and PBE0 functionals both give values very close to this weak peak occurring at 940 cm⁻¹. One can now appreciate the difficulty of identifying/assigning the Mo=O bond in the IR spectrum. Without computational methods, only an educated guess could have been taken.

$4.2.2 \quad [MoO(S_2C_2MePh)_2]^{2-}$

With a reliable computational approach established, computational methods can be used to identify key features of the other synthesised analogues of the target

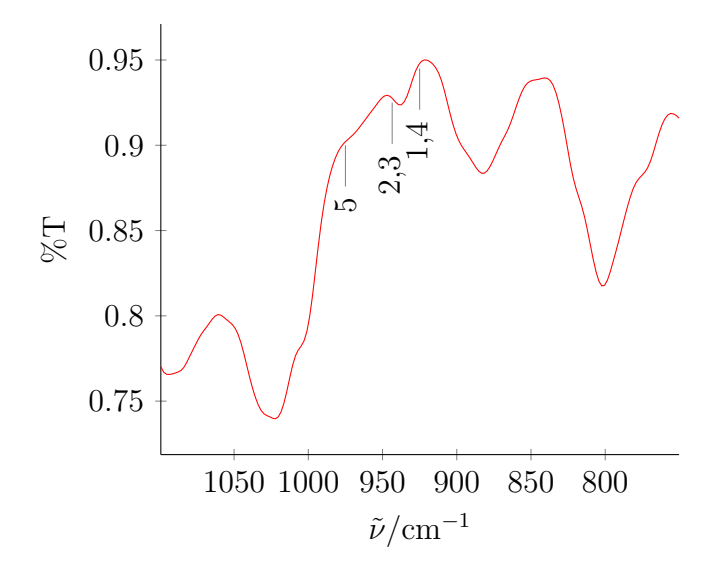


Figure 4.10: The Experimental KBr IR Spectrum of the Target Complex **30** Overlaid with the Calculated IR Frequencies.

complex. Geometry optimisation showed no significant difference in outcome when different rotational angles and coordinates were input. As a result, the subsequent IR stretching calculations were simplified. The IR spectrum of **78** is less ambiguous than that of **30**, with a weak, isolated peak appearing at 931 cm⁻¹, the typical region the Mo=O stretch can be found (Figure 4.11). One can then hypothesise with a great deal of confidence that this peak corresponds to Mo=O. Computational methods can be used to prove this hypothesis.

Table 4.5: Calculated Energies of the Mo=O bond in $[MoO(MoO(S_2C_2MePh)_2)_2]^{2-}$ (78).

Entry	Functional	$\tilde{\nu}/\mathrm{cm}^{-1}$
1	BP86	932
2	B3LYP	937
3	PBE0	955
4	TPSS	931
5	$\omega B97X$	972

Table 4.5 shows the calculated vibrational energy of the Mo=O bond in

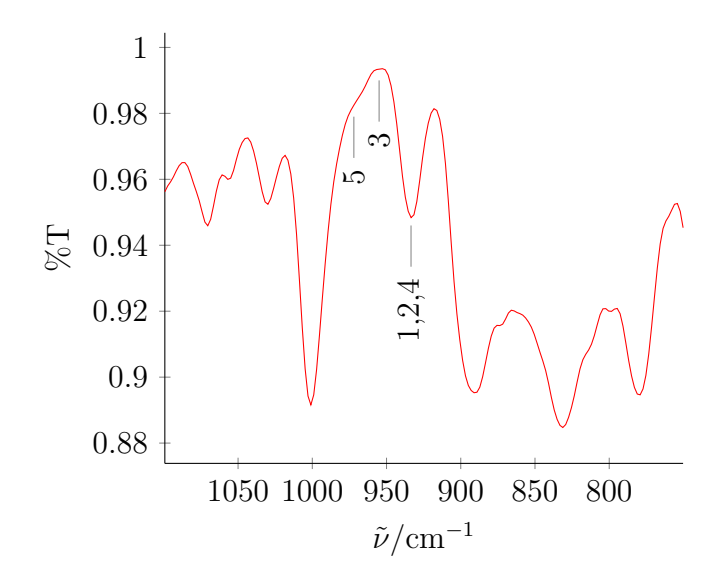


Figure 4.11: The Experimental KBr IR Spectra of $[MoO(S_2C_2MePh)_2]^{2-}$ (78) with Calculated IR Frequencies.

 $MoO(S_2C_2MePh)_2^{2-}$ (78) according to the various functionals. Overlaying these values over the experimental IR spectrum clearly shows which functional accurately predicted where the Mo=O will occur at 930 cm⁻¹. The BP86 functional was the most accurate, however, the B3LYP functional was not far off.

$4.2.3 \quad [MoO(S_2C_2HBnOH)_2]^{2-}$

Like the methyl substituted analogue (30) obtaining a single crystal of 80 suitable for XRD has proved elusive. A cursory glance allows one to similarly identify the potential for many isomers as well as the possibility of *cis* and *trans* isomerisation. Computational DFT analysis utilising the five functionals used above, with varying starting coordinates of the benzyl alcohol substituent, all identified several possible isomers after geometry optimisation shown in Figure 4.12.

The relative difference in energy of the six isomers of **80** is tiny, mirroring **30** (Table 4.12). Such a small difference in energy suggests a dynamic equilibrium in solution, implying equal distribution of isomers upon crystallisation is likely.

Table 4.6: Calculated relative energy values for $[MoO(S_2C_2HBnOH)_2]^{2-}$ (80) using the B3LYP functional.

Entry	Isomer	$E/\mathrm{kJ}\mathrm{mol}^{-1}$
1	cis up,up	-2.89
2	cis up,down	-2.83
3	cis down,down	0
4	trans up,up	-2.95
5	trans up,down	3.23
6	trans down,down	4.86

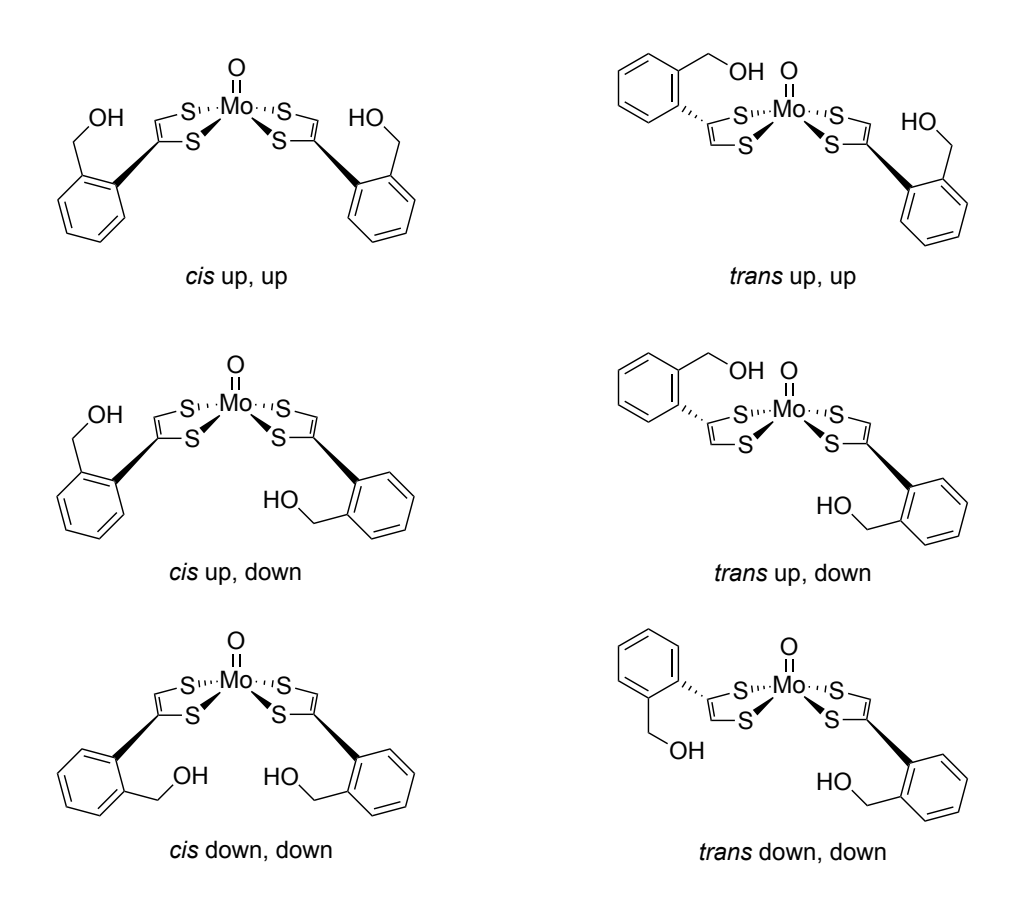


Figure 4.12: The Isomers of $[MoO(S_2C_2HBnOH)_2]^{2-}$ (80).

Therefore, obtaining a suitable crystal for X-ray diffraction would be very difficult.

Table 4.7: Calculated Energies of the Mo=O bond in $[MoO(S_2C_2HBnOH)_2]^{2-}$.

Entry	Functional	$\tilde{\nu}/\mathrm{cm}^{-1}$
1	BP86	782
2	B3LYP	892
3	PBE0	899
4	TPSS	817
5	$\omega \mathrm{B}97\mathrm{X}$	920

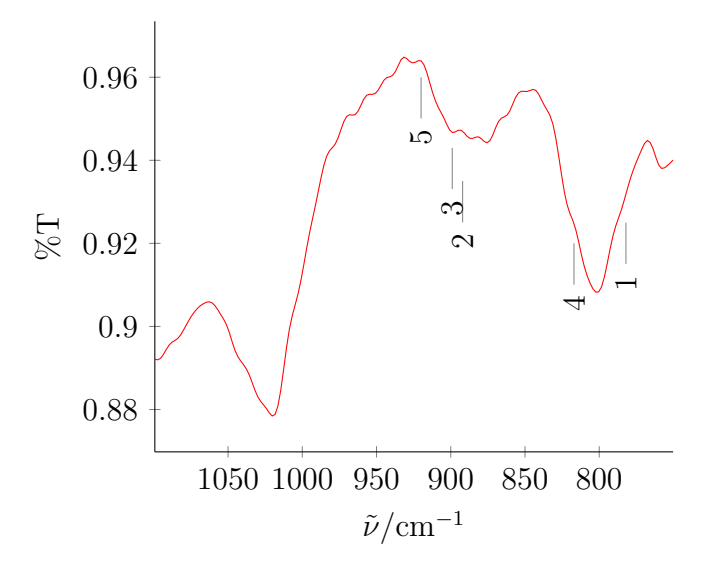


Figure 4.13: The Experimental IR Spectrum of the Complex **71** with the Calculated IR Frequencies of the Mo=O Bond.

With this complex, identifying the Mo=O bond in the experimental IR spectrum (Figure 4.13) can be achieved without DFT analysis provided one has a degree of familiarity with such bond assignments. However, there are three peaks within and close to the 900–1000 cm⁻¹ region where most Mo=O bonds are expected to appear. Overlaying the calculated values, shown in Table 4.7, on the experimental spectrum shows that two of the five functionals seem to suggest a peak outside what would be considered the normal range. Using what we know so far about this

bond, we can determine from its relative intensity and where it appears that it is unlikely that this is the Mo=O peak. Therefore, we can determine that the Mo=O band occurs at 890 cm⁻¹. This dramatic shift for the stretch of **80** when compared to the Mo=O stretch belonging to **30** shows how the primary substituents of the dithiolene have a clear influence on the strength of the Mo=O bond.

$4.2.4 \quad [MoO(S_2C_2HPh)_2]^{2-}$

Synthesis of $[MoO(S_2C_2HPh)_2]^{2-}$ was straightforward and has been previously prepared in the literature, $\mathbf{41\text{-}sdt}$.¹⁰¹ Davies and co-workers report the Mo=O value as occurring at 879 cm⁻¹ (highlighted as 'L' in Figure 4.14). Unfortunately, the paper does not include an image of the IR spectrum for $\mathbf{41\text{-}sdt}$ so direct comparison with our complex of $\mathbf{41}$ is difficult. 'L' appears to sit between two peaks for the experimental IR spectrum of $\mathbf{41}$ so using computational methods to confirm which peak corresponds to the Mo=O bond is well worth doing.

Table 4.8: Calculated Energies of the Mo=O bond in $[MoO(S_2C_2HPh)_2]^{2-}$ (41).

Entry	Functional	$\tilde{\nu}/\mathrm{cm}^{-1}$
1	BP86	911
2	B3LYP	921
3	PBE0	909
4	TPSS	909
5	$\omega \mathrm{B97X}$	921

Using DFT, five values were obtained using the five different functionals (Table 4.8). Each value indicates that the correct peak occurs within the expected region. Overlaying these values with the experimental IR spectrum, Figure 4.14 clearly identifies the Mo=O peak as belonging to the band at 900 cm⁻¹ with PBE0 and TPSS being the most accurate.

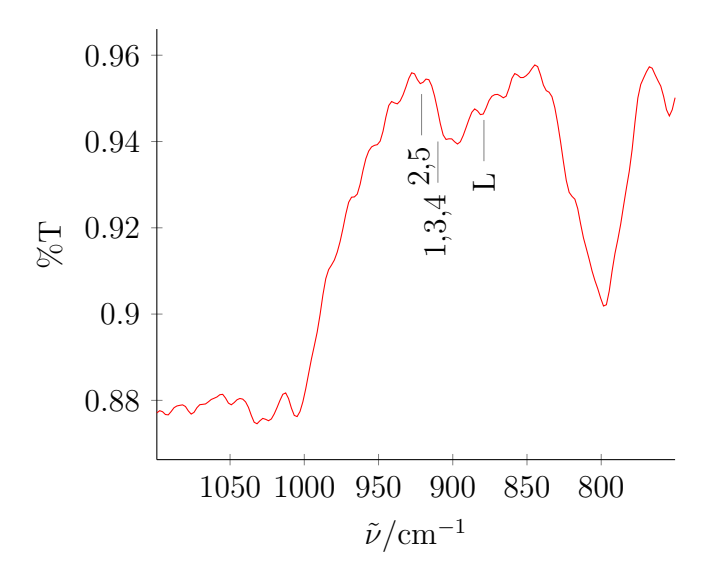


Figure 4.14: The Experimental IR Spectrum of the Target Complex **41** Overlaid with the Calculated IR Frequencies of the Mo=O bond.

4.2.5 Summary

DFT confirmed that there is an equilibrium between the isomers in solution for more functionalised ligands, with this equilibrium evident in the 1 H NMR spectrum of 30. The equilibrium of isomers provides a possible reason why it is so difficult to obtain crystals suitable for X-ray diffraction. But first it was important to properly identify the orbital geometry and subsequent SAMO to understand the correct spin multiplicity parameter of molybdenum-oxo bis-dithiolene complexes. Simultaneously, DFT has been used to help correctly assign peaks in the experimental infrared spectra and these results have been summarised in Table 4.9. From this table it is possible to identify when to use which functional for any particular molybdenum-oxo bis-dithiolene complex by comparing the results with each other. It appears that for simpler systems, with fewer isomers, the BP86 functional gives more accurate results, while B3LYP and PBE0 work better with more complex systems. From this chapter, efficiency in all areas would be improved if, when synthesising a new complex, a DFT calculation using the B3LYP and

PBE0 functionals is performed simultaneously so the Mo=O bond can be used as a diagnostic feature for synthesis. These DFT-based assignments should be supported by future studies aimed at obtaining experimental evidence, for example, via oxygen isotope labelling studies. Kirk and co-workers used the ¹⁸O isotope to characterise the Mo=O stretch on the DMSOR enzyme found in *R. sphaeroides* so such experiments are not unheard of for these types of complexes.²²¹

Table 4.9: A Summary of the Most Accurately Calculated Mo=O IR Stretch Against the Experimental Value.

Complex	Functional	M=O Str	$etch \tilde{\nu}/cm^{-1}$
		Calculated	Experimental
$\overline{\left[\text{MoO(S}_2\text{C}_2\text{MeBnOH)}_2\right]^{2-} \left(30\right)}$	B3LYP	944	942
$[{ m MoO(S_2C_2MePh)_2}]^{2-}$ (78)	BP86	932	932
$[MoO(S_2C_2HBnOH)_2]^{2-}$ (80)	B3LYP	892	890
$[{ m MoO(S_2C_2HPh)_2}]^{2-}$ (41)	PBE0/TPSS	909	900

Chapter 5

Electrochemistry

5.1 Introduction

Electrochemical methods are used to investigate the behaviour of redox-active species, from organic systems, inorganic solids and the most ubiquitous use, transition metal complexes.²²² To truly utilise electrochemical methods effectively, whether that be as a characterisation tool or an analytical technique, an understanding of the theory of the subject is required. This chapter will first describe the fundamentals of electrochemical analysis followed by the application of these methods on the prepared bio-mimetic dithiolene metal complexes.

5.1.1 Redox Processes and the Nernst Equation

At the surface of an electrode, a species can undergo a single electron reduction or oxidation to form the reduced or oxidised species. E° is the standard reduction potential required to establish a dynamic equilibrium between both the oxidised and reduced species, where there is no change in the Gibbs free energy ΔG° . The standard reduction potential is measured under standard conditions: the concentration of the species being 1 M and the temperature at the time of measure-

ment being 298 K. The values are also standardised against the standard hydrogen electrode (SHE) which is defined as 0 V. However, like the ideal gas equation, often conditions deviate. When this occurs, the redox potential can be calculated using the Nernst equation, where R is the ideal gas constant, T is the temperature, n is the number of electrons transferred in the process, F is Faraday's constant, [B] is the concentration of the reduced species, and [A] is the concentration of the oxidised species (Equation 5.1).

$$E = E^{\circ} - \frac{RT}{nF} \ln \left(\frac{[B]}{[A]} \right) \tag{5.1}$$

5.1.2 Diffusion

When performing a cyclic voltammetry experiment, the solutions are not stirred. This results in a difference between the contents of the solution at the electrode and the contents of the bulk solution. There is a higher concentration of one species at the electrode than in the bulk solution, and as a consequence, a concentration gradient is generated. As a result, a phenomenon known as the electric double layer forms. This double layer can affect the rates of electrode processes by 'blocking' ions from approaching the electrode, and therefore these ions experience less potential by an amount. These ions must diffuse through this layer and can be defined by Fick's laws of diffusion. Diffusion of the substrate towards the electrode is often the slowest step during a redox process, and as a result, the flow of current across a voltammetric cell is dictated by the flux of the substrate to the electrode.²²⁴ Therefore, it is recommended to stir the solution between electrochemical experiments to remove the double electric layer.

5.1.3 Cyclic Voltammetry

Cyclic voltammetry (CV) is the most widely utilised electrochemical method. It allows for the rapid determination of the equilibrium potentials of reversible processes, as well as whether those responses to a change in potential are reversible redox reactions, and their response to the addition of a substrate.^{222,225,226} To perform a CV, the potential is swept from an electrode at a constant rate $(v, V s^{-1})$ from a starting potential E_{initial} , to a vertex potential E_{vertex} , and then back to a final potential E_{final} , often the same value as E_{initial} .

During this sweep, a redox process might occur. Imagine the oxidation of a species A to species B. As the potential of the electrode approaches and exceeds the reduction potential of A, the current response increases until a limit is reached. At this point, the concentration of A at the electrode is depleted, and further reduction of A is dependent on the diffusion of species A across the double electric layer to replace the spent analyte; this is represented by a decrease in the current response. The potential is swept until the E_{vertex} is reached where the potential is then swept back to E_{initial} . During this 'reverse' scan, the reduced product B that remains at the electrode is oxidised back into A; this process is shown by a current response where another peak is reached until it diminishes due to mass transport limitations. For a redox process to be considered fully reversible, the current peaks (oxidised and reduced) must only be separated by 57 mV; this is the theoretical typical value for a fully reversible single electron transfer at room temperature.

An ideal fully reversible process, with a high rate of electron transfer (k_e) , is represented by a 'duck' shaped CV. This k_e value is explained by Marcus theory.²²³ Marcus theory states that where the potential energy surfaces for A and B are similar with respect to the reaction coordinate, then the transition state energy and thus activation energy is low and electron transfer can occur.²²⁷ However, if there is a significant change in the geometry of the molecules when A is oxidised to B, the

activation energy is obviously higher and the electron transfer is sluggish. If the rate of electron transfer is slow due to changes in geometry between A and B, or if there is an electronic rearrangement known as spin crossover, the electrochemical process is irreversible, and the CV is distorted from this ideal shape (often seen by a reduction in current magnitude of one or both peaks).

Another key point of a CV is the scan rate; provided it is sufficiently high, the result is that the electrochemical/redox change can be fully reversible. The dependence of current response on scan rate therefore carries information about the lifetimes of electrochemically generated species. Commonly, the rate of chemical change is comparable to the time taken to reverse a CV sweep. Logically, this means that the size and position of the reverse wave will show a dependence on the scan rate. One can analyse reversibility by plotting peak currents against the square root of the scan rates. This relationship is described by the Randles-Ševčik equation (Equation 5.2)

$$i_{\text{peak}} = -0.4463nF \left(\frac{nF}{RT}\right)^{1/2} c_0^{\infty} \sqrt{Dv}$$
 (5.2)

where i_{peak} is the peak current, n is the number of electrons passed, F is Faraday's constant, R is the ideal gas constant, T is the temperature, D is the diffusion coefficient, c_0^{∞} is the bulk concentration, and v is the scan rate.

5.1.4 Molybdenum Dithiolenes

For all of the molybdenum-oxo dithiolene complexes found in the literature (Figure 3.1) most are published with some degree of electrochemical studies. Table 5.1 shows a collection of the complexes and their associated redox potentials, solvent, supporting electrolyte, and internal reference.

Table 5.1: Complete Catalogue of ${\rm Mo^{IV}}$ Dithiolene Complexes and Their Associated Redox Potentials. b Quasireversible. c Irreversible.

i					1
Complex	Supporting Electrolyte Solvent	Solvent	Reference	$E_{1/2}$	$E_{1/2} \; (\mathrm{V})$
				$\mathrm{Mo^{IV}/Mo^{V}}$	$\mathrm{Mo^{IV}/Mo^{V}}$ $\mathrm{Mo^{V}/Mo^{VI}}$
$10 ext{-qpdt}^{112}$	$\mathrm{Bu}_4\mathrm{NOCl}$	MeCN	Ag/AgCl/KCl(sat)	-0.19	0.6 b
$11 ext{-}\mathrm{Hqpdt}^{103}$	${ m Bu_4NOCl}$	MeCN	Ag/AgCl/KCl(sat)	-0.34	0.4^{-b}
$12 ext{-}2\mathrm{Hqpdt}^{103}$	${ m Bu_4NOCl}$	MeCN	Ag/AgCI/KCI(sat)	-0.51	0.3^{-b}
$\mathbf{20\text{-}bdt}^{100}$	${\rm Bu_4NPF_6}$	MeCN	SCE	-0.39	0.56
$6 ext{-}\mathbf{mohbdt}^{104}$	${ m Bu_4NPF_6}$	MeCN	${ m Fc}/{ m Fc}^*$	-0.62	
34^{154}	${\rm Bu_4NPF_6}$	MeCN	SCE	-0.51	0.25
$35\text{-}\mathbf{edt}^{100}$	${ m Bu_4NPF_6}$	MeCN	SCE	-0.61	C
36^{154}	${\rm Bu_4NPF_6}$	MeCN	SCE	99.0-	0.11
${f 37\text{-}mnt}^{100}$	${ m Bu_4NPF_6}$	MeCN	SCE	0.48	C
$\bf 39\text{-}bdtCl_2^{108}$	${ m Bu_4NPF_6}$	MeCN	SCE	-0.1	C
$41 ext{-}\mathrm{sdt}^{101}$	${\rm Bu_4NPF_6}$	DMF	SCE	-0.48	C
$42 ext{-}\mathrm{cdt}^{105}$	${ m Bu_4NPF_6}$	Ċ	${ m Fc}/{ m Fc}^*$	-0.72	
$43\text{-}\mathbf{tcdt}^{105}$	${ m Bu_4NPF_6}$	ċ	${ m Fc}/{ m Fc}^*$	-0.87	

Table 5.1: Complete Catalogue of $\mathrm{Mo^{IV}} = \mathrm{O}$ bis-Dithiolene Complexes and Their Associated Redox Potentials. ^b Quasi-reversible. ^c Irreversible (cont.).

Complex	Supporting Electrolyte	Solvent	Reference	$E_{1/2}$	$E_{1/2}$ (V)
				$\mathrm{Mo^{IV}/Mo^{V}}$	$\mathrm{Mo^{IV}/Mo^{V}}$ $\mathrm{Mo^{V}/Mo^{VI}}$
44 -tldt 105	${ m Bu_4NPF_6}$	ć	$\mathrm{Fc}/\mathrm{Fc}^*$	-0.95	
$\mathbf{45\text{-}Me_{4}bdt^{100}}$	${\rm Bu_4NPF_6}$	MeCN	SCE	-0.53	-0.16^{b}
$f 46 ext{-}opedt^{101}$	${\rm Bu_4NPF_6}$	DMF	SCE	-0.42	
$\textbf{47-} \boldsymbol{m} \mathbf{p} \mathbf{e} \mathbf{d} \mathbf{t}^{101}$	${\rm Bu_4NPF_6}$	DMF	SCE	-0.39	C
$48 ext{-}p\mathrm{pedt}^{101}$	${\rm Bu_4NPF_6}$	DMF	SCE	-0.35	
49^{109}	${\rm Bu_4NPF_6}$	MeCN	SCE	-0.56	0.19
50^{109}	${\rm Bu_4NPF_6}$	MeCN	SCE	-0.57	0.18
51^{109}	${\rm Bu_4NPF_6}$	MeCN	SCE	7.0-	0.00
${f 52-dmit}^{96}$	$\mathrm{Bu_4}\mathrm{NOCl}$	MeCN	SCE	0.12	0.52^b
$53\text{-}(\text{edt})(\text{mnt})^{100}$	${\rm Bu_4NPF_6}$	MeCN	SCE	-0.08	0.54^b
54^{97}	$\mathrm{Bu_4}\mathrm{NOCl}$	MeCN	Ag/AgCI/KCI(sat)	-0.029	0.82c
${f 57 ext{-}fdt}^{107}$	${\rm Bu_4NPF_6}$	MeCN	${ m Fc}/{ m Fc}^*$	-1.33	-0.04^{c}
${f 58 ext{-}qedt}^{101}$	$\mathrm{Bu}_4\mathrm{NPF}_6$	DMF	SCE	-0.28	

Table 5.1: Complete Catalogue of $\mathrm{Mo^{IV}} = \mathrm{O}$ bis-Dithiolene Complexes and Their Associated Redox Potentials. ^b Quasi-reversible. ^c Irreversible (cont.).

Complex	Supporting Electrolyte Solvent	Solvent	Reference	$E_{1/2}$ (V)	(V)
				$\mathrm{Mo^{IV}/Mo^{V}}$ $\mathrm{Mo^{V}/Mo^{VI}}$	$\mathrm{Mo^{V}/Mo^{VI}}$
$59 ext{-} ext{ntdt}^{111}$	${ m Bu_4NPF_6}$	MeCN	${ m Fc}/{ m Fc}^*$	-0.89	
$\mathbf{60-tfd}_{100}$	${\rm Bu_4NPF_6}$	MeCN	SCE	0.18	0.64^b
61^{106}	${\rm Bu_4NPF_6}$	MeCN	SCE	-0.24	
62^{95}	$\mathrm{Et}_4\mathrm{NOCl}$	MeCN	SCE	0.84^{c}	C
$64 ext{-}\mathrm{NH}_2 ext{-}\mathrm{ptedt}^{101}$	${\rm Bu_4NPF_6}$	DMF	SCE	-0.35	
$\mathbf{65\text{-}NC(H)(Me)}_{2\text{-}\mathrm{ptedt}^{101}}$	${\rm Bu_4NPF_6}$	DMF	SCE	-0.33	
$\mathbf{66\text{-}L\text{-}S_{2}}^{100}$	${\rm Bu_4NPF_6}$	MeCN	SCE	-0.71	0.04
$67 ext{-} ext{PPh}_3 ext{Sibdt}^{98}$	${ m Bu_4NOCl}$	DMF	SCE	-0.41	
68 -td t^{98}	${ m Bu_4NOCl}$	DMF	SCE	-0.45	
${f 69-PPh_3Sitdt}^{98}$	${ m Bu_4NOCl}$	DMF	SCE	-0.46	0.52
$70 ext{-}\mathrm{adt}^{110}$	${\rm Bu_4NPF_6}$	MeCN	SCE	-0.56	
${f 71 ext{-}ecpdt}^{110}$	${\rm Bu_4NPF_6}$	MeCN	SCE	-0.21	

However, before the redox potential of each complex can be compared faithfully, they must all be standardised against each other because a global common standard method has not been used. For example, across Table 5.1 there is a variety of approaches to the electrochemical set-ups utilised. Ten complexes utilise dimethylformamide (DMF) as the solvent (41, 46–48, 58, and 64–69), where the rest of the cyclic voltammograms are conducted in acetonitrile (MeCN). Although both have a similar dielectric constant, 'direct' comparison of the CVs between the two solvents is obviously not feasible as the molar conductivity (Λ_M) is significantly different. A difference in the supporting electrolyte is not as detrimental to the comparison of redox potentials between complexes because the supporting electrolyte provides a different function: the majority of the current in the bulk solution is carried by the electrolyte and limits mass transport among other features. The remaining variable is the method by which the redox potentials were referenced. Within the complexes listed, three methods have been implemented:

- the saturated calomel electrode (SCE) which operates based on the reaction of elemental mercury and mercury chloride.
- the Ag/AgCl/KCl_(sat) reference. This reference is characterised by a Ag wire with an end coated with AgCl sitting in a potassium chloride saturated solution. A porous frit serves as the salt bridge to the bulk solution. In essence, it is a self-contained unit. This has largely replaced the SCE reference electrode.
- the ferrocene/ferrocenium couple (Fc/Fc*) is used in conjunction with a
 pseudo-reference, which is often silver wire. The Fc/Fc* couple is treated as
 0 V and the other values are adjusted accordingly.

Fortunately, work by Addison and co-workers allows one to convert between the different referencing methods; this work has been performed in acetonitrile and therefore conversions when the solvent is dimethyl formamide are dubious so two separate tables have been created for CVs per formed in acetonitrile (Table 5.2) and dimethyl formamide (Table 5.3). 230

Table 5.2: A Complete Catalogue of $Mo^{IV}=O$ bis-Dithiolene Complexes and Their Adjusted Redox Potentials to the Fc/Fc* Couple Split by Solvent Type (Acetonitrile). ^b Quasi-reversible. ^c Irreversible.

Complex	Solvent	$E_{1/2} (V)$	
		$\mathrm{Mo}^{\mathrm{IV}}/\mathrm{Mo}^{\mathrm{V}}$	$\mathrm{Mo^{V}/Mo^{VI}}$
$\overline{10\text{-}\mathbf{qpdt}^{112}}$	MeCN	-0.617	0.123^{b}
$11\text{-}\mathbf{Hqpdt}^{103}$	MeCN	-0.767	-0.027^{b}
${f 12\text{-}2Hqpdt}^{103}$	MeCN	-0.937	-0.127^{b}
$20 ext{-}\mathbf{b}\mathbf{dt}^{100}$	MeCN	-0.77	0.18
$6 ext{-}\mathbf{mohbdt}^{104}$	MeCN	-0.62	
34^{154}	MeCN	-0.89	-0.13
$35 ext{-}\mathbf{edt}^{100}$	MeCN	-0.99	c
36^{154}	MeCN	-1.04	-0.27
$37 ext{-mnt}^{100}$	MeCN	0.10	
$\mathbf{39\text{-}bdtCl_2}^{108}$	MeCN	-0.48	c
$f 42 ext{-}{ m cdt}^{105}$?	-0.72	
$f 43 ext{-}tcdt^{105}$?	-0.87	
$f 44 ext{-tldt}^{105}$?	-0.95	
$\mathbf{45\text{-}Me_4bdt^{100}}$	MeCN	-0.91	-0.54^{-b}
49^{109}	MeCN	-0.94	-0.19
50^{109}	MeCN	-0.95	-0.2
51^{109}	MeCN	-1.08	-0.32

Table 5.2: Complete Catalogue of $Mo^{IV}=O$ bis-Dithiolene Complexes and Their Adjusted Redox Potentials to the Fc/Fc* Couple Split by Solvent Type (Acetonitrile).

^b Quasi-reversible. ^c Irreversible (cont.).

Complex	Solvent	$E_{1/2} (V)$	
		$\mathrm{Mo}^{\mathrm{IV}}/\mathrm{Mo}^{\mathrm{V}}$	$\mathrm{Mo^{V}/Mo^{VI}}$
$oxed{52 ext{-dmit}^{96}}$	MeCN	-0.26	0.14 ^b
$53\text{-}(\mathrm{edt})(\mathrm{mnt})^{100}$	MeCN	-0.46	0.16^{-b}
${f 54}^{97}$	MeCN	-0.457	0.393^{c}
${f 57\text{-}fdt}^{107}$	MeCN	-1.33	-0.04^{-c}
${f 59} ext{-}{f ntdt}^{111}$	MeCN	-0.89	
$f 60 ext{-tfd}^{100}$	MeCN	-0.20	0.26^{-b}
61^{106}	MeCN	-0.62	
62^{95}	MeCN	-1.22 ^c	
$\mathbf{66\text{-}L\text{-}S_2}^{100}$	MeCN	-1.09	-0.34
$70 ext{-} ext{adt}^{110}$	MeCN	-0.87	
$71 ext{-}\mathrm{ecpdt}^{110}$	MeCN	-0.52	

Analysing Table 5.2 and Table 5.3 offers a fascinating insight into how the ligands affect the electrochemistry of these molybdenum-oxo dithiolene complexes. The Mo^{IV}/Mo^V redox couple is well documented and is reversible for all the complexes except **53**. Oddly, the Mo^V/Mo^{VI} redox couple is much more poorly documented, so one assumes that whenever the data point is missing, the implication is that the wave is irreversible. The Mo^V/Mo^{VI} couple has been documented as quasi-reversible six times and reversible seven times. Looking at the ligands and comparing them with each other offers some commonalities in the scaffolds (Figure 3.1). The

Table 5.3: A Complete Catalogue of $\mathrm{Mo^{IV}}=\mathrm{O}\ bis$ -Dithiolene Complexes and Their Adjusted Redox Potentials to the Fc/Fc* Couple Split by Solvent Type (Dimethylformamide).

Complex	Solvent	$E_{1/2}$ (V) $\mathrm{Mo^{IV}/Mo^{V}}$ $\mathrm{Mo^{V}/Mo^{VI}}$	
		$\mathrm{Mo^{IV}/Mo^{\acute{V}}}$	Mo ^V /Mo ^{VI}
$\overline{\mathbf{41\text{-}sdt}^{101}}$	DMF	-0.86	\overline{c}
$oldsymbol{46-o}{ m pedt}^{101}$	DMF	-0.8	
47 - m pedt 101	DMF	-0.77	c
$m{48-p}{ m pedt}^{101}$	DMF	-0.73	
$oldsymbol{58} ext{-}\mathbf{qedt}^{101}$	DMF	-0.66	
$64\text{-NH}_2\text{-ptedt}^{101}$	DMF	-0.73	
$65\text{-NC(H)(Me)}_2 ext{-ptedt}^{101}$	DMF	-0.71	
67-PPh ₃ Sibdt ⁹⁸	DMF	-0.79	
$\mathbf{68-tdt}^{98}$	DMF	-0.83	
69 -PPh $_3$ Sit dt^{98}	DMF	-0.84	0.14

reversible ligands are usually 'simple', alkyl, and aryl substituents which lack adjacent functionality. When considering Marcus theory, perhaps obtaining the Mo^{VI} oxidation state is inherently unstable due to the rearrangement of the ligands, resulting in the electron transfer being significantly slowed, giving an irreversible wave; simpler, more constrained ligand scaffolds would likely not greatly suffer from the effects of severe rearrangements, and this issue is mitigated. Looking at which ligands give quasi-reversible waves offers some credence to this logic. Ligands synthesised by Fontecave and their associated complexes (10, 11, and 12) could be thought of as conserved because of the constraining nature of the pyran ring, but still adding an element of functionality. This conserved status means very little geometrical changes can occur when the oxidation state changes. This feature can be seen for other quasi-reversible systems.

Trying to identify some trend between ligand scaffold and the value of the redox potential is very challenging. But generally, two factors contribute to the value. Firstly, the simpler systems that lack withdrawing groups give more positive redox potentials; one can assume that the electron density is forced to be centralised around the metal centre giving more negative redox potentials. Secondly, the more reducing a ligand is, the more negative the redox potential. This can be seen when looking at Fontecave and co-workers ligands; ^{103,161} the more reduced the ligand, the more negative the redox potential of the reported couples.

Interestingly, the peak separation values of the redox couples have some similarities. Seven of the sixteen recorded redox couple pairs have a peak separation of 750 ± 20 mV. Unfortunately, as mentioned previously, the Mo^V/Mo^{VI} couple is poorly documented, so using these complexes to identify trends is impossible. These seven well documented complexes are the 10-qpdt, 11-Hqpdt, 34, 36, 49, 50, 51 and 66. A general commonality between the ligands belonging to these complexes is that they could be considered highly conserved and conjugated. For the other nine, there does not appear to be any reason why one gives a different value to the other.

5.2 Cyclic Voltammetry of

$$(\mathrm{Et_4N})_2[\mathrm{MoO}(\mathrm{S_2C_2MeBnOH})_2]$$

The electrochemical experiments on the molybdenum-oxo bis-dithiolene complexes, synthesised previously in the thesis, were performed in acetonitrile in the presence of tetrabutylammonium tetrafluoroborate as the electrolyte, a glassy carbon working electrode, platinum wire counter electrode, and a silver wire as the pseudo reference electrode (the potentials were then internally referenced to the Fc/Fc* couple). A key aspect of these complexes is their sensitivity to oxygen. This feature was taken into account when performing the electrochemical experiments, so all cyclic voltammograms were performed in a glovebox under an argon atmosphere.

Upon oxidation of complex 30, the $\mathrm{Mo^{IV}/Mo^{V}}$ and $\mathrm{Mo^{V}/Mo^{VI}}$ couple occurred

at $-0.916\,\mathrm{V}$ and $-0.229\,\mathrm{V}$, respectively; therefore, there is a peak separation of $669\,\mathrm{mV}$ (Figure 5.1). This separation is most similar to the seven complexes highlighted in the previous subsection, which indicates that there are similar electronic effects from the ligands but the observed potentials are still different enough to warrant further thought. Compared to the 'second most simple complex', 36, the separation is $100\,\mathrm{mV}$ less. With one of the methyl groups replaced by a benzyl alcohol, it highlights the influence that the non-innocence of the dithiolene ligand has on the redox potential of the molybdenum.

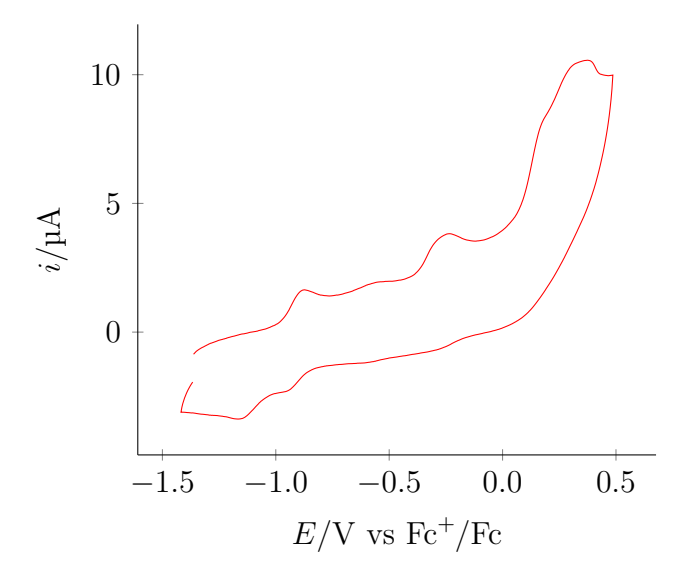


Figure 5.1: The Cyclic Voltammogram of 30 in MeCN/NBu₄BF₄ (0.1 M) at $50\,\mathrm{mV\,s^{-1}}$ Using an Unmodified Glassy Carbon Electrode. The Potentials were Internally Referenced to the Fc/Fc* Couple.

To determine the reversibility of a couple, there are three parameters to make a judgment by: the peak separation of the oxidation and reduction potentials, the overall shape of the peak, and the response of the peak current of the oxidation/reduction waves to changes in scan rate. It is important to note that the theoretical difference between the two peak potentials for a one-electron couple is 57 mV; however, the experimental values often differ from the theoretical values

and can exceed 80 mV whilst maintaining reversibility.

By inspection, it is clear that the first wave is fully reversible; however, the second peak is much less clear. A plot of peak current against scan rate shows that the current response is indeed linear; however, the rate of current change between the oxidation and reduction currents differs substantially. Consequently, it can be deduced that the Mo^V/Mo^{VI} couple is quasi-reversible (Figure 5.2). The quasi-reversibility of this wave suggests that upon reduction of $\mathrm{Mo^{VI}}$ to $\mathrm{Mo^{V}}$ there is a significant change in the geometry of the complex resulting in sluggish electron transfer. The smaller peak current seen for the reduction of $\mathrm{Mo^{VI}}$ back into $\mathrm{Mo^{V}}$ can be further rationalised by a square scheme analysis. Figure 5.3 describes a system where the initial electron transfer from Mo_a^V to Mo_a^{VI} is followed by a rapid structural change to species Mo_b^{VI} ; this is demonstrated by the wave at $-0.2\,\mathrm{V}$. This $\mathrm{Mo_b^{VI}}$ species could now be different enough in structure that it can be considered completely independent; this new species may not show up with the current scan parameters. In other words, a chemically irreversible process has occurred instead of an electrochemical one. With less of the Mo_a^{VI} species at the electrode, the current of the reduction back to Mo_a^V is a lot smaller.

5.3 Cyclic Voltammetry of

$(\mathrm{Et_4N})_2[\mathrm{MoO}(\mathrm{S_2C_2MePh})_2]$

One might think that the hydroxy group is electronically isolated from the metal centre, but upon synthesis of **78**, the subsequent electrochemical experiments showed that this was not the case. The cyclic voltammogram, shown in Figure 5.4, demonstrated that the $\mathrm{Mo^{IV}/Mo^{V}}$ and $\mathrm{Mo^{V}/Mo^{VI}}$ couple had shifted slightly in value to $-0.975\,\mathrm{V}$ and $-0.245\,\mathrm{V}$, respectively, resulting in a peak separation of 730 mV, a 60 mV increase. Without the benzyl alcohol moiety, the redox couples

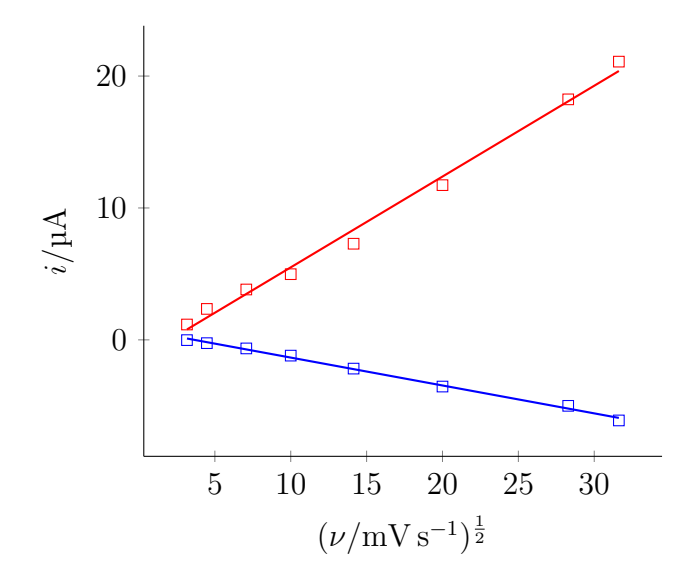


Figure 5.2: A Plot of the Peak Current Against the Square Root of the Scan Rate for the Redox Process at $-0.229\,\mathrm{V}$ of 30 in MeCN/NBu₄BF₄. Red Squares are for the Oxidation Waves and Blue Squares are for the Reduction Waves.

$$\begin{array}{c|c} Mo_a^{VI} \xrightarrow{k_1} Mo_b^{VI} \\ \hline -e^- + e^- & -e^- + e^- \\ Mo_a^{V} \xrightarrow{k_3} Mo_b^{V} \end{array}$$

Figure 5.3: An Example of a Square Scheme for a One Electron Electrochemical Process. 231

themselves have become more negative by 60 mV and 16 mV, respectively. Whether this difference is due to a more indirect effect — going through the ligand scaffold and up into the metal centre — or more direct — a consequence of the missing interactions between the molybdenum/sulphurs and the hydrogen atoms of the hydroxy group — is hard to determine, but the electron-withdrawing proton relay definitely influences the behaviour of the molybdenum redox couples.

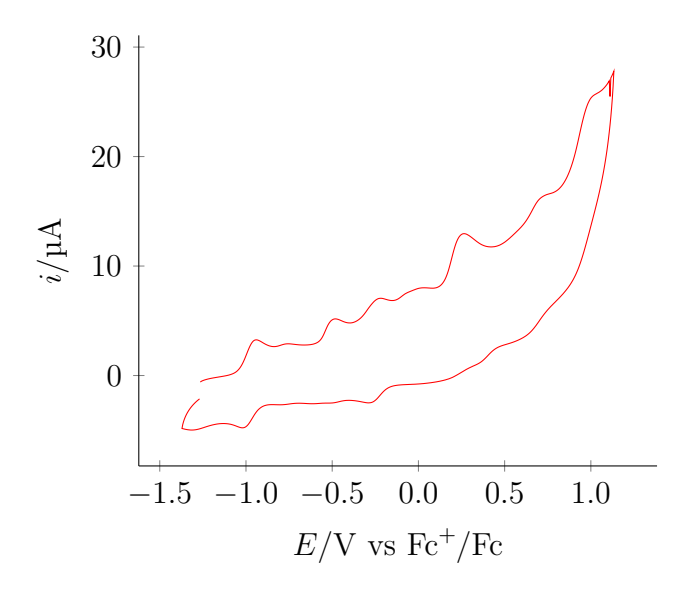


Figure 5.4: The Cyclic Voltammogram of **78** in MeCN/NBu₄BF₄ (0.11 M) at $50\,\mathrm{mV\,s^{-1}}$ Using an Unmodified Glassy Carbon Electrode. The Potentials were Internally Referenced to the Fc/Fc* Couple.

The CV of 78 has many more features occurring in the oxidative wave, for example, waves occurring at $-0.508\,\mathrm{V}$ and $0.253\,\mathrm{V}$. These are likely due to the redox capabilities of the dithiolene ligand. As to why these features are not present for 30 one can postulate that without the electron-withdrawing effect of the benzyl alcohol, the phenyl substituent to the dithiolene can form resonance structures with the dithiolene; these electrochemical changes are then seen in the CV. 232

For the $\mathrm{Mo^{IV}/Mo^{V}}$ redox couple for 78, just by inspection it is clear that the first wave is fully reversible. The second wave corresponding to the $\mathrm{Mo^{V}/Mo^{VI}}$

couple at $-0.245\,\mathrm{V}$ is more difficult to identify because of its proximity to other features in the oxidative path. Again, a plot of peak current against scan rate, Figure 5.5, shows that the current response is linear but the magnitude of the response differs from the oxidative and reductive scans. However, this difference in magnitude is less pronounced than the $\mathrm{Mo^V/Mo^{VI}}$ couple for 30, following the trend of more conserved systems tending to have a reversible $\mathrm{Mo^V/Mo^{VI}}$ couple. Therefore, this couple can be assigned the reversible designation.

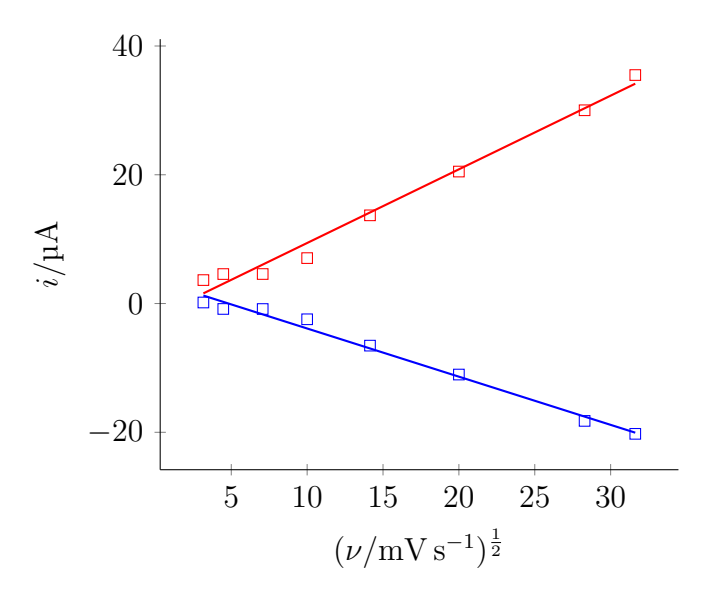


Figure 5.5: A Plot of Peak Current Against the Square Root of the Scan Rate for the Redox Process at $-0.245\,\mathrm{V}$ of **78** in MeCN/NBu₄BF₄. The Red Squares are for Oxidation Waves and The Blue Squares are for Reduction Waves.

5.4 Cyclic Voltammetry of

$(\mathrm{Et_4N})_2[\mathrm{MoO}(\mathrm{S_2C_2HBnOH})_2]$

Studying the electrochemistry of 80, Figure 5.6, allows us to see the influence of swapping the methyl substituent with a hydrogen. The $\mathrm{Mo^{IV}/Mo^{V}}$ and $\mathrm{Mo^{V}/Mo^{VI}}$ couple saw significant shifts in potential with values of $-0.874\,\mathrm{V}$ and $-0.217\,\mathrm{V}$,

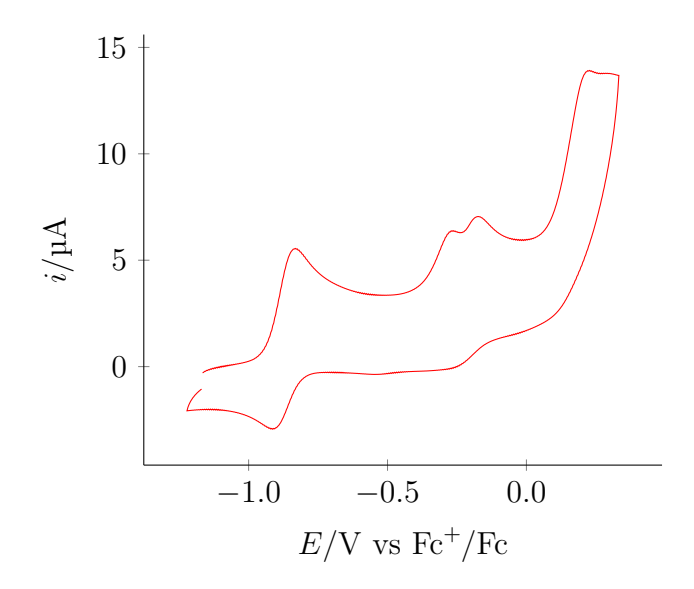


Figure 5.6: The Cyclic Voltammogram of 80 in MeCN/NBu₄BF₄ (0.1 M) at $50 \,\mathrm{mVs^{-1}}$ Using an Unmodified Glassy Carbon Electrode. The Potentials were Internally Referenced to the Fc/Fc* Couple.

respectively, moving approximately 50 mV each. The peaks were separated by 656 mV, a similar value to the methyl substituted analogue. The lack of a significant change in the peak separation perhaps indicates that the secondary substituent is less influential on the redox chemistry of the metal centre as it affects both couples equally. However, the redox couples themselves have been shifted to more positive values in comparison with the methyl substituted complex. This highlights the electron donating effect of the methyl substitutent as without electron density being directed towards the metal centre through the dithiolene ligands, the redox couples reflect this loss by becoming more positive.

The most dramatic change in this series of cyclic voltammograms can be seen in the shape of the Mo^{IV}/Mo^V couple, now reminiscent of the ferrocene/ferrocenium couple with regards to how reversible the shape of the wave appears and how tight the oxidation/reduction peaks are to each other (70 mV). This increased reversibility when compared with the Mo^{IV}/Mo^V couple of the other complexes

could be because of fewer moieties present on the ligand (the methyl group is no longer present); such a wave is seen when the **36** system is investigated as the proton groups are likely to move quickly when a change in geometry is needed to satisfy the new oxidation state. The reversibility of the Mo^V/Mo^{VI} couple is more difficult to determine via inspection. Plotting the peak current against scan rate, Figure 5.7, shows that the current response is linear for both oxidation and reduction waves; however, the magnitude of both responses clearly shows the Mo^V/Mo^{VI} couple is quasi-reversible (the absolute magnitudes of the slope for oxidation and reduction are not equal). Similar reasoning applied to **30** can be applied for **80**: the geometry rearrangement of going from Mo^{VI} to Mo^V causes a sluggish electron transfer. As to why the current peaks for the reduction wave are not equal in magnitude to the oxidation wave for the Mo^{IV}/Mo^V couple one could postulate that upon oxidation some of the newly formed Mo^{VI} species undergo a chemically irreversible change and are consumed at the electrode. Therefore, upon reduction a lower current response is seen as less material is available for reduction.

5.5 Cyclic Voltammetry of

 $(\mathrm{Et_4N})_2[\mathrm{MoO}(\mathrm{S_2C_2HPh})_2]$

Although previously prepared in the literature, complex 41 was examined electrochemically as a proof of concept for previous electrochemical experiments and to understand how this complex behaves in acetonitrile since it was previously reported in dimethylformamide (DMF) (Figure 5.8).¹⁰¹ The potential of the $\mathrm{Mo^{IV}/Mo^{V}}$ couple measured in acetonitrile differed significantly from the DMF reported value of $-0.86\,\mathrm{V}$ appearing at $-0.908\,\mathrm{V}$; the $\mathrm{Mo^{V}/Mo^{VI}}$ couple was unreported in the literature (including the CV itself) but occurred at $-0.217\,\mathrm{V}$ in acetonitrile. Peak

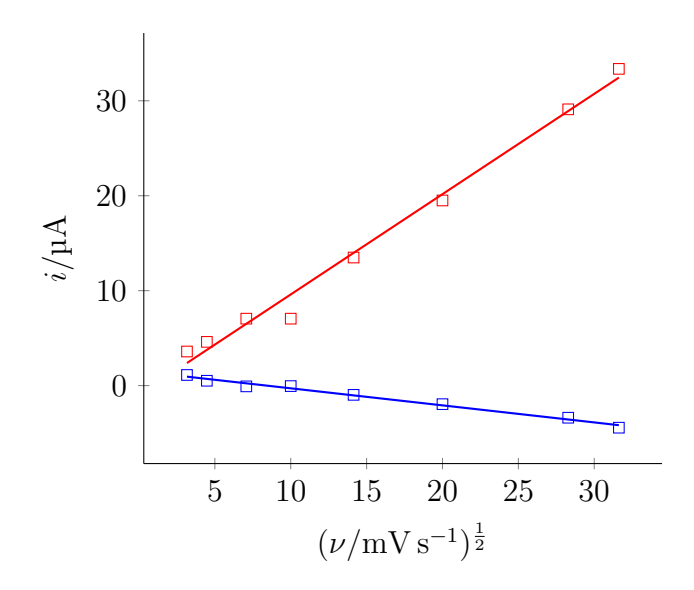


Figure 5.7: A Plot of the Peak Current Against the Square Root of Scan Rate for the Redox Process at $-0.217\,\mathrm{V}$ of **80** in MeCN/NBu₄BF₄. The Red Squares are for Oxidation Waves and the Blue Squares are for Reduction Waves.

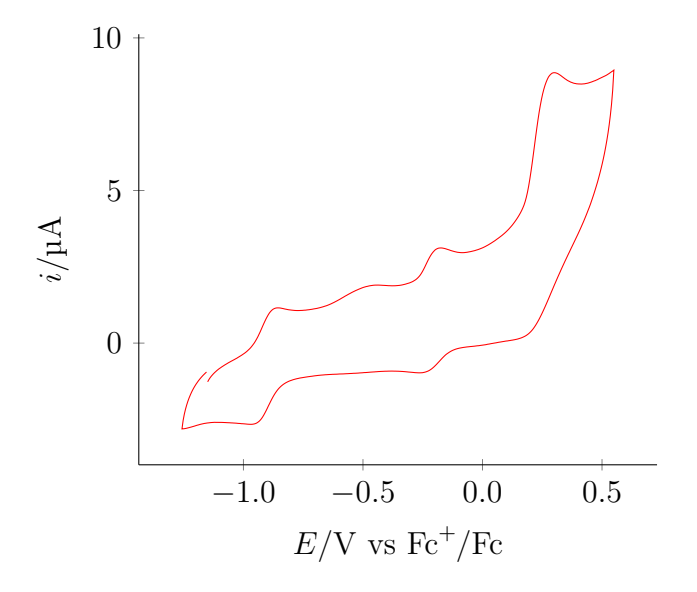


Figure 5.8: The Cyclic Voltammogram of 41 in MeCN/NBu₄BF₄ (0.1 M) at $50\,\mathrm{mVs^{-1}}$ Using an Unmodified Glassy Carbon Electrode. The Potentials were Internally Referenced to the Fc/Fc* Couple.

separation was recorded at 691 mV again showing that the hydroxy group does influence the redox activity of the metal centre. The potential of both of the redox couples was more negative than the hydroxy functionalised analogue, suggesting that the proton relay does have an electron-withdrawing effect on the metal centre.

The number of secondary features found on the oxidative path of the CV is noticeably less than when compared to the methyl substituted analogue. These peaks were previously attributed to the dithiolene ligand, so, when the methyl group is no longer present, and these peaks no longer occur, it means that the dithiolene redox processes cannot occur. Perhaps the electron inductive effect of the methyl group is instrumental in stabilising the dithiolene to allow different redox states to be achieved.

By inspection it is difficult to identify, in acetonitrile, whether the Mo^{IV}/Mo^V couple was indeed reversible and the Mo^V/Mo^{VI} couple is irreversible since one would argue that at a glance, the Mo^V/Mo^{VI} couple was reversible due to its similar appearance to the Mo^{IV}/Mo^V peak. The fact that not even an image of the CV exists in the literature does not help assuage fears of mischaracterising the couples. Therefore, for both, the peak current was plotted against the square root of the scan rate showing linear responses for each plot (Figure 5.9 and Figure 5.10); the magnitudes of the plots are also symmetric enough to make a clear-cut characterisation difficult. The peak separations are also within the tolerance to be considered reversible. Fortunately, the shape of the peaks offers enough of a clue for a characterisation to be made. The classic 'duck' shape of a reversible peak is much more pronounced in the Mo^{IV}/Mo^V couple than the Mo^V/Mo^{VI} couple indicating that they are assigned reversible and quasi-reversible, respectively.

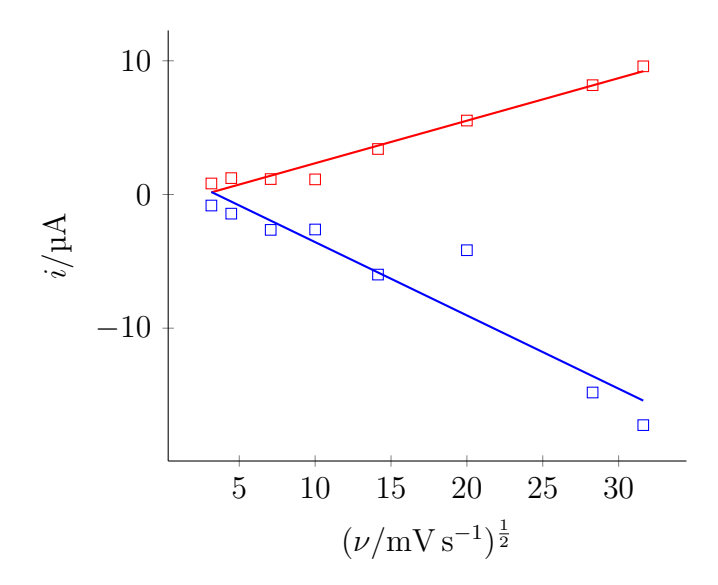


Figure 5.9: A Plot of the Peak Current Against the Square Root of the Scan Rate for the Redox Process at $-0.908\,\mathrm{V}$ of 41 in MeCN/NBu₄BF₄. The Red Squares are for Oxidation Waves and The Blue Squares are for Reduction Waves.

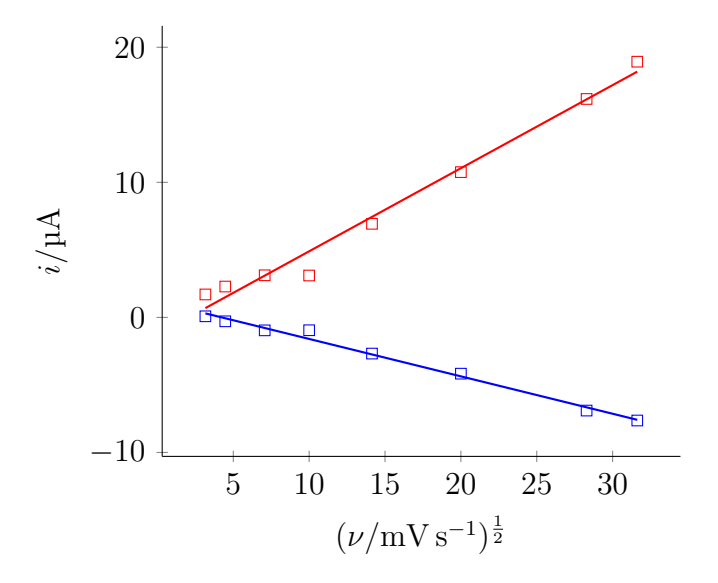


Figure 5.10: A Plot of the Peak Current Against the Square Root of the Scan Rate for the Redox Process at $-0.217\,\mathrm{V}$ of 41 in MeCN/NBu₄BF₄. Red Squares are for Oxidation Waves and Blue Squares are for Reduction Waves.

5.6 Cyclic Voltammetry of

$Mo(CO)_2(S_2C_2MeBnOH)_2$

Even more scarce in the literature are the molybdenum dithiolene complexes with carbonyl moieties coordinated at the terminal position; the majority of the synthesised complexes belong to Holm's portfolio of research. Within the group, electrochemical studies on 22 have been previously reported (Figure 5.11). The CV reveals two reversible waves occurring at $-1.45\,\mathrm{V}$ and $-0.95\,\mathrm{V}$ for the $\mathrm{Mo^{IV}/Mo^{V}}$ than the $\mathrm{Mo^{V}/Mo^{VI}}$ respectively, separated by $467\,\mathrm{mV}$. This value is $100\,\mathrm{mV}$ less than that of the simple dithiolenes reported by the Holm group. This contraction highlights the influence of the ligand substituents on the dithiolene ligand.

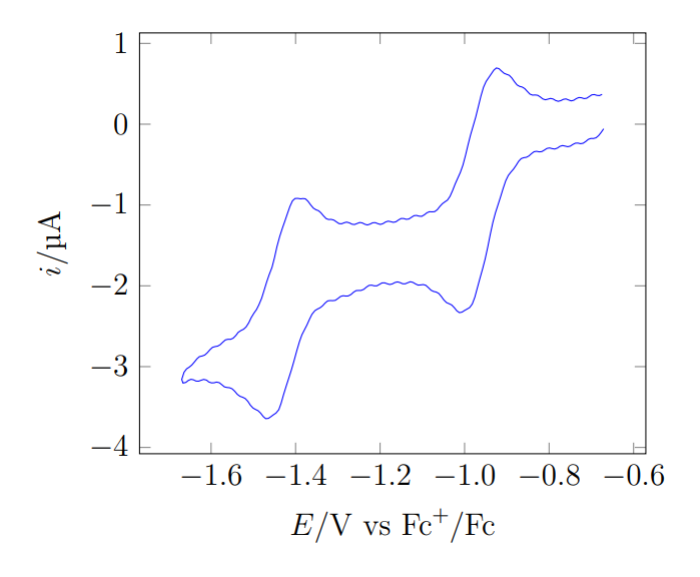


Figure 5.11: The CV of $Mo(CO)_2(S_2C_2MeBnOH)_2$ (22) in CH_2Cl_2/NBu_4BF_4 (100 mm) at 25 mV s⁻¹. Reproduced with Permission from Reference [146].

This carbonyl system shows a stark difference when compared to its oxo functionalised analogue. For both redox couples, their potentials have become much more negative, shifting by 534 mV and 721 mV respectively; the peak separation

is also contracted by 200 mV. This shows that the two carbonyl ligands induct much more electron density than the oxo ligand. That both redox couples are reversible is an interesting difference. It stands to reason that the geometries of the complex remain largely unchanged upon oxidation/reduction to allow rapid electron transfer.

5.7 Cyclic Voltammetry of $(Et_4N)_2[WO(S_2C_2MeBnOH)_2]$

With the synthesis of the novel tungsten analogue of the target complex (90), it is possible to investigate, via cyclic voltammetry, the influence a change of the metal centre has on the redox properties of the complex (Figure 5.12). The W^{IV}/W^{V} and W^{V}/W^{VI} redox couples occurred at $-1.11\,V$ and $-0.413\,V$, respectively, with a peak separation of 700 mV, a slight increase of 30 mV when compared with the molybdenum analogue.

The W^{IV}/W^V wave is clearly reversible by inspection, following the similar behaviour seen for the molybdenum analogues. Again, determining the nature of the W^V/W^{VI} couple is much less transparent. The plot of the square root of the scan rate against the peak current demonstrates that there is a stark difference in magnitude between the forward and reverse waves, despite maintaining a linear relationship (Figure 5.13). The peak separation between the oxidation and reduction waves also exceeds the tolerance of what can be considered experimentally reversible. One can conclude that the W^V/W^{VI} couple is irreversible, a result of slow electron transfer. Perhaps an irreversible chemical change occurs when the complex is oxidised from W^V to W^{VI} resulting in less material present for the reverse reduction, resulting in a drop in the observed current.

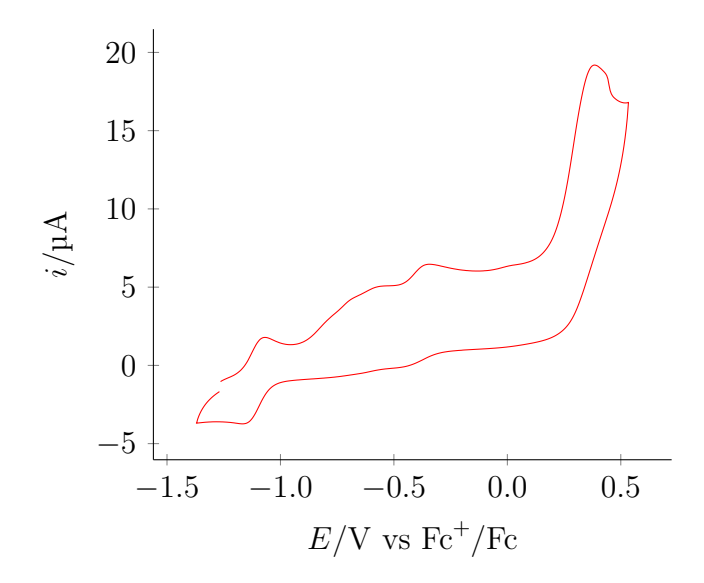


Figure 5.12: The Cyclic Voltammogram of $\bf 90$ in MeCN/NBu₄BF₄ (0.1 M) at $50\,\mathrm{mVs^{-1}}$ Using an Unmodified Glassy Carbon Electrode. The Potentials were Internally Referenced to the Fc/Fc* Couple.

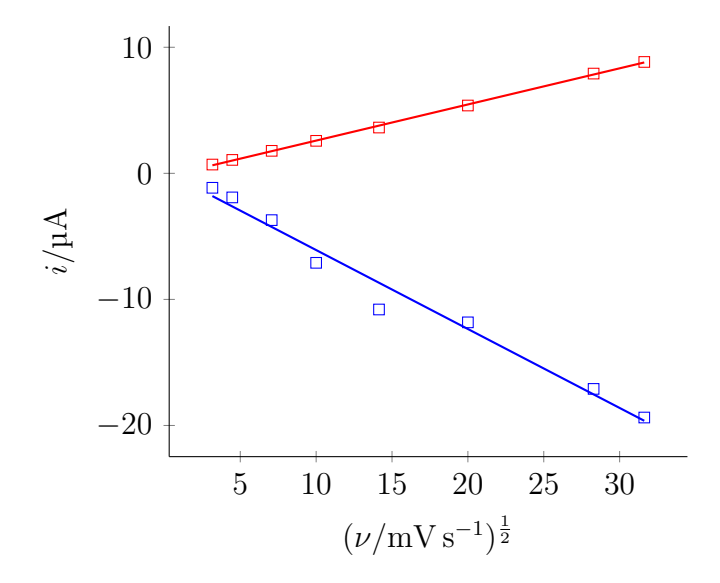


Figure 5.13: A Plot of the Peak Current Against the Square Root of the Scan Rate for the Redox Process at $-0.413\,\mathrm{V}$ of $\mathbf{90}$ in MeCN/NBu₄BF₄. The Red Squares are for Oxidation Waves and The Blue Squares are for Reduction Waves.

5.8 Summary

Using cyclic voltammetry, the electrochemical properties of a variety of synthesised complexes have been investigated. From these experiments, we can begin to build an understanding of the structure-activity relationship between the substituents of the dithiolenes and the metal centre. Table 5.4 summarises these findings.

Table 5.4: A Summary of the Electrochemical Properties of the Synthesised Complexes. ^b Quasi-reversible. ^c Irreversible.

Complex	$E_{1/2}$	(V)
		Mo ^V /Mo ^{VI}
$\frac{\text{(Et}_{4}N)_{2}[\text{MoO}(S_{2}C_{2}\text{MeBnOH})_{2}]} (30)$	-0.916	-0.229^{-b}
$(Et_4N)_2[MoO(S_2C_2MePh)_2]$ (78)	-0.975	-0.245
(Et4N)2[MoO(S2C2HBnOH)2] (80)	-0.874	-0.217^{-b}
$(Et_4N)_2[MoO(S_2C_2HPh)_2]$ (41)	-0.908	-0.217^{-b}
$Mo(CO)_2(S_2C_2MeBnOH)_2$ (22)	-1.45	-0.95
$(\mathrm{Et_4N})_2[\mathrm{WO}(\mathrm{S_2C_2MeBnOH})_2] \ (90)$	-1.11	-0.413 ^c

The most dramatic effects to the potential of the redox couples is seen when the terminal functional groups are changed followed by a change in the 'primary' substituents of the dithiolene (the immediate group adjacent to the carbon of the dithiolene, for example, a methyl or proton). The proton relay shifts the redox potential positively indicating they have electron-withdrawing character. As expected, the more electron-dense tungsten metal centre gives more negative redox potentials but sacrifices the quasi-reversibility of the V/VI couple. The more constrained the system, the more reversible the associated couples were, indicating that, according to Marcus' theory, the speed at which the geometrical rearrangement of the dithiolene ligands occurs is heavily influenced by the size of the ligand.

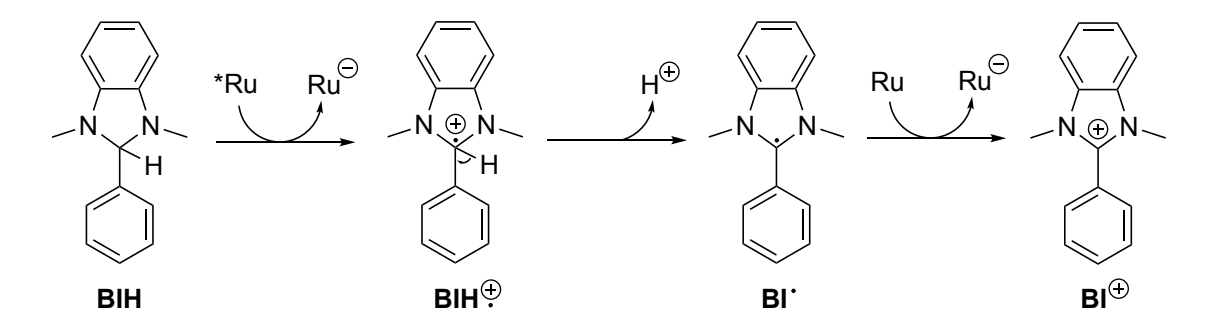
Chapter 6

Catalysis

6.1 Introduction

Over the 60 years of bio-mimetic DMSOR/FDH, oxo-molybdenum bis-dithiolene complexes, starting in 1968, only a handful have been tested as catalysts for their catalytic reduction properties: 10, 11, and 12. The rest have had some investigations into their ability as oxygen atom transfer systems. Fontecave and co-workers were the first to report a molybdenum-oxo bis-dithiolene complex as a catalyst for the electro- and/or photo-reduction of protons and carbon dioxide. ^{103,112} For their photocatalytic studies, the reaction conditions were defined according to the standard conditions and reagents developed by Ishitani and co-workers for testing the carbon dioxide catalytic reduction abilities of a Re—Ru catalyst: a photosensitiser, a sacrificial electron/proton donor, and a base. ²³³ The photosensitiser is a complex that absorbs photons, and in this case, [Ru(bpy)₃]Cl₂ is utilised; the sacrificial electron/proton donor 1,3-dimethyl-2-phenyl-2,3-dihydro-1*H*-benzo[d]imidazole (BIH) performs like its namesake and produces electrons and protons, working in conjunction with a base (B).

All three are necessary to produce the electrons and protons necessary for



Scheme 6.1: The Electron Transfer Mechanism for BIH.²³³

photocatalysis. Scheme 6.1 shows how the ruthenium complex initially absorbs a photon, resulting in a singlet metal-to-ligand-charge-transfer (MLCT) excited state ¹(*Ru). Intersystem crossing occurs to generate the triplet state ³(*Ru). Reductive quenching of this triplet state by BIH releases an electron. BIH is now positively charged and a proton is lost to the base, giving a radical BIH and a charged base B⁺. The BIH intermediate is extremely reducing, so the radical electron is easily lost through an electron transfer.

The compounds 10, 11 and 12 each gave different TONs with respect to formate, carbon monoxide, and hydrogen production. Compound 10 had the largest cumulative TONs followed by 12 and then 11. Interestingly, the reverse is true for the complexes with the most CO₂ derived reduction products, that being 12, 11, and 10 (see Table 1.1 for specifics).¹⁰³

Schulzke and co-workers investigated the oxygen atom transfer (OAT) catalysis of their novel complex $\bf 6$ by using the model OAT reaction developed by Berg and Holm in 1985. 104,234 The reaction involves the OAT from dimethyl sulphoxide (DMSO) to the catalyst and then to an acceptor like triphenylphosphine (PPh₃) to give triphenylphosphine oxide (PPh₃O). The reaction proceeded very slowly with a maximum conversion of 93% of 9 mM over approximately 60 hours. When trimethylamine N-oxide (Me₃NO), a stronger oxidiser, was used instead of DMSO, there was a 37% conversion of PPh₃O in 15 hours. Through the use of UV/VIS

spectroscopy, Schulzke reasoned that the inert $\text{Mo}^{\text{V}}_{2}\text{O}_{3}$ species was forming, resulting in the slow conversion times recorded.

The complexes synthesised in previous chapters were tested as photocatalysts for the reduction of carbon dioxide to formate, carbon monoxide, and hydrogen and as pure proton reduction catalysts using cyclic voltammetry. The carbon dioxide to formate reaction is a reversible process in nature, so complexes were also tested as oxidation catalysts of formate. The OAT catalysis ability of these complexes was also investigated.

6.2 Reduction Catalysis

6.2.1 Electrocatalytic Reduction of Protons to Hydrogen

One of the main aims of this thesis was to examine the synthesised transition metal complexes' ability to act as reduction catalysts, more specifically with regards to the reduction of carbon dioxide to formate. However, Fontecave and co-workers have noted that these molybdenum-oxo bis-dithiolene complexes can reduce carbon dioxide to carbon monoxide and the sacrificial protons to hydrogen gas. Using cyclic voltammetry, by observing changes in the catalytic wave, depending on the substrate added, one can begin to understand the selectivity of the catalyst towards proton and carbon dioxide reduction.

The addition of equivalents of trifluoroacetic acid (TFA) to a solution of 30 in acetonitrile unfortunately showed the immediate decomposition of the *bis*-complex. When observing Figure 6.1 one can see that after the addition of 5 equivalents of TFA, the easily identifiable Mo^{IV}/Mo^V and Mo^V/Mo^{VI} couple are no longer present. This is in contrast to what is observed when the same experiment is performed for 22 where the peak shapes are conserved. Such behaviour indicates that the oxo terminal functionality results in a complex much more sensitive to changes

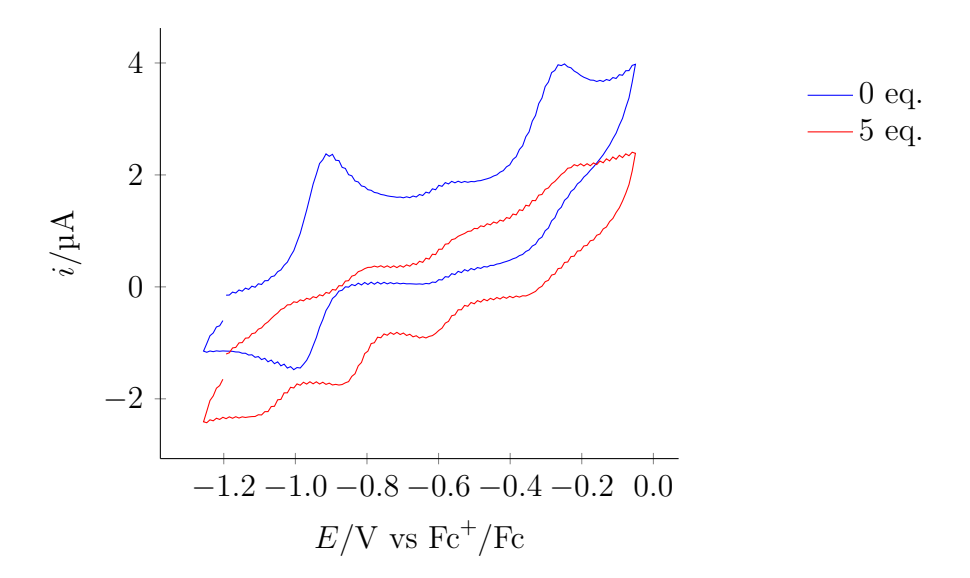


Figure 6.1: Cyclic Voltammograms of 30 in MeCN/NBu₄BF₄ (0.1 M) in the Presence of Varying Amounts of Trifluoroacetic Acid at $100 \,\mathrm{mV \, s^{-1}}$.

in pH. This sensitivity to acidity was observed when **78** was also tested, as the CV immediately changed to a shape analogous to what is seen for **30** upon the addition of TFA.

The electrocatalytic carbon dioxide reduction capabilities of these complexes were also investigated through cyclic voltammetry. Cyclic voltammograms of **30** were taken in argon and carbon dioxide saturated solutions (with a proton source of 2,2,2-trifluoroethanol) to examine if a catalytic wave appeared with regard to carbon dioxide reduction. Unfortunately, there was no difference in the currents of either cyclic voltammogram which suggests that no catalysis was occurring.

6.2.2 Photocatalytic Reduction of Carbon Dioxide to Formate

To a 4 mL Young's tap quartz cuvette, the photosensitiser ($[Ru(bpy)_3]Cl_2$, 0.5 mM), the base, triethanolamine, and carbon dioxide saturated acetonitrile (1 : 5, v/v),

the sacrificial proton and electron donor (BIH, Scheme 6.1, 0.1 M) and the catalyst (30, 0.05 mM) were added. This solution was irradiated for 15 hours using a xenon lamp (400 nm–1200 nm). After the 15 hours, there were no obvious changes to the solution. A sample of the cuvette head space was taken and run through a gas chromatography machine to test for carbon monoxide and hydrogen production. To test for formate production, a sample of the solution was passed through an ion exchange chromatography system. In terms of gases, none were observed as having been produced. However, it can not be said with absolute certainty that no gas was produced as it must be noted that the machine has a detection limit of 0.5 µmol for hydrogen and 8.2 µmol for carbon monoxide. Therefore, any gases produced at an amount lower than this detection limit would not be detected. Formate was detected, but this was in line with the amount generated in the blank run; this was likely produced from the [Ru(bpy)₃]Cl₂, a complex previously reported for its capabilities in CO₂ to HCOO⁻ reduction. Similar results were obtained in experiments with complex 78.

6.3 Oxidation Catalysis

In terms of reduction catalysis, both 30 and 78 had failed to show any signs of activity. However, one must remember that formate dehydrogenase catalyses the inter-conversion of carbon dioxide and formate. Since no reduction activity has been seen, going from carbon dioxide to formate, it was still worth investigating the oxidative abilities of these complexes. DuBois and co-workers focused on nickel-based catalysts for formate oxidation, where, from a series of cyclic voltammograms,

they were able to determine the turnover frequency (TOF) of their catalysts.

$$i_{\text{cat}} = n_{\text{cat}} FA[\text{catalyst}] (Dk[HHCO_2^-]^x)^{1/2}$$
(6.1)

$$i_{\rm p} = 0.4463 \left(\frac{F^3}{RT}\right)^{1/2} n_{\rm p}^{3/2} A D^{1/2} [{\rm catalyst}] \nu^{1/2}$$
 (6.2)

$$\frac{i_{\text{cat}}}{i_{\text{p}}} = \frac{n_{\text{cat}}}{0.4463} \sqrt{\frac{RT}{F\nu n_{\text{p}}^3}} \sqrt{k[H\text{HCO}_2^-]^x}$$
 (6.3)

$$TOF = k[HHCO_{2}^{-}]^{x} = \frac{F\nu n_{p}^{3}}{RT} \left(\frac{0.4463}{n_{cat}}\right)^{2} \left(\frac{i_{cat}}{i_{p}}\right)^{2}$$
(6.4)

The catalytic current enhancement, $i_{\rm cat}/i_{\rm p}$ (current in the presence and absence of catalyst, respectively), can be converted into a catalytic rate using Equations 6.1–6.4. Dividing Equation 6.1 by Equation 6.2 handily eliminates the area of the electrode (A), the diffusion coefficient (D), and the concentration of the catalyst; this results in Equation 6.3 where the catalytic rate enhancement is expressed in terms of the number of electrons in the catalytic process $(n_{\rm cat})$, the universal gas constant (R), the temperature in kelvin (T), Faraday's constant (F), the scan rate in V s⁻¹ (ν) , the number of electrons in the absence of the substrate $(n_{\rm p})$ and the observed rate constant for the catalytic reaction (k). Rearranging Equation 6.3 to Equation 6.4 allows one to determine the turnover frequency.^{235–238}

Determining the parameters of the above, specifically $n_{\rm cat}$ and $n_{\rm p}$, is performed through inspection of the CV and knowledge of the reaction that is being catalysed. As mentioned above $n_{\rm p}$ and $n_{\rm cat}$ denote the number of electrons transferred for the wave with and without the presence of the substrate. With regards to the electrochemical behaviour observed in the cyclic voltammograms for both 30 and 78, $n_{\rm p}$ can be given the value of one. This is because one must assume that this wave is representative of the one electron oxidation of the ligand, its presence highlighting the redox non-innocence of the dithiolene (Figure 1.6). The theoretical oxidation of formate by catalysts 30 and 78 results in carbon dioxide, a proton,

and two electrons; therefore, n_{cat} has a value of two.

6.3.1 The Synthesis of Tetrabutylammonium Formate

Formate itself is clearly an anion. This implies a cation is necessary to balance the charge of the molecule. The most recognisable cation would be a proton to produce the formic acid molecule. Although formic acid is soluble in acetonitrile, one must remember how sensitive the Mo=O bond of these complexes is to changes in acidity as evidenced by earlier incidences where hydrochloric acid and trifluoroacetic acid were present and ultimately resulted in the oxidation of the complex. The exact mechanism by which this occurs is currently unknown. However, looking at the DMSO reductase enzyme mechanism (Scheme 1.3) offers a potential insight. In that mechanism, the active site is subject to two protonations and electron transfers. From this, it is not unreasonable to assume a similar process occurs when 30 is subject to acidic conditions: the Mo^{IV}=O is protonated twice, giving Mo^V-OH and then Mo^{VI} + H₂O. This new Mo^{VI} electrophile scavenges a dithiolene from an adjacent unit to balance the charge of the complex, generating the Mo^{VI} (dithiolene)₃ complex. Fortunately, cations are not limited to just protons, and other less acidic analogues can be explored.

Scheme 6.2: The Synthesis of $NBu_4HCO_2 \cdot HCO_2H$ (92).

DuBois and co-workers similarly wished to avoid using formic acid as their

formate carrier because of the potential variability of electrocatalytic rates with water concentration in the formic acid. 142,238 The solution to this was to synthesise an ammonium analogue of formic acid, tetrabutylammonium formate. The synthesis was straightforward (Scheme 6.2). This salt was obtained by adding formic acid to aqueous tetrabutylammonium hydroxide, followed by extraction in ethyl acetate and recrystallisation.

The salt was characterised by ¹H and ¹³C NMR spectroscopy. DuBois and co-workers noted through XRD and ¹H NMR spectroscopy that each formate and formic acid pair shares one proton, which appears at 18.7 ppm in the ¹H NMR spectrum in CD₃CN. Although this salt is slightly acidic due to this proton (between a pH of 6.0 and 6.5), fortunately **30** did not oxidise in the presence of NBu₄HCO₂·HCO₂H and, therefore, the complex is tolerable to this level of acidity.

6.3.2 Electrocatalytic Oxidation of Formate using $(Et_4N)_2$ $[MoO(S_2C_2MeBnOH)_2]$

Figure 6.2 shows cyclic voltammograms of $(Et_4N)_2[MoO(S_2C_2MeBnOH)_2]$ (30) with varying concentrations of 92. As previously noted in Chapter 5, the reversible wave at $-0.916\,\mathrm{V}$ belongs to the $\mathrm{Mo^{IV}/Mo^{V}}$ couple and the quasi-reversible wave at $-0.229\,\mathrm{V}$ corresponds to the $\mathrm{Mo^{V}/Mo^{VI}}$ couple. The magnitude of either peak remained unchanged, whereas the current of the ligand peak at $0.255\,\mathrm{V}$ increased with subsequent additions of formate. Since formate oxidation would release electrons, this increase in current implies that formate oxidation does not occur at the metal centre but on the ligand (Equation 1.1).

As mentioned above, using the data obtained from a cyclic voltammogram in combination with Equation 6.4, the turn over frequency at varying **92** equivalents can be obtained. Plotting these TOF values against the change in formate concentration allows one to investigate the kinetics of the catalyst **30**, shown in

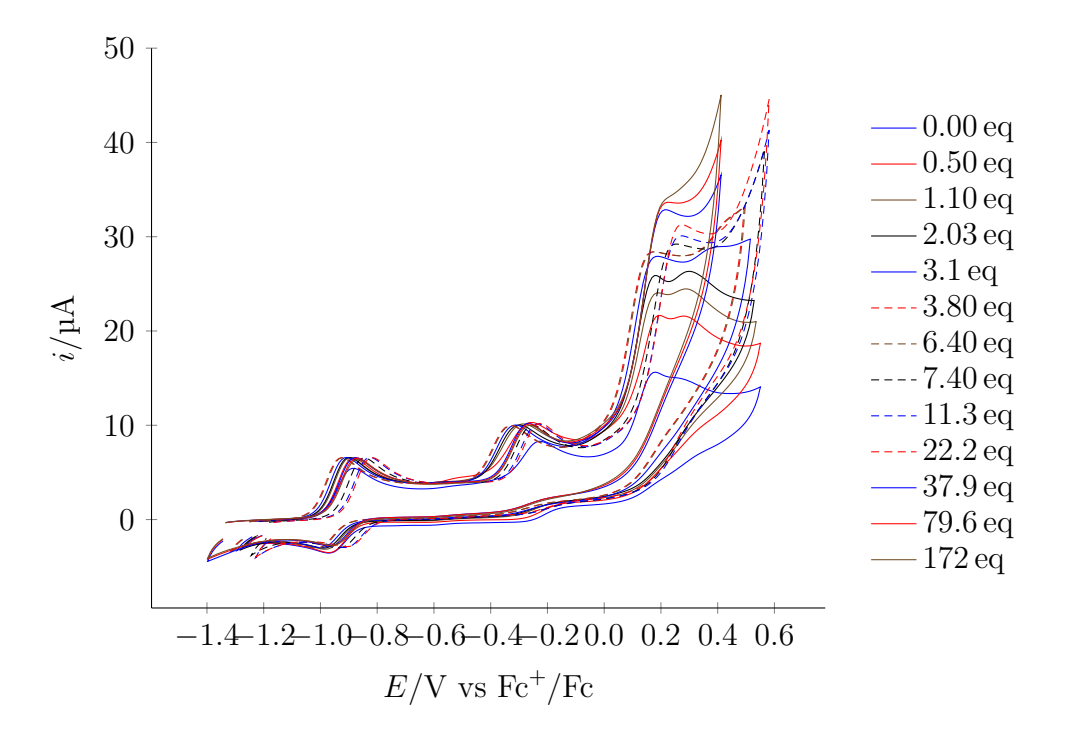


Figure 6.2: The Cyclic Voltammograms of $\bf 30~(0.05~mM)$ in MeCN/NBu₄BF₄ (0.1 M) in the Presence of Varying Equivalents of Tetrabutylammonium Formate ($\bf 92$) at $100~mV~s^{-1}$.

Figure 6.3. Up to 3.1 eq, there is a rapid increase in the TOF values in a linear fashion. However, after this concentration, current ceases to increase much more and stagnates at higher concentrations.

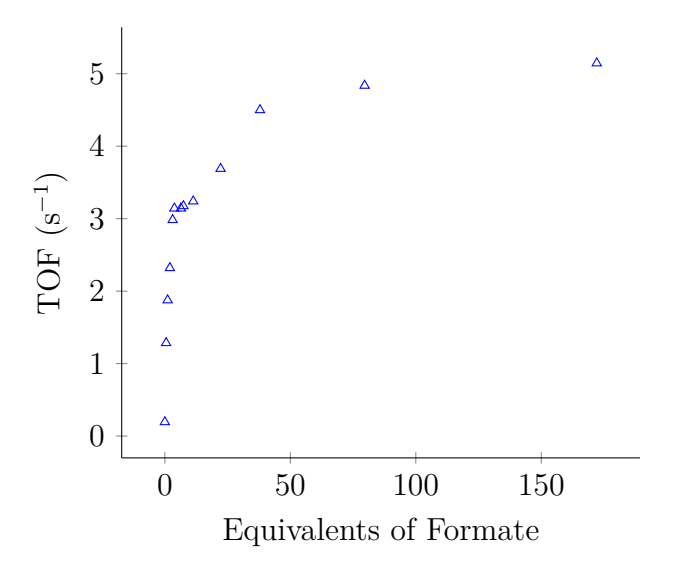


Figure 6.3: The Change in Turn Over Frequency of $30 (0.05 \,\mathrm{mM})$ as a Response to the Change in Concentration of Tetrabutylammonium Formate (92).

Figure 6.4 demonstrates how the cyclic voltammogram of an excess of tetrabutylammonium formate (92) responds to changes in the concentration for the catalyst 30. Just by inspection, it is clear that the catalytic wave, indicating formate oxidation, increases with catalyst concentration. Figure 6.5 describes how the catalytic wave current (i_{cat}) changes with varying concentrations of 30. The relationship is clearly linear and, therefore, it is first-order in catalyst.

Combining what has been learnt from Figure 6.3 and Figure 6.4 suggests that at low concentrations of formate, the rate-determining step is set by the reaction of the catalyst and formate, whilst at higher concentrations of formate the rate of reaction is still first-order with respect to the catalyst but becomes independent of formate concentration. Understanding the formate-independent region is difficult because of how the rate of increase in TOF drops off at higher concentrations.

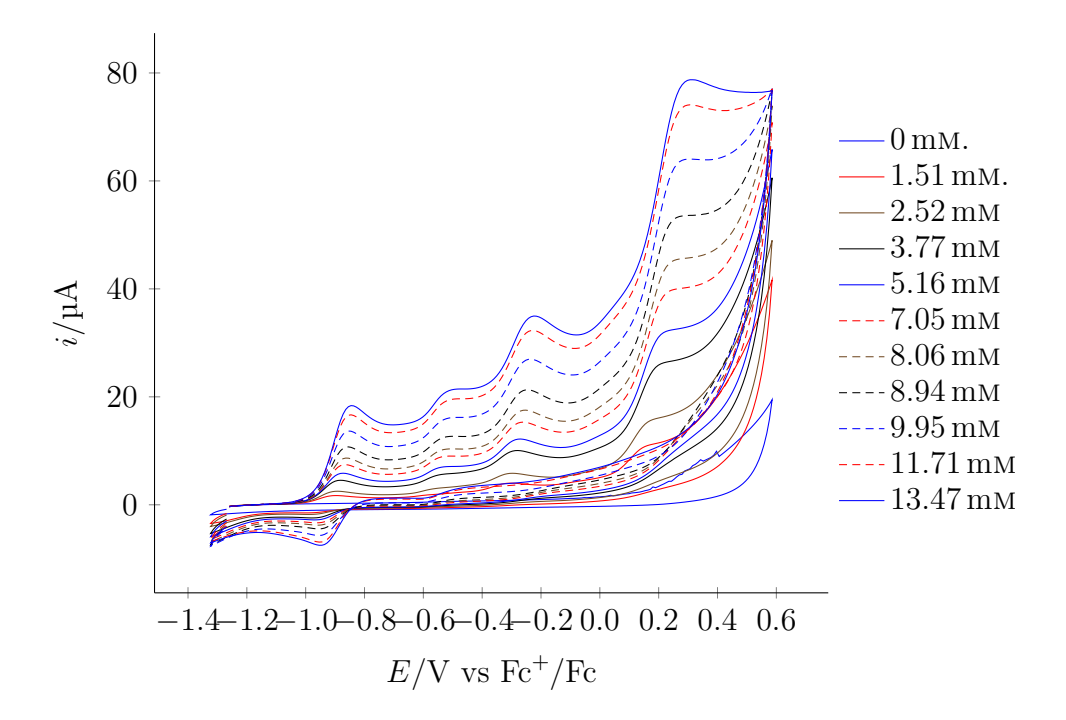


Figure 6.4: The Cyclic Voltammograms of Tetrabutylammonium Formate (92) (8.2 mm) with Increasing Concentrations of 30 in MeCN/NBu₄BF₄ (0.1 m) at $100\,\mathrm{mV\,s^{-1}}$.

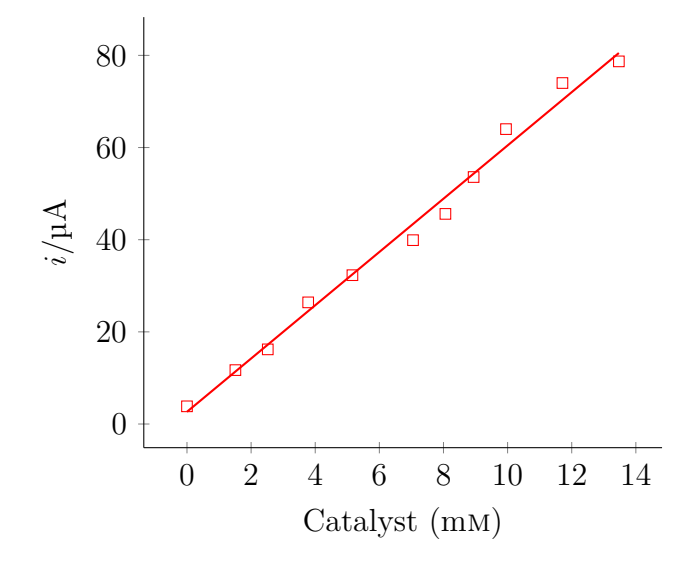


Figure 6.5: The Current Response to a Change in the Concentration of Catalyst **30** in a Solution of MeCN/NBu₄BF₄ (0.1 M) and Tetrabutylammonium Formate (**92**) (8.2 mM) at $100 \,\mathrm{mV \, s^{-1}}$.

This is likely because of catalyst inhibition since the rate begins to slow down, but the TOF does not decrease as a function of formate concentration. If catalyst poisoning were occurring, one would expect to see the TOF begin to decrease as the concentration of formate increases because more of the poison would be present. Perhaps a product from the oxidation of formate is blocking the site of catalysis, slowing down the kinetics. Further evidence to suggest that a product of formate oxidation is causing catalyst inhibition rather than any catalyst decomposition occurring is that in Figure 6.5 when catalyst concentrations are low and formate concentrations are high, no decomposition is visible in the CV.

6.3.3 Electrocatalytic Oxidation of Formate using $(Et_4N)_2$ $[MoO(S_2C_2MePh)_2]$

The complex (Et₄N)₂[MoO(S₂C₂MePh)₂] (78) was examined to investigate the influence the proton relays had on the catalysis of formate oxidation. Figure 6.6 shows the cyclic voltammograms of (Et₄N)₂[MoO(S₂C₂MePh)₂] (78) as a function of formate concentration. As previously noted in Chapter 5, the reversible wave at -0.975 V belongs to the Mo^{IV}/Mo^V couple and the quasi-reversible wave at -0.245 V is assigned to the Mo^V/Mo^{VI} couple. Both waves maintain their shape as formate concentration increases, which implies that neither couple interacts directly with formate. However, the dithiolene/ligand wave at 0.246 V does see a current response with increases in formate concentration, giving more positive current values, matching the behaviour seen in 30. A positive increase in the current means that there is a surplus of electrons present; one can infer that these electrons are a result of formate oxidation (Equation 1.1).

Similarly to the analysis performed for 30, the catalytic current enhancement $(i_{\text{cat}}/i_{\text{p}})$ can be converted to the catalytic rate (TOF) using Equation 6.4. Figure 6.7 is a plot of the TOF of 78 versus the equivalents of tetrabutylammonium formate

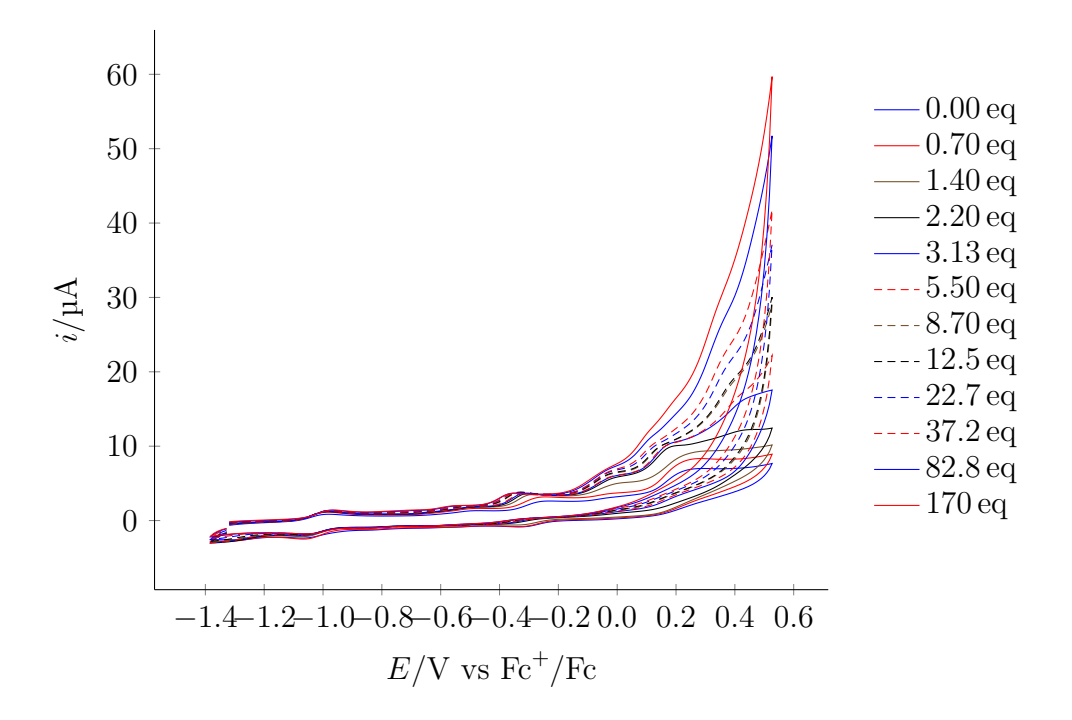


Figure 6.6: The Cyclic Voltammograms of **78** (0.05 mM) in MeCN/NBu₄BF₄ (0.1 M) in the Presence of Varying Amounts of Tetrabutylammonium Formate (**92**) at $100 \,\mathrm{mV}\,\mathrm{s}^{-1}$.

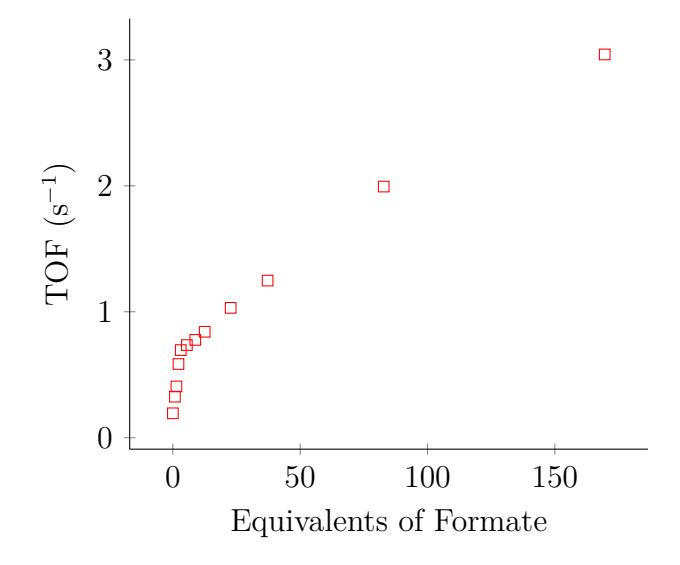


Figure 6.7: The Change in the Turn Over Frequency of **78** as a Function of the Change in Concentration of Tetrabutylammonium Formate (**92**) in a Solution of $MeCN/NBu_4BF_4$ (0.1 M) at $100\,mV\,s^{-1}$.

present in solution. To begin with, the TOF increases linearly in response to a change in the concentration of formate. However, from 3.1 eq this linear behaviour disappears as the electrode becomes flooded with **92**. An initial linear relationship implies first-order kinetics of TOF on formate concentration.

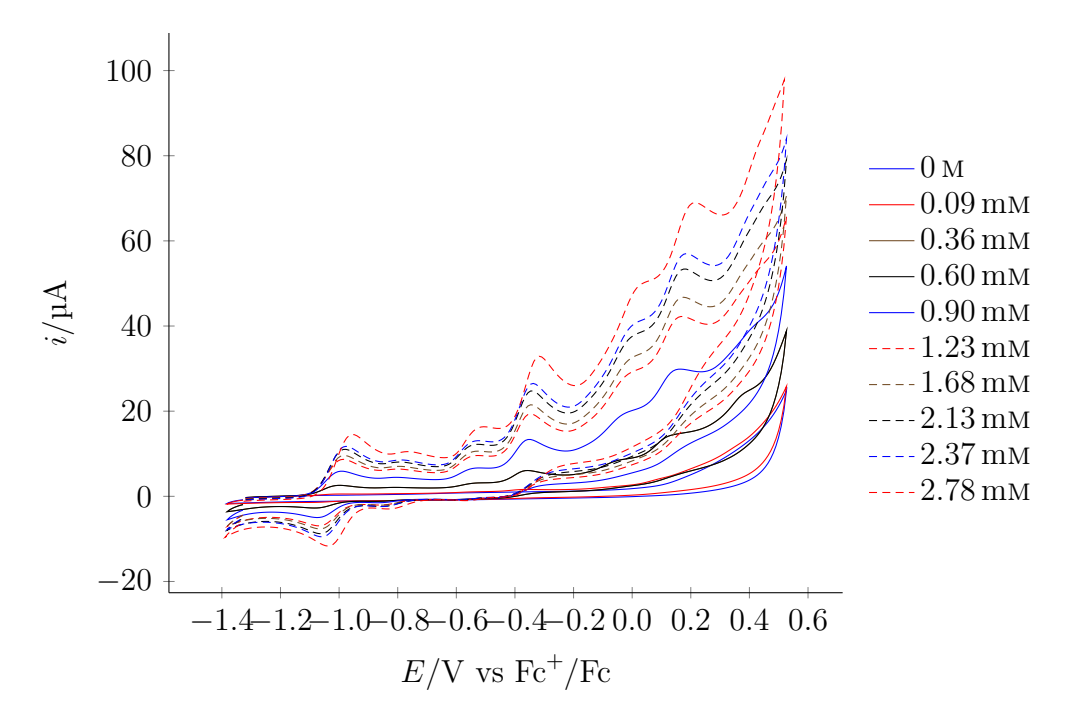


Figure 6.8: Cyclic Voltammograms of Tetrabutylammonium Formate (92) (8.2 mM) with Increasing Concentrations of 78 in MeCN/NBu₄BF₄ (0.1 M) at $100 \,\mathrm{mV \, s^{-1}}$.

Figure 6.8 shows the change in electrochemical behaviour of excess NBu₄HCO₂ · HCO₂H (92) in response to a change in the concentration of the catalyst 78. The catalytic wave indicating formate oxidation is shown to increase with increasing catalyst concentration. Figure 6.9 is a plot of the change in the current of the catalytic wave (i_{cat}) versus the change in the concentration of the catalyst in solution. The relationship between the two is quite clearly linear, suggesting the catalytic reaction is first-order in catalyst.

Similarly to what occurred for the oxidation of formate using **30** as the catalyst, the relationships shown in Figure 6.7 and Figure 6.9 describe that at low

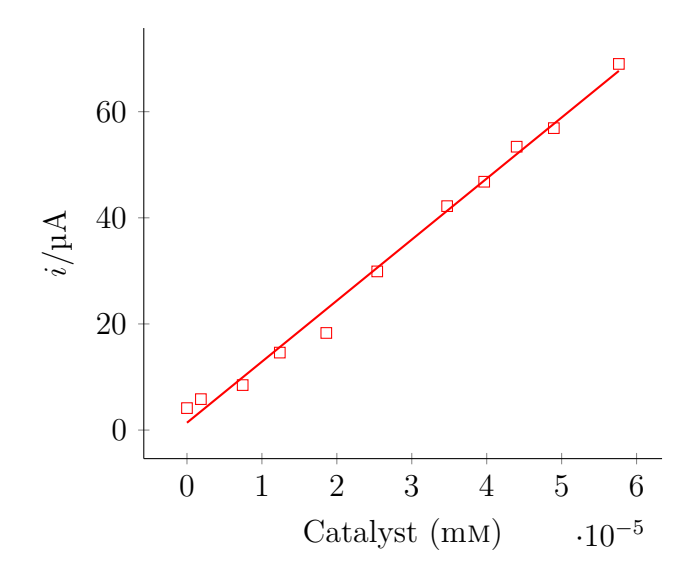


Figure 6.9: The Current Response to a Change in the Concentration of Catalyst **78** in a Solution of MeCN/NBu₄BF₄ (0.1 M) and Tetrabutylammonium Formate (**92**) (8.2 mM) at 100 mV s⁻¹.

concentrations, the rate-determining step is determined by the reaction of formate and the catalyst, whilst at higher concentrations of formate the reaction maintains first-order behaviour with respect to the catalyst but becomes independent of formate oxidation. As to why the TOF decays at higher concentrations, it is likely the same reason as for 30, that a product of formate oxidation inhibits catalysis. This can be reasoned from how the TOF increases from the previous measurement does not decrease, and how there is no catalyst decomposition present in the CV when the concentration of tetrabutylammonium formate far exceeds that of the catalyst.

6.3.4 The Effect of Proton Relays on Oxidation Catalysts

When one compares the cyclic voltammograms of 30 and 78 it is not immediately obvious the effect that proton relays have on the oxidative catalysis of formate. Both appear to show that catalysis occurs with or without the proton relays being

present, with catalysis occurring at the ligand scaffold rather than the metal.

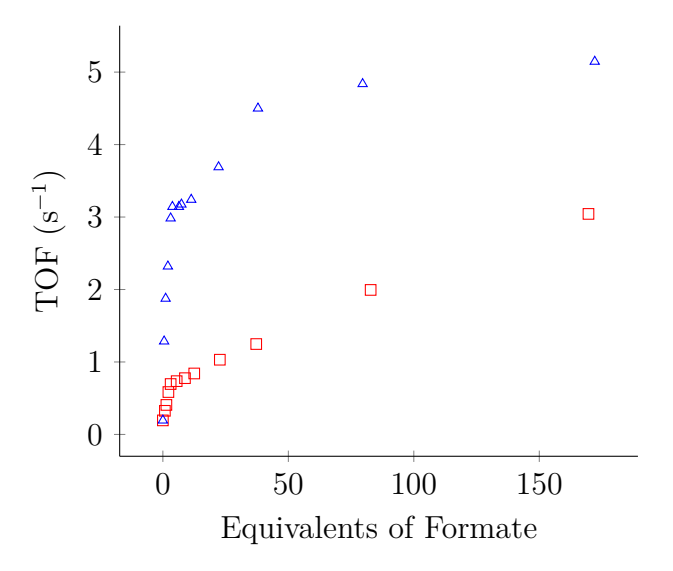


Figure 6.10: The Change in the Turn Over Frequency of **30** (Blue Triangles) and **78** (Red Squares) (0.05 mM) as a Function of the Change in Equivalents of Formate in a Solution of MeCN/NBu₄BF₄ (0.1 M) at $100 \,\mathrm{mV \, s^{-1}}$.

The comparative plot shown in Figure 6.10 is simply Figure 6.3 and Figure 6.7 layered on top of each other. This plot clearly shows the influence that the addition of a proton relay to the ligand scaffold has on the TOF with regard to the oxidation of formate. This improvement can be seen in both the TOF, where the TOFs for analogous concentrations are four times greater, and the ability to remain catalytically first order for slightly higher concentrations of tetrabutylammonium formate (92). Since the only structural difference between the two catalysts is the presence of the benzyl alcohol moiety, one could hypothesise that this moiety both aids in increased TOFs and in preventing catalyst inhibition at the site of catalysis.

Since catalysis appears to not be influenced by the metal and occurs on the ligand, it is important to perform a control experiment to investigate whether the metal is even necessary for catalysis to occur. The pro-ligand 27 was investigated for oxidation catalysis of formate by cyclic voltammetry. Figure 6.11 showcased

that no redox processes were visible with equivalents of formate present in solution. There was also no change in the current at 0.2 V where previous instances of the catalytic oxidation of formate occurred. Therefore, one can conclude that coordination to a metal is vital for the oxidation catalysis on the ligand to occur.

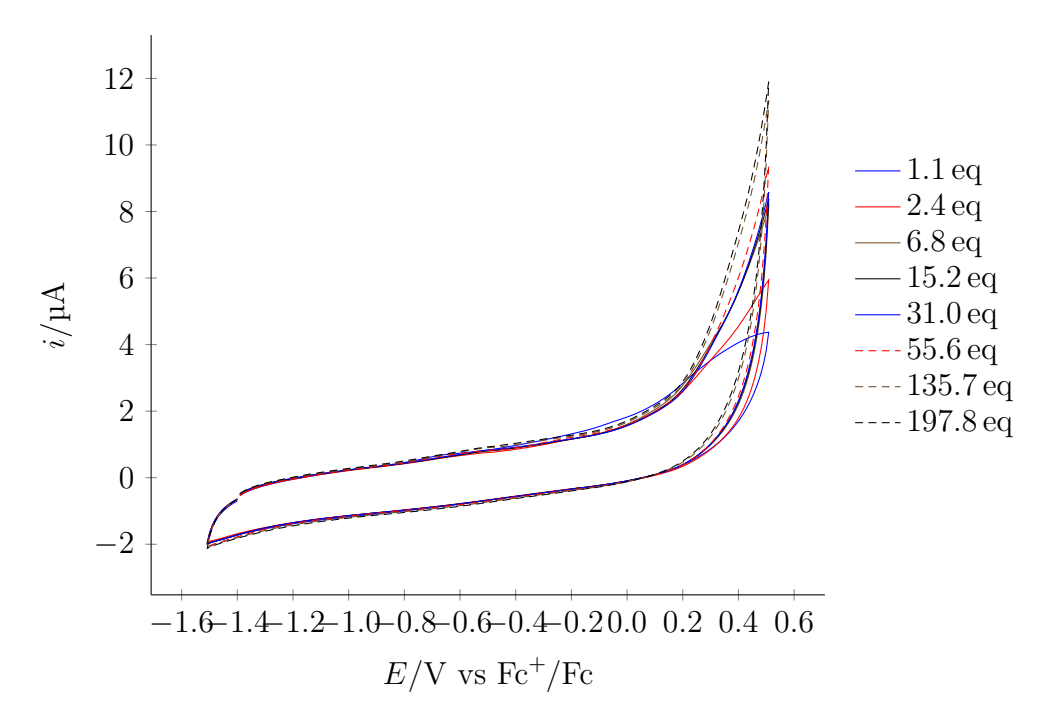


Figure 6.11: The Cyclic Voltammograms of $\bf 27~(0.05\,\rm mM)$ in MeCN/NBu₄BF₄ (0.1 M) in the Presence of Varying Amounts of Tetrabutylammonium Formate ($\bf 92$) at $100\,\rm mV\,s^{-1}$.

6.4 OAT Catalysis

The oxygen atom transfer catalysis of the proton relay functionalised complexes, 30, 80 and their non-functionalised counterparts 78 and 41 were tested. Following the conditions laid out by Schulzke and Holm, the transfer reaction of the oxygen between deuterated dimethyl sulphoxide and triphenylphosphine was monitored by ³¹P NMR spectroscopy. ^{104,234} What was expected was for the triphenylphosphine

peak at approximately 6 ppm to reduce in size while simultaneously forming a new peak at approximately 30 ppm. As expected, the unfunctionalised complexes **78** and **41** showed no change in the size of the triphenylphosphine peak, but unfortunately the functionalised analogues showed only a minute change over the 30-hour period (Figure 6.12), showing that the proton relays had only a slight effect in improving this catalytic reaction.

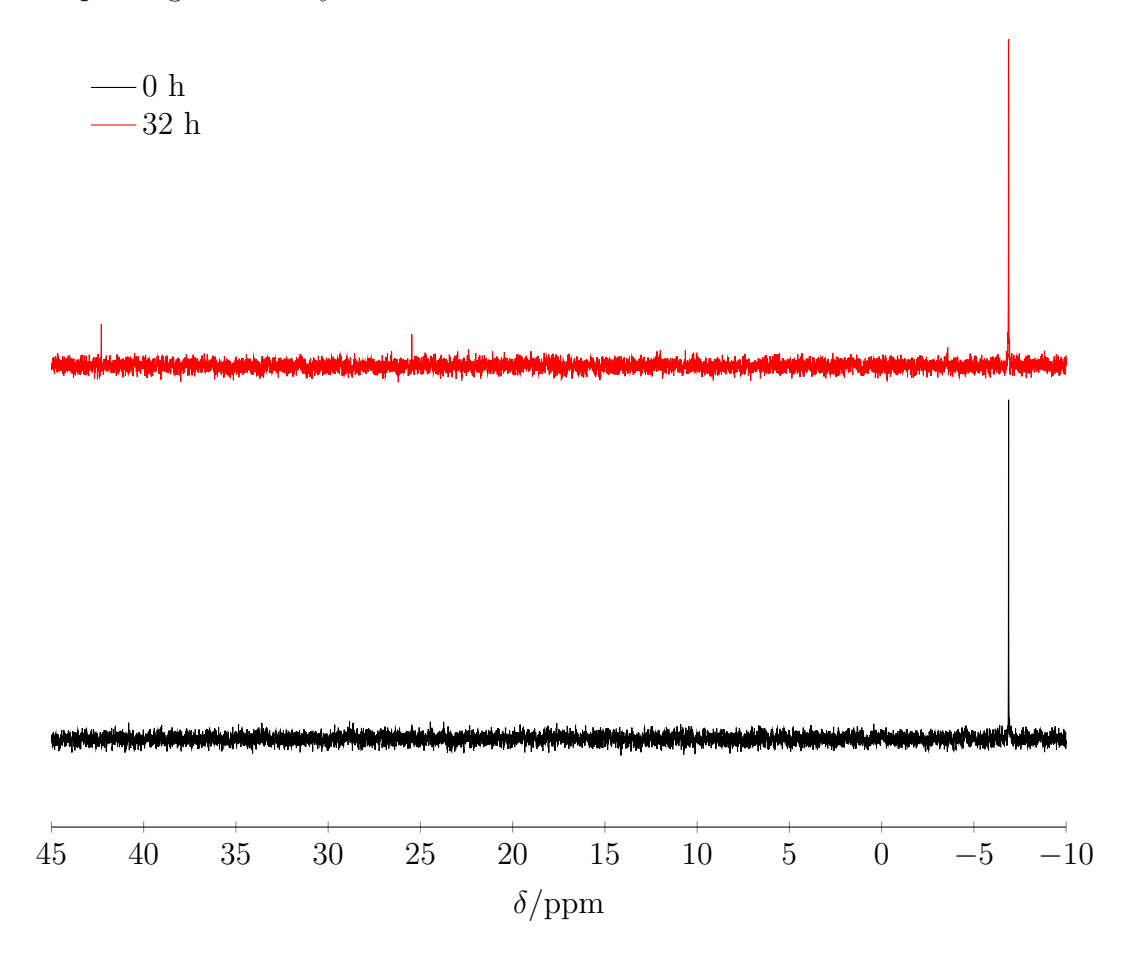


Figure 6.12: The 31 P NMR Spectrum of the OAT Catalysis Experiment of Over 32 Hours for 30.

The nearly non-existent reaction rate was theorised to be due to the mild nature of the oxidising substrate. Consequently, the relatively stronger trimethylamine N-oxide was used to identify whether this was the limiting factor for catalysis.

The OAT experiment was repeated, but instead with $12\,\mathrm{mM}$ of trimethylamine N-oxide along with $3\,\mathrm{mM}$ of catalyst and $9\,\mathrm{mM}$ of triphenylphosphine, in $0.5\,\mathrm{mL}$ of deuterated DMSO. The reaction was monitored using $^{31}\mathrm{P}$ NMR spectroscopy.

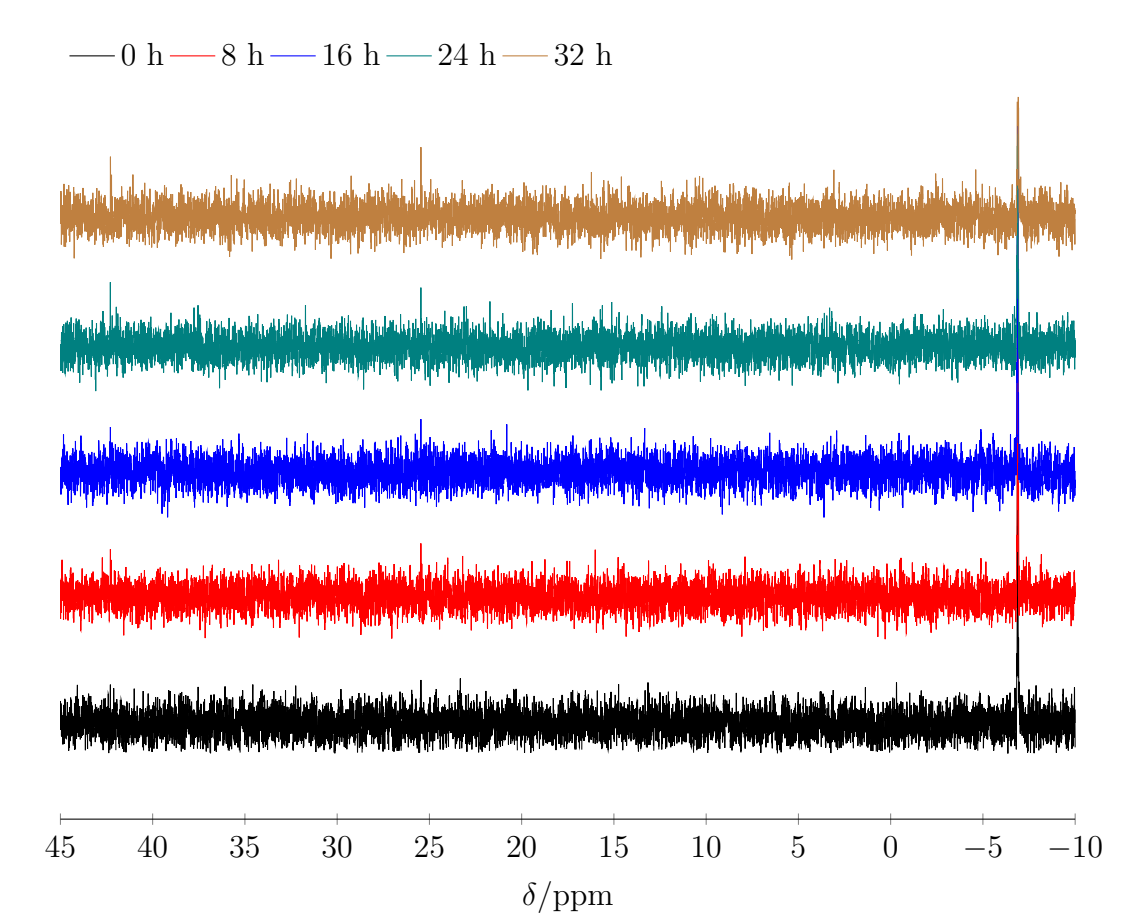


Figure 6.13: The 31 P NMR Spectrum of the OAT Catalysis Experiment of **30** Over 32 Hours with Me₃NO as the Oxidiser.

There was no noticeable increase in the reaction rate; therefore, it was unlikely that the oxidiser was the limiting factor for OAT catalysis. In both cases, an unexpected peak appeared at 45 ppm. With no direct methods to confirm its identity, one can only speculate. Holm has synthesised Mo-O-X dithiolene complexes using electron donating substituted silyl groups; perhaps this third peak corresponds to a similar species where the phosphine binds to the molybdenum-oxo,

giving a Mo-O-PPh₃ environment.¹⁰⁰

Schulzke and co-workers reasoned their catalyst performed more poorly than expected because of the formation of the chemically inert Mo^V₂O₃ species through the initial formation of the $\mathrm{Mo^{VI}O_2}$ complex. This hypothesis was checked by tracking changes in the UV/VIS spectrum of the 3 mm of complex 6 in the presence of trimethylamine N-oxide in acetonitrile. It was observed that there was an initial formation of $Mo^{VI}O_2$ species that quickly decomposed whilst the signal for $Mo_2^{V}O_3$ rose over the 56-hour course of the experiment. They reasoned that this was particularly an issue for ligand scaffolds made of aliphatic substituents. Aromatic substituents are known to be much more stable and, hence, much less reactive than those with aliphatic dithiolene systems..²³⁹ Whether the substituent is electron-withdrawing or donating influences the strength of the Mo-S bonds. This is felt by the Mo=O bond and affects whether it is more or less stable to form the mononuclear or dinuclear species. For example, electron-donating substituents push electron density up the scaffold, through the Mo-S bonds, and reduce the Lewis acidity of the molybdenum. The combination of the destabilising nature of the aliphatic substituents and the electron-donating character heavily weakens the Mo=O bond allowing the bridging oxo species to form more readily. The high number of hydroxyl functional groups and their ability to form hydrogen bonds with each other would certainly not detract from the ability of these complexes to form dinuclear complexes (Figure 6.14).

These conclusions from Schulzke and co-workers were tested to see if they hold true for the novel complexes herein. Figure 6.15 shows how the UV/Vis spectrum of complex 30 changes in the presence of trimethylamine N-oxide over a 56-hour time period. Dramatic shifts in the curve at $375 \,\mathrm{nm}$ seem to indicate that there has been the formation of a dinuclear complex. To see if the hydroxyl groups influenced the formation of the dinuclear species, the same UV/VIS spectroscopy experiment

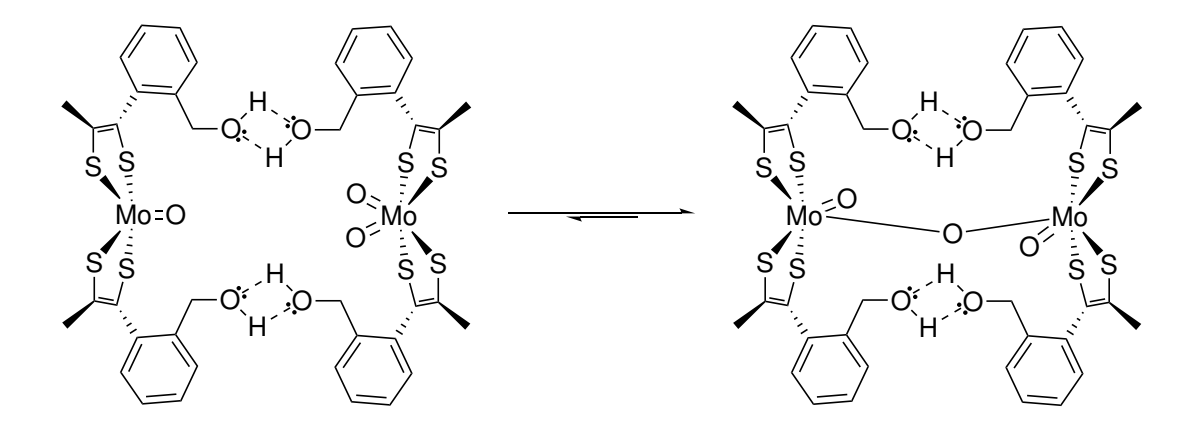


Figure 6.14: Possible Hydrogen Bonding Between Monomers Leading to Dinuclear Complex Formation.

was also carried out for **78**. There was no obvious change in rate between the two complexes; therefore, there must be another factor in play with regard to the poor OAT activity/rapid dinuclear formation, as it is not influenced by hydrogen bonding.

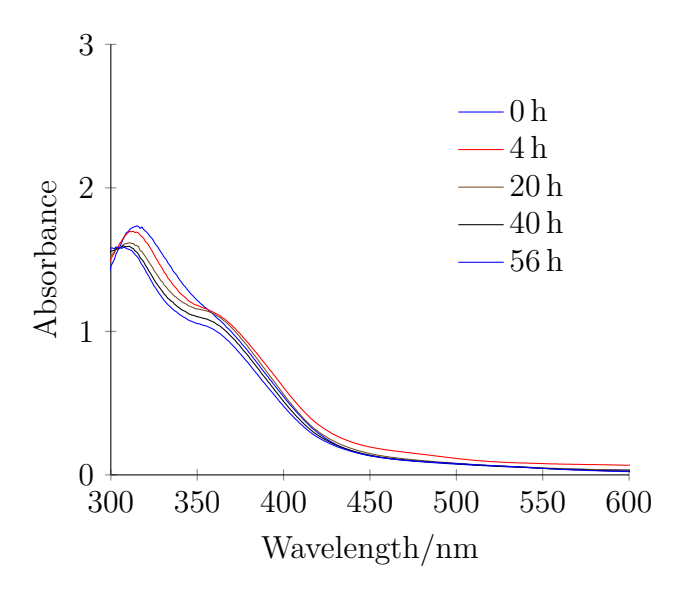


Figure 6.15: The UV/VIS Spectrum of ${\bf 30}$ in MeCN at 1 mm with Trimethylamine N-Oxide.

6.5 Summary

In Chapter 6, several methods have been implemented to better understand the behaviour of these molybdenum dithiolene systems and the influence that the addition of a benzyl alcohol group has as opposed to a phenyl group. With regard to the catalytic reduction capabilities, for both the reduction of protons and carbon dioxide, of the synthesised molybdenum dithiolene complexes, they underperform substantially. However, we are able to report the first molybdenum-oxo bis-dithiolene complexes that exhibit the ability to catalytically oxidise formate. In terms of both reduction and oxidation, there is a substantial difference between the FDH enzyme and the mimic; Hirst and co-workers determined that the enzyme has a reductive TOF of $282 \, \mathrm{s}^{-1}$ and oxidative TOF of $3380 \, \mathrm{s}^{-1}$ however these results are an important first step for understanding the process that occur at the FDH active site. Comparing the ligand structure of 30 and the reduction catalysts synthesised by Fontecave (10, 11 and 12) offers an insight into the requirements of what is necessary for reduction catalysis (Figure 6.16).

Figure 6.16: The Wright Ligand vs. The Fontecave Ligand vs. Moco. 103

There are three key differences between the Wright group ligand, the Fontecave group ligand, and pyranopterindithiolenene (Moco): conjugation, reducing power, and steric bulk. By comparing each ligand to each other, certain hypothesis can be

drawn as to the true driving force behind catalysis. Comparing Moco and 10, one could argue that electronic communication/conjugation between the pterin, pyran ring and the dithiolene is actually reduced in Moco; subsequently, ideas of a highly electronically linked ligand being the key influence for catalysis can be ruled out. Each ligand synthesised by Fontecave produced markedly different redox potentials for the Mo^{IV}/Mo^V and the Mo^V/Mo^{VI} redox couples, in most cases significantly more positive than 30 and 78, and yet catalysis was achieved with all three; thus, this rules out the reducing power of the complex in being a key aspect of catalysis. When examining the 2015 paper from Fontecave, ¹⁶¹ where the proton reduction capabilities of 10 are investigated, they did not observe the oxidative degradation of their complex that was seen upon addition of TFA to 30 and were able to achieve catalytic reduction. Therefore, either the corresponding Mo=O bond was stabilised by the ligand through donating effects or there was a barrier to entry for catalyst oxidation. If one considers that there is limited space for the coordination of ligands around a metal centre and that this problem is exacerbated with bulkier, charged ligands, one can hypothesise that the energy barrier for a third dithiolene ligand to coordinate and cause oxidation of the complex increases as a function of steric bulk. In other words, the bulk of the ligand prevents oxidative degradation to the molybdenum tris-dithiolene complex. This reasoning would help to rationalise the OAT results and the predilection to form the Mo₂O₃ bridged complex in the presence of an oxidiser since the ligands are not sufficiently bulky to prevent a second complex from coming into close contact to form the dinuclear complex.

Proton relays are effective in achieving improved oxidation catalysis of formate, with a four fold increase in the TOF at low concentrations of the substrate. This can be reasoned as the ligands offering a nearby site, the lone pair belonging to the oxygen, to which the proton can bind upon oxidation of the substrate. To determine where on the ligand catalysis takes place, **41** and a singly-methyl

substituted analogue must be tested.

Although not directly comparable, the cyclic voltammogram studies conducted for catalytic proton reduction of **10** and **22**, shows that the Mo^{IV}/Mo^V wave changes with increasing TFA concentration. This indicates that catalysis occurs on the metal centre. Therefore, one can hypothesise that perhaps an oxidative process occurs on the ligand and reductive processes occur on the metal centre.

Chapter 7

Summary and Conclusions

The initial method to target the proton relay functionalised mimic was through the transmetallation of a nickel dithiolene to a molybdenum carbonyl dithiolene, and then to the molybdenum-oxo: this failed. Syntheses aiming to transmetallate from the nickel compound directly to a molybdenum-oxo derivative were also unsuccessful. Finally, after ensuring absolute purity of reagents from the first steps, coordination from the dithione to the molybdenum-oxo precursor gave the target complex, $(Et_4N)_2[MoO(S_2C_2MeBnOH)_2]$. The original synthetic route was shortened by 3 steps, resulting in an improved atom economy, and the ligand synthesis was streamlined. Characterisation of this complex was not straightforward because of its extreme sensitivity to air, poor longevity outside of a freezer, inability to form crystals suitable for X-ray diffraction, 'apparent' paramagnetism, and small difference between the oxidised molybdenum tris-dithiolene and reduced molybdenum-oxo bis-dithiolene compounds in the infrared spectrum. The most powerful diagnostic technique was MALDI-TOF mass spectrometry, where the sample could be loaded onto the sample plate in the glove box, sealed in an airtight container, and transported to the machine. The heavier-than-air nature of argon and overpressure of the glove box meant that when the sample plate was sealed, any leaks would have argon pushing out against the atmosphere.

The synthetic route from the alkyne to dithione and then to the analogous complex allowed for rapid access to novel functional models of the formate dehydrogenase active site where the selectivity of the radical cyclisation reaction to the alkyne opens the door to the straightforward synthesis of numerous biomimetic complexes. However, developing reliable methods to synthesise sulphido and tungsten functionalised analogues remains elusive.

Density functional theory was employed to correctly assign the Mo=O band in the IR spectrum of the novel complexes. Obtaining the spin multiplicity parameter was performed through a detailed analysis of symmetry adapted molecular orbital theory. These parameters were trialled against literature systems as a method of benchmarking subsequent results. DFT allowed for the deconvolution of the 'fingerprint' region of the IR spectrum, where the band belonging to the Mo=O of the biomimetic compounds can now be used as a diagnostic feature with a high degree of certainty. Simultaneously, functionals have been identified, which when paired with the def2-TZVP basis set, can accurately predict features of these complexes for specific ligand scaffold types: 'simpler' scaffolds respond better to the BP86 functional whereas B3LYP and PBE0 work better with more complex systems. Geometry refinement also identified the presence of a high number of isomers for any compound with a degree of extended functionality. The high number of isomers predicts an extremely flat energy surface. With no obvious driver, the initial mixture of isomers in solution will be statistical. Therefore, in solution, there is likely an even distribution of each isomers. For any redistribution of isomers to occur, especially with regards to the cis/trans isomerisation, the process depends on the ligand binding energy. The molybdenum-dithiolene bond is strong, and therefore it is unlikely to dissociate, and a redistribution from the initial coordination between molybdenum and the dithiolene cannot occur to a lower energy arrangement. Instead, the substituents can move freely in solution since they are only bound to each other through single bonds and are free to rotate. This phenomenon can be seen on a NMR spectroscopy timescale where lowering the temperature of the experiment improved the resolution of the peaks since the unique environments are now spatially locked. The number of isomers also explains the difficulty in obtaining a crystal suitable for X-ray diffraction. The idea that molybdenum-oxo bis-dithiolenes form a number of isomers is not unheard of in the literature; Fontecave and co-workers gave similar reasoning as to why they had difficulty in obtaining a crystal structure for 12 stating that seven isomers were possible. To mitigate these issues, future ligands should be designed with a spatial constraint in mind to mitigate isomerisation to encourage single-crystal formation and reduced NMR spectroscopy ambiguity.

Electrochemistry was used to better understand how substituting the ligand bound to the dithiolene influenced redox behaviour at the metal centre. Predictably, the electron-withdrawing and donating nature of the substituent dictated its effect on the redox couples; removal of the electron-withdrawing benzyl alcohol shifted the redox couples negatively; removal of the electron-donating methyl group shifted potentials positively. The reversibility of the waves was directly related to the size of the ligand; bulkier ligands tended to show poor reversibility for the Mo^V/Mo^{VI} couple.

The catalytic properties of the proton relay complex (30) did not accomplish the goal to photocatalytically reduce carbon dioxide to formate. Initially, determining why was difficult. The same non-activity was observed when the complexes were tested using cyclic voltammetry for their ability to reduce protons to hydrogen. Typically, the current at some point of the wave would become increasingly negative as a result of electrons being taken from the 'circuit' to form the bond between the two protons to generate hydrogen. However, additions of equivalents of trifluoro-

acetic acid caused the almost immediate decomposition of the molybdenum-oxo bis-dithiolene complex to the molybdenum tris-dithiolene complex, indicated by a rapid change in colour of the electrolyte solution from red to green, indicating oxidation of Mo^{IV} to Mo^{VI} . FDH is known to inter-convert carbon dioxide and formate, so since these catalysts are intended to mimic this enzyme, it seemed pertinent to test their oxidation catalytic activity. Again, cyclic voltammetry was the best method to test their catalytic behaviour in this regard. Formate was shown to oxidise catalytically, on the ligand specifically, four times faster when proton relays were attached than without. However, to know which of the oxidation products is most common (CO_2 , H_2CO_3 , HCO_3^- , or CO_3^{2-}) bulk electrolysis experiments must be performed. The FDH enzyme also falls under the purview of the DMSO reductase family of molybdo/tungstoenzymes. Therefore, the OAT ability was examined. Again, poor rates of reaction were observed. This was hypothesised to be caused by the complexes' predilection to form the inert Mo₂^VO₃ bridging complex based on literature precedent. 104 The poor reduction and OAT catalysis can be deduced to be the result of insufficient steric bulk on the ligand.

From what has been learnt throughout this thesis, an informed decision on the next generation of ligands with the goal of having a higher chance of granting reduction catalysis can be ascertained. The first key point, is that the scaffold should be extended to more closely match what has succeeded before (the Fontecave ligand and Moco itself). Often, the most challenging part of novel dithiolene ligand synthesis comes in the insertion of the dithiolene functionality. The radical insertion synthesis detailed within this thesis allows for a great deal of freedom in ligand design, since, as long as an alkyne is inserted at some point the high degree of selectivity towards an alkyne means the bulk of the ligand will remain untouched upon utilising the radical cyclised dithione insertion reaction. Once a working mimic has been established within the group, the ability to customise the ligand can

allow for quick identification of what is $absolutely\ necessary$ for reduction catalysis to be performed.

Chapter 8

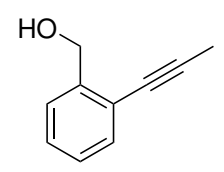
Experimental

8.1 General

All reactions were conducted under a dry argon atmosphere using standard Schlenk techniques unless otherwise specified. Starting materials were purchased from Sigma-Aldrich, Alfa Aesar, FluroChem, BLDPharma, or ThermoFisher and were used without further purification. In the case of tetrahydrofuran and diethyl ether, Na/(C₆H₅)₂CO were used as drying agents; methanol was taken from a Sure/Seal bottle and left over 3 Å molecular sieves; acetonitrile, dichloromethane, toluene, and n-hexane were taken from a MBraun SPS machine. Thin Layer Chromatography (TLC) was carried out using 0.2 mm thick silica gel plates (60778-25EA Sigma-Aldrich) with visualisation by illumination using UV light ($\lambda = 254 \, \mathrm{nm}$). Silica gel from Sigma-Aldrich, 60 Å 230-400 mesh particle size, was used as the stationary phase for column chromatography; where specified, by the term 'automatic column', a Teledyne CombiFLASH NEXTGEN 100 was also used. High-performance liquid chromatography (HPLC) was carried out using an Agilent Technologies 1200 Series. Ion exchange chromatography was carried out using a ThermoScientific DIONEX ICS-6000 DC, with a DionexCS12A 2 × 250 mm analytical column. Masses were

measured using a Sartorius analytical balance. FT-IR spectra were recorded using a Bruker Vertex 80 instrument. NMR spectra were recorded on a Bruker AvanceIII 500, operating at room temperature unless specified otherwise; ¹H NMR spectra were collected at 500 MHz and ¹³C NMR spectra were collected at 126 MHz using broad-band decoupling. Abbreviations used in NMR analysis are: s (singlet), d (doublet), t (triplet), q (quartet), dd (doublet of doublets), tt (triplet of triplets), td (triplet of doublets), sx (sextet), hept (heptet), and m (multiplet). Chemical shifts are given in parts per million (δ) and quoted relative to the residual solvent peak. Mass spectrometry was carried out in-house using a Shimadzu Axiama Performance (MALDI-TOF) and an Agilent Technologies 6460 Triple Quad (LC-MS). Cyclic voltammetry measurements were carried out in a glove box with an argon atmosphere using an Autolab PGstat 30 potentiostat/galvanostat. A 3 mm diameter glassy carbon electrode was used as the working electrode for the voltammetry experiments and was polished on a felt pad with alumina before each experiment. The counter electrode was a platinum wire cleaned between experiments by washing with acetone and burning off any remaining material using a Bunsen burner. A silver wire pseudo reference electrode was used and calibrated to an internal reference using ferrocene after the measurements had been performed. The cyclic voltammetry experiments were performed in a three-compartment cell with glass bridges between each compartment. Between each experiment, the cell was cleaned with Piranha solution (3:7, hydrogen peroxide: sulphuric acid), and then washed with distilled water.

8.2 2-(Propyn-1-yl)benzyl Alcohol (24)



The reaction was carried out following the method reported by Sashida and Yu with slight adjustments. 147,148 n-Butanol (700 mL) was degassed, followed by the addition of potassium hydroxide (79.7 g, 1420 mmol) under inert conditions. 2-Iodobenzyl alcohol (25 g, 106.8 mmol), copper(I) iodide (0.814 g, 4.272 mmol), and tetrakis(triphenylphosphine)palladium(0) (2.486 g, 2.134 mmol) were added to a cold-finger vessel. Subsequently, degassed tetrahydrofuran (250 mL) and piperidine (200 mL) were added, affording a gold solution. To the refluxing potassium hydroxide solution (120 °C), 1,2-dibromopropane (32 mL, 320.8 mmol) was added dropwise to allow for the in situ generation of propyne gas which was sparged through the gold solution; at half addition of 1,2-dibromopropane, a colourless precipitate was seen in the coldfinger vessel. After the full addition of 1,2-dibromopropane, the cold-finger solution was left to stir overnight at room temperature. To a cooled 6 M HCl solution (600 mL, 5 °C), the gold solution was transferred via cannula and left to stir for one hour. This afforded a red precipitate which was filtered out. The resulting solution was washed with ethyl acetate $(3 \times 250 \,\mathrm{mL})$ and the organic layer was extracted; the organic layer was neutralised with sodium bicarbonate $(2 \times 150 \,\mathrm{mL})$; washed with brine $(2 \times 150 \,\mathrm{mL})$; dried with magnesium sulphate and cleaned with carbon. The solvent was removed under reduced pressure. The resulting cream powder was sublimed $(55 \,^{\circ}\text{C}, 4.6 \times 10^{-4} \,\text{bar})$ to give a white powder of $9.435 \,\text{g}$ (60.4%). ¹H NMR $(500 \,\mathrm{MHz}, \,\mathrm{CDCl_3}) \,2.1 \,\mathrm{(s, 3H, Me)}, \, 2.12 \,\mathrm{(t, \it J=6.6\,Hz, 1H, OH)}, \, 4.79 \,\mathrm{(d, \it J=6.5\,Hz, 1H, OH)}, \, 4.70 \,\mathrm{(d, \it J=6.5\,Hz, 2H, OH)}, \, 4.70 \,\mathrm{(d, \it J=6.5\,Hz, 2H, OH)}, \, 4.70 \,\mathrm{(d, \it$ 2H, Ph-CH₂-OH), 7.22 (td, $J_1 = 7.5 \,\text{Hz}$, $J_2 = 1.4 \,\text{Hz}$, 1H, Ph-H), 7.28 (td, J_1 = 7.5 Hz, $J_2 =$ 1.5 Hz, 1H, Ph=H), 7.36-7.43 (m, 2H, Ph=H); $^{13}{\rm C}$ NMR (126 MHz,

CDCl₃) 4.62 (PhCC–CH₃), 64.36 (HO–CH₂–Ph), 90.90 (Ph–CC–CH₃), 122.35 (Ph–CCCH₃), 127.46 (Ph), 127.56 (Ph), 128.11 (Ph), 132.39 (Ph), 142.51 (Ph); $\tilde{\nu}_{\rm max}/{\rm cm}^{-1} = 3312$ (O–H), 2851 (C–H), 1477 (w), 1040 (s). (The experimental data agreed with the literature values). 147,148

8.3 2-Ethynylbenzyl Alcohol (76)

The reaction was carried out following the method reported by Johnston and co-workers with slight adjustments. 163 To a cold-finger, 2-iodobenzyl alcohol (20 g, 85 mmol), copper(I) iodide (0.689 g, 3.6 mmol), and tetrakis(triphenylphosphine)palladium(0) (1.965 g, 1.75 mmol) were added to a cold-finger vessel. Subsequently, degassed tetrahydrofuran (250 mL) and piperidine (120 mL) were added affording a gold solution. The solution was cooled to 0°C and freeze-pump-thawed trimethylsilylacetylene (14.5 mL, 101.9 mmol) was added dropwise to the solution; addition of half the trimethylsilylacetylene gave a cloudy precipitate. This was left to stir at 0°C for 30 minutes, and then at room temperature overnight. The gold solution was filtered into a cooled 6 M HCl solution (500 mL, 5 °C) and was left to stir for one hour. The resultant red precipitate was filtered out from the gold solution. The resulting solution was washed with ethyl acetate $(3 \times 250 \,\mathrm{mL})$ and the organic layer was extracted; the organic layer was neutralised with sodium bicarbonate $(2 \times 150 \,\mathrm{mL})$; washed with brine $(2 \times 150 \,\mathrm{mL})$; dried with magnesium sulphate and cleaned with carbon. The solvent was removed under reduced pressure. This was then taken up in methanol (65 mL) and potassium carbonate (621.5 mg, 5 mmol) was added and left to stir for one hour. Filtering the solid and taking the

liquor to dryness gave a yellow powder which was sublimed (55 °C, 4.6 × 10⁻⁴ bar). This gave a white powder (6.62 g, 59%). ¹H NMR (500 MHz, CDCl₃) 3.34 (s, 1H, OH), 4.84 (s, 2H, Ph–C**H**₂–OH), 7.24–7.28 (m, 1H, Ph–H), 7.37 (td, $J_1 = 7.6$ Hz, $J_1 = 1.4$ Hz, 1H, Ph–H), 7.43–7.46 (m, 1H, Ph–H), 7.51 (dd, $J_1 = 7.6$ Hz, $J_2 = 1.3$ Hz, 1H, Ph–H); ¹³C NMR (126 MHz, CDCl₃) 63.93 (HO–CH₂–Ph), 81.39 (Ph–CC–H), 82.09 (Ph–CC–H), 120.34(Ph), 127.45 (Ph), 127.58 (Ph), 129.37 (Ph), 132.99 (Ph), 143.33 (Ph); $\tilde{\nu}_{\rm max}/{\rm cm}^{-1}$ 3180 (O–H), 2835 (vw), 2030 (vw), 1433 (w), 1196 (w), 1011 (m). (The experimental data agreed with the literature values). ¹⁶³

8.4 Phenylprop-1-yne (72)

The reaction was carried out following the method reported by Davies and coworkers. ¹⁶² To a flame-dried cold-finger, iodobenzene (10 g, 49 mmol), tetrakis(triphenylphosphine)palladium(0) (1.13 g, 0.98 mmol), and copper(I) iodide (0.373 g, 1.96 mmol) were added and purged. Subsequent addition of tetrahydrofuran (120 mL) and piperidine (60 mL) afforded a gold solution. In a separate three-necked flask, n-butanol (350 mL) was degassed, followed by the addition of potassium hydroxide (33 g, 588 mmol). Upon reaching reflux (120 °C), 1,2-dibromopropane (15 mL, 147 mmol) was added dropwise to release propyne gas, which was transferred to the cold-finger vessel. This was left to stir overnight at room temperature. To a cooled 6 M HCl solution (300 mL, 5 °C), the gold solution was transferred via cannula and left to stir for one hour. This afforded a red precipitate which was filtered out. The resulting solution was washed with ethyl acetate (3 × 125 mL) and the

organic layer was extracted; the organic layer was neutralised with sodium bicarbonate (2 × 100 mL); washed with brine (2 × 100 mL); dried with magnesium sulphate and cleaned with carbon. Flash chromatography with hexane afforded a clear green oil (3.62 g, 63.7%). ¹H NMR (500 MHz, CDCl₃) 2.08 (s, 3H, CH₃), 7.27–7.33 (m, 3H, Ph-H), 7.42-7.44 (m, 2H, Ph-H); ¹³C NMR (126 MHz, CDCl₃) 4.39 (C-CH₃), 79.96 (Ph-CC-CH₃), 85.90 (Ph-CC-CH₃), 124.16 (Ph-CC-CH₃), 127.62 (Ph), 128.31 (Ph), 131.60 (Ph); $\tilde{\nu}_{\text{max}}/\text{cm}^{-1} = 2914$ (CH₃), 2247 (vw), 1489 (m), 754 (vs), 691 (s). (The experimental data agreed with the literature values). ¹⁶²

8.5 Potassium *Iso*propyl Xanthate (25)

The reaction was carried out following the method reported by Hounslow and co-workers. Potassium hydroxide (34.2 g, 610 mmol) was left to dissolve in isopropanol (600 mL, 7.85 mol). A solution of carbon disulphide (34 mL, 560 mmol) dissolved in isopropanol (35 mL) was added dropwise to give an orange precipitate; this was left to stir for one hour. The solution was washed with ethyl acetate (2 × 300 mL) and left to dry under vacuum giving a light orange powder (66.327 g, 50%). H NMR (500 MHz, D₂O) 1.34 (d, J = 6.2 Hz, 6H, CH(CH₃)₂), 5.53 (hept., J = 6.3 Hz, 1H, CH(CH₃)₂); NMR (126 MHz, D₂O) 20.73 (C(CH₃)₂), 77.95 (C(CH₃)₂); $\tilde{\nu}_{\rm max}/{\rm cm}^{-1} = 2966$ (C-H), 1458 (vw), 1369 (w), 1126 (w), 1045 (vs). (The experimental data agreed with the literature values).

8.6 Di*iso*propyl Xanthogen Disulphide (26)

The reaction was carried out following the method reported by Patel and co-workers with slight modifications. Potassium hydroxide (7.45 g, 132.8 mmol) and iodine (172.5 g, 679.63 mmol) were dissolved in distilled water (720 mL) which afforded a dark brown solution; this was cooled to 0 °C. Potassium isopropyl xanthate (226 g, 1.296 mol) was dissolved in a minimum of distilled water and added dropwise to the iodine solution. This was left to stir overnight, resulting in a green oil with a yellow precipitate. Ethyl acetate (400 mL) was added and the organic layer was extracted. The organic layer was washed with sodium thiosulphate to remove any excess iodine (2 × 100 mL). The organic layer was dried using brine (2 × 200 mL) and magnesium sulphate. The solution was then cleaned with carbon. The solvent was removed under reduced pressure to give green crystals (55.875 g, 31.8%). ¹H NMR (500 MHz, CDCl₃) 1.40 (d, J = 6.3 Hz, 6H, CH(CH₃)₂), 5.69 (hept., J = 6.2 Hz, 1H, CH(CH₃)₂); ¹³C NMR (126 MHz, CDCl₃) 21.26 (C(CH₃)₂), 80.40 (C(CH₃)₂), 206.96 (OCSS); $\tilde{\nu}_{\text{max}}/\text{cm}^{-1} = 2980$ (CH₃), 1447 (vw), 1352 (w), 1265 (s), 1082 (s), 1001 (vs). (The experimental data agreed with the literature values). ¹⁵⁰

8.7 1,3-Dithiol-2-one-4-benzyl alcohol-5-methyl (27)

To a flame-dried hexa-Schlenk flask, 2-(Propyn-1-yl)benzyl alcohol (1.03 g, 7 mmol× 6) and di isopropyl xanthogen disulphide (1.89 g, 7 mmol \times 6) were added (\times 6 refers to how many reactions are performed simultaneously using the hexa-Schlenk glassware). Following three purges, ortho-xylene (7 mL \times 6, dry, degassed) was syringed into each Schlenk flask. The solutions were warmed (40 °C) to dissolve any remaining material. Subsequently, the radical initiator, 1,1'-azobis(cyanocyclohexane) (1.71 g, 7 mmol × 6), was added. This was left to reflux (140 °C, 18 hours), giving a deep red, clear solution. The solutions were collected and reduced to dryness. This was taken up in acetone (50 mL) and the resulting white precipitate was filtered off. The solution was dry loaded with silica and passed through an automatic column (2:8, ethyl acetate: hexane) to give a viscous orange oil $(3.813\,g, \, 43.4\%)$. 1H NMR (500 MHz, CDCl₃) 2.01 (s, 3H, C \mathbf{H}_3 -CCS), 2.03 (s, 1H, C \mathbf{H}_2 -O \mathbf{H}), 4.67 (s, 2H, Ph-C**H**₂-OH), 7.27 (dd, $J=7.5\,\mathrm{Hz},\,1\mathrm{H},\,\mathrm{Ph-H}),\,7.34$ (td, $J_1=6.9\,\mathrm{Hz},\,J_2=6.9\,\mathrm{Hz}$ $1.4\,\mathrm{Hz},\,1\mathrm{H},\,\mathrm{Ph-H}),\,7.45~\mathrm{(td},\,J_{1}=7.5\,\mathrm{Hz},\,J_{2}=1.4\,\mathrm{Hz},\,2\mathrm{H},\,\mathrm{Ph-H}),\,7.58~\mathrm{(m},\,1\mathrm{H},\,1\mathrm{Hz},\,2\mathrm{H},\,\mathrm{Ph-H})$ Ph-H); 13 C NMR (126 MHz, CDCl₃) 15.13 (CH₃-CCS), 62.55 (Ph-CH₂-OH), 126.06 (CH₃-CC-Ph), 128.08 (Ph), 128.32 (Ph), 130.01 (Ph), 130.85 (Ph), 129.17 (Ph), 125.71 (Ph), 140.51 (CH₃-CC-Ph), 192.28 (C=O); $\tilde{\nu}_{\text{max}}/\text{cm}^{-1}$ 3360 (O-H), 2918 (C-H), 1623 (C=O), 1582 (C=C); HRMS m/z: M calcd for $C_{11}H_{10}O_2S_2 + H^+$: 239.01; found: 239.02.

8.8 1,3-Dithiol-2-one-4-phenyl-5-methyl (73)

The reaction was carried out following the method reported by Gareau and coworkers with slight adjustments. ¹⁴⁵ To a flame-dried hexa-Schlenk flask, di *iso* propyl xanthogen disulphide (1.89 g, 7 mmol \times 3) was added and purged (\times 3 refers to how many reactions are performed simultaneously using the hexa-Schlenk glassware). Phenylprop-1-yne (1.89 g, 7 mmol \times 3) was syringed in followed by ortho-xylene $(7 \text{ mL} \times 3, \text{ dry, degassed})$. Once 1,1'-azobis(cyanocyclohexane) (1.71 g, 7 mmol × 3) was added, the solutions were refluxed (140 °C, 18 hours) to give dark brown, clear solutions. The solutions were collected and reduced to dryness. The precipitate was filtered from the oil; the precipitate was washed with acetone $(2 \times 30 \,\mathrm{mL})$. The solution was dry loaded with silica and passed through an automatic column (0.2 : 9.8, ethyl acetate : hexane) to give a runny orange oil (1.704 g, 39%). ¹H NMR (500 MHz, CDCl₃) 2.22 (s, 3H, C H_3 -CCS), 7.35–7.43 (m, 5H, Ph-H); ¹³C NMR ($126 \text{ MHz}, \text{CDCl}_3$) 15.15 ($\text{CH}_3 - \text{CCS}$), 124.88 ($\text{CH}_3 - \text{CC} - \text{Ph}$), 128 (Ph), 128.96 (2C, Ph), 129.45 (2C, Ph), 131.46 (Ph), 145.32 (CH₃-CC-Ph), 191.55 (C=O); $\tilde{\nu}_{\rm max}/{\rm cm}^{-1}$ 2934 (C-H), 1668 (C=O), 1633 (C=C); HRMS m/z: M calcd for $C_{10}H_8OS_2 + H^+$: 209.00; found: 209.01.

8.9 1,3-Dithiol-2-one-4-phenyl-5-ethyl (74)

The reaction was carried out following the method reported by Gareau and coworkers with slight adjustments. ¹⁴⁵ To a flame-dried hexa-Schlenk flask, di *iso* propyl xanthogen disulphide (1.89 g, 7 mmol \times 3) was added and purged (\times 3 refers to how many reactions are performed simultaneously using the hexa-Schlenk glassware). 1-phenylprop-1-butyne (0.9113 g, 7 mmol \times 3) was syringed in, followed by orthoxylene $(7 \,\mathrm{mL} \times 3, \,\mathrm{dry}, \,\mathrm{degassed})$ and the flask was heated to dissolve all components $(50 \,^{\circ}\text{C})$. Once 1,1'-azobis(cyanocyclohexane) (1.734 g, 7 mmol \times 2) was added, the solutions were refluxed (140 °C, 18 hours); clear, orange solutions were afforded. The solutions were collected and taken to dryness under reduced pressure. The residual oil was taken up in a minimum of acetone, and the resulting white precipitate was filtered off. The oil was dry loaded with silica and passed through an automatic column (8.5: 1.5, hexane: ethyl acetate). A runny, orange oil was obtained (2.643 g, 56%). ¹H NMR (500 MHz, CDCl₃) 1.11 (t, J = 7.5 Hz, 2H, C-CH₂-CH₃), 2.53 $(q, J = 7.5 \,\text{Hz}, 1\text{H}, \text{C} - \text{C} \mathbf{H}_2 - \text{C} \text{H}_3), 7.3 \,(\text{m}, 5\text{H}, \text{Ph} - \text{H}); ^{13}\text{C} \,\text{NMR} \,(126 \,\text{MHz}, 126 \,\text{MHz})$ $CDCl_3$) 15.41 ($C-CH_2-CH_3$), 23.22 ($C-CH_2-CH_3$), 127.23 ($-CC-CH_2$), 128.95 (Ph), 128.99 (Ph), 129.41 (Ph), 131.52 (Ph), 132.61 (-CC-CH₂), 191.64 (C=O); $\tilde{\nu}_{\rm max}/{\rm cm}^{-1}$ 2934 (C-H), 1688 (C=C), 1643 (C=O). (The experimental data agreed with the literature values). 145

8.10 1,3-Dithiol-2-one-4-phenyl (75)

The reaction was carried out following the method reported by Gareau and coworkers with slight adjustments. 145 To a flame-dried hexa-Schlenk flask, phenylacetylene $(1.03 \,\mathrm{g}, 7 \,\mathrm{mmol} \times 3)$ and diisopropyl xanthogen disulphide $(1.89 \,\mathrm{g}, 7 \,\mathrm{mmol} \times 3)$ were added and purged (×3 refers to how many reactions are performed simultaneously using the hexa-Schlenk glassware). ortho-Xylene $(7 \text{ mL} \times 3, \text{ dry}, \text{ degassed})$ was syringed in and the flask was heated to dissolve all components (50°C). Once 1,1'-azobis(cyanocyclohexane) (1.71 g, $7 \text{ mmol} \times 3$) was added, the solutions were refluxed (140°C, 18 hours) to give clear dark red solutions. The solutions were collected and taken to dryness under reduced pressure. The resulting oil was taken up in a minimum of acetone and the white precipitate was filtered out. The oil was dry loaded with silica and columned through an automatic column (hexane: toluene, 7:3). A red-crystalline material was obtained and redissolved in acetone. Cleaning with carbon, filtering, and then removing the solvent afforded a yellow crystalline powder (6.30 g, 30%). ¹H NMR (500 MHz, CDCl₃) 6.71 (s, 1H, CH), $7.04 \text{ (m, 5H, Ph-H)}^{13}\text{C NMR (126 MHz, CDCl}_3) 111.80 \text{ (H-C-C-)}, 126.50 \text{ (Ph)},$ 129.36 (Ph), 132.85 (Ph), 135.17 (Ph), 192.52 (C=O) $\tilde{\nu}_{\rm max}/{\rm cm}^{-1}$ 1643 (C=O), 1622 (C=C), 872 (m), 739 (s); LCMS m/z: M calcd for $C_9H_6OS_2$: 193.99; found: 193.97.

8.11 1,3-Dithiol-2-one-4-benzyl Alcohol (21)

To a flame-dried Schlenk flask, 2-ethynylbenzyl alcohol (0.925 g, 7 mmol) and diisopropyl xanthogen disulphide (1.89 g, 7 mmol) were added and purged. ortho-Xylene (7 mL, dry, degassed) was syringed in and the flask was heated to dissolve all components (50 °C). Once 1,1'-azobis(cyanocyclohexane) (1.71 g, 7 mmol) was added, the solutions were refluxed (140 °C, 18 hours) to give a clear, orange oil. This was taken to dryness under reduced pressure to give an orange oil and subsequently dry loaded with silica. An automatic column was performed (hexane : ethyl acetate, 7.5 : 2.5). A yellow, crystalline solid was obtained (0.745 g, 37%). ¹H NMR (500 MHz, CDCl₃) 1.92 (s, 1H, OH), 4.62 (s, 2H, OH), 6.75 (s, 1H, CH), 7.25 (d, J = 4.6, 2H, Ph-H), 7.32 (m, 1H, Ph), 7.43 (d, J = 7.4 Hz, 1H, Ph-H); ¹³C NMR (126 MHz, CDCl₃) 62.82 (Ph-CH $_2-$ OH), 115.63 (Ph-CC-H), 128.22 (Ph), 129.51 (Ph), 129.55 (Ph), 130.15 (Ph), 131.80 (Ph), 132.34 (Ph), 138.59 (CH-CC-Ph), 193.13 (C=O); $\tilde{\nu}_{\text{max}}/\text{cm}^{-1}$ 3277 (O-H), 1627 (C=O), 1547 (C=C).

8.12 1,3-Dithiol-2-one-4-para-aniline (77)

$$S \longrightarrow S$$
 H_2N

To a flame-dried Schlenk flask, 4-ethynylaniline (0.82 g, 7 mmol) and diisopropyl xanthogen disulphide (1.89 g, 7 mmol) were added and purged. ortho-Xylene (7 mL, dry, degassed) was syringed in and the flask was heated to dissolve all components (50 °C). Once 1,1'-azobis(cyanocyclohexane) (1.71 g, 7 mmol × 3) was added, the solutions were refluxed (140 °C, 18 hours) to give a brown/red solution. The solution was taken to dryness under reduced pressure and dry loaded with silica. An automatic column was performed (hexane : ethyl acetate, 7 : 3) and after the fractions were collected, an orange solid was obtained (0.356 g, (24%). 1 H NMR (500 MHz, CDCl₃) 3.85 (s, 2H, NH₂), 6.60 (s, 1H, CH), 6.63–6.72 (m, 2H, Ph-H), 7.15–7.25 (m, 2H, Ph-H); 13 C NMR (126 MHz, CDCl₃) 111.80 (H-C-C-), 126.50 (Ph), 129.36 (Ph), 132.85 (Ph), 135.17 (Ph), 192.52 (C=O); $\tilde{\nu}_{\rm max}/{\rm cm}^{-1}$ 3369 (N-H), 1626 (C=O), 1435 (vs); LCMS m/z: M calcd for ${\rm C_9H_7NOS_2 + H^+}$: 210.00; found: 210.00.

8.13 Di-(1,3-dithiol-2-one-5-methyl-4-benzyl)ethyl Malonate (82)

To a flame-dried Schlenk flask, 1,3-dithiol-2-one-4-benzyl alcohol-5-methyl (0.715 g, 3 mmol), malonyl chloride (0.226 g, 1.6 mmol) and sodium hydrogenearbonate (0.311 mmol, 3.7 mmol) were added. After purging, the compounds were dissolved in dichloromethane (70 mL, dry, degassed). Effervescence was observed, and the solution was left to stir overnight, affording a deep orange solution. Distilled water (50 mL) was added to dissolve any residual sodium hydrogenearbonate, and the

organic phase was subsequently separated. The organic phase was dried with brine (100 mL) and magnesium sulphate. The solvent was removed under reduced pressure, and the final product was purified via flash chromatography (hexane : ethyl acetate, 85 : 15) to give a yellow oil (0.398 g, (51%). ¹H NMR (500 MHz, CDCl₃) 2.00 (s, 6H, Me), 3.44 (s, 2H, OC-CH₂-CO), 5.17 (s, 4H, Ph-CH₂-O), 7.31–7.33 (m, 2H, Ph-H), 7.38–7.43 (m, 4H, Ph-H), 7.45–7.47 (m, 2H, Ph-H); ¹³C NMR (126 MHz, CDCl₃) 15.16 (Me), 41.42 (OC-CH₂-CO), 64.70 (Ph-CH₂-O), 125.12 (CH₃-Ph), 127.09 (Ph), 129.18 (Ph), 129.86 (Ph), 130.03 (Ph), 130.53 (Ph), 131.18 (Ph), 135.03 (Ph-C=C), 165.90 (O-C=O), 191.43 (S-C=O) $\tilde{\nu}_{\rm max}/{\rm cm}^{-1}$ 2919 (C-H), 1732 (C=O), 1632 (C=O), 1138 (s); LC-HRMS m/z: M calcd for $C_{25}H_{20}O_6S_4 + H^+$: 545.01; found: 545.02.

8.14 1,3-Dithiol-2-one-5-methyl-4-benzyloxy-(tert-butyl)dimethylsilane (28)

To a flame-dried Schlenk flask, 1,3-dithiol-2-one-4-benzyl alcohol-5-methyl (1.191 g, 5 mmol) was added with imidazole (0.362 g, 5.25 mmol) and purged. *tert*-Butyldime thylsilyl chloride (0.79 g, 5.25 mmol) was added to the vessel and dissolved in dimethylformamide (50 mL). This was left to stir overnight, affording a yellow solution. After transferring the solution to a separating funnel, distilled water (500 mL) was added along with ethyl acetate (200 mL); the organic layer was separated from the aqueous layer. A further washing with lithium chloride solution

(5%, 150 mL) removed any residual traces of dimethylformamide. The organic layer was dried using brine (2 × 100 mL) and magnesium sulphate. Flash chromatography was used to purify the product (40 : 60, ethyl acetate : hexane). The excess solvent was removed under reduced pressure to give a gold oil (1.70 g, 96%). ¹H NMR (500 MHz, CDCl₃) 0.09 (s, 6H, (CH₃)₂Si), 0.94 (s, 9H, (CH₃)₃CSi)), 2.00 (s, 3H, CH₃-CCS), 4.69 (s, 2H, Ph-CH₂-O-Si), 7.25 (dd, 1H, Ph-H), 7.31 (td, J = 6.9 Hz, 1H, Ph-H), 7.42 (td, J = 7.5 Hz, 2H, Ph-H), 7.59 (dd, J = 7.8 Hz, 1H, Ph-H); ¹³C NMR (126 MHz, CDCl₃) -5.19 ((CH₃)₂Si)), 15.11 (SC-CH₃), 18.52 ((CH₃)₃C), 26.07 (CH₃)₃C), 62.6 (Si-O-CH₂), 125.97 (Ph), 126.74 (Ph), 127.4 (Ph), 127.8 (Ph), 128.47 (CH₃-CC-S), 129.7 (Ph), 130.4 (Ph), 141.02 (CH₃-CC-S), 192.28 (CO); $\tilde{\nu}_{\rm max}/{\rm cm}^{-1}$ 2955 (C-H), 1659 (C=O); LC-HRMS m/z: M calcd for C₂₅H₂₀O₆S₄ + H⁺: 545.01; found: 545.02.

8.15 $Ni(S_2C_2MeBnOH)_2)$ (29)

To a flame-dried Schlenk flask, 1,3-dithiol-2-one-5-methyl-4-benzyloxy(tert-butyl) dimethylsilane (0.353 g, 1 mmol) was dissolved in toluene (25 mL, dry, degassed) and cooled to 0 °C. n-Butyllithium (2 M, 1 mL) was added to the solution and left to stir overnight, affording a gold solution. In another flame-dried Schlenk flask, nickel(II) bis(acetylacetonate) (0.129 g, 0.5 mmol) was added and dissolved in toluene (25 mL, dry, degassed) to give a green solution. This nickel solution was then transferred dropwise via cannula to the ligand solution; this afforded a black solution which was left to stir for 1 hour. Iodine (0.1269 g, 0.5 mmol) was

added, and the solution was left to stir for another hour; the solution remained black. After removing the toluene under reduced pressure to give a black oil, tetrahydrofuran (20 mL) was added, resulting in an extremely dark purple solution. To deprotect the ligand, HCl (1 M, 15 mL) was added and left to stir at room temperature for 1 hour. Ethyl acetate (2 × 75 mL) was added and the organic layer was collected. This was neutralised with sodium bicarbonate solution (100 mL), and dried with brine (100 mL) and magnesium sulphate. Removing the solvent under reduced pressure afforded a dark purple oil. Flash chromatography (hexane : ethyl acetate : methanol, 1 : 1 : 0.01) afforded a dark blue solution, and upon removal of all solvent gave a black solid (0.19 g, 38%). ¹H NMR (500 MHz, CDCl₃) 2.03 (s, 3H, Me), 2.19 (s, 1H, O-H) 4.45 (s, 2H, Ph-CH₂-OH), 7.19 (dd, J = 7.4, 1.3 Hz, 1H, Ph-H), 7.37 (td, J = 7.5, 1.3 Hz, 2H, Ph-H), 7.61 (m, 1H, Ph-H); MADLI-TOF m/z: M calcd for ⁵⁸NiC₂₀H₂₀O₂S₄: 477.97; found: 477.91.

8.16 $Ni(S_2C_2Ph_2)_2$ (31)

The reaction was carried out following the method reported by Schrauzer and co-workers with slight adjustments. Benzoin (5 g, 23.56 mmol) and phosphorus pentasulphide (7.5 g, 16.87 mmol) were refluxed in dioxane (35 mL). The precipitate was filtered to give an orange solution. Nickel(II) chloride (2.5 g, 19.29 mmol) was dissolved in water (50 mL, distilled) and added rapidly. This was left to stir (65 °C, 2 hours). After cooling to room temperature, another filtration was performed. After removing the solvent, the sample was dry-loaded onto a silica column and

washed with methanol until the eluent ran clean. A subsequent wash with toluene eluted a green fraction. The solvent was removed under reduced pressure affording a green solid (4.437 g, 23%). 1 H NMR (500 MHz, CDCl₃) 7.26–7.30 (m, Ph-**H**), 7.34–7.41 (m, Ph-**H**); 13 C NMR (126 MHz, CDCl₃) 128.54 (Ph), 129.09 (Ph), 141.34 (Ph), 181.80 (**C**-Ph); MALDI-TOF m/z: M calcd for 58 NiC₂₈H₂₀S₄: 541.98; found: 542.43. (The experimental data agreed with the literature values). 153

8.17 $Mo(CO)_2(MeBnOH)_2$ (22)

To a flame-dried Schlenk flask, Ni(S₂C₂MeBnOH)₂ (0.07 g, 0.13 mmol) was dissolved in ethyl acetate (20 mL, dry, degassed) to give a deep blue solution. To another flame-dried Schlenk flask, η^3 -toluenetricarbonylmolybdenum(0) (0.03 g, 0.11 mmol) was dissolved in ethyl acetate (20 mL, dry, degassed). The nickel solution was transferred rapidly via cannula to the molybdenum solution, which gave a dark purple solution. This was left to stir overnight and had no visible change. All the solvent was evacuated from the Schlenk flask and an air-sensitive column was prepared (silica dried at 120 °C overnight under reduced pressure) using hexane: ethyl acetate (1:1, dry, degassed) as the eluent. The purple residue was taken up in a minimum of eluent and transferred to the column by cannula. The first purple fraction was collected, reduced to dryness, and gave a purple solid (0.062 g, 80%). $\tilde{\nu}_{\rm max}/{\rm cm}^{-1}$ (KBr) 3462 (O–H), 2962 (C–H), 2038 (vw, C=O), 1980 (vw, C=O), 1263 (s), 1099 (s).

8.18 $Mo(CO)_2(S_2C_2Ph_2)_2$ (33)

The reaction was carried out following the method reported by Holm and coworkers with slight adjustments. To a flame-dried Schlenk flask, Ni(S₂C₂Ph₂)₂ (0.6885 g, 1.26 mmol) and η^3 -toluenetricarbonylmolybdenum(0) (0.03 g, 0.11 mmol) were dissolved in dichloromethane (100 mL, dry, degassed) to give a black solution. This was left to stir for 2 days at room temperature, where the solution took on a purple colour. An air sensitive column was prepared (silica dried at 120 °C overnight under reduced pressure) using pentane: benzene (7:3, dry, degassed) as the eluent. The volume of solvent was taken to a minimum under reduced pressure and transferred across to the column using a cannula. The first purple fraction was collected, reduced to dryness, and gave a purple solid (0.0539 g, 77%). $\tilde{\nu}_{\rm max}/{\rm cm}^{-1}$ (ethyl acetate) 1985 (w, C=O), 2029 (w, C=O); Absorption spectrum (ethyl acetate) $\lambda_{\rm max}(\epsilon_{\rm M})$ 403 (4850), 563 (10 840), 685 (1590), 853 (400). (The experimental data agreed with the literature values).

8.19 $K_3Na[MoO_2(CN)_4] \cdot 6H_2O$ (13)

WARNING: Large quantities of hydrogen cyanide are released upon the addition of acetic acid; perform this experiment in the fume hood far away from the sash.

The reaction was carried out following the method reported by Roodt and co-workers. 152 To a Schlenk flask under an atmosphere of argon, sodium molybdate dihydrate (1.2098 g, 5 mmol), potassium borohydride (0.556 g, 10.5 mmol), and potassium cyanide (0.814 g, 12.5 mmol) were dissolved in distilled water (30 mL) and cooled to 0°C. This was followed by the dropwise addition of acetic acid (0.44 mL, 13 mmol) over a 10-minute period. Another aliquot of potassium cyanide (0.814 g, 12.5 mmol) and acetic acid (0.44 mL, 13 mmol) were added over a 10-minute period. A mixture of sodium hydroxide (1.681 g, 42.2 mmol) and potassium hydroxide (2.380 g, 42.2 mmol) were added, followed by the slow addition of ethanol (7 mL). This was left to stir overnight. A pink precipitate was filtered out of the solution and washed with ethanol: water (9:1, 200 mL). This was recrystallised in a minimum of water along with the addition of potassium hydroxide and sodium hydroxide (0.4 g each), followed by the slow addition of ethanol. Pink crystals were obtained and, after drying, weighed 3.55 g (71%). Elemental Analysis: C: 10.00; H: 2.52; N: 11.66. calcd. (%): C: 10.24; H: 2.27; N: 10.01. $(K_3Na[MoO_2(CN)_4] \cdot 6H_2O)_{0.95}$ $(C_2H_5OH)_{0.05}$

8.20 $K_3Na[WO_2(CN)_4] \cdot 6H_2O$ (87)

$$K_3Na\begin{bmatrix} NC & II & CN \\ NC & II & CN \\ NC & II & CN \end{bmatrix} 6H_2O$$

WARNING: Large quantities of hydrogen cyanide are released upon the addition of acetic acid; perform this experiment in the fume hood far away from the sash.

The reaction was carried out following the method reported by Kanas and co-

workers.¹⁷⁸ $K_3Na[WO_2(CN)_4] \cdot 6H_2O$ was prepared similarly to $K_3Na[MoO_2(CN)_4] \cdot 6H_2O$. To a Schlenk flask, under an atmosphere of argon, sodium tungstate dihydrate (1.649 g, 5 mmol), potassium borohydride (0.814 g, 12.5 mmol), and potassium cyanide (0.556 g, 10.5 mmol) were dissolved in distilled water (30 mL) and were cooled to $0^{\circ}C$. This was followed by the dropwise addition of acetic acid (0.74 mL) over 10 minutes. Another aliquot of potassium cyanide (0.556 g, 10.5 mmol) was added and acetic acid (0.74 mL) was added over 10 minutes. A mixture of sodium hydroxide (1.681 g, 42.2 mmol) and potassium hydroxide (2.380 g, 42.2 mmol) were added, followed by the slow addition of ethanol (7 mL). This was left to stir overnight. A cream precipitate was filtered out of the solution and washed with ethanol/water (9:1, 200 mL). This was recrystallised in a minimum of water along with the addition of potassium hydroxide and sodium hydroxide (0.4 g each), followed by the slow addition of ethanol. Brown crystals were obtained and, after drying, weighed 2.160 g (76%). C: 8.68; H: 1.45; N: 9.00. calcd. (%): C: 8.45; H: 2.13; N: 9.86.

8.21 Ammonium Tetrathiomolybdate (84)

$$(H_4N)_2 \begin{bmatrix} S \\ II \\ S & S \\ S & S \end{bmatrix}$$

The reaction was carried out following the method reported by Krüss. 172 Ammonium heptamolybdate (10 g, 8.592 mmol) was dissolved in distilled water (50 mL) and ammonium hydroxide solution (100 mL, 28% to 30%). Hydrogen sulphide gas was generated in situ through the reaction of finely ground iron sulphide (100 g, 1.137 mmol) with HCl (12 M, 100 mL). The gas was sparged through the solution until it had taken on a deep red colour. The vessel was then sealed and left to

recrystallise in a fridge at 2 °C for one week. Red crystals were obtained by filtering the resulting solution, where after drying weighed 10.2 g (70%). S: 49.92; H: 3.03; N: 11.12. calcd. (%): S: 49.27; H: 3.1; N: 10.76.

8.22 Tetraethylammonium Tetrathiomolybdate (85)

$$(\mathsf{Et_4N})_2 \left[\begin{array}{c} \mathsf{S} \\ \mathsf{II} \\ \mathsf{S} \\ \mathsf{S} \\ \mathsf{S} \\ \mathsf{S} \\ \mathsf{S} \\ \mathsf{S} \end{array} \right]$$

The reaction was carried out following the method reported by Bensch and coworkers. ¹⁷⁴ In a beaker, the crystalline ammonium tetrathiomolybdate (3.67 g, 14.1 mmol) was dissolved in distilled water (90 mL). In a separate beaker, tetraethylammonium bromide (5.92 g, 24.7 mmol) and sodium hydroxide (0.986 g, 24.7 mmol) were also dissolved in distilled water (90 mL). The tetrathiomolybdate solution was added to the tetraethylammonium bromide and sodium hydroxide solution. This was left to stir for 30 minutes. The solution took on a progressively deeper red colour. The solution was taken to dryness under reduced pressure and then redissolved in a minimum of acetonitrile, giving a white precipitate. The precipitate was filtered off and the resultant solution taken to dryness once again to give a red crystalline powder (6.42 g, 93.7%). S: 22.19; C: 38.73; H: 8.23; N: 5.91. calcd. (%): S: 26.46; C: 39.65; H: 8.32; N: 5.78.

8.23
$$(\text{Et}_4\text{N})_2[\text{MoS}(\text{S}_4)_2]$$
 (86)

$$(\mathsf{Et_4N})_2 \left[\begin{array}{c} S & S \\ S & \mathsf{Mo} \\ S - S & S - S \end{array} \right]$$

The reaction was carried out following the method reported by Coucouvanis and coworkers. To a flame-dried Schlenk flask, tetraethylammonium tetrathiomolybdate (6.42 g, 13.2 mmol) was added and dissolved in acetonitrile (180 mL). Elemental sulphur (2.09 g, 65.3 mmol) was subsequently added. After 5 minutes of stirring, a brown precipitate began to precipitate out, and the solution was left to stand for 10 minutes. The liquor was filtered out of the solution, leaving the brown precipitate behind to be washed with carbon disulphide (25 mL) and diethyl ether (60 mL). The precipitate was recrystallised from a minimum of dimethylformamide and diethyl ether to give brown crystals (7.58 g, 89%). S: 44.73; C: 29.79; H: 6.20; N: 4.38. calcd. (%): S: 44.73; C: 29.79; H: 6.25; N: 4.34.

8.24 $(Et_4N)_2[MoO(S_2C_2MeBnOH)_2]$ (30)

To a flame-dried side-arm flask, 1,3-dithiol-2-one-4-benzyl alcohol-5-methyl (0.477 g, 2 mmol) was dissolved in methanol (51 mL, dry, degassed) and cooled to 0 °C. Addition of the potassium hydroxide (0.281 g, 5 mmol) followed quickly and the solution was left to stir for 2 hours. In another Schlenk flask K₃Na[MoO₂(CN)₄] · 6 H₂O (0.480 g, 1 mmol) was dissolved in water (20 mL, distilled, degassed). The dithione solution was heated to 50 °C and the molybdenum precursor solution was transferred via cannula rapidly, turning the yellow solution black. After leaving this to stir for 45 minutes, tetraethylammonium bromide (0.420 g, 2 mmol) was added. Following another 45 minutes of stirring at 50 °C, the solution was red in appearance. The solvent was removed under reduced pressure and acetonitrile

(80 mL, dry, degassed) was added. This was filtered into another Schlenk flask and the solution was concentrated under reduced pressure. Subsequent, slow addition of diethyl ether (80 mL, dry, degassed) gave a red precipitate. The remaining solvent was filtered off and the red precipitate was recrystallised once more. Removing all the solvent under vacuum gave a red solid (0.118 g, 18%). ¹H NMR (500 MHz, CD₃CN) 1.17 (tt, $J_1 = 7$ Hz, $J_2 = 1.8$ Hz, 24H, N-CH₂-CH₃), 2.00 (t, J = 4 Hz, -CH₂-OH), 2.09 (s, 3H, C-CH₃), 2.35 (s, -CH₂-OH), 3.10 (q, J = 7.2 Hz, 16H, N-CH₂-CH₃), 3.98-4.05 (m, -CH₂-OH), 4.28 (m, -CH₂-OH), 4.51 (m, -CH₂-OH), 6.8-7.37 (m, Ph-H); ¹³C NMR (126 MHz, CD₃CN) 7.76 (N-CH₂-CH₃), 23.12 (N-C-CH₃), 53.04 (t, (N-CH₂-CH₃), 64.51 (-CH₂-OH), 126.53 (Ph), 126.55 (Ph), 127.75 (Ph), 127.78 (Ph); $\tilde{\nu}_{\rm max}/{\rm cm}^{-1}$ 3425 (O-H), 2966 (C-H), 1261 (m), 937 (Mo=O); MALDI-TOF m/z: M calcd for ⁹⁷MoC₂₀H₂₀O₃S₄: 533.94; found: 533.82.

8.25 $(Et_4N)_2[MoO(S_2C_2MePh)_2]$ (78)

To a flame-dried side-arm flask, 1,3-dithiol-2-one-4-phenyl-5-methyl (0.415 g, 2 mmol) was dissolved in methanol (51 mL, dry, degassed) and cooled to 0 °C. Addition of the potassium hydroxide (0.281 g, 5 mmol) followed quickly, and the solution was left to stir for 2 hours. In a separate Schlenk flask, $K_3Na[MoO_2(CN)_4] \cdot 6 H_2O$ (0.480 g, 1 mmol) was dissolved in water (20 mL, distilled, degassed). The dithione solution was heated to 50 °C and the molybdenum salt solution was transferred via cannula across, giving the solution a red colour. After stirring for 45 minutes, tetraethylammonium bromide (0.420 g, 2 mmol) was added and the solution was

left to stir for a further 45 minutes. The red/yellow solution was reduced to dryness and then taken up in acetonitrile (80 mL, dry, degassed). The red solution was filtered into a fresh Schlenk flask and concentrated. Diethyl ether (50 mL, dry, degassed) was added and a cream solid precipitated out. The recrystallisation was repeated twice more until the mother liquor was clear. Taking the solution to dryness gave a red film (0.263 g, 36%). 1 H NMR (500 MHz, CD₃CN) 1.14 (tt, $J_1 = 7$ Hz, $J_2 = 1.8$ Hz, 24H, N-CH₂-CH₃), 2.17 (s, 6H, C-CH₃), 3.11 (q, J = 7.2 Hz, 16H, N-CH₂-CH₃) 7.25 (m, 10H, Ph-H); 13 C NMR (126 MHz, CD₃CN) 7.74 (N-CH₂-CH₃), 24.20 (N-C-CH₃), 52.98 (t, (N-CH₂-CH₃), 125.32 (Ph), 128.17 (Ph), 130.02 (Ph), 136.16 (CH3-C), 148.23 (Ph-C); $\tilde{\nu}_{\rm max}/{\rm cm}^{-1}$ (KBr) 2982 (C-H), 1171 (s), 1001 (m), 932 (Mo=O,w), 891 (m); MALDI-TOF m/z: M calcd for 97 MoC₁₈H₁₆OS₄: 473.91; found: 473.76.

8.26 $(Et_4N)_2[MoO(S_2C_2HPh)_2]$ (41)

$$(\mathsf{Et_4N})_2 \left[\begin{array}{c} 0 \\ 1 \\ S \\ S \end{array} \right]$$

To a flame-dried side-arm flask, 1,3-dithione-2-one-4-phenyl (0.194 g, 1 mmol) was left to dissolve in methanol (25 mL, dry, degassed) for 15 minutes; the solution was cooled to 0 °C. Addition of the potassium hydroxide (0.141 g, 2.5 mmol) followed quickly and the solution was left to stir for 2 hours. In another Schlenk flask K₃Na[MoO₂(CN)₄] · 6 H₂O (0.240 g, 0.5 mmol) was dissolved in water (11 mL, distilled, degassed). The dithione solution was heated to 50 °C and the molybdenum salt solution was transferred via cannula across rapidly turning the yellow solution black and then quickly to red. After leaving this to stir for 45 minutes, tetraethylammonium bromide (0.210 g, 1 mmol) was added. Following another 45 minutes of

stirring at 50 °C the solution was red in appearance. The solvent was removed under reduced pressure. The residue was dissolved in acetonitrile (80 mL, dry, degassed) to give a red solution and yellow precipitate. This was filtered into a Schlenk flask and the solution was concentrated under reduced pressure. Subsequent, slow addition of diethyl ether (50 mL, dry degassed) gave a red precipitate. The remaining solvent was filtered off and the red precipitate was recrystallised once more. Removing all the solvent under vacuum gave a red solid (0.092 g, 26%). ¹H NMR (500 MHz, CD₃CN) 1.19 (tt, $J_1 = 7$ Hz, $J_2 = 1.8$ Hz, 24H, N-CH₂-CH₃), 3.12 (q, J = 7.2 Hz, 16H, N-CH₂-CH₃), 7.07 (t, J = 7.3 Hz, 2H, C-H), 7.23 (m, 7H, Ph-H), 7.86 (m, 3H, Ph-H); ¹³C NMR (126 MHz, CD₃CN) 7.70 (N-CH₂-CH₃), 53.01 (t, (N-CH₂-CH₃), 114.07 (C-H), 125.82 (Ph), 127.27 (Ph), 128.52 (Ph), 130.55 (Ph), 143.96 (Ph-C); $\tilde{\nu}_{\text{max}}/\text{cm}^{-1}$ (KBr) 2968 (C-H), 1018 (m), 878 (vw, Mo=O), 799 (m); MALDI-TOF m/z: M calcd for ⁹⁷MoC₁₆H₁₂OS₄: 445.88; found: 445.77.

8.27 $(Et_4N)_2[MoO(S_2C_2EtPh)_2]$ (79)

To a flame-dried side-arm flask 1,3-dithiol-2-one-4-phenyl-5-ethyl (0.445 g, 2 mmol) was added and dissolved in methanol (51 mL, dry, degassed). This solution was cooled to 0 °C and potassium hydroxide (0.281 g, 5 mmol) was added. After leaving the solution to stir for 2 hours, $K_3Na[MoO_2(CN)_4] \cdot 6H_2O$ (0.480 g, 1 mmol) was dissolved in water (11 mL distilled, degassed), and added to the gold, dithione solution. The subsequent blue solution was left to stir for 2 hours and 30 minutes at 50 °C

where it moved through a variety of colours before settling as a red/yellow colour. Tetraethylammonium bromide was added and the solution was left to stir for 45 minutes. After reducing the solution to dryness, acetonitrile (80 mL, dry, degassed) was added resulting in yellow residue and red liquor. The residue was filtered from the liquor and reduced to a minimum. Slow addition of diethyl ether elucidated a red precipitate. Removing the liquor and taking to dryness gave a red/yellow film (0.244 g, 32%). ¹H NMR (500 MHz, CD₃CN) 1.16 (tt, $J_1 = 7$ Hz, $J_2 = 1.8$ Hz, 24H, N-CH₂-CH₃), 3.15 (q, J = 7.3 Hz, 16H, N-CH₂-CH₃) 7.25 (m, 10H, PhH); ¹³C NMR (126 MHz, CD₃CN) 7.80 (N-CH₂-CH₃), 16.32 (-CH₂-CH₃), 30.47 (-CH₂-CH₃), 53.05 (t, N-CH₂-CH₃)), 125.50 (CH₂-CC-C), 126.80 (Ph), 128.07 (Ph), 128.25 (Ph), 128.68 (Ph), 129.83 (Ph), 130.54 (Ph), 136.95 (CH₂-CC-C); $\tilde{\nu}_{\text{max}}/\text{cm}^{-1}$ (KBr) 2966 (C-H), 1017 (m), 939 (Mo=O), 879 (w); MALDI-TOF m/z: M calcd for ⁹⁷MoC₂₀H₂₀OS₄: 501.95; found: 501.92.

8.28 $(Et_4N)_2[MoO(S_2C_2HBnOH)_2]$ (80)

$$(\mathsf{Et_4N})_2 \left[\begin{array}{c} \mathsf{OH} & \mathsf{OH} \\ \mathsf{O} & \mathsf{OH} \\ \mathsf{S} & \mathsf{NO} \\ \mathsf{S} & \mathsf{S} \end{array} \right]$$

To a flame-dried side-arm flask, 1,3-dithiol-2-one-4-benzyl alcohol (0.224 g, 1 mmol) was added and purged. This was dissolved in methanol (25 mL, dry, degassed) and cooled to 0 °C. Potassium hydroxide (0.141 g, 2.5 mmol) dissolved swiftly upon addition; the solution was left to stir for 2 hours affording a deep gold solution. The solution was then heated to 50 °C and $K_3Na[MoO_2(CN)_4] \cdot 6 H_2O$ (0.240 g, 0.5 mmol), dissolved in distilled water (11 mL, degassed), was transferred via cannula which rapidly gave a red solution (5 minutes). After leaving to stir

for 45 minutes, tetraethylammonium bromide (0.210 g, 1 mmol) was added and left to stir for another 45 minutes. The red solution was taken to dryness, redissolved in acetonitrile (40 mL, dry, degassed), and the liquor was removed from the yellow residue to a fresh Schlenk. After recrystallisation from diethyl ether, the red film obtained (0.080 g, 21%). ¹H NMR (500 MHz, CD₃CN) 1.19 (tt, $J_1 = 7$ Hz, $J_2 = 1.8$ Hz, 24H, N-CH₂-CH₃), 3.17 (q, J = 7.3 Hz, 16H, N-CH₂-CH₃), 4.50 (s, 4H, CH₂-OH), 6.65 (s, 2H, C-H), 7.16 (m, 5H, Ph-H), 7.32 (m, 5H, Ph-H); ¹³C NMR (126 MHz, CD₃CN) 7.75 (N-CH₂-CH₃), 53.09 (N-CH₂-CH₃), 64.37 (-CH₂-OH), 126.67 (Ph), 127.59 (Ph), 129.59 (Ph), 130.54 (Ph), 131.50 (Ph); $\tilde{\nu}_{\rm max}/{\rm cm}^{-1}$ (KBr) 3431 (O-H), 2925 (C-H), 1024 (w), 887 (vw, Mo=O); MALDI-TOF m/z: M calcd for ⁹⁷MoC₁₈H₁₆O₃S₄: 505.90; found: 505.86.

8.29 $(Et_4N)_2[MoO(S_2C_2HPhNH_2)_2]$ (81)

$$(\mathsf{Et_4N})_2 \left[\begin{array}{c} \mathsf{H_2N} \\ \\ \mathsf{S} \\ \\ \mathsf{S} \end{array} \right] \stackrel{\mathsf{NH_2}}{\longrightarrow} \left[\begin{array}{c} \mathsf{NH_2} \\ \\ \mathsf{S} \\ \\ \mathsf{S} \end{array} \right]$$

Within a flame-dried side-arm flask, 1,3-dithiol-2-one-4-para-aniline (0.105 g, 0.5 mmol) was dissolved in methanol (13 mL, dry degassed). After cooling to 0 °C, potassium hydroxide (0.0842 g, 1.5 mmol) was dissolved in the solution and left to stir for 2 hours. Separately, K₃Na[MoO₂(CN)₄] · 6 H₂O (0.120 g, 0.25 mmol) was dissolved in water (5 mL, distilled, degassed). After the two hours had elapsed, the dithione solution was heated to 50 °C and the molybdenum solution was transferred across and left to stir for 45 minutes. Tetraethylammonium bromide (0.105 g, 0.5 mmol) was added to the red solution and left to stir for another 45 minutes. This was reduced to dryness, taken up in acetonitrile (20 mL, dry, degassed) and the liquor filtered off from the yellow residue. The subsequent solution was reduced to a minimum, and

with the slow addition of diethyl ether (dry, degassed) a red/brown film was obtained (0.053 g, 29%). ¹H NMR (500 MHz, CD₃CN) 1.19 (tt, $J_1 = 7$ Hz, $J_2 = 1.8$ Hz, 12H, N-CH₂-CH₃), 3.17 (q, J = 7.2 Hz, 8H, N-CH₂-CH₃), 4.05 (s, 2H, NH₂), 6.56 (m, 4H, Ph-H), 6.95 (s, 1H, chC-H), 7.60 (d, $J_2 = 8.2$ Hz, 1H, Ph-H); ¹³C NMR (126 MHz, CD₃CN) 7.80 (N-CH₂-CH₃), 16.32 (-CH₂-CH₃), 30.47 (-CH₂-CH₃), 53.05 (t, N-CH₂-CH₃), 125.50 (CH₂-CC-C), 126.80 (Ph), 128.07 (Ph), 128.25 (Ph), 128.68 (Ph), 129.83 (Ph), 130.54 (Ph), 136.95 (CH₂-CC-C); $\tilde{\nu}_{\text{max}}/\text{cm}^{-1}$ (KBr) 3319 (N-H), 2976 (C-H), 1094 (s), 876 (Mo=O), 802 (s); MALDI-TOF m/z: M calcd for ⁹⁷MoC₁₆H₁₄OS₄ + H⁺: 476.90; found: 476.37.

8.30 $(Et_4N)_2[MoO(S_2C_2Ph_2)_2]$ (34)

To a flame-dried side-arm flask, $Mo(CO)_2(S_2C_2Ph_2)_2$ (0.083 g, 0.21 mmol) was dissolved in tetrahydrofuran (3 mL, dry, degassed) to give a purple solution. 25% in methanol tetraethylammonium hydroxide (227 µL, 0.41 mmol) was added to give a rapid formation of a red precipitate. The solution was left to stir for 8 hours and then reduced to dryness. The brown powder was taken up in acetonitrile (7 mL, dry, degassed) and filtered into a fresh Schlenk flask. Slow addition of diethyl ether (20 mL, dry, degassed) gave an orange precipitate. The recrystallisation with acetonitrile and ether was repeated twice more. Reducing to dryness gave a red solid (0.056 g, 31%). ¹H NMR (500 MHz, CD₃CN) 1.09 (tt, $J_1 = 7$ Hz, $J_2 = 1.8$ Hz, 24H, N-CH₂-CH₃), 3.04 (q, J = 7.2 Hz, 16H, N-CH₂-CH₃), 6.94-7.17 (m, 20H, Ph-H); $\tilde{\nu}_{max}/cm^{-1}$ (KBr) 2964 (C-H), 1261 (m), 1097 (s), 880 (s);

Raman Spectroscopy (Acetonitrile) 904 (Mo=O); MALDI-TOF m/z: M calcd for 97 MoC₂₈H₂₀OS₄: 597.95; found: 597.68.

8.31 $(Et_4N)_2[WO(S_2C_2HPh)_2]$ (88)

$$(\mathsf{Et_4N})_2 \boxed{ \begin{array}{c} 0 \\ 0 \\ S \end{array} \\ \begin{array}{c} 0 \\ S \end{array} \\$$

To a flame-dried side-arm flask, 1,3-dithiol-2-one-4-phenyl (0.194 g, 1 mmol) was added and purged. This was dissolved in methanol (25 mL, dry, degassed) and cooled to 0°C. Potassium hydroxide (0.141 g, 2.5 mmol) followed quickly and the solution was left to stir for 2 hours. In another Schlenk flask K₃Na[WO₂(CN)₄] · 6 H₂O (0.282 g, 0.5 mmol) was dissolved in water (11 mL, distilled, degassed). The dithione solution was heated to 50 °C and the molybdenum salt solution was transferred via cannula rapidly, giving a gold solution. After leaving this to stir for 45 minutes, tetraethylammonium bromide (0.420 g, 2 mmol) was added. Following another 45 minutes of stirring at 50 °C the solution was red in appearance. The solvent was removed under reduced pressure and acetonitrile (80 mL, dry, degassed). This was filtered into another Schlenk and the solution was concentrated under reduced pressure. Subsequent, slow addition of diethyl ether (80 mL, dry, degassed) gave a red precipitate. The remaining solvent was filtered off and the red precipitate was recrystallised once more. Removing all the solvent under vacuum gave a red solid (0.079 g, 20%). MALDI-TOF m/z: M calcd for $^{184}WC_{16}H_{12}OS_4$: 531.94; found: 531.93.

8.32 $(Et_4N)_2[WO(S_2C_2MeBnOH)_2]$ (90)

To a flame-dried side-arm flask, the dithione, 1,3-dithiol-2-one-4-benzyl alcohol-5-methyl (0.238 g, 1 mmol), was added and purged. The dithione was dissolved in methanol (26 mL, dry, degassed) and cooled to 0 °C. Potassium hydroxide (0.141 g, 2.5 mmol) was added to this gold solution and left to stir for 2 hours; the temperature of the solution was then raised to 55 °C. The tungsten precursor, $K_3Na[WO_2(CN)_4] \cdot 6 H_2O$ (0.282 g, 0.5 mmol), was dissolved in distilled water (11 mL, degassed) and transferred to the dithione solution whereupon the solution turned pink. Leaving this solution to stir for 45 minutes saw its colour change to red/yellow and tetraethylammonium bromide (0.210 g, 1 mmol) was added; this was left to stir for another 45 minutes. The solution was taken to dryness and dissolved in acetonitrile (40 mL, dry, degassed). The yellow residue was filtered off leaving behind a red liquor. Subsequent recrystallisation from diethyl ether yielded a dark red film (0.070 g, 16%). $\tilde{\nu}_{\rm max}/{\rm cm}^{-1}$ (KBr) 3292 (O–H), 2978 (C–H), 2054 (s), 1454 (s), 1034 (s), 797 (m); MALDI-TOF m/z: M calcd for $^{184}WC_{20}H_{20}O_3S_4$: 619.98; found: 619.84.

8.33 $NBu_4HCO_2 \cdot HCO_2H$ (92)

$$\begin{array}{c|c} & & & & & & & \\ & & & & & & & \\ & & & & & & \\ & & & & & & \\ & & & & & & \\ & & & & & & \\ & & & & & & \\ & & & & & & \\ & & & & & \\ & & & & & \\ & & & & & \\ & & & & & \\ & & & & & \\ & & & & & \\ & & & & \\ & & & & \\ & & & & \\ & & & & \\ & & & \\ & & & \\ & & & \\ & & & \\ & & & \\ & & & \\ & & & \\ & & \\ & & & \\ & \\ & \\ & \\ & \\ & & \\ & \\ & & \\ & \\ & \\ & \\ & \\ & \\ & \\ & \\ & \\ & \\ & \\ & \\ & \\ & \\ & \\ &$$

The reaction was carried out following the method reported by DuBois and coworkers. 142 To a Schlenk flask, tetrabutylammonium hydroxide (12.6 mL, 19 mmol, 1.5 M) was added followed by the dropwise addition of formic acid (0.96 mL, 19 mmol) over a 5-minute period. This was then left to stir at room temperature for 3 hours affording a colourless solution. Water (0.5 mL, distilled) was added and the organic phase was extracted using ethyl acetate $(3 \times 15 \,\mathrm{mL})$. After drying over magnesium sulphate, filtering, and reducing to dryness under reduced pressure, diethyl ether was sonicated through the resultant colourless oil. The diethyl ether was taken off and the oil was dried overnight. The white solid was recrystallised by dissolving the solid in a minimum of tetrahydrofuran and layering with hexane. A white solid was afforded (1.75 g (32%). ¹H NMR (500 MHz, CD₃CN) $0.97 \text{ (t, } J = 7.4 \text{ Hz, } 12 \text{H, } -\text{CH}_2 - \text{CH}_2 - \text{CH}_2 - \text{CH}_3), 1.35 \text{ (sx, } J = 7.4 \text{ Hz, } 8 \text{H,}$ $-CH_2-CH_2-CH_2-CH_3$, 1.55–1.65 (m, 8H, $-CH_2-CH_2-CH_2-CH_3$), 3.05-3.12(m, 8H, $-CH_2-CH_2-CH_2-CH_3$), 8.46 (s, 2H, $HCO_2 \cdot HCO_2H$); ¹³C NMR (126 MHz, $CD_3CN)$ 13.78 ($-CH_2-CH_2-CH_2-CH_3$), 20.33 (t, $-CH_2-CH_2-CH_2-CH_3$), 24.31 $-CH_2-CH_2-CH_2-CH_3$, 59.33 ($-CH_2-CH_2-CH_2-CH_3$), 166.49 ($HCO_2 \cdot HCO_2H$).

8.34 DFT Calculations

All calculations were performed using the Orca computational package. 205,206 Geometry optimisations were carried out using the triple- ζ basis set, def2-TZVP. Generalised-gradient approximation (GGA), meta-generalised approximation (meta-GGA), and hybrid functionals were used in the geometry optimisation: BP86, B3LYP, PBE0, TPSS, and ω B97X. $^{188-190,192,193,204,216,217,240}$ Structures were geometry optimised in the gas phase with the default convergence criteria and confirmed as minima through frequency calculations where imaginary stretches (negative frequencies) were looked for. Initial atom coordinates for the molybdenum-oxo bis-dithiolene core were obtained from the [Mo^V(bdt)₂]⁻ crystal structure, and subsequent structural additions were refined from there through geometry optimisations. 130

8.35 Catalytic Studies

8.35.1 Electrocatalytic Proton Reduction Studies

To the working electrode compartment of a three-compartment cell under an argon atmosphere, the catalyst (0.05 mm) was dissolved in a tetrabutylammonium tetrafluoroborate/acetonitrile solution (0.1 m). Equivalents of trifluoroacetic acid were added (not in a glove box), and then CVs were taken.

8.35.2 Photocatalytic Carbon Dioxide Reduction Studies

To a 4 mL Young's tap quartz cuvette under an argon atmosphere, the photosensitiser ($[Ru(bpy)_3]Cl_2$, 0.5 mM), the base, triethanolamine, and carbon dioxide saturated acetonitrile (1:5, v/v), the sacrificial proton and electron donor (BIH, Scheme 6.1, 0.1 M) and the catalyst (0.05 mM) were added. This solution was

irradiated for 15 hours using a xenon lamp (400 nm–1200 nm). A sample of the cuvette head space was taken and a gas chromatogram was recorded to test for any carbon monoxide and hydrogen production. To test for formate production, a sample of the solution was passed through an ion exchange chromatography system.

8.35.3 Electrocatalytic Formate Oxidation Studies: Order with Respect to Formate

In a glove box with an argon atmosphere, to the working electrode compartment of a three-compartment cell, the catalyst (0.05 mM) was dissolved in a tetrabutylammonium tetrafluoroborate/acetonitrile solution (0.1 M). A 3 mm diameter glassy carbon electrode was used as the working electrode; the counter electrode was a platinum wire; a silver wire as a pseudo-reference electrode. Starting with zero equivalents of tetrabutylammonium formate (92), twelve CVs were performed until 170 equivalents of the formate salt were added. After the final addition of tetrabutylammonium formate (92), ferrocene was added as an internal reference. The changes in the CV wave currents were measured and the appropriate plots were constructed to determine the order with respect to formate.

8.35.4 Electrocatalytic Formate Oxidation Studies: Order with Respect to Catalyst

In a glove box with an argon atmosphere, to the working electrode compartment of a three-compartment cell, tetrabutylammonium formate (92) 8.2 mM was dissolved in a solution of tetrabutylammonium tetrafluoroborate/acetonitrile (0.1 M). Aliquots of catalyst were added until the concentration of catalyst reached 6 mM. A 3 mm diameter glassy carbon electrode was used as the working electrode; the counter electrode was a platinum wire; a silver wire was used as a pseudo-reference electrode.

After the final addition of catalyst, ferrocene was added as an internal reference. The changes in the CV wave currents were measured and the appropriate plots were constructed to determine the order with respect to the catalyst.

8.35.5 Oxygen Atom Transfer Catalytic Studies: ³¹P NMR Spectroscopy

In a glove box with an argon atmosphere, to a Young's tap NMR tube, 3 mm of catalyst, and 9 mm of triphenylphosphine were added. Outside of the glove box, DMSO (dry, degassed, 0.5 mL) was added to dissolve the solid material in the NMR tube. The experiment was monitored over a 32-hour period using ³¹P NMR spectroscopy, where a spectrum was taken every 4 hours.

8.35.6 Oxygen Atom Transfer Catalytic Studies: UV/Vis Spectroscopy

In a glove box with an argon atmosphere, to a Young's tap NMR tube, $3 \,\mathrm{mM}$ of catalyst, $9 \,\mathrm{mM}$ of triphenylphosphine, and trimethylamine N-oxide ($12 \,\mathrm{mM}$) were added. Outside of the glove box, DMSO (dry, degassed, $0.5 \,\mathrm{mL}$) was used to dissolve the solids in the NMR tube. The experiment was monitored over a 32-hour period using $^{31}\mathrm{P}$ NMR spectroscopy, where a spectrum was taken every 4 hours.

8.36 X-Ray Crystallography

For each sample, crystals were suspended in oil and one was mounted on a glass fibre and fixed in the nitrogen stream of the diffractometer. Data was collected using either Cu- $K\alpha$ radiation ($\lambda = 1.541\,84\,\text{Å}$) using a Rigaku FR-E++ equipped with a copper rotating anode, equipped with confocal mirrors (75) or Mo- $K\alpha$

 $(\lambda=0.710\,73\,\text{Å})$ radiation (84, 85, 86). Data was collected and processed using CrystalClear-SM Expert and CrysAlisPro. 241

Structures were determined through dual space methods in SHELXT-2018²⁴² and refined by full-matrix least-squares methods on F^2 in SHELXL-2018.²⁴³ Nonhydrogen atoms were refined with anisotropic thermal parameters. Hydrogen atoms bound to carbon were included in idealised positions and their $U_{\rm iso}$ values were set to ride on the $U_{\rm eq}$ values of the parent atom.

Table 8.1: A Summary of the X-ray data for compounds 64, 73, 74 and 75.

	75	84	82	98
Formula	$C_9H_6S_2O$	$\mathrm{MoN}_2\mathrm{S}_4$	$\mathrm{MoS_4N_2C_8H_{20}}$	$C_{16}H_{40}MoN_2S_9$
Formula Weight	194.26	252.20	368.44	645.97
Crystal system	Orthorhombic	Orthorhombic	Triclinic	Orthorhombic
Space group	Pbca	Pnma	$Par{1}$	Ibca
$a/ ext{Å}$	10.47280(10)	9.5363(5)	12.9034(4)	13.1131(4)
$b/{ m \AA}$	8.01040(10)	6.9342(4)	13.5531(4)	15.4439(5)
$c/ ext{Å}$	20.4451(2)	12.1017(6)	15.8472(4)	27.2501(8)
$lpha/\circ$	06	06	110.944(2)	06
β/\circ	06	06	112.816(3)	06
o/ <i>L</i>	06	06	90.998(2)	06
$V/ m \AA^3$	1715.17(3)	800.24(7)	2346.23(13)	5518.6(3)
Z	∞	4	20	∞
T/K	295.76(10)	110(3)	102.15	100.04(12)
Crystal size/mm	$0.098 \times 0.116 \times 0.401$	$0.103 \times 0.262 \times 0.465$	$0.283 \times 0.557 \times 0.711$	$0.255 \times 0.489 \times 0.891$
$\lambda/ ilde{ m A}$	1.54184	0.71073	0.71073	0.71073
$_{\circ}/ heta$	77.646	30.766	30.889	30.653
Reflections Measured	7489	4570	33883	15535
Unique Reflections	1682	1082	11796	3508
R_{int}	0.0213	0.0744	0.0513	0.0323
No. parameters	109	40	431	133
$R_1(I>2\sigma_I)$	0.0336	0.0541	0.0596	0.0220
wR_2 (all data)	0.0913	0.1434	0.1651	0.0517

8.37 Non-Standard Glassware: The Hexa-Schlenk Flask

The Hexa-Schlenk flask was developed as a workaround to the scalability problem affecting the radical dithione insertion reactions by performing six reactions simultaneously. It comprises six Schlenk flasks joined together through glass bridges in a hexagonal formation, with two Young's Taps for connection to the Schlenk line. Figure 8.1 shows the glassware.



Figure 8.1: The Non-Standard Glassware, the Hexa-Schlenk.

References

- (1) S. Shafiee and E. Topal, Energ. Policy, 2009, 37, 181–189.
- (2) M. Wiatros-Motyka, N. Fulghum and D. Jones, *Global electricity review 2024*, https://ember-energy.org/latest-insights/global-electricity-review-2024/ (visited on 06/03/2025).
- (3) S. Rehman, L. M. Al-Hadhrami and M. M. Alam, *Renew. Sustain. Energy Rev*, 2015, **44**, 586–598.
- (4) T. Bauer, C. Odenthal and A. Bonk, Chem. Ing. Tech., 2021, 93, 534–546.
- (5) M. Zheng, The Environmental Impacts of Lithium and Cobalt Mining, 2023, https://earth.org/lithium-and-cobalt-mining/ (visited on 06/03/2025).
- (6) K. Mazloomi and C. Gomes, *Renew. Sustain. Energ. Rev.*, 2012, **16**, 3024–3033.
- (7) S. Lipiäinen, K. Lipiäinen, A. Ahola and E. Vakkilainen, *Int. J. Hydrogen Energ.*, 2023, **48**, 31317–31329.
- (8) J. Rostrup-Nielsen, in *Studies Surface Sci. Catal.* Elsevier, 2004, vol. 147, pp. 121–126.
- (9) R. W. Howarth and M. Z. Jacobson, Energy Sci. Eng., 2021, 9, 1676–1687.

- (10) G. A. Schmidt, R. A. Ruedy, R. L. Miller and A. A. Lacis, J. Geophys. Res., 2010, 115.
- (11) S. Wang, A. Lu and C.-J. Zhong, Nano Converg., 2021, 8, 1–23.
- (12) M. Maier, K. Smith, J. Dodwell, G. Hinds, P. R. Shearing and D. J. L. Brett, *Int. J. Hydrogen Energ.*, 2022, 47, 30–56.
- (13) W. Li, R. Cao, L. Xu and L. Qiao, Corrosion Commun., 2021, 4, 23–32.
- (14) E. Wiberg and N. Wiberg, *Inorganic Chemistry*, Academic Press, 2001.
- (15) K. Müller, K. Brooks and T. Autrey, *Energ. Fuels*, 2017, **31**, 12603–12611.
- (16) Y. Zhang, S. Rump and V. N. Gladyshev, Coord. Chem. Rev., 2011, 255, 1206–1217.
- (17) T. M. Buscagan and D. C. Rees, *Joule*, 2019, **3**, 2662–2678.
- (18) R. Hille, Chem. Rev., 1996, **96**, 2757–2816.
- (19) C. Scott, T. W. Lyons, A. Bekker, Y.-A. Shen, S. W. Poulton, X.-L. Chu and A. D. Anbar, *Nature*, 2008, 452, 456–459.
- (20) K. K. Bertine and K. K. Turekian, Geochim. Cosmochim. Acta, 1973, 37, 1415–1434.
- (21) S. R. Taylor and S. M. McLennan, Rev. Geophys., 1995, 33, 241–265.
- (22) R. Hille, Trends Biochem. Sci., 2002, 27, 360–367.
- (23) L. B. Maia and J. J. G. Moura, Chem. Rev., 2014, 114, 97.
- (24) R. J. P. Williams and J. J. R. F. Da Silva, Biochem. Biophys. Res. Commun., 2002, 292, 293–299.
- (25) D.-Y. Huang, A. Furukawa and Y. Ichikawa, *Arch. Biochem. Biophys.*, 1999,364, 264–272.

- (26) R. M. Garrett, J. L. Johnson, T. N. Graf, A. Feigenbaum and K. V. Rajagopalan, Proc. Natl. Acad. Sci. USA, 1998, 95, 6394–6398.
- (27) L. B. Maia and J. J. G. Moura, in Reference Module in Chemistry, Molecular Sciences and Chemical Engineering, Netherlands, 2018, pp. 1–19.
- (28) S. Grimaldi, B. Schoepp-Cothenet, P. Ceccaldi, B. Guigliarelli and A. Magalon, *Biochim. Biophys. Acta*, 2013, **1827**, 1048–1085.
- (29) C. Hesberg, R. Hänsch, R. R. Mendel and F. Bittner, J. Biol. Chem., 2004, 279, 13547–13554.
- (30) R. Hille, J. Hall and P. Basu, Chem. Rev., 2014, 114, 3963–4038.
- (31) H. Dobbek, L. Gremer, R. Kiefersauer, R. Huber and O. Meyer, *Proc. Natl. Acad. Sci. USA*, 2002, 99, 15971–15976.
- (32) M. Seo, H. Koiwai, S. Akaba, T. Komano, T. Oritani, Y. Kamiya and T. Koshiba, *Plant J.*, 2000, 23, 481–488.
- (33) J. Johannes, M.-C. Unciuleac, T. Friedrich, E. Warkentin, U. Ermler and M. Boll, *Biochemistry*, 2008, 47, 4964–4972.
- (34) J. O. Sass, A. Gunduz, C. Araujo Rodrigues Funayama, B. Korkmaz, K. G. Dantas Pinto, B. Tuysuz, L. Yanasse Dos Santos, E. Taskiran, M. de Fátima Turcato, C.-W. Lam, J. Reiss, M. Walter, C. Yalcinkaya and J. S. Camelo Junior, *Brain Dev.*, 2010, 32, 544–549.
- (35) C. Kisker, H. Schindelin, A. Pacheco, W. A. Wehbi, R. M. Garrett, K. V. Rajagopalan, J. H. Enemark and D. C. Rees, *Cell*, 1997, **91**, 973–983.
- (36) R. S. Byrne, R. Hänsch, R. R. Mendel and R. Hille, J. Biol. Chem., 2009,284, 35479–35484.
- (37) M. J. Romão, Dalton Trans., 2009, 4053–4068.

- (38) G. N. George, J. Hilton, C. Temple, R. C. Prince and K. V. Rajagopalan, J. Am. Chem. Soc., 1999, 121, 1256–1266.
- (39) B. E. Schultz, R. Hille and R. H. Holm, J. Am. Chem. Soc., 1995, 117, 827–828.
- (40) S. D. Garton, J. Hilton, H. Oku, B. R. Crouse, K. V. Rajagopalan and M. K. Johnson, J. Am. Chem. Soc., 1997, 119, 12906–12916.
- (41) G. N. George, J. Hilton and K. V. Rajagopalan, J. Am. Chem. Soc., 1996,118, 1113–1117.
- (42) T. Hartmann and S. Leimkühler, FEBS J., 2013, **280**, 6083–6096.
- J. C. Boyington, V. N. Gladyshev, S. V. Khangulov, T. C. Stadtman and
 P. D. Sun, *Science*, 1997, 275, 1305–1308.
- (44) M. Jormakka, S. Tornroth, B. Byrne and S. Iwata, Science, 2002, 295, 1863–1868.
- (45) H. C. A. Raaijmakers and M. J. Romão, J. Biol. Inorg. Chem., 2006, 11, 849–854.
- (46) M. Jormakka, S. Törnroth, J. Abramson, B. Byrne and S. Iwata, *Acta Cryst. D*, 2002, **58**, 160–162.
- (47) L. B. Maia, L. Fonseca, I. Moura and J. J. G. Moura, J. Am. Chem. Soc., 2016, 138, 8834–8846.
- (48) M. Kathiresan, B. Ambrose, N. Angulakshmi, D. E. Mathew, D. Sujatha and A. M. Stephan, *J. Mater. Chem. A*, 2021, **9**, 27215–27233.
- (49) D. Niks and R. Hille, in *Methods in Enzymology*, Elsevier, 2018, vol. 613, pp. 277–295.

- (50) C. S. Mota, M. G. Rivas, C. D. Brondino, I. Moura, J. J. G. Moura, P. J. González and N. M. F. S. A. Cerqueira, J. Biol. Inorg. Chem., 2011, 16, 1255–1268.
- (51) N. M. F. S. A. Cerqueira, P. A. Fernandes, P. J. Gonzalez, J. J. G. Moura and M. J. Ramos, *Inorg. Chem.*, 2013, 52, 10766–10772.
- (52) M. Tiberti, E. Papaleo, N. Russo, L. De Gioia and G. Zampella, *Inorg. Chem.*, 2012, 51, 8331–8339.
- (53) G. Dong and U. Ryde, J. Biol. Inorg. Chem., 2018, 23, 1243–1254.
- (54) W. E. Robinson, A. Bassegoda, E. Reisner and J. Hirst, J. Am. Chem. Soc., 2017, 139, 9927–9936.
- (55) H. Kumar, M. Khosraneh, S. S. M. Bandaru, C. Schulzke and S. Leimkühler, *Molecules*, 2023, **28**, 1537.
- (56) R. K. Thauer, B. Käufer and G. Fuchs, Eur. J. Biochem., 1975, **55**, 111–117.
- (57) H. Raaijmakers, S. Macieira, J. M. Dias, S. Teixeira, S. Bursakov, R. Huber, J. J. Moura, I. Moura and M. J. Romão, Structure, 2002, 10, 1261–1272.
- (58) M. M. Wuebbens and K. Rajagopalan, J. Biol. Chem., 1993, 268, 13493– 13498.
- (59) J. A. Santamaria-Araujo, V. Wray and G. Schwarz, J. Biol. Inorg. Chem., 2012, 17, 113–122.
- (60) M. M. Wuebbens and K. Rajagopalan, J. Biol. Chem., 2003, 278, 14523– 14532.
- (61) A. Matthies, M. Nimtz and S. Leimkühler, *Biochemistry*, 2005, 44, 7912–7920.
- (62) W. R. Hagen, Coord. Chem. Rev., 2011, **255**, 1117–1128.

- (63) H. Tomatsu, J. Takano, H. Takahashi, A. Watanabe-Takahashi, N. Shibagaki and T. Fujiwara, *Proc. Natl. Acad. Sci.*, 2007, **104**, 18807–18812.
- (64) I. Baxter, B. Muthukumar, H. C. Park, P. Buchner, B. Lahner, J. Danku, K. Zhao, J. Lee, M. J. Hawkesford, M. L. Guerinot and D. E. Salt, PLoS Genet., 2008, 4, e1000004.
- (65) M. Tejada-Jiménez, A. Galván and E. Fernández, *Proc. Natl. Acad. Sci.*, 2011, **108**, 6420–6425.
- (66) A. Llamas, R. R. Mendel and G. Schwarz, J. Biol. Chem., 2004, 279, 55241–55246.
- (67) S. Leimkühler, M. M. Wuebbens and K. Rajagopalan, Coord. Chem. Rev., 2011, 255, 1129–1144.
- (68) A. Llamas, T. Otte, G. Multhaup, R. R. Mendel and G. Schwarz, J. Biol. Chem., 2006, 281, 18343–18350.
- (69) R. R. Mendel, J. Biol. Chem., 2013, 288, 13165–13172.
- (70) H. K. Joshi, J. J. A. Cooney, F. E. Inscore, N. E. Gruhn, D. L. Lichtenberger and J. H. Enemark, *Proc. Natl. Acad. Sci. USA*, 2003, **100**, 3719–3724.
- (71) F. E. Inscore, R. McNaughton, B. L. Westcott, M. E. Helton, R. Jones, I. K. Dhawan, J. H. Enemark and M. L. Kirk, *Inorg. Chem.*, 1999, 38, 1401–1410.
- (72) J. McMaster, M. D. Carducci, Y.-S. Yang, E. I. Solomon and J. H. Enemark, Inorg. Chem., 2001, 40, 687–702.
- (73) J. W. Lauher and R. Hoffmann, J. Am. Chem. Soc., 1976, 98, 1729–1742.
- (74) M. J. van Stipdonk, P. Basu, S. A. Dille, J. K. Gibson, G. Berden and J. Oomens, J. Phys. Chem. A, 2014, 118, 5407–5418.
- (75) C. K. Jørgensen, Coord. Chem. Rev., 1966, 1, 164–178.

- (76) R. Eisenberg and H. B. Gray, *Inorg. Chem.*, 2011, **50**, 9741–9751.
- (77) R. K. Szilagyi, B. S. Lim, T. Glaser, R. H. Holm, B. Hedman, K. O. Hodgson and E. I. Solomon, J. Am. Chem. Soc., 2003, 125, 9158–9169.
- (78) R. R. Kapre, E. Bothe, T. Weyhermüller, S. DeBeer George and K. Wieghardt, *Inorg. Chem.*, 2007, **46**, 5642–5650.
- (79) K. Ray, S. DeBeer George, E. I. Solomon, K. Wieghardt and F. Neese, Chem. Eur. J., 2007, 13, 2783–2797.
- (80) D. R. Gisewhite, J. Yang, B. R. Williams, A. Esmail, B. Stein, M. L. Kirk and S. J. N. Burgmayer, J. Am. Chem. Soc., 2018, 140, 12808–12818.
- (81) C. Gates, H. Varnum, C. Getty, N. Loui, J. Chen, M. L. Kirk, J. Yang and S. J. Nieter Burgmayer, *Inorg. Chem.*, 2022, 61, 13728–13742.
- (82) H. Schindelin, C. Kisker and D. C. Rees, J. Biol. Inorg. Chem., 1997, 2, 773–781.
- (83) P. Basu and S. J. N. Burgmayer, Coord. Chem. Rev., 2011, 255, 1016–1038.
- (84) D. Collison, C. D. Garner and J. A. Joule, Chem. Soc. Rev., 1996, 25, 25–32.
- (85) S. J. N. Burgmayer, M. Kim, R. Petit, A. Rothkopf, A. Kim, S. BelHamdounia, Y. Hou, A. Somogyi, D. Habel-Rodriguez, A. Williams and M. L. Kirk, J. Inorg. Biochem., 2007, 101, 1601–1616.
- (86) Y. Yan, C. Keating, P. Chandrasekaran, U. Jayarathne, J. T. Mague, S. DeBeer, K. M. Lancaster, S. Sproules, I. V. Rubtsov and J. P. Donahue, Inorg. Chem., 2013, 52, 6743–6751.
- (87) D. Niks and R. Hille, *Protein Sci.*, 2019, **28**, 111–122.
- (88) J.-J. Wang, S. Groysman, S. C. Lee and R. Holm, J. Am. Chem. Soc., 2007, 129, 7512–7513.

- (89) S. S. Pawar, R. N. Ketkar, P. B. Gaware, K. U. Jagushte, D. Dhawne, S. N. Save, S. Sharma, G. Periyasamy, N. Chimthanawala, S. Sathaye, S. V. Joshi and N. Sadhukhan, *Dalton Trans.*, 2024, 53, 5770–5774.
- (90) J. H. Enemark, J. J. A. Cooney, J.-J. Wang and R. H. Holm, Chem. Rev., 2004, 104, 1175–1200.
- (91) B. S. Lim, M. W. Willer, M. Miao and R. H. Holm, J. Am. Chem. Soc., 2001, 123, 8343–8349.
- (92) S. Groysman, J.-J. Wang, R. Tagore, S. C. Lee and R. H. Holm, J. Am. Chem. Soc., 2008, 130, 12794–12807.
- (93) J. Mitra and S. Sarkar, *Inorg. Chem.*, 2013, **52**, 3032–3042.
- (94) J. A. McCleverty, J. Locke, B. Ratcliff and E. J. Wharton, *Inorg. Chim. Acta*, 1969, 3, 283–286.
- (95) M. A. Ansari, J. Chandrasekaran and S. Sarkar, *Inorg. Chim. Acta*, 1987,133, 133–136.
- (96) G.-E. Matsubayashi, T. Nojo and T. Tanaka, *Inorg. Chim. Acta*, 1988, **154**, 133–135.
- (97) D. Coucouvanis, A. Hadjikyriacou, A. Toupadakis, S. M. Koo, O. Ileperuma,
 M. Draganjac and A. Salifoglou, *Inorg. Chem.*, 1991, 30, 754–767.
- (98) H. Oku, N. Ueyama, M. Kondo and A. Nakamura, *Inorg. Chem.*, 1994, 33, 209–216.
- (99) H. Oku, N. Ueyama and A. Nakamura, *Inorg. Chem.*, 1997, **36**, 1504–1516.
- (100) J. P. Donahue, C. R. Goldsmith, U. Nadiminti and R. H. Holm, J. Am. Chem. Soc., 1998, 120, 12869–12881.

- (101) E. S. Davies, R. L. Beddoes, D. Collison, A. Dinsmore, A. Docrat, J. A. Joule, C. R. Wilson and C. D. Garner, J. Chem. Soc., Dalton Trans., 1997, 3985–3996.
- (102) T. Fogeron, J.-P. Porcher, M. Gomez-Mingot, T. K. Todorova, L.-M. Chamoreau, C. Mellot-Draznieks, Y. Li and M. Fontecave, *Dalton Trans.*, 2016, 45, 14754–14763.
- (103) T. Fogeron, P. Retailleau, L.-M. Chamoreau, Y. Li and M. Fontecave, Angew. Chem. Int. Ed., 2018, 57, 17033–17037.
- (104) M. Ahmadi, C. Fischer, A. C. Ghosh and C. Schulzke, Front. Chem., 2019,7, 486.
- (105) P. Samuel, Ph.D. Thesis, University of Göttingen, 2011.
- (106) H. Sugimoto, K. Suyama, K. Sugimoto, H. Miyake, I. Takahashi, S. Hirota and S. Itoh, *Inorg. Chem.*, 2008, 47, 10150–10157.
- (107) C. Schulzke, Dalton Trans., 2005, 713–720.
- (108) H. Sugimoto, M. Tarumizu, K. Tanaka, H. Miyake and H. Tsukube, *Dalton Trans.*, 2005, 3558–3565.
- (109) H. Sugimoto, M. Harihara, M. Shiro, K. Sugimoto, K. Tanaka, H. Miyake and H. Tsukube, *Inorg. Chem.*, 2005, 44, 6386–6392.
- (110) M. Ahmadi, Ph.D. Thesis, Mathematisch-Naturwissenschaftliche Fakultät der Universität Greifswald, 2019.
- (111) A. C. Ghosh, P. P. Samuel and C. Schulzke, *Dalton Trans.*, 2017, 46, 7523–7533.
- J.-P. Porcher, T. Fogeron, M. Gomez-Mingot, E. Derat, L.-M. Chamoreau,Y. Li and M. Fontecave, Angew. Chem. Int. Ed., 2015, 127, 14296–14299.

- (113) R. A. Rothery, B. Stein, M. Solomonson, M. L. Kirk and J. H. Weiner, Proc. Natl. Acad. Sci. USA, 2012, 109, 14773–14778.
- (114) T. Fogeron, T. K. Todorova, J.-P. Porcher, M. Gomez-Mingot, L.-M. Chamoreau, C. Mellot-Draznieks, Y. Li and M. Fontecave, ACS Catal., 2018, 8, 2030–2038.
- (115) C. S. Seu, A. M. Appel, M. D. Doud, D. L. DuBois and C. P. Kubiak, Energ. Environ. Sci., 2012, 5, 6480–6490.
- (116) D. K. Bediako, B. H. Solis, D. K. Dogutan, M. M. Roubelakis, A. G. Maher, C. H. Lee, M. B. Chambers, S. Hammes-Schiffer and D. G. Nocera, Proc. Natl. Acad. Sci. USA, 2014, 111, 15001–15006.
- (117) C. G. Margarit, N. G. Asimow, M. I. Gonzalez and D. G. Nocera, J. Phys. Chem. Lett., 2020, 11, 1890–1895.
- (118) J. Hawecker, J.-M. Lehn and R. Ziessel, *J. Chem. Soc., Chem. Commun.*, 1985, 56–58.
- (119) H. Ishida, T. Terada, K. Tanaka and T. Tanaka, *Inorg. Chem.*, 1990, 29, 905–911.
- (120) Y. Arikawa, I. Tabata, Y. Miura, H. Tajiri, Y. Seto, S. Horiuchi, E. Sakuda and K. Umakoshi, *Chem. Eur. J.*, 2020, **26**, 5603–5606.
- (121) Y. Arikawa, T. Nakamura, S. Ogushi, K. Eguchi and K. Umakoshi, *Dalton Trans.*, 2015, 44, 5303–5305.
- (122) R. Tatematsu, T. Inomata, T. Ozawa and H. Masuda, *Angew. Chem. Int. Ed.*, 2016, **55**, 5247–5250.
- (123) T. C. Johnson, D. J. Morris and M. Wills, Chem. Soc. Rev., 2010, 39, 81–88.

- (124) R. Kanega, N. Onishi, L. Wang and Y. Himeda, *ACS Catal.*, 2018, **8**, 11296–11301.
- (125) A. Kumar, S. Semwal and J. Choudhury, ACS Catal., 2019, 9, 2164–2168.
- (126) D. V. Fomitchev, B. S. Lim and R. H. Holm, *Inorg. Chem.*, 2001, **40**, 645–654.
- (127) A. Thapper, R. J. Deeth and E. Nordlander, *Inorg. Chem.*, 2002, 41, 6695–6702.
- (128) U. Ryde, C. Schulzke and K. Starke, J. Biol. Inorg. Chem., 2009, 14, 1053– 1064.
- Y. Ha, A. L. Tenderholt, R. H. Holm, B. Hedman, K. O. Hodgson and
 E. I. Solomon, J. Am. Chem. Soc., 2014, 136, 9094–9105.
- (130) P. Hrobárik, O. L. Malkina, V. G. Malkin and M. Kaupp, Chem. Phys., 2009, 356, 229–235.
- (131) T. Amano, N. Ochi, H. Sato and S. Sakaki, J. Am. Chem. Soc., 2007, 129, 8131–8138.
- (132) T. Waters, X.-B. Wang, X. Yang, L. Zhang, R. A. O'Hair, L.-S. Wang and A. G. Wedd, J. Am. Chem. Soc., 2004, 126, 5119–5129.
- (133) M. Hofmann, J. Biol. Inorg. Chem., 2007, 12, 989–1001.
- (134) J. Fritscher, P. Hrobárik and M. Kaupp, *Inorg. Chem.*, 2007, **46**, 8146–8161.
- (135) J. P. McNamara, I. H. Hillier, T. S. Bhachu and C. D. Garner, *Dalton Trans.*, 2005, 3572–3579.
- (136) T. Reda, C. M. Plugge, N. J. Abram and J. Hirst, Proc. Natl. Acad. Sci. USA, 2008, 105, 10654–10658.
- (137) J. P. Collin, A. Jouaiti and J. P. Sauvage, *Inorg. Chem.*, 1988, 27, 1986–1990.

- (138) L. Chen, Z. Guo, X.-G. Wei, C. Gallenkamp, J. Bonin, E. Anxolabéhère-Mallart, K.-C. Lau, T.-C. Lau and M. Robert, J. Am. Chem. Soc., 2015, 137, 10918–10921.
- (139) S.-N. Pun, W.-H. Chung, K.-M. Lam, P. Guo, P.-H. Chan, K.-Y. Wong, C.-M. Che, T.-Y. Chen and S.-M. Peng, J. Chem. Soc., Dalton Trans., 2002, 575–583.
- (140) F. Franco, C. Cometto, F. F. Vallana, F. Sordello, E. Priola, C. Minero,C. Nervi and R. Gobetto, Chem. Commun., 2014, 50, 14670–14673.
- (141) S. Roy, B. Sharma, J. Pécaut, P. Simon, M. Fontecave, P. D. Tran, E. Derat and V. Artero, J. Am. Chem. Soc., 2017, 139, 3685–3696.
- (142) B. R. Galan, J. Schöffel, J. C. Linehan, C. Seu, A. M. Appel, J. A. S. Roberts, M. L. Helm, U. J. Kilgore, J. Y. Yang, D. L. DuBois and C. P. Kubiak, J. Am. Chem. Soc., 2011, 133, 12767–12779.
- (143) P. Kang, C. Cheng, Z. Chen, C. K. Schauer, T. J. Meyer and M. Brookhart, J. Am. Chem. Soc., 2012, 134, 5500-5503.
- (144) P. Kang, T. J. Meyer and M. Brookhart, Chem. Sci., 2013, 4, 3497–3502.
- (145) Y. Gareau and A. Beauchemin, *ChemInform*, 1999, **30**, no-no.
- (146) F. Haque, Ph.D. Thesis, University of East Anglia, 2022.
- (147) H. Sashida, K. Ohyanagi, M. Minoura and K.-Y. Akiba, *J. Chem. Soc.*, *Perkin Trans.* 1, 2002, 606–612.
- (148) H. Yu, R. N. Richey, M. W. Carson and M. J. Coghlan, Org. Lett., 2006, 8, 1685–1688.
- (149) A. M. Hounslow, S. F. Lincoln and E. R. T. Tiekink, J. Chem. Soc., Dalton Trans., 1989, 233–236.
- (150) L. Jamir, R. Yella and B. K. Patel, J. Sulfur Chem., 2009, 30, 128–134.

- (151) P. Chandrasekaran, K. Arumugam, U. Jayarathne, L. M. Pérez, J. T. Mague and J. P. Donahue, *Inorg. Chem.*, 2009, 48, 2103–2113.
- (152) J. P. Smit, W. Purcell, A. Roodt and J. G. Leipoldt, *Polyhedron*, 1993, 12, 2271–2277.
- (153) G. N. Schrauzer and V.-P. Mayweg, J. Am. Chem. Soc., 1965, 87, 1483– 1489.
- (154) B. S. Lim, J. P. Donahue and R. H. Holm, *Inorg. Chem.*, 2000, **39**, 263–273.
- (155) D. Tate, W. R. Knipple and J.-M. Augl, *Inorq. Chem.*, 1962, 1, 433–434.
- (156) G. Schrauzer, V. Mayweg and W. Heinrich, J. Am. Chem. Soc., 1966, 88, 5174–5179.
- (157) W. Ried and M. Wegwitz, Justus Liebigs Ann. Chem., 1975, 1975, 89–94.
- (158) A. Sugawara, T. Sato and R. Sato, Bull. Chem. Soc. Jpn., 1989, 62, 339–341.
- (159) S. Yamada, N. Mino, N. Nakayama and M. Ohashi, J. Chem. Soc., Perkin Trans. 1, 1984, 2497–2499.
- (160) H. Jin, C. Gu, Z. Xiao, Q. Tan, L. Liu, L.-B. Han, W.-H. Chen and T. Chen, Eur. J. Org. Chem., 2023, 26, e202300397.
- (161) J.-P. Porcher, T. Fogeron, M. Gomez-Mingot, L.-M. Chamoreau, Y. Li and M. Fontecave, Chem. Eur. J., 2016, 105, 4447–4453.
- (162) J. F. Briones and H. M. L. Davies, Org. Lett., 2011, 13, 3984–3987.
- (163) B. M. Nugent, A. L. Williams, E. Prabhakaran and J. N. Johnston, *Tetra-hedron*, 2003, 59, 8877–8888.
- (164) S. Menning, M. Krämer, B. A. Coombs, F. Rominger, A. Beeby, A. Dreuw and U. H. Bunz, J. Am. Chem. Soc., 2013, 135, 2160–2163.

- (165) S. Mondal, T. Pain, K. Sahu and S. Kar, ACS Omega, 2021, 6, 22922–22936.
- (166) S. Boyde, C. D. Garner, J. A. Joule and D. J. Rowe, J. Chem. Soc., Chem. Commun., 1987, 800–801.
- (167) S. Groysman and R. Holm, *Inorg. Chem.*, 2007, **46**, 4090–4102.
- (168) H. Sugimoto, H. Tano, K. Suyama, T. Kobayashi, H. Miyake, S. Itoh, R. P. Mtei and M. L. Kirk, *Dalton Trans.*, 2011, 40, 1119–1131.
- (169) K. G. Matz, R. P. Mtei, R. Rothstein, M. L. Kirk and S. J. N. Burgmayer, Inorg. Chem., 2011, 50, 9804–9815.
- (170) D. R. Gisewhite, A. L. Nagelski, D. C. Cummins, G. P. A. Yap and S. J. N. Burgmayer, *Inorg. Chem.*, 2019, 58, 5134–5144.
- (171) G. J. Brewer, P. Hedera, K. J. Kluin, M. Carlson, F. Askari, R. B. Dick, J. Sitterly and J. K. Fink, Arch. Neurology, 2003, 60, 379–385.
- (172) G. Krüss, Justus Liebigs Ann. Chem., 1883, 225, 1–57.
- (173) E. Simhon, N. Baenziger, M. Kanatzidis, M. Draganjac and D. Coucouvanis, J. Am. Chem. Soc., 1981, 103, 1218–1219.
- (174) M. Poisot, W. Bensch, S. Fuentes and G. Alonso, *Thermochim. Acta*, 2006, 444, 35–45.
- (175) M. Draganjac, E. Simhon, L. Chan, M. Kanatzidis, N. Baenziger and D. Coucouvanis, *Inorg. Chem.*, 1982, **21**, 3321–3332.
- (176) C. A. Goddard and R. Holm, *Inorg. Chem.*, 1999, **38**, 5389–5398.
- (177) E. S. Davies, G. M. Aston, R. L. Beddoes, D. Collison, A. Dinsmore, A. Docrat, J. A. Joule, C. R. Wilson and C. D. Garner, J. Chem. Soc., Dalton Trans., 1998, 3647–3656.
- (178) A. Samotus, M. Dudek and A. Kanas, J. Inorg. Nucl. Chem., 1975, 37, 943–948.

- (179) P. Hohenberg and W. Kohn, *Phys. Rev.*, 1964, **136**, B864.
- (180) W. Kohn and L. J. Sham, *Phys. Rev.*, 1965, **140**, A1133.
- (181) E. S. Kryachko and E. V. Ludena, *Phys. Rep.*, 2014, **544**, 123–239.
- (182) N. H. March, Adv. Phys., 1957, 6, 1–101.
- (183) E. H. Lieb, Rev. Mod. Phys., 1981, **53**, 603.
- (184) J. P. Perdew, A. Ruzsinszky, G. I. Csonka, O. A. Vydrov, G. E. Scuseria, L. A. Constantin, X. Zhou and K. Burke, *Phys. Rev. Lett.*, 2008, **100**, 136406.
- (185) J. C. Slater, Phys. Rev., 1930, **36**, 57.
- (186) S. F. Boys, *Proc. Royal Soc. A*, 1950, **200**, 542–554.
- (187) V. A. Rassolov, J. A. Pople, M. A. Ratner and T. L. Windus, J. Chem. Phys., 1998, 109, 1223–1229.
- (188) C. Lee, W. Yang and R. G. Parr, *Phys. Rev. B*, 1988, **37**, 785.
- (189) S. H. Vosko, L. Wilk and M. Nusair, Can. J. Phys., 1980, 58, 1200–1211.
- (190) P. J. Stephens, F. J. Devlin, C. F. Chabalowski and M. J. Frisch, J. Phys. Chem., 1994, 98, 11623–11627.
- (191) Y. Izumi, T. Glaser, K. Rose, J. McMaster, P. Basu, J. H. Enemark, B. Hedman, K. O. Hodgson and E. I. Solomon, J. Am. Chem. Soc., 1999, 121, 10035–10046.
- (192) A. D. Becke, *Phys. Rev. A*, 1988, **38**, 3098.
- (193) J. P. Perdew, Phys. Rev. B, 1986, **33**, 8822.
- (194) K. Peariso, R. L. McNaughton and M. L. Kirk, J. Am. Chem. Soc., 2002, 124, 9006–9007.
- (195) K. Pal, P. K. Chaudhury and S. Sarkar, Chem. Asian J., 2007, 2, 956–964.

- (196) R. H. W. J. Ditchfield, W. J. Hehre and J. A. Pople, J. Chem. Phys., 1971, 54, 724–728.
- (197) P. J. Hay and W. R. Wadt, J. Chem. Phys., 1985, 82, 270–283.
- (198) Y. Yang, M. N. Weaver and K. M. Merz Jr, J. Phys. Chem. A, 2009, 113, 9843–9851.
- (199) W. J. Stevens, M. Krauss, H. Basch and P. G. Jasien, Can. J. Chem., 1992,70, 612–630.
- (200) J. Snijders, P. Vernooijs and E. Baerends, Atom. Data Nucl. Data, 1981,26, 483–509.
- (201) A. Schäfer, C. Huber and R. Ahlrichs, J. Chem. Phys., 1994, 100, 5829–5835.
- (202) D. Andrae, U. Haeussermann, M. Dolg, H. Stoll and H. Preuss, *Theor. Chim. Acta*, 1990, 77, 123–141.
- (203) K. B. Wiberg, J. Comput. Chem., 2004, 25, 1342–1346.
- (204) J. Tao, J. P. Perdew, V. N. Staroverov and G. E. Scuseria, *Phys. Rev. Lett.*, 2003, 91, 146401.
- (205) F. Neese, Wiley Interdiscip. Rev. Comput. Mol. Sci., 2012, 2, 73–78.
- (206) F. Neese, F. Wennmohs, U. Becker and C. Riplinger, *J. Chem. Phys.*, 2020, **152**.
- (207) F. Weigend and R. Ahlrichs, Phys. Chem. Chem. Phys., 2005, 7, 3297–3305.
- M. J. Frisch, G. W. Trucks, H. B. Schlegel, G. E. Scuseria, M. A. Robb,
 J. R. Cheeseman, G. Scalmani, V. Barone, G. A. Petersson, H. Nakatsuji,
 X. Li, M. Caricato, A. V. Marenich, J. Bloino, B. G. Janesko, R. Gomperts,
 B. Mennucci, H. P. Hratchian, J. V. Ortiz, A. F. Izmaylov, J. L. Sonnenberg,
 D. Williams-Young, F. Ding, F. Lipparini, F. Egidi, J. Goings, B. Peng,

- A. Petrone, T. Henderson, D. Ranasinghe, V. G. Zakrzewski, J. Gao, N. Rega, G. Zheng, W. Liang, M. Hada, M. Ehara, K. Toyota, R. Fukuda, J. Hasegawa, M. Ishida, T. Nakajima, Y. Honda, O. Kitao, H. Nakai, T. Vreven, K. Throssell, J. A. Montgomery, Jr., J. E. Peralta, F. Ogliaro, M. J. Bearpark, J. J. Heyd, E. N. Brothers, K. N. Kudin, V. N. Staroverov, T. A. Keith, R. Kobayashi, J. Normand, K. Raghavachari, A. P. Rendell, J. C. Burant, S. S. Iyengar, J. Tomasi, M. Cossi, J. M. Millam, M. Klene, C. Adamo, R. Cammi, J. W. Ochterski, R. L. Martin, K. Morokuma, O. Farkas, J. B. Foresman and D. J. Fox, *Gaussian 16 Revision C.01*, Gaussian Inc. Wallingford CT, 2016.
- (209) Y. Jean, Molecular orbitals of transition metal complexes, Oxford University Press, Oxford, UK, 2005.
- (210) A. D. Beck, J. Chem. Phys., 1993, **98**, 5648–6.
- (211) C. R. Groom, I. J. Bruno, M. P. Lightfoot and S. C. Ward, Struct. Sci., 2016, 72, 171–179.
- (212) N. Maheswari and G. Muralidharan, Appl. Surf. Sci., 2017, 416, 461–469.
- (213) S. K. Das, P. K. Chaudhury, D. Biswas and S. Sarkar, J. Am. Chem. Soc., 1994, 116, 9061–9070.
- (214) S. S. Saleem and G. Aruldhas, *Pramana J. Phys.*, 1983, **97**.
- (215) C. W. Kee, J. Chem., 2015, **2015**.
- (216) J.-D. Chai and M. Head-Gordon, J. Chem. Phys., 2008, 128.
- (217) A. D. Becke, J. Chem. Phys., 1992, 96, 2155–2160.
- (218) J. P. Perdew, M. Ernzerhof and K. Burke, J. Chem. Phys., 1996, 105, 9982–9985.
- (219) C. Adamo and V. Barone, J. Phys. Chem., 1999, 110, 6158–6170.

- (220) A. D. Becke, J. Chem. Phys., 1997, 107, 8554–8560.
- (221) M. L. Kirk, J. Lepluart and J. Yang, J. Inorg. Biochem., 2022, 235, 111907.
- (222) N. Elgrishi, K. J. Rountree, B. D. McCarthy, E. S. Rountree, T. T. Eisenhart and J. L. Dempsey, J. Chem. Ed., 2018, 95, 197–206.
- (223) R. Holze, R. Compton and C. Banks, *Understanding cyclic voltammetry*, Springer, Berlin, 2007.
- (224) A. Bard and L. Faulkner, *Electrochemical Methods, Fundamentals and Applications*, Wiley, Weinheim, Germany, 2000.
- (225) P. T. Kissinger and W. R. Heineman, J. Chem. Ed., 1983, 60, 702.
- (226) J. F. Rusling and S. L. Suib, Adv. Mater., 1994, 6, 922–930.
- (227) T. P. Silverstein, J. Chem. Educ., 2012, 89, 1159–1167.
- (228) C. Reichardt and T. Welton, Solvents and solvent effects in organic chemistry, John Wiley & Sons, New York, 2011.
- (229) W. J. Geary, Coord. Chem. Rev., 1971, 7, 81–122.
- (230) V. V. Pavlishchuk and A. W. Addison, *Inorg. Chim. Acta*, 2000, **298**, 97–102.
- (231) G. Balducci and G. Costa, J. Electroanal. Chem., 1993, **348**, 355–365.
- (232) Y. Wang, Y. Xie, P. Wei, H. F. Schaefer and G. H. Robinson, *Dalton Trans.*, 2019, **48**, 3543–3546.
- (233) Y. Tamaki, K. Koike, T. Morimoto and O. Ishitani, *J. Catal.*, 2013, **304**, 22–28.
- (234) J. M. Berg and R. Holm, J. Am. Chem. Soc., 1985, **107**, 917–925.
- (235) R. S. Nicholson and I. Shain, *Anal. Chem.*, 1964, **36**, 706–723.
- (236) J. Saveant and E. Vianello, *Electrochim. Acta*, 1965, **10**, 905–920.

- (237) J. Savéant and E. Vianello, *Electrochim. Acta*, 1967, **12**, 629–646.
- (238) U. J. Kilgore, J. A. Roberts, D. H. Pool, A. M. Appel, M. P. Stewart, M. R. DuBois, W. G. Dougherty, W. S. Kassel, R. M. Bullock and D. L. DuBois, J. Am. Chem. Soc., 2011, 133, 5861–5872.
- (239) C. Fischer and L. Fischer, Comparative Kinetics of Enzymes and Models, Royal Society of Chemistry, London, 2016.
- (240) C. Adamo, M. Cossi and V. Barone, J. Mol. Struct. THEOCHEM, 1999, 493, 145–157.
- (241) CrystalClear-SM Expert, Rigaku Americas Corporation, The Woodlands, Texas, USA, 2013.
- (242) G. M. Sheldrick, Acta Cryst. A, 2015, 71, 3–8.
- (243) G. M. Sheldrick, Acta Cryst. C, 2015, 71, 3–8.